The Structural Basis for Ion Selectivity in Transition-Metal Ion Transporters of the SLC11/NRAMP Family

Dissertation

zur Erlangung der naturwissenschaftlichen Doktorwürde
(Dr. sc. nat.)

vorgelegt der

Mathematisch-naturwissenschaftlichen Fakultät der

Universität Zürich

von

Ines Anna Ehrnstorfer

aus
Österreich

Promotionskomitee

Prof. Dr. Raimund Dutzler (Leitung und Vorsitz)
PD Dr. Ian Forster
Prof. Dr. Martin Jinek

Zürich, 2015

To My Beloved Grandmothers
For Their Encouragement And Love.

*Ursula Ehrnstorfer *30.9.1925 - †19.8.2009*
*Anna Aher *9.8.1916 - †22.2.2010*

ACKNOWLEDGEMENTS

These last years have been an incredible experience for me: a turbulent start was followed by period of meager results that, mid-way through my thesis, serendipitously transitioned into a fruitful 2013 and an unparalleled 2014.

Many people have contributed, either directly or indirectly, to the successful completion of this work. Hereafter, I would like to convey my heart-felt thanks to some in particular.

Firstly, I wish to thank my supervisor Raimund Dutzler for the opportunity to carry out my PhD thesis in his lab, for providing an excellent scientific environment and for his support and trust throughout my time in his group.

I am grateful to Ian Forster for being part of my thesis committee and for generously sharing his professional insights into electrophysiology.

I would like to thank Martin Jinek for being on my thesis committee and for helping me when I encountered early problems in coot.

My thanks also extends to my colleagues at the institute who provided scientific advice and the necessary infrastructure. To this end, I would like to thank Stefan and Steve for keeping everything IT-related up and running, and for poster printing under short deadlines; Adi, Sascha and Lukas for keeping an eye on our precious equipment, including emergency repairs, and for the self-made HPL6 - it is gorgeous and I love it! Many thanks to our secretaries for keeping our institute running, and especially Sabine

for her kind and competent assistance for all organizational matters. Of course, I cannot miss thanking Beat and Céline of our crystallization-facility, who are both incredibly professional and cooperative, and always cheerful. I enjoyed our (scientific) chats and our memorable competition on track 12 at the SOLA! A special thanks goes to all of my L-floor colleagues for our collaborations and countless "hallway"-chats about science and beyond (and especially Alessia, Magda and Heidi - my enzyme kinetics guru).

The former and current members of the Dutzler lab provided help, support and scientific discussions concerning my project and a good atmosphere in general – I am grateful for this. I want to thank Jürg and Fabian for their contribution to the "DMT project" during their Master theses and for the nice time we had during their stay in the Dutzler lab.

In particular I am grateful to:

Eric: For so many things! For the relaxing atmosphere and the great music in L38, for being a pleasant bench mate, for your unique humor, for sharing funny stories of your PhD-time, for cheering me up in tough times and for our numerous discussions about everything under the sun; I cherish your great knowledge - thank you for answering my countless scientific questions with great patience - usually with article references including authors and year of publication!

Yvonne: Thank you for your endless effort to make our lab a pleasant and fun place to be. I have rarely met a person as generous and altruistic as you. You have my maximum respect for this!

Siby: thank you for your continuous cheerfulness "Little Miss Sunshine"; our tea breaks were always welcome to recharge our batteries on long and cold working days. Merci vielmal für dini Geduld und Higab mit dere du immer no versuechsch mir richtigs Schwiizerdütsch bizbringe.

Vandy: Thank you for the nice atmosphere in L38 and in the electrophysiology lab. Hope to see you soon at the micropipette puller!

Emilie: Thank you for sharing all the ups and downs during the PhD studies, according to the motto: A problem shared is a problem halved. We can do it!

Cristina & Cristina: I want to thank both of you for being the most wonderful Cristina's I have ever known. Although you both joined the lab only recently, we have had lots of fun together! Cristina, working with you in a team has been a great experience and I am looking forward to coming back to the lab to push our projects forwards together. Cristina, thank you for bringing a fresh breeze into the lab, your lively character is contagious!

Special thanks go to Antonio Baici for sharing his skills and passion for the violin in spontaneous private lessons with a novice like me.

Last but certainly not least, I would like to thank my partner Murat who embarked with me on this journey - unaware of what it would take – or how long! Thank you for your continuous support and for your understanding when science once again took priority.

Liebe Eltern, ich danke euch für eure bedingungslose Unterstützung und euer Vertrauen in mich. Ohne euch wäre all dies unmöglich gewesen. Vielen Dank!

Table of Contents

LIST OF FIGURES

LIST OF TABLES

LIST OF ABBREVIATIONS

BLAST	Basic local alignment search tool
CDR	Complementarity determining region
CMC	Critical micelle concentration
DcytB	Duodenal cytochrome B
DDM	n-dodecyl- β -D-maltopyranosid
DM	n-decyl- β -D-maltopyranosid
DSMZ	Deutsche Sammlung von Mikroorganismen und Zellkulturen
EGFP	Enhanced green fluorescent protein
ELISA	Enzyme-linked immunosorbent assay
FPN	Ferroportin
FSEC	Fluorescence size exclusion chromatography
FX	Fragment-exchange
GFP	Green fluorescent protein
HA	hemagglutinin A
Hepcidin	Hepatic bactericidal protein
HIF	Hypoxia-inducible factor
HILIDE	High concentrations of lipid and detergent method
HJV	Hemojuvelin
HPLC	High-performance liquid chromatography
HRG1	Heme responsive gene 1
HRP	Horseradish peroxidase
IMAC	Immobilized metal affinity chromatography
IPTG	Isopropyl- β -D-thiogalactopyranosid
IRE	Iron responsive element
ITC	Isothermal titration calorimetry
LPR	Lipid to protein ratio
MALDI	Matrix assisted laser desorption/ionization
MBP	Maltose biinding protein
MS	Mass spectrometry
NCS	Non-crystallographic symmetry
NM	n-Nonyl- β -D-Maltopyranoside
NRAMP	Natural resistance-associated macrophage protein
NRAT	NRAMP aluminium transporter
OM	n-Octyl- β -D-Maltopyranoside
PEG	Polyethylen glycol
ROS	Reactive oxygen spicies
SAD	Single anomalous dispersion
ScFv	Single chain variable fragment
SDS-PAGE	Sodium dodecyl sulfate-polyacrylamide gel-electrophoresis
SEC	Size exclusion chromatography
SLC	Solute carrier
SMAD	*C. elegans* small body size & MAD *D. melanogaster* mothers against decapentaplegic
STEAP	Six-transmembrane epithelial antigen of the prostate
TFR	Transferrin receptor
UTR	Untranslated region

ABSTRACT

Transporters of the SLC11 family catalyze the selective flow of divalent metal ions across cellular membranes of pro- and eukaryotic organisms. Mammals express two SLC11 proteins, NRAMP1 and DMT1 (or NRAMP2). These transporters play an important role in iron uptake and supply, the recycling of iron from senescent erythrocytes and they are part of the host defense strategy against bacterial invaders. Whereas the dysfunction of DMT1 causes iron-storage diseases, such as hereditary hemochromatosis and hypochromic microcytic anemia, mutations in NRAMP2 are associated with an increased susceptibility to bacterial infections. With respect to sequence the SLC11 family is highly conserved from pro- to eukaryotes with members found in all kingdoms of life. The properties of mammalian NRAMP proteins have been studied by electrophysiology and in rodent animal models. Besides the profound functional characterization detailed structural knowledge was thus far not available. To understand the mechanisms of divalent metal-ion binding and transport, high-resolution structural data is inevitable.

During the course of my PhD studies it was my aim to determine the first high-resolution structure of a SLC11 family member and to characterize its ion binding and transport properties. Due to the numerous sequenced bacterial genomes and the high degree of conservation between NRAMP proteins, bacterial homologs were chosen as suitable candidates for structural studies. In the course of this work I have cloned more than 100 prokaryotic SLC11 homologs and studied their overexpression properties in *Escherichia coli* and assessed their biochemical behavior in a detergent solubilized state. After selecting few proteins with superior properties I succeeded to crystallize one

homolog from *Staphylococcus capitis* (ScaDMT), although the crystals only diffracted to low (6.5 Å) resolution. To improve the crystallization and diffraction properties of ScaDMT I have investigated N-terminal truncations of the protein, which allowed the identification of a truncated version of ScaDMT ($ScaDMT^{tru}$) that diffracted to slightly higher resolution (5.5-6.0 Å). However, also these crystals were of insufficient quality for structure determination. In another attempt to improve the resolution ScaDMT-specific nanobodies were generated in collaboration with Jan Steyaert's laboratory at the free University of Brussels. The nanobodies were used for co-crystallization of complexes with the full-length and truncated version of ScaDMT. Crystallization of one nanobody in combination with the truncated version of ScaDMT has allowed structure determination of the complex at 3.1 Å resolution. Phases were obtained by the single anomalous dispersion method, which required collection of anomalous data from crystals grown with seleno-methionine-derivatized protein.

ScaDMT adopts a familiar fold that was previously identified in the amino-acid transporter LeuT and other unrelated transport proteins. The transporter crystallized in an inward-facing conformation with a substrate-binding site that is accessible from the cytoplasm. Putative substrates including Mn^{2+}, Fe^{2+} and Cd^{2+} were soaked into the crystals, which allowed the identification of a highly conserved binding site located in the center of the protein. In parallel cadmium binding to ScaDMT was assayed by isothermal titration calorimetry (ITC), which revealed the binding to a single binding site with micromolar affinity. To investigate its functional properties, a fluorescence-based assay with proteoliposomes containing the reconstituted transporter was established that confirmed the transport of the transition-metal ions Mn^{2+}, Cd^{2+}, Co^{2+} and Ni^{2+}. Undisturbed uptake of manganese in the presence of high concentrations of earth-alkaline metal ions revealed that neither Ca^{2+} nor Sr^{2+}or Ba^{2+} are transported by ScaDMT. Point mutations of metal ion binding site residues (i.e. Asp49, Asn52, Met226) weakened binding of Cd^{2+}, as confirmed by ITC. Investigation of the transport properties of corresponding residues in human DMT1, by two-electrode voltage-clamp electrophysiology revealed a 19 fold higher K_m value for the asparagine mutant (N89A). When mutating the binding site aspartate (D86A) or methionine (M265A) no cadmium-induced currents could be observed.

The results of this thesis thus have allowed me to provide first structural insight into the SLC11 family by determining the first high-resolution structure of a close prokaryotic homolog. This structure revealed the location of conserved residues in the

center of the protein that coordinate divalent transition-metal ions but not alkaline earth metal ions. The results of this work have thus paved the war for future investigations to unravel the mechanism of ion transport of this important class of membrane proteins.

ZUSAMMENFASSUNG

Proteine der Solute carrier 11 (SLC11) Familie katalysieren den selektiven Fluss divalenter Metallionen durch die Membranen pro- und eukaryotischer Organismen. Säugetiere besitzen zwei verwandte SLC11 Proteine: NRAMP1 und DMT1 (oder NRAMP2). Beide Transporter spielen eine wichtige Rolle sowohl bei der Aufnahme und Verteilung von Eisen im Körper als auch bei dessen Wiedergewinnung aus alternden Erythrozyten. In Makrophagen ist NRAMP1 ausserdem ein wichtiger Teil des Immunsystems im Kampf gegen bakterielle Eindringlinge. Ist DMT1 genetisch verändert und als Konsequenz nicht funktionsfähig führt dies zu Eisenspeicherkrankheiten wie der erblich bedingten Hämochromatose oder der hypochromischen microzytischen Eisenmangelanämie. Mutationen in NRAMP2 sind ferner mit einer erhöhten Infektanfälligkeit für bestimmte bakterielle Infektionen verbunden. Die Funktion der SLC11 Transporter wurde zuvor mittels elektrophysiologischer Studien und anhand von Tiermodellen, untersucht. Obgleich es zahlreiche Studien zur Funktion dieser Eisentransport-Proteine gibt, war ihr struktureller Aufbau bisher unbekannt. Strukturdaten bei hoher Auflösung sind allerdings unerlässlich um den Transportmechanismus von Eisen und anderen Metallionen im Detail zu verstehen.

Aus diesem Grund habe ich es mir als Ziel gesetzt, im Verlauf meiner Doktorarbeit die erste hochaufgelöste Röntgenkristallstruktur eines Mitglieds der SLC11-Familie aufzuklären, und dessen Ionenbindung und Transporteigenschaften genauer zu untersuchen. Aufgrund der hohen Konservierung innerhalb der SLC11 Familie sind bakterielle Homologe attraktive Kandidaten für die Röntgenkristallstrukturanalyse. Auf

die genetische Information dieser bakteriellen Transporter kann mit Hilfe von Dantenbanken, die eine Vielzahl vollständig sequenzierter bakterieller Genome enthalten, zurückgegriffen werden. Während meiner Arbeit an diesem Projekt habe ich über 100 prokaryotische SCL11-Homologe kloniert, sie in *E. coli* über-exprimiert und ihre biochemischen Eigenschaften, nach Extraktion mit Detergenzien, getestet. Mit Hilfe dieser Strategie ist es mir gelungen einige (wenige) Homologe mit herausragenden biochemischen Eigenschaften zu identifizieren. Obwohl ich ein Homolog (ScaDMT), aus dem Bakterium *Staphylococcus capitis*, erfolgreich kristallisieren konnte waren die Diffraktionseigenschaften dieser Kristalle mit einer maximalen Auflösung von 6.5 Å nicht von ausreichender Qualität für die Strukturaufklärung. Um dies zu verbessern habe ich systematisch N-terminal verkürzte Konstrukte getestet, wobei es mir gelungen ist Kristalle eines verkürzten Proteins ($ScaDMT^{tru}$) zu erhalten. Leider waren die Kristalle des $ScaDMT^{tru}$ -Konstruktes für die Strukturaufklärung ebenfalls ungeeignet, da diese sich nur marginal besser verhielten (5.5-6.0 Å Auflösung) als die (Kristalle) des ursprünglichen Konstrukts. In einem weiteren Versuch die Qualität der Kristalle zu verbessern habe ich, in Kollaboration mit Jan Steyaerts Labor an der Freien Universität Brüssel, Lama-Nanobodies, die spezifisch an ScaDMT binden, generiert. Nanobody-Transporter-Komplexe wurden sowohl mit ScaDMT als auch mit $ScaDMT^{tru}$ für Kristallisationsexperiments genutzt was mir erlaubt hat den entscheidenden Durchbruch zur Strukturaufklärung zu erzielen. Daten mit einer Auflösung von 3.1 Å konnten von einem Komplex, bestehend $ScaDMT^{tru}$ und einem Nanobody, gesammelt werden. Das Phasenproblem wurde mittels Anomaler Streuexperimente von Kristallen, die aus mit Seleno-Methionin derivatisiertem Protein hergestellt wurden, gelöst.

Die ScaDMT Struktur zeigt eine bekannte Faltung der Proteinkette, die zuvor in anderen Transportproteinen, wie dem Aminosäure Transporter LeuT, gefunden wurde. In den Kristallen, liegt ScaDMT in einer nach innen gewandten Konformation vor, in der die Substratbindungsstelle von der cytoplasmatischen Seite her zugänglich ist. Zur Bestimmung der Substratinteraktion wurden Kristalle mit den divalenten Metallionen Mangan, Eisen und Cadmium derivatisiert. Dadurch konnte eine Ionenbindungsstelle im Protein identifiziert werden, die aus stark konservierten Aminosäureseitenketten besteht. Mittels Titrationskalorimetrie (ITC) konnte ich nachweisen, dass Cadmium mit mikromolarer Affinität an ScaDMT bindet. Der selektive Import von Mn^{2+}, Cd^{2+}, Co^{2+} und Ni^{2+} in Proteoliposomen, die ScaDMT enthalten, konnte mittels Metall-sensitiver Fluorophore gemessen werden. Diese Versuche haben auch gezeigt dass hohe

Konzentrationen von Kalzium, Strontium oder Barium den Import von Mangan nicht beeinflussen, was darauf schliessen lässt, dass diese keine Substrate für ScaDMT sind. ITC Messungen von Punktmutanten einzelner Reste in der Substratbindungsstelle zeigten eine stark reduzierte Affinität für Cadmium. Um die Konservierung der Ionenbindungsstelle im humanen Transporter zu untersuchen habe ich parallel die entsprechenden Reste in DMT1 mutiert und mit Hilfe elektrophysiologischer Methoden untersucht. Die Messungen zeigten einen starken Einfluss der Mutationen auf die Transporteigenschaften, mit einer Mutante bei der die Ionenabhängigkeit zu höheren Konzentrationen verschoben ist und zwei weiteren Mutanten die keinerlei Cadmium-induzierten Transport mehr erlauben.

Die Ergebnisse meiner Doktorarbeit geben Einblick in die erste hochaufgelöste Röntgenkristallstruktur eines nahen bakteriellen Verwandten der Eisentransporter der SLC11 Familie. Dank dieser Struktur konnte eine Substratbindungstasche identifiziert werden, welche sich im Zentrum des Proteins befindet. Die Aminosäurereste der Bindungstasche koordinieren divalente Übergangsmetalle aber keine Erdalkalimetalle. Diese Arbeit bildet deshalb eine wichtige Grundlage um den Transportmechanismus dieser Membranproteine im Detail verstehen zu können.

1. INTRODUCTION

1.1. Principles of ion transport

Cells are enclosed by a physical boundary, the lipid membrane that separates the interior from the exterior environment. Lipid Membranes are mainly composed of phospholipids and proteins. Phospholipids are amphiphilic molecules comprised of a hydrophilic head group, usually containing phosphate attached as ester to a glycerol molecule, and a hydrophobic tail of two fatty acid esters linked to the glycerol. In water phospholipids spontaneously assemble to a lipid bilayer, where the head groups are exposed to the aqueous solution and the polar tails point towards the interior. This barrier is impermeable for hydrophilic molecules. To allow communication and exchange between the internal and external environment, transport proteins are embedded in the membrane and catalyze the movement of various compounds through the lipid bilayer.
The importance of these molecules, is reflected in the large number of genes encoding membrane proteins, which make up ~26 % of all genes in humans (Fagerberg et al., 2010). Depending on the underlying mechanism by which membrane proteins facilitate the transport of solutes they can be divided into two major classes, namely channels and transporters.

Channels allow their substrates, predominantly ions, to flow along their electrochemical gradient, which is dependent on the membrane potential and the ion concentration gradient. This process is independent of metabolic energy and is thus referred to as passive transport or facilitated diffusion. Ion channels are conductors usually selective for a specific ion or a class of ions (e.g. anions or cations). At the narrowest part of the pore, ion channels have a so-called selectivity filter, which is responsible for the discrimination of the ions. Because under typical cellular conditions ions need to be kept at non-equilibrium conditions, opening and closing of most ion channels is regulated. Ion channel gating can be triggered by different stimuli, such as changes in membrane potential (voltage-gating), by the intra- or extracellular binding of ligands (ligand-gating), by mechanical forces (in mechanosensitive channels), light (light gating) or temperature (temperature-gating).

In contrast to channels many transporters are able to catalyze the translocation of ions against their electrochemical potential. This process is called active transport because an energy source is needed in order to allow this thermodynamically unfavorable process to take place. Primary active transports, such as ATP-driven pumps, couple chemical energy derived from the hydrolysis of ATP to the movement of ions against its

gradient. Secondary active transporters use the energy stored in the electrochemical gradient of another solute that is co-transported either in the same direction (symport) or the opposite direction (antiport). A prerequisite, for the efficient coupling of ion transport, is the presence of at least two distinct states in which the binding site for the molecules is accessible to only one side of the membrane at a time. This principle underlies the alternating access model, first proposed by P. Mitchell in 1957 (Mitchell, 1957) and later refined by O. Jardetzky in 1966 (Jardetzky, 1966). It is the most widely accepted scheme to describe the series of conformational changes necessary for ion transport.

Our understanding of how membrane transport proteins work has enormously advanced over the last decades. We now know better how they are integrated in the membrane during translation (Park and Rapoport, 2012; White and von Heijne, 2004), how they are regulated (Hicke and Dunn, 2003), how proteins might have evolved that share the same fold but perform completely unrelated tasks (Bernsel et al., 2008; Fagerberg et al., 2010; von Heijne, 2006) and in many cases we have gained knowledge on the functions of membrane proteins in health and disease (Ng et al., 2012; Sanders and Nagy, 2000). Structural biology has significantly contributed to the present understanding of membrane proteins. Despite the recent advances, there are still many open questions concerning membrane transport processes that are to date not understood.

1.2. The solute carrier 11 family

With over 384 members the solute carrier families constitute the second largest family of membrane proteins, following the G protein-coupled receptors with over 800 genes. The SLC tables classify these human membrane transport proteins based on their function. In general these transporters are membrane proteins with an α-helical transmembrane core. Different SLC families do not share significant sequence homology. Within the families the members need to share a sequence homology of at least 20-25%. Members of the currently 52 SLC families transport a variety of solutes ranging from organic and inorganic ions to complex organic molecules such as sugars and fatty acids. The SLC transporters also include the Multidrug and toxin extrusion (MATE) family (SLC47). From a mechanistic perspective, SLC proteins can be either secondary active or facilitative transporters (uniporters).

In humans the solute carrier 11 family consists of two members, the proton-coupled divalent metal ion transporters 1 and 2 also known as natural resistance-associated macrophage protein NRAMP1 and NRAMP2 (DMT1). In the late 70s of the last century J. Plant and A.A. Glynn identified a gene locus on mouse chromosome 1 that conveys resistance to several intracellular pathogens, including *Salmonella typhimurium*, *Leeishmania donovani*, *Mycobacterium bovis* and *Mycobacterium lephraemurium* (Plant and Glynn, 1974, 1976, 1979). In 1993 Vidal et al. proposed, based on the tissue distribution of mouse NRAMP 1 mRNA transcripts and computer-assisted analysis, that the gene is localized to macrophages and encodes for a membrane transport protein (Vidal et al., 1993). In 1994 two groups simultaneously published the successful cloning of the human cDNA of NRAMP (later NRAMP1) located on chromosome 2 (Cellier et al., 1994; Kishi, 1994). Remarkably, in the publication of Kishi the first 67 residues are not present and the gene starts only 6 residues before the DPGN motif. Soon after that, the second family member NRAMP2 was identified in several mammals (Cellier et al., 1995; Dosik et al., 1994; Gruenheid et al., 1995). Human NRAMP2 is located on chromosome 12 and was successfully cloned by Vidal et al. in 1995.

1.3. NRAMP1 and NRAMP2

The first functional characterized mammalian homolog was ratNRAMP2 in 1997 (Gunshin et al., 1997). The authors of this study have overexpressed ratNRAMP2 in *Xenopus laevis* oocytes and measured the transport of Fe^{2+} but also other transition metal ions such as Mn^{2+}, Co^{2+}, Cd^{2+}, Cu^{2+}, Ni^{2+}, Pb^{2+} and to a very low extent Zn^{2+}, by two-electrode voltage-clamp electrophysiology. By this they revealed the broad substrate specificity of this transport family and in further experiments they could show that the transport of Fe^{2+} is driven by a proton electrochemical gradient. Via *in situ* hybridization of ratNRAMP2 mRNA with a labeled cRNA probe in cryosections of different tissues, the authors were able to identify the distribution of rat NRAMP2 mRNA in the duodenum and to a lesser extent in kidney, liver, brain, heart, lung and testis (Gunshin et al., 1997).

Human NRAMP1 and NRAMP2 share a sequence identity of ~63% and a similarity of ~73%. Depending on the isoform they are between 550 and 598 amino acids long (uniprot NRAMP1 P49279, NRAMP2 P49282).

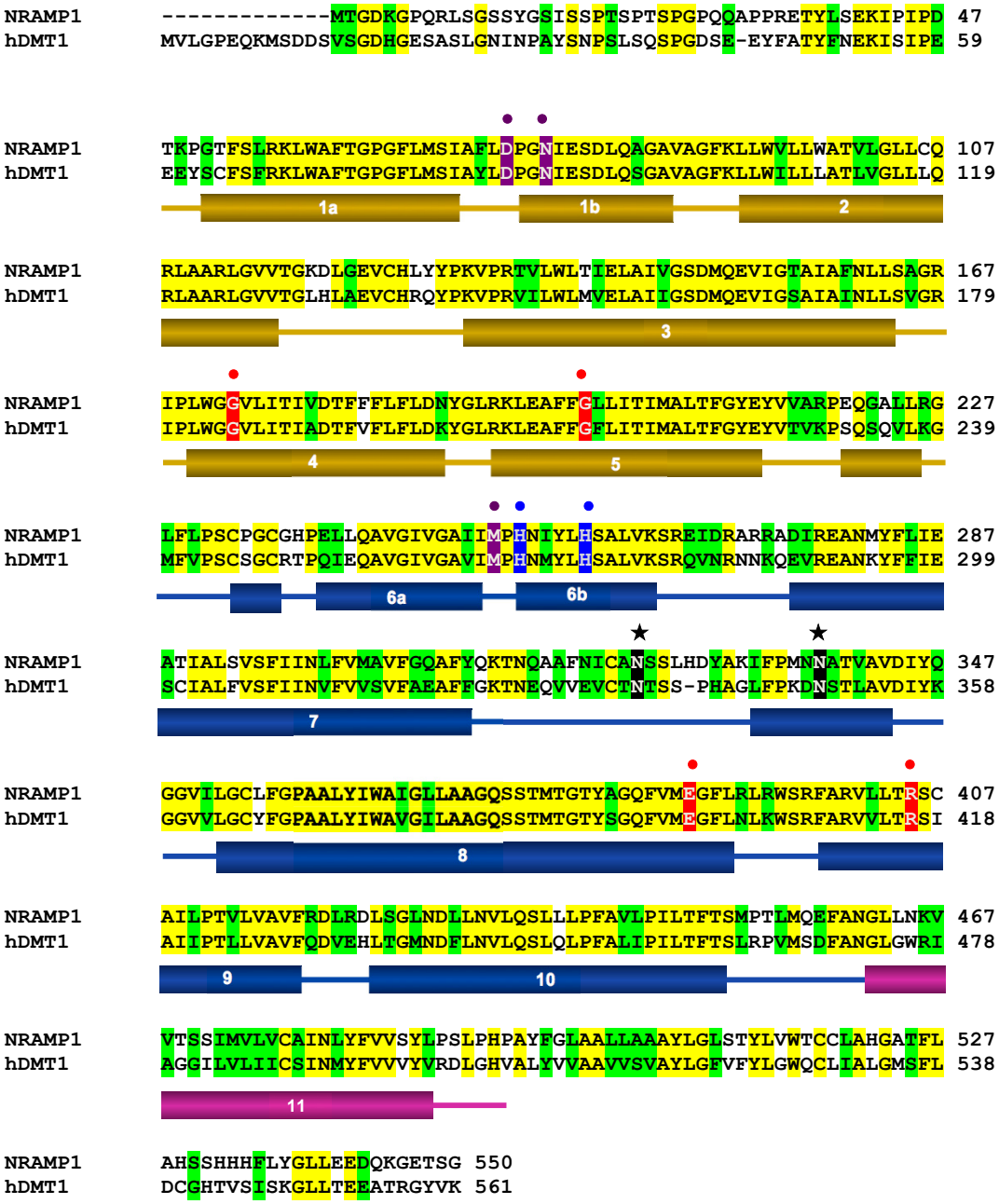

Figure 1 Sequence alignment of NRAMP1 and NRAMP2.

The two sequences were aligned with CLUSTALW. Identical residues are shown in yellow, similar amino acids are marked in green. Secondary structure elements and binding site residues originate from an alignment with ScaDMT. Important residues are highlighted: The three residues involved in ion binding are marked in violet, the two highly conserved histidine residues are marked by a blue dot, residues associated with diseases are in red, the two N-linked glycosylation sites are marked with a black star.

In Figure 1 a sequence alignment of human NRAMP1 (isoform 1) and NRAMP2 (DMT1, isoform 3) is shown, where key residues highlighted.

Four splice-variants of NRAMP2 are known. They differ in their N and C terminal regions as well as in their 3` untranslated regions (UTRs). Isoform 1 (1B-IRE(+)) contains an iron responsive element (IRE) in the 3`UTR. Isoform 2 (1B-IRE(-)) has no IRE at its 3`UTR and additionally IRE(-) isoforms have a specific 3`coding region that is 25 amino acids in length and differs from the 18 amino acid C-terminal residues in IRE(+) isoforms. The variants 1A-IRE(+) and 1A-IRE(-) (isoform 3 and 4 respectively) start both from exon 1A, and have therefore N termini that are 29 amino acid longer than the 1B variants (Mackenzie et al., 2007). The iron responsive element is believed to modulate the mRNA stability in response to the iron status in the cell. The N-terminal variants (exon 1A or 1B) are thought to operate as cell specific signals for the subcellular localization in different compartments (Shawki et al., 2012). Mackenzie et al. found that all four human NRAMP2 variants transport iron with similar efficiency. Expression levels in *Xenopus laevis oocytes*, however, are significantly higher for isoform 3 (1AIRE(+), Mackenzie et al. 2007).

For human NRAMP1 no splice variants are known. Although there are two isoforms annotated in the UniProt Knowledgebase, the expression of only one has been confirmed. Based on our studies, it is questionable whether isoform 2 is a functional NRAMP transporter variant, since the missing amino acids 14 – 131 (compared to isoform 1) contain the highly conserved DPGN motif, which is part of the metal ion binding site identified in the bacterial homolog ScaDMT (Ehrnstorfer et al., 2014).

Both hNRAMP members are predicted to contain 12 transmembrane spanning helices, with both termini located in the cytoplasm. This predicted topology is valid for most of the eukaryotic family members. Some yeast homologs are predicted to have one additional transmembrane segment at their N terminus. Human NRAMP1 and NRAMP2 both contain two conserved N-linked glycosylation sites (N-X-S/T motif, Vidal et al. 1993). Originally they were predicted to be localized in a loop connecting TM 5 and 6. From the X-ray structure of a prokaryotic transporter described in this thesis it is now clear that the relevant asparagines (N365, N379) are located in the loop connecting TM7 and TM8 (Figure 2). hNRAMP1 and 2 are heavily glycosylated, on SDS-PAGE the glycosylation accounts for ~40% of the molecular weight of these proteins (Gruenheid et al., 1999). Disruption of the two glycosylation sites in hNRAMP1 did not change the correct endosomal targeting when overexpressed as EGFP-fusion

protein in RAW 264.7 cells (a mouse leukemic monocyte macrophage cell line). The authors thus concluded that the loss of glycosylation does not interfere with folding and sorting (in the glycosylation deficient mutant) of hNRAMP1 (White et al., 2004).

1.4. Physiological roles of mammalian NRAMP2/DMT1

NRAMP2 has two pivotal roles in our body: One is the uptake of dietary iron from the gut. This is why NRAMP2 is well expressed in enterocytes of the duodenum (Gunshin et al., 1997; Tandy et al., 2000). Inorganic iron that is ingested is mainly present in its ferric form as trivalent cation, since the divalent ferrous iron easily oxidizes. The ferrireductase Duodenal cytochrome B (DcytB) is expressed in the brush border of the duodenum, at the same locations as NRAMP. It has thus been suggested to reduce ferric iron to its ferrous form, which can subsequently be transported by NRAMP2 (McKie, 2008; McKie et al., 2001). The slightly acidic pH at the proximal duodenum (pH 6.0) may help to stabilize ferrous iron (Fallingborg, 1999). Remarkably, however, a study with DcytB knockout mice, did not show any pronounced effect on iron acquisition (Gunshin et al., 2005).

A small part of the ferrous iron that is imported by NRAMP2 is bound to ferritin and stored within the cells (Anderson et al., 2009; Andrews, 2008). The remainder is exported by ferroportin, an iron transporter located at the basolateral side of the enterocyte (Donovan et al., 2005). There the ferrous iron is oxidized by the ferroxidase hephaestin and bound to the soluble protein transferrin which transports iron in the body (Vulpe et al., 1999). Figure 2A illustrates the uptake and the export of iron in the enterocyte.

Transferrin is a ~80 kDa large glycoprotein that can tightly bind two ferric iron atoms at the neutral pH of the blood with an extraordinary small dissociation constant of 10^{-23} M (10 yocto mol) (De Domenico et al., 2008). Transferrin is expressed and secreted in hepatocytes (Zakin, 1992). Under physiological conditions 20-30% of the transferrin population circulating in the blood is present as apo-transferrin (with no iron bound). This reduces free plasma iron to a minimum, thus preventing that toxic iron radicals accumulate. In addition to its role in dietary iron absorption in enterocytes, NRAMP2 is essential for cells to take up iron from the blood (Gruenheid et al., 1999). In this tightly regulated process iron-bound transferrin binds to the transferrin receptor 1 TFR1, which is highly expressed in reticulocytes (erythroid precursors) and on all dividing cells (Ponka and Lok, 1999).

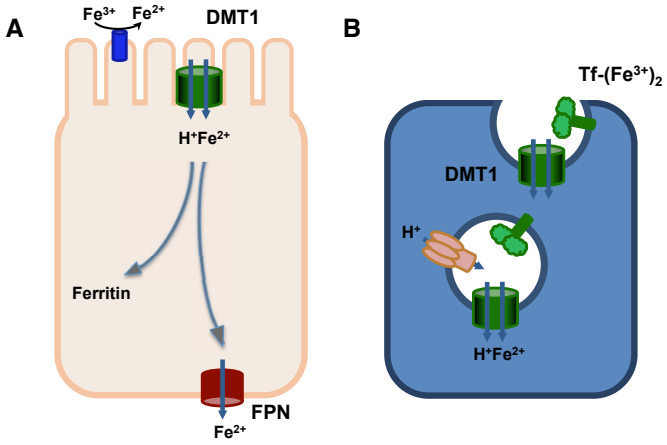

Figure 2 Dietary iron uptake in enterocytes and transferrin mediated iron uptake in cells. (A) The ferrireductase DcytB (blue) reduces ferric iron to ferrous iron, which is then imported along a proton gradient by the membrane protein DMT1 (green). Cytoplasmic iron is either bound to Ferritin or exported via the iron exporter Ferroportin (red). (B) Iron-bound transferrin is docking to the Transferrin receptor TFR1 (light green) at the plasma membrane. An endocytotic vesicles is formed. Upon acidification of the lumen, through an ATPase (brown), ferric iron is released from transferrin. A ferrireductase (not shown) reduces the iron, which then gets transported to the cytoplasm by DMT1.

The TFR1-transferrin-2Fe(III) complex is then internalized by receptor mediated endocytosis via clathrin-coated pits, which in turn fuse with endosomes (Jefferies et al., 1984; Soda and Tavassoli, 1984). Endosomes are acidified by an ATP-dependent proton pump resulting in a luminal pH of ~5.5, which causes the release of iron from the transferrin complex triggered by a conformational change of the protein, (Dautry-Varsat et al., 1983; Sipe and Murphy, 1991). A metalloreductase known as STEAP3 (6-transmembrane epithelial antigen of the prostate 3, Ohgami et al. 2006; Sendamarai et al. 2008), reduces ferric iron to ferrous iron, which is subsequently transported by NRAMP2 into the cytoplasm, where it is either bound by ferritin or exported by ferroportin (Munro and Linder, 1978). The transferrin receptor and apotransferrin remain bound to each other under acidic conditions. Only when reaching the cell surface via endosome fusion the complex disassembles once it faces the higher pH of the outside (Dautry-Varsat et al., 1983). The process is illustrated in Figure 2 (B).

1.5. Physiological roles of mammalian NRAMP1

In contrast to NRAMP2, the expression of NRAMP1 is primarily confined to phagocytes (which include neutrophils, eosinophils, basophils, monocytes and macrophages), the spleen and the liver (Govoni et al., 1997). NRAMP2 plays a critical role in the recycling of iron from senescent red blood cells (Soe-Lin et al., 2009). Human erythrocytes circulate on average 115 days in the blood (Mock et al., 2011) and they contain more than 50% of the total iron of the human body. Daily 200 billion of senescent erythrocytes are ingested by macrophages and degraded in their lysosomes (de Back et al., 2014). In order to regain the iron, the enzyme heme oxygenase 1 degrades heme and releases iron, biliverdin and carbon monoxide (Abraham and Kappas, 2008; Schacter, 1988). Subsequently the ferric iron is oxidized by the ferroxidase Seap3 (Zhang et al., 2012a). NRAMP1 (Soe-Lin et al., 2008) and NRAMP2 (Jabado et al., 2002; Soe-Lin et al., 2010) are transporting the ferrous iron from the phagocytotic vesicles to the cytosol where it is either bound to ferritin or exported via ferroportin (FPN, SLC40A1; Figure 3(A)). Due to the efficient recycling of iron in the human body we only need to take up 1-2 mg of dietary iron per day, albeit we daily need ~20-30 mg of iron for the production of new erythrocytes (Ganz and Nemeth, 2012).

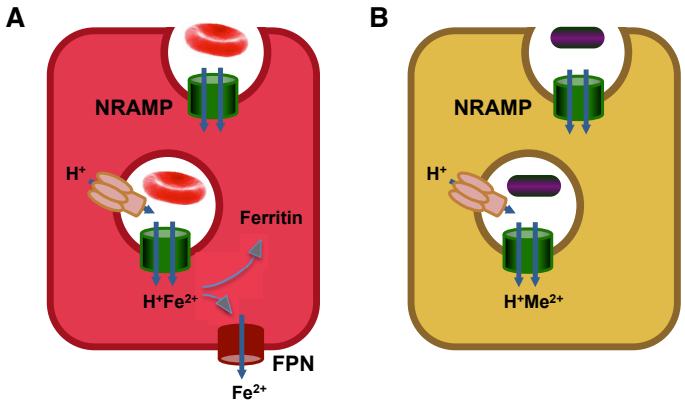

Figure 3 Iron recycling from erythrocytes and iron transport across phagosomes.
(A) The macrophage takes up senescent erythrocytes (red ellipsoid) via endocytosis. An ATPase (brown) acidifies the vesicle to allow the transport of iron to the cytoplasm mediated by NRAMP1 and DMT1 (green). Cytoplasmic iron will be exported via ferroportin (red) or gets bound to ferritin. (B) In case a bacterium is taken up from a macrophage by phagocytosis the principle is the same as shown in (A). The bacterium (violet) is trapped in the vesicle, which gets depleted from divalent metal ions through proton coupled metal symport via NRAMP1 and DMT1 (green).

Even before NRAMP1 was identified as a key player for iron recycling from senescent erythrocytes ingested by macrophages, the gene locus of NRAMP1 was associated with a resistance to certain bacterial infections in laboratory mice (Plant and Glynn, 1979). Mice found to be susceptible to certain bacterial infections had a point mutation within an aspartate at position 169 instead of the native glycine residue (Malo et al., 1994). In studies with knockout $^{Nramp1-/Nramp1-}$mice the same phenotype, namely higher susceptibility for several Mycobacteria, or *S. typhimurium* and *L.donovani*, was observed indicating the deleterious effect of the G169D point mutation in mouse NRAMP1 (Vidal et al., 1995b). Based on experiments where increased dietary iron in $^{wt/wt}$mice fostered the replication of *Mycobacterium avium* (Gomes et al., 2001). It was concluded that NRAMP1 depletes the bacterium from divalent metal ions, after ingestion by macrophages. At the same time another group suggested that NRAMP1 imports iron into phagosomes (Kuhn et al., 1999, 2001). However there have been several studies showing that NRAMP1 (Forbes and Gros, 2003; Jabado, 2000) acts similarly as its closely related family member NRAMP2 as proton coupled symporter (Canonne-Hergaux et al., 2001; Gunshin et al., 1997; Mackenzie et al., 2006, 2007). Given the fact that NRAMP1 and NRAMP2 both share two highly conserved motifs (DPGN, $MPHNX_3H$), which contain an aspartate, asparagine and methionine that have been identified to coordinate divalent metal ions in ScaDMT (the homolog from *Staphylococcus capitis*, investigated in this study) it more likely that NRAMP1 and NRAMP2 share the same direction of divalent metal transport. The process is illustrated in Figure 3 (B).

1.6. Iron homeostasis - a tightly controlled regulatory network

NRAMP1 and 2 are up to now the only iron importers in mammals that have been identified. The corresponding exporter is ferroportin. Both transporters import iron as free ions. Additionally iron can be taken up as complex with heme and although the import of heme is less well understood, there has been recent progress in the identification and initial characterization of a mammalian heme transporter termed HRG1 (for heme responsive gene 1) (Rajagopal et al., 2008; White et al., 2013). Because of the high reactivity of ferrous iron, which would lead to the generation of reactive oxygen species (ROS), detrimental to living cells, iron is tightly regulated in our body.

Several proteins involved in iron metabolism, are controlled at the mRNA level: Besides the gene encoding for DMT1 also the transferrin receptor TFR1 gene contains at its 3`UTR a so-called iron responsive element IRE (Casey et al., 1989). In the absence of iron, iron-regulatory proteins (IRP1 or IRP2) bind to the stable stem loops formed by the 3`IRE elements, consequently protecting the mRNA from cleavage by endonucleases (Caughman et al., 1988; Rouault et al., 1988). Ferritin mRNA contains IRE elements as well, but they are encoded at its 5` UTR (Aziz and Munro, 1987). Under iron-depletion, IRPs inhibit translation of the ferritin encoding mRNA by binding to the hairpin structure formed at its 5`end (Hentze et al., 1987). Ferritin and transferrin are the major iron storage proteins in our body. In contrast to transferrin, which binds two ferric iron molecules per transferrin dimer, ferritin is a 24 subunit multimer, which can hold up to 4500 iron atoms per complex (Harrison and Arosio, 1996). Ferritin has ferroxidase activity that allows it to oxidize ferrous iron to ferric iron, which it stores as inorganic complex in the core of the protein. Besides the multiple regulatory elements on the mRNA level, there are additional regulatory mechanisms at the protein level that influence iron uptake and storage. An example for post-translational regulation is the hepcidin/ferroportin system.

Hepcidin is a 25 amino acid long peptide-hormone mainly expressed by hepatocytes that is up-regulated during iron overload (Pigeon et al., 2001). At high iron levels, hepcidin binds to the ferroportin transporter inducing its internalization and degradation, thereby reducing cellular iron release in macrophages and enterocytes (Nemeth et al., 2004). The process is illustrated in Figure 4. Since, additionally to the regulation of iron homeostasis hepcidin also acts as antimicrobial substance, that is able to disrupt bacterial membranes (Maisetta et al., 2013; Park et al., 2001), it was given the name hepatic bactericidal protein. Besides the regulation by IREs and hepcidin, high levels of dietary iron are known to reduce the levels of DMT1 and DcytB present at the apical membrane of enterocytes by a mechanism that is not well understood (Yeh et al., 2000). It is hypothesized that DMT1 and DcytB might be internalized or that the expression levels of the two proteins might be down regulated (Yeh et al., 2009). Besides the discussed processes that contribute to the complex network regulating iron levels in our body, there may be other regulatory mechanisms that are still less well understood, e.g. the effect of hypoxia on hepcidin levels through hypoxia-inducible factor (HIF) proteins (Liu et al., 2012).

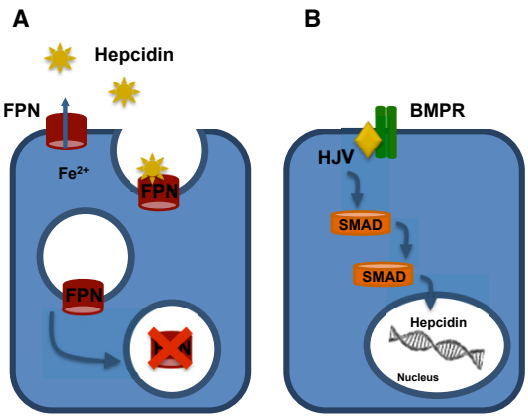

Figure 4 Iron regulation

(A) Ferroportin regulation by hepcidin. Binding of hepcidin to ferroportin causes the internalization of the transporter by endocytosis and its subsequent degradation in lysosomes. (B) Regulation of hepcidin expression in response to changing iron levels. Binding of HJV to BMPR induces a signaling cascade mediated via SMAD proteins, which bind to the hepcidin gene and regulates its transcription.

1.7. Diseases associated with iron imbalance

Because iron levels are controlled in a concerted multi-layered process, malfunction of either of the involved proteins can have a deleterious effect on iron metabolism.

Iron-overload disorders. Point mutations in four different genes have been associated with the most common iron-overload disorder in humans, hereditary hemochromatosis. The most prevailing type of hereditary hemochromatosis is caused by a recessive mutation in the HFE gene (Feder et al., 1996). The HFE protein is distantly related to the major histocompatibility complex and binds to the TRF1 receptor in endosomes, thereby competing with transferrin for binding to the receptor (Giannetti and Björkman, 2004; Ramalingam et al., 2000). Patients with mutations in their HFE gene have low hepcidin levels and suffer from iron accumulation in the liver, pancreas and heart, which can lead to hepatic cirrhosis, diabetes and heart failure. Type II hereditary hemochromatosis is caused by a mutation in the membrane-bound hemojuvelin (HJV) protein, which affects hepcidin expression via binding to BMPR (Bone morphogenic protein receptor) and SMAD signaling (Figure 4B). The disease is also called juvenile hemochromatosis due to its fast progression that might lead to premature death (Babitt et al., 2006). Type III hereditary hemochromatosis is the result of a mutation in the TFR2 receptor causing a similar phenotype as in type I

hemochromatosis (Chen and Enns, 2012; Roetto et al., 2002). Type IV hemochromatosis originates from mutations in the FPN gene, causing iron accumulation either in macrophages (Fernandes et al., 2009), or in hepatocytes because the liver is known to have the highest relative iron uptake rate compared to other tissues in our body (Craven et al., 1987).

Iron-deficiency disorders. Anemia is a widespread pathological condition in the entire human population. The World Health Organization WHO projects a global anemia rate of ~25%, based on their "worldwide anemia prevalence survey", conducted from 1993-2005 (World Health Organization, 2008). Lowest rates were found in Europe (~10% of the population are anemic) and in other First World countries. More than 45% of the population in South East Asia and Africa has anemic hemoglobin concentrations. Main causes are nutritional iron-deficiency and infections with the ubiquitously present bacterium Helicobacter pylori (De Domenico et al., 2008; Hentze et al., 2010; Hershko and Skikne, 2009). Despite the fact that in developing countries iron deficiency is predominantly caused by environmental factors, there are also hereditary causes that have been identified in patients with anemic conditions (Canonne-Hergaux et al., 2000; Finberg et al., 2008). Mutations in DMT1 are known to cause hypochromic microcytic anemia. Although patients are severely anemic and show reduced iron uptake, they additionally suffer from hepatic iron overload. This can be explained by the impaired iron recycling from erythrocytes in this disease, with iron stores that accumulate in the liver (Iolascon and De Falco, 2009). DMT1 mutations identified in patients include, the conservative point mutation E399D causing exon 12 skipping (Mims et al., 2005), R416C causing a complete loss-of-function of DMT1 (Iolascon et al., 2006), G212V in combination with an in-frame deletion of Val114 (Beaumont et al., 2006). Recently a patient carrying a novel N491S mutation and the known G212V mutation has been identified (Bardou-Jacquet et al., 2011).

Hypochromic microcytic anemia is treated with erythropoietin or its glycosylated successor darbopoietin combined with oral or intravenous iron supplementation, which helps to maintain hemoglobin levels and relieves the strongest symptoms (Iolascon and De Falco, 2009; Steinbicker and Muckenthaler, 2013). Besides this combination therapy there is no other adequate treatment known for these patients. Patients with hereditary hemochromatosis are treated with ferritin, iron-chelating infusions and regular phlebotomy to slow down disease-progression (Camaschella and Poggiali, 2011). There is currently no treatment available that helps to slow hepatic iron overload, which as long-

term condition can cause liver cirrhosis. In 2007 a study reported that hepatic iron overload was reduced in iron-loaded mice that were treated with the calcium channel blocker nifedipine (Ludwiczek et al., 2007). Based on $^{59}Fe^{2+}$ uptake measurements in COS-7 and HEK293 cells overexpressing DMT1, the authors concluded that nifedipine increases DMT1-mediated iron transport, which might be a new therapeutic approach for the treatment of iron overload disorders. However these results were challenged by Mackenzie et al, who reported in 2010 that nifedipine did not increase iron transport in Xenopus oocytes or in transiently transfected HEK293 cells overexpressing different isoforms of hDMT1 (Mackenzie et al., 2010).

To date mechanisms for the regulation of hepcidin by pharmacological compounds, can be considered the most promising direction to treat the most prevalent iron-overload disorders. A review published in 2007 draws an analogy between hepcidin in hemochromatosis and the role of insulin in diabetes (Pietrangelo, 2007). The development of a reliable serum-hepcidin blood test may thus significantly ease the diagnosis of iron-related disorders (Delaby et al., 2014). Increased iron levels have also been found in neurodegenerative diseases such as Parkinson's (Andersen, 2004; Berg et al., 2001) and Alzheimer's disease (Smith et al., 1997). Elevated DMT1 expression levels in animal models of Parkinson's (Salazar et al., 2008) and Alzheimer's disease (Zheng et al., 2009) have fostered the hypothesis that DMT1 might play an important role in the progression of neurodegenerative diseases (Hirsch, 2009; Lee and Andersen, 2010). Further knowledge on iron transport and its regulation is thus needed to better understand the complex system of iron homeostasis in health and disease. As one of the predominant proteins in cellular iron transport processes, a detailed structural and mechanistic understanding of DMT1 will in that respect be of large importance.

1.8. Plant Nramps

Plants are highly dependent on the availability of transition metal ions. Shortage in iron or manganese reduces their capacity for photosynthesis and thus limits their growth. Proteins of the photosystem I and II contain iron (as [2Fe-2S], [4Fe-4S] iron sulfur clusters) and manganese (as Mn_4CaO_5), which are both essential cofactors for electron transport (Amunts and Nelson, 2009; Liu et al., 2011). For that reason chloroplasts, the organelles where photosynthesis takes place, are in need for the large quantities of iron and manganese (Yruela, 2013). There is a large diversity of metal transporters that

catalyze transition metal ion transport in plants. The model system *Arabidopsis thaliana* contains in total 8 different metal ATPases, 15 different ZIPs (zinc-regulated-iron-regulated-like proteins and 6 different NRAMP homologs (Maser, 2001; Mills et al., 2003; Williams et al., 2000). This variety of low- and high affinity metal transporters ensures metal ion supply under different environmental conditions (Hall and Williams, 2003). NRAMP homologs of *A. thaliana* (AtNRAMP 1-6) are confined to distinct organelles, which allows the separate regulation of each subtype, which caused speculations about altered substrate specificity of different AtNRAMP proteins (Curie et al., 2000; Thomine et al., 2000). The best characterized plant NRAMP transporters include the AtNRAMPs (Lanquar et al., 2010; Williams et al., 2000) and the NRAMPs 1-6 identified in *Oryza sativa* (Belouchi et al., 1995; Takahashi et al., 2011).

Besides the analysis of loss-of-function mutants in the corresponding plant, yeast complementation assays have been used to characterize the metal transport properties of plant NRAMPs (Cailliatte et al., 2009, 2010; Oomen et al., 2009; Thomine et al., 2000). AtNRAMP1 has been identified as iron transporter that is up-regulated in the root under iron-deficiency (Curie et al., 2000). AtNRAMP3 and 4, in contrast, are located in the vacuolar membrane and are involved in iron and cadmium transport (Cailliatte et al., 2010; Lanquar et al., 2010). OsNRAMP5 was found to transport manganese and cadmium (Sasaki et al., 2012). Comparison of the amino acid sequences of AtNRAMP1-6 and OsNRAMP1-3 (Williams et al., 2000) reveal that they all contain the conserved motifs DPGN and MPHNX$_3$H, two sequence motifs that contain residues that are part of a binding site in the NRAMP homolog ScaDMT from the bacterium *Staphylococcus capitis* (Ehrnstorfer et al., 2014) that coordinates different transition metal ions. It is thus unclear whether different NRAMP homologs in plants have different selectivity properties. Due to the numerous NRAMP homologues present it plants it can be expected that additional subtypes will be discovered in future studies. Recently a new subtype of NRAMP transporters, termed NRAMP aluminum transporter 1 (NRAT1), was identified in *O. sativa*. The authors overexpressed NRAT1 in yeast and detected their aluminum content by ICP-MS (Li et al., 2014). NRAT1 is 57% identical to OsNRAMP1, 35% identical to ScaDMT and 30% identical to hDMT1. Despite the fact that two of the three residues responsible for metal ion binding in ScaDMT are conserved in NRAT1, the glycine of the DPGN motif is replaced by a serine. Remarkably, in this transporter the MPHNX$_3$H motif is changed to TPYNX$_3$H, which places a threonine instead of the strictly conserved methionine that was found as part of the coordination site of transition

metal ions. In this conserved sequence stretch the close-by histidine residue is replaced by a tyrosine. It will thus be interesting to investigate whether NRAT1 has an altered substrate specificity compared to other family members.

1.9. Prokaryotic DMTs

Soon after the first characterization of mammalian NRAMP proteins (Gunshin et al., 1997), prokaryotic homologs were identified by sequence analysis of prokaryotic genomes (Agranoff et al., 1999; Kehres et al., 2000; Makui et al., 2000). On average, bacterial NRAMPs share a sequence identity of 30-35% with hNRAMP2, which is unusually high compared to other transport proteins. Among the first prokaryotic transporters to be identified, were the NRAMP homologs from *Salmonella typhimurium* and *Escherichia coli*. With radioactive uptake measurements of $^{54}Mn^{2+}$ into bacteria expressing the respective homolog, Kehres et al. could show that both proteins transport Mn^{2+}, independent of the presence of calcium or magnesium (Kehres et al., 2000). Addition of "cold" Ni^{2+}, Cu^{2+}, Zn^{2+}, Co^{2+}, Fe^{2+} or Cd^{2+} inhibited uptake of $^{54}Mn^{2+}$ thus suggesting that these ions may also be transported substrates. Maximum uptake of $^{54}Mn^{2+}$ was increased at lower pH, without shift in the apparent K_m of the ion thus suggesting that transport may be coupled to protons. Although NRAMPs have been shown to have a broad substrate specificity, the relevant ion in a physiological context is manganese since iron is taken up by bacteria mainly as complex with siderophores or porphyrins (Guerinot, 1994; Makui et al., 2000). Mn^{2+} is an essential cofactor for enzymes such as superoxide dismutases, pyruvate carboxylases and ribonucleotide reductase (Kehres and Maguire, 2003). An important aspect of bacterial manganese and iron aquisition has to be viewed in the context of host-pathogen interaction (Chu et al., 2010; Forbes and Gros, 2001; Nairz et al., 2010, 2014; Plant and Glynn, 1974). E.P. Skaar described in his review "The battle for iron between pathogens and their vertebrate hosts" (Skaar, 2010), strategies of the bacteria and their eukaryotic host to sequester metal ions. G. Schatz wrote a delightful short-story on the metal manganese where he does not miss to mention the war between bacterial and human NRAMP transporters being a matter of life and death (Schatz, 2003).

The transmembrane topology of the *E. coli* NRAMP homolog Mnth (for H^+ stimulated Mn^{2+} transporter) has been investigated by fusing reporter proteins into the loops predicted by hydropathy analysis. A secreted form of the antibiotic β-lactamase

was used as indicator for periplasmic localization and chloramphenicol acetyltransferase served as reporter protein for cytoplasmic localization (Courville et al., 2004). The experimental data confirmed the prediction of 11 transmembrane segments with a cytoplasmic N terminus and a periplasmic C terminus. It was not until 2009 that the topology of murine NRAMP2 was investigated by similar methods (Czachorowski et al., 2009). In this case the 10 amino acid long hemagglutinin A (HA) peptide was fused into the predicted loops of mNRAMP2. The extra- or intracellular localization of the HA-tag was detected by immunofluorescence (with a rhodamine coupled secondary antibody). The study with mNRAMP2 indicated that mammalian NRAMP transporters have an additional twelfth transmembrane segment resulting in a cytoplasmatic N and C terminus. The structural relationship of SCL11/NRAMP transporter with a large class of transport proteins was recently proposed based on sequence analysis (Cellier, 2012a, 2012b). This proposal could be confirmed in my work by the structure determination of the first family member.

1.10. Aim of this thesis

While functional data on the SLC11 transporters has clarified their role as H^+ coupled transporter of transition metal ions, the detailed structural organization of the family was unknown. Because high-resolution structural data is inevitable in order to understand the mechanisms of divalent metal-ion binding and transport it was my aim to determine the first high-resolution structure of a SLC11 family member. In order to understand the ion selectivity properties of SLC11 proteins, I have established a transport assay that allowed the characterization of metal ion selectivity in a prokaryotic family member.

2. RESULTS

2.1. Selection of prokaryotic homologs of the SLC11 family suitable for structural studies

Members of the SLC11 family are found in all kingdoms of live and are highly conserved from bacteria to mammals. Bacterial and archaeal homologs share 25-35% sequence identity and 40-65% homology with the human SLC11 transporters, and were thus straightforwardly identified after the discovery of the human SLC11 gene (Makui et al., 2000; Zaharik et al., 2004). All SLC11 transporters share a common topology of 10 highly conserved (predicted) transmembrane segments (Courville et al., 2008). All eukaryotic SLC11 transporters contain two additional transmembrane helices (Courville et al., 2004; Czachorowski et al., 2009; Xue et al., 2009) on their C terminus, whereas in bacteria two topologies are present. While a small number of prokaryotic SLC11 homologs supposedly contain 12 transmembrane segments, like eukaryotic transporters, in the majority of transporters the last α-helix is absent and proteins thus contain 11 transmembrane segments with a predicted extracellular C terminus. Termini and loop regions are the least conserved parts of SLC11 transporters and they are usually shorter in bacteria. Due to their widespread occurrence, their high sequence conservation and compactness I have selected a large set of bacterial homologs to identify SLC11 transporters amenable for structural studies.

2.1.1. In silico homolog selection

The protein sequence of human DMT1 (including and excluding the last two predicted transmembrane segments) was used as query for BLAST (basic local alignment search tool) searches on all available annotated bacterial and archaeal genomes. Pairwise sequence alignments were scored based on the Blosum62 block substitution matrix (NCBI BLASTp; Altschul et al. 1990, States & Gish 1994) according to their degree of sequence conservation.

The number of sequenced genomes has been increasing almost exponentially over the last years. By the end of 2013 more than 10 000 bacterial genomes were available in the GOLD genome database (Pagani et al., 2012). Above 3000 of these were fully sequenced, annotated and available for sequence based homology searches (Pagani et al., 2012) at that time. To further select among the large number of homologs

identified in BLAST searches, additional criteria were applied: Homologs from extremophilic organisms were prioritized in the first round due to the stability of their proteins under extreme conditions (e.g. temperature, ionic strength, pH, pressure, de Champdoré et al. 2007), despite their on average lower sequence conservation compared to eubacterial strains. Additionally, proteins with short and compact termini and loops were given preference, since flexible parts might be disadvantageous for crystallization. Genomes of microorganisms classified in biosafety level 2 were only included if the genomic DNA was available. Interestingly, the genome of *Ralstonia metallidurans*, a bacterium known to grow in heavy metal polluted sediments, that proved to be a promising source of different ion transport proteins, was one of the few organisms that appears not to contain any homolog of the SLC11 family. In addition to the described selection criteria, proteins from bacteria containing two different branches of the phylogenetic tree were chosen to ensure a genetically diverse pool. By this selection bias to a small subset was avoided to reduce the risk of excluding a subfamily of proteins that may show superior biochemical properties, despite the fact that they may not optimally match the chosen selection criteria. The 35 homologs selected in round 1 based on a BLAST search with human DMT1 as query are depicted in Table 1.

After characterization of the first set of homologs, a second round of target selection was performed, which was based on the results of the first selection. The expression screening was carried out in a similar way for both selections. The sequences of the two best-behaved homologs identified in round one (29LLA, 99CCU) were used as input query in order to increase the chance of selecting homologs with superior biochemical properties suitable for structural studies. This BLASTp search lead to the identification of 51 additional SLC11 transporters selected for expression screening (Table 2). For all but four homologs, 11 transmembrane helices were predicted by OCTOPUS (Anon 2011, Viklund et al. 2008) a tool, designed to predict alpha-helical transmembrane segments and signal sequences (Table 1, Table 2). As a second transmembrane helix prediction tool TOPCONS (Bernsel et al., 2008, 2009), developed by the Bioinformatics Center of the University of Stockholm, was used. In two cases less than 11 transmembrane segments were predicted, (with 7 and 9 segments respectively for the homologs 50MTU and 94CLI). Transport of a DMT homolog from *Oncorhynchus mykiss* with 10 putative transmembrane segments has been reported but it is not clear if fewer segments would still fold into a functional transporter. It can thus be assumed that the sequences available for 50MTU and 94CLI were incomplete (Cooper et al., 2007).

Together with the master student Jürg Laederach more homologs were selected based on the most stable proteins in the first and second screening round (i.e. with the transporter 29LLA, 88BEG, 98ELE, 99CCU, 135SCA, and hDMT1 as query; Laederach, 2011). This search resulted in the identification of three novel homologues that were characterized together with the master student Fabian Arnold (Arnold, 2013). When including the results of the third screening 105 prokaryotic DMT genes were successfully cloned and investigated with respect to expression levels, extractability and biochemical stability. The work on these homologs is described in the respective master theses and will therefore not be discussed in this work.

Figure 5 shows the phylogenetic tree calculated from a multiple sequence alignment generated by ClustalW2 (Goujon et al., 2010; McWilliam et al., 2013) from the 86 selected homologs together with human DMT1.

Homolog name	Bacterial strain	DSM/ATCC No.	% identity to hDMT1	% homology to hDMT1	length (aa)	size (kDa)	predicted TMs
2SPH	*Sphingomonas sp. SKA58*	DSM 11094	37.4	57.3	447	47.5	11
3GAU	*Gemmatimonas aurantiaca T-27*	DSM 14586	36.3	57.5	443	47.8	11
6SAU	*Staphylococcus aureus RF122*	DSM 20231	36.7	56.5	450	49.7	11
12ATU	*Agrobacterium tumefaciens str. C58*	DSM 5172	32.5	55.3	456	48.8	11
23NPU	*Nostoc punctiforme PCC 73102*	ATCC 29133	35.6	56.9	435	47.5	11
29LLA	*Lactococcus lactis subsp. cremoris*	DSM 20388	37.6	49.6	510	55.9	12
32BSU	*Bacillus subtilis subsp. subtilis str. 168*	DSM 1971	31.8	54.3	425	45.7	11
34DGE	*Deinococcus geothermalis*	DSM 11300	29.6	51.8	442	46.7	11
35DRA	*Deinococcus radiodurans R1*	DSM 20539	29.6	53.0	436	46.7	11
36SFU	*Syntrophobacter fumaroxidans MPOB*	DSM 10017	33.1	53.4	411	44.0	11
46CTE	*Chlorobium tepidum TLS*	DSM 12025	27.2	52.2	419	45.4	11
52PAR	*Pyrobaculum arsenaticum*	DSM 13514	23.7	46.5	371	38.7	11
56NPH	*Natronomonas pharaonis*	DSM 2160	19.7	46.2	401	41.4	11
60CPI	*Chitinophaga pinensis*	DSM 2588	30.5	43.8	625	68.7	12
61SLI	*Spirosoma linguale*	DSM 74	34.8	58.6	448	48.3	11
65TRO	*Thermomicrobium roseum*	DSM 5159	30.5	53.6	429	45.8	11
66CAG	*Chloroflexus aggregans*	DSM 9485	33.3	53.9	420	44.9	11
69DTU	*Dictyoglomus turgidum*	DSM 6724	28.0	52.5	414	45.9	11
76KFL	*Kribbella flavida*	DSM 17836	25.6	51.3	450	4.7	11
77DLO	*Dorea longicatena*	DSM 13814	24.5	51.0	413	44.8	11
78BCA	*Bifidobacterium catenulatum*	DSM 16992	27.8	51.9	424	45.0	11
79BCO	*Bacteroides coprocola*	DSM 17136	25.8	51.4	418	45.7	11
83BAN	*Bifidobacterium angulatum*	DSM 20098	26.7	52.5	438	46.4	11
84BPS	*Bifidobacterium pseudocatenulatum*	DSM 20438	26.9	52.2	443	46.7	11
86BIN	*Bacteroides intestinalis*	DSM 17393	26.0	51.2	420	45.8	11
87BPL	*Bacteroides plebeius*	DSM 17135	26.0	50.6	420	46.1	11
89PJO	*Parabacteroides johnsonii*	DSM 18315	25.7	50.6	417	45.3	11
97CLI	*Corynebacterium lipophiloflavum*	DSM 44291	21.2	46.5	396	40.5	11
99CCU	*Cryptobacterium curtum*	DSM 15641	19.6	45.6	415	43.2	11
100SWA	*Staphylococcus warneri L37603*	DSM 20316	37.1	57.3	448	49.2	11
103LIN	*Listeria innocua Clip11262*	DSM 20649	36.1	58.2	448	48.7	11
125DMA	*Desulfovibrio magneticus RS-1q*	DSM 13731	26.1	51.8	429	45.7	11
126DVU	*Desulfovibrio vulgaris str. 'Miyazaki F'*	DSM 19637	16.8	51.9	441	46.9	11
129ECO	*Escherichia coli O157:H7 EDL933*	ATCC 43895	29.4	53.1	412	44.2	11
130MTU	*Mycobacterium tuberculosis H37Rv*	ATCC 25618	26.6	51.2	428	45.0	11

Table 1 Homologs selected for screening, round 1.

BLASTp search was carried out with hDMT1 as query sequence. 32 of the 35 bacterial strains were either obtained from DSMZ (Deutsche Sammlung von Mikroorganismen und Zellkulturen) or ATCC. 33 homologs are predicted to contain 11 transmembrane helices.

Homolog name	Bacterial strain	DSM/ATCC No.	% identity to hDMT1	% homology to hDMT1	length (aa)	size (kDa)	predicted TMs
5FPS	Flavobacterium psychrophilum JIP02/86	DSM 3660	30.6	39.8	623	68.5	11
16SIN	Streptococcus infantarius subsp. infantarius	DSM 22960	26.2	48.7	448	48.8	11
17RPA	Rhodopseudomonas palustris BisB18	DSM 123	33.0	53.8	462	48.7	11
19STH	Streptococcus thermophilus LMD-9	DSM 20617	34.0	54.7	444	48.6	11
25SMU	Streptococcus mutans UA159	DSM 20523	31.1	52.2	446	48.8	11
39CSA	Chromohalobacter salexigens	DSM 3043	31.4	52.7	431	46.4	11
49PME	Prevotella melaninogenica	DSM 7089	28.5	50.3	420	45.4	11
50MTU	Mycobacterium tuberculosis KZN 1435	ATCC 27294	24.8	38.1	262	27.4	7
53PCA	Pyrobaculum calidifontis JCM 11548	DSM 21063	22.9	43.9	376	38.8	11
58LUL	Lactobacillus ultunensis	DSM 16047	30.6	52.4	509	55.7	12
68GBR	Gordonia bronchialis	DSM 43247	30.4	49.7	401	42.0	11
72XCE	Xylanimonas cellulosilytica	DSM 15894	27.5	48.9	436	45.2	11
88BEG	Bacteroides eggerthii	DSM 20697	25.3	48.8	419	45.6	11
90BCO	Bacteroides coprophilus	DSM 18228	25.2	48.7	420	46.0	11
91BDO	Bacteroides dorei	DSM 17855	25.2	48.5	417	45.7	11
92VPA	Veillonella parvula	DSM 2008	26.5	48.4	419	45.9	11
93AUR	Actinomyces urogenitalis	DSM 15434	26.7	48.1	434	45.3	11
94CLI	Corynebacterium lipophiloflavum	DSM 44291	27.6	41.8	315	32.3	9
98ELE	Eggerthella lenta	DSM 2243	20.0	44.3	416	43.6	11
101FJO	Flavobacterium johnsoniae UW101	DSM 2064	29.8	38.9	622	68.6	12
106SSP	Sphingobacterium spiritivorum	DSM 11722	29.8	39.2	624	69.6	11
107SCA	Staphylococcus carnosus subsp. carnosus TM300	DSM 20501	36.0	53.9	447	48.8	11
112DAC	Delftia acidovorans SPH-1	DSM 39	31.8	54.3	456	47.9	11
113LPL	Lactobacillus plantarum subsp. plantarum	DSM 20174	34.5	55.7	464	50.4	11
118OCA	Oligotropha carboxidovorans OM5	DSM 1227	34.1	54.0	455	48.0	11
119RET	Rhizobium etli CFN 42	DSM 11541	34.1	54.6	446	47.7	11
128SWO	Shewanella woodyi	DSM 12036	21.4	43.8	397	42.2	11
135SCA	Staphylococcus capitis SK14	DSM 20326	35.7	54.0	448	49.3	11
137LWE	Listeria welshimeri serovar 6b str. SLCC5334	DSM 20650	36.4	56.9	448	48.7	11
138CGL	Chryseobacterium gleum	DSM 16776	35.8	55.5	444	48.8	11
141CSE	Caulobacter segnis	DSM 7131	34.0	54.6	444	46.7	11
142GAD	Granulicatella adiacens	DSM 9848	33.1	53.1	444	48.5	11
146NHA	Nitrobacter hamburgensis X14	DSM 10229	35.6	55.7	464	49.8	11
147BIN	Beijerinckia indica subsp. indica	DSM 1715	34.7	54.7	450	48.3	11
148LME	Leuconostoc mesenteroides subsp. mesenteroides	DSM 20346	32.5	53.1	464	50.3	11
149GOX	Gluconobacter oxydans 621H	DSM 2343	36.4	55.4	451	48.3	11
153WPA	Weissella paramesenteroides	DSM 20288	32.9	54.6	447	48.5	11
155BPU	Bacillus pumilus	DSM 27	31.5	52.6	425	45.6	11
156BXE	Burkholderia xenovorans LB400	DSM 17367	32.6	52.3	448	47.3	11
157MLU	Micrococcus luteus SK58	DSM 46257	29.2	49.6	424	44.0	11
162HTU	Haloterrigena turkmenica	DSM 5511	19.0	42.7	401	41.5	11
164ACH	Arthrobacter chlorophenolicus A6	DSM 12829	29.3	49.2	416	42.8	11
165BLO	Bifidobacterium longum subsp. infantis	DSM 20219	27.5	50.7	436	46.2	11
167RER	Rhodococcus erythropolis PR4	DSM 43066	31.6	50.3	415	43.2	11
168ESI	Exiguobacterium sibiricum 255-15	DSM 17290	31.0	49.7	406	43.3	11
169AAC	Alicyclobacillus acidocaldarius subsp. acidocaldarius	DSM 446	29.2	50.8	432	46.9	11
172SSA	Staphylococcus saprophyticus subsp. saprophyticus	DSM 20229	20.7	43.3	406	43.2	11
178BTH	Bacteroides thetaiotaomicron VPI-5482	DSM 2079	24.4	47.6	418	45.6	11
179BFR	Bacteroides fragilis YCH46	DSM 2151	24.7	48.0	417	45.4	11
180POR	Prevotella oris F0302	DSM 18711	27.4	48.9	420	45.4	11
184HVO	Haloferax volcanii DS2	DSM 3757	32.2	50.5	410	43.2	11

Table 2 Homologs selected for screening, round 2.

51 Homologs were selected based on a BLASTp search with 29LLA and 99CCU as query sequences. 58LUL and 101FJO were both predicted to contain 12 transmembrane helices. 50MTU and 94CLI were predicted to contain 7 and 9 transmembrane helices respectively.

The sequences cluster in two main branches: 25% of the selected bacterial homologs cluster in relative proximity to human DMT1 and 75% of the selected bacterial SLC11 genes cluster in a second group distinct from human DMT1. The two stable proteins 29LLA and 99CCU, used as query for a second round of BLASTp searching, are located in either of the two main families. ScaDMT, the bacterial homolog that could successfully be crystallized, is closer in sequence to 29LLA than to human DMT1. Three of the four homologs predicted to contain 12 transmembrane spanning segments cluster in the same branch of the phylogenetic tree.

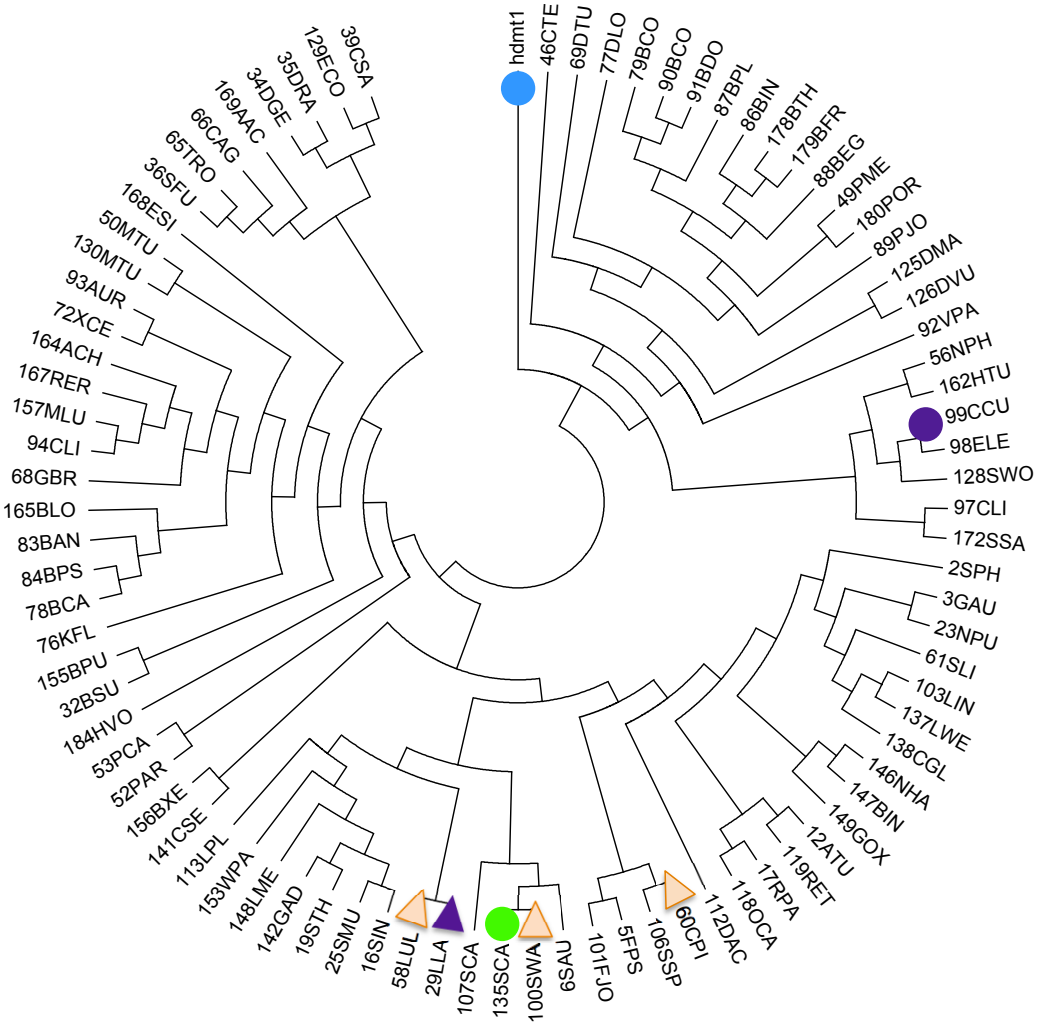

Figure 5 Phylogenetic tree of hDMT1 and 86 homologs selected in two rounds of BLASTp searches.

Human DMT1 is highlighted in blue. The two stable homologs 29LLA and 99CCU identified in round one are marked in violet. The homolog (135SCA) selected for structural and functional studies is depicted in green. The four homologs predicted to have 12 TMs (OCTOPUS) are marked with triangles (29LLA, 58LUL, 60CPI, 100SWA).

2.1.2. Cloning of prokaryotic DMT homologs

Bacterial strains were purchased from DMSZ either as freeze-dried cell pellets or as growing cultures, depending on their availability. The genomic DNA was isolated by phenol-chloroform extraction. For all risk-2 strains, genomic DNA was ordered from DSMZ. 65 genes of interest could be successfully amplified from genomic DNA by the use of different DNA polymerases and a variation of PCR conditions. 19 genes could

not be amplified by the applied methods and were thus not pursued. The primers included specific 5' and 3' SapI sites suitable for the FX (fragment exchange) cloning procedure and were designed in an automated fashion by a python script available at www.fxcloning.org (Geertsma and Dutzler, 2011).

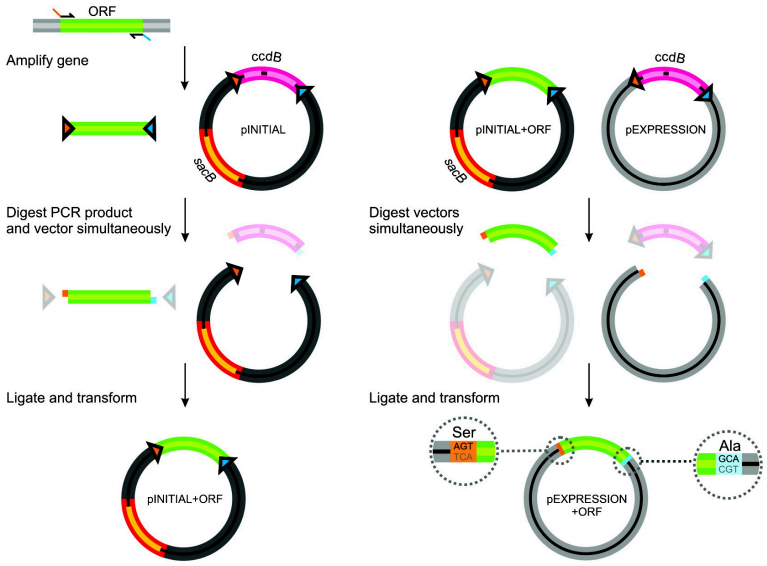

Figure 6 Schematic view of FX-cloning.

The gene of interest (green) is amplified with primers containing flanking SapI sites (arrows indicate the orientation of the SapI sites). The digested PCR product is then ligated to the digested entry plasmid pINITIAL, thereby replacing the ccdB cassette (pink). For expression, the gene is subcloned through SapI digest of pINITIAL (+ gene of interest) and the desired expression vector, followed by ligation. Once the gene replaced the ccdB cassette in the expression vector SapI sites are lost, adding an N terminal serine and a C terminal alanine to the gene of interest (modified from Geertsma and Dutzler, 2011).

The shuttle vector pINITIAL and the three expression vectors used in this study (pBXNH3, pBXC3H, pBXC3GH) are part of the FX vector collection designed by Eric Geertsma (Geertsma and Dutzler, 2011). The FX-cloning method exploits advantages of the type II restriction enzyme SapI (Saccharopolyspora species) for the generation of constructs. SapI cuts 5' distal from the recognition sequence and therefore enables the generation of different overhangs for directed insertion into vectors. The SapI site will be removed upon digestion, depending on the orientation of the recognition sequence. The SapI sites in the shuttle vector pINITIAL are maintained on the plasmid after digestion, to allow a simple strategy for sub-cloning into the desired expression vectors (Figure 6**)**. The vectors used for expression screening carry two SapI sites oriented in a way that the

recognition sequence is lost upon digestion. The selection for vectors with correct inserts by the FX-cloning method is highly efficient due to the presence of a so-called 'kill-cassette' in original vectors. This cassette is located between the two SapI sites and encodes the Control-of-cell-death-gene B (CcdB) gene. The cytotoxic CcdB protein targets the subunit GyrA of the DNA gyrase (a subunit of the bacterial topoisomerase II), which then causes double strand breaks in the DNA. Vectors containing the CcdB gene are maintained in cells encoding for GyrA462 (Arg462 to Cys substitution) a mutant of the GyrA subunit that is resistant to CcdB (Bahassi et al., 1999; Bernard and Couturier, 1992). For cloning, the digested insert is ligated into the digested vector and the plasmids are subsequently transformed to CcdB sensitive cells. Only cells carrying a plasmid where the insert has replaced the CcdB cassette will survive. The different overhangs generated by SapI prevent re-ligation of the empty vector and they ensure a directed insertion of the insert.

The expression vectors pBXNH3, pBXC3H and pBXC3GH are schematically depicted in Figure 7. pBXNH3 encodes for an N-terminal His_{10}-tag cleavable by a 3C human rhino virus protease (3C protease). The vector pBXC3H has the same 3C cleavable His_{10}-tag but in this case the tag is located on the C terminus of the gene. pBXC3GH encodes for a C-terminal 3C cleavable GFP- His_{10}-fusion-tag (GFP, green fluorescent protein). The C-terminal GFP-fusion construct was chosen as a folding indicator and for detection purposes in high-throughput applications due to its fluorescence properties (Drew et al., 2005, 2006; Geertsma et al., 2008a; Kawate and Gouaux, 2006). Furthermore fusion-tags have been reported to enhance expression (Esposito and Chatterjee, 2006; Wagner et al., 2007; Waldo et al., 1999; Xie and Hong, 2009). The GFP-fusion protein can only correctly fold in the cytoplasm (Drew et al., 2002). For several homologs 11 transmembrane segments were predicted, resulting in a periplasmic C terminus and therefore leading to unfolded non-fluorescent GFP. However, since the results were obtained from hydropathy analysis and thus the location of the C terminus was not always conclusive, I decided to investigate C-terminal GFP-fusion constructs for all selected homologs.

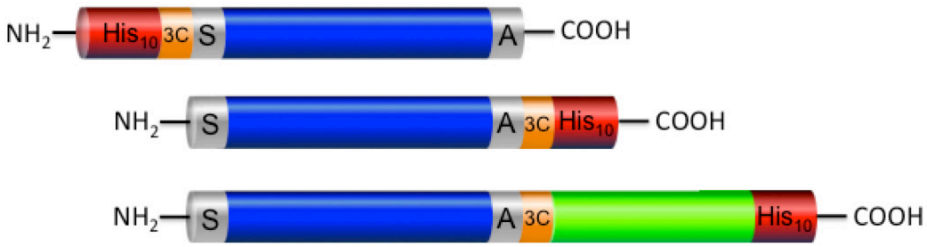

Figure 7 Constructs used for the expression screening of prokaryotic SLC11 homologs. The three different constructs incorporate either an N-terminal (pBXNH3) or a C-terminal (pBXC3H) His_{10}-tag (red), which in all cases includes a cleavage site for 3C protease (orange). pBXC3GH has in addition GFP (green) fused to C terminus of the SLC11 homolog (blue). The two additional amino acids serine (S) and alanine (A) are introduced by the FX-cloning method (grey).

For crystallographic studies it is preferable to have the fusion tag N-terminally as it leaves only two additional amino acids from the 3C cleavage-site after proteolysis, compared to five additional amino acids remaining after cleavage on the C terminus. As a third construct the C-terminal His_{10} –tag was tested. This construct does not contain GFP and therefore is applicable independent on the localization of the C terminus of the protein. The His_{10}-tag included in all constructs can be used for detection in western blot analysis and serves as an affinity-tag for immobilized metal affinity chromatography (IMAC) purification by binding to Ni-NTA beads.

2.1.3. Expression and extraction screening of selected SLC11 homologs

Protein crystallography has strict requirements with respect to the biochemical stability of the target protein. Preferably milligram amounts of well-folded protein need to be produced and purified to homogeneity before crystallization experiments are set-up. Additionally, membrane proteins have to be stable in a detergent solubilized state, ideally at protein concentrations of several milligrams per milliliter. Therefore the successful overexpression of a target protein is a critical hurdle scientists need to overcome along the path to a new high-resolution structure.

One approach to identify the most promising constructs for further investigations, involves the screening of many homologs. The use of GFP as fusion protein had a major impact on the ease of detection in all experimental steps during screening, starting from overexpression, extraction, detergent exchange and the use of fluorescence size exclusion chromatography (FSEC) to reveal the monodispersity of the target protein (Geertsma et al., 2008a; Kawate and Gouaux, 2006).

When fused to the C terminus of the membrane protein, GFP can also be used as folding indicator (Geertsma et al., 2008a). The GFP moiety will only fold properly and become fluorescent if the N-terminally fused protein is correctly folded as well. Thus the measurement of the GFP-fluorescence in intact cells allows for the initial assessment of functional target protein overexpression. Later, the fluorescence of GFP can be exploited to quantitate the amount of target protein extracted from the lysate and the population of protein that is retained in the supernatant after removal of insoluble proteins by ultracentrifugation. In-gel fluorescence measurements can detect stable membrane protein – GFP-fusions since GFP does not unfold under standard SDS-PAGE conditions (Drew et al., 2006, 2008). The fusion protein with the folded, and therefore globular GFP moiety migrates faster in the SDS-PAGE gel compared to the unfolded non-fluorescent fraction. The comparison of the in-gel GFP fluorescence image with the corresponding anti-His western blot from the same gel can be utilized to distinguish between folded and unfolded protein fractions (Geertsma et al., 2008a). Furthermore Kawate and Gouaux showed in 2006 that the GFP fluorescence can be exploited to record the size exclusion chromatography profile of the fusion protein when crude lysate is injected to a HPLC system equipped with a fluorescence detector (Kawate and Gouaux, 2006).

Proteins expressed without GFP were analyzed for their expression and extraction properties by western blot with an antibody recognizing the His_{10} -tag. In these cases the stability in detergent solution and the monodispersity were assessed after scale-up of the expression in 2.5 liter cultures followed by affinity purification and injection to size exclusion chromatography.

For expression purposes the pBAD promotor was chosen since it allows tight control of transcriptional activity in dependence on the inducer concentration. This is particularly important for membrane proteins, as in these cases a strong overexpression often causes the misfolding of the protein. By titration of the inducer its ideal concentration, at which the functional overexpression is maximized, can be determined.

For protein expression the strain *Escherichia coli* MC1061, which has a disrupted *ara* gene and is therefore unable to metabolize arabinose, was used as host.

Homolog	pBXC3GH				pBC3H			pBNH3		
	exp.	ext.	FSEC	SEC	exp.	ext.	SEC	exp.	ext.	SEC
2SPH										
3GAU										
5FPS	+	+	-	-	-	-		-	-	
6SAU	-	-			-	-		-	-	
12ATU	++	+	-					-	-	
16SIN					-	-				
17RPA					-	-		-	-	
19STH					-	-		-	-	
23NPU	+	-								
25SMU					-	-				
29LLA	++	++	+	+	+	-		+	-	
32BSU										
34DGE										
35DRA										
36SFU										
39CSA	+	-			+	-		+	-	
46CTE										
49PME	-	-			+	+	-			
50MTU										
52PAR										
53PCA	-	-			+	-		-	-	
56NPH	-	-			+	-		-	-	
58LUL	+	+	+	-	+	-		+	-	
60CPI	+	-			+	-		+	-	
61SLI	+	+			-	-		-	-	
65TRO										
66CAG	+	+			+	-		+	-	
68GBR	-	-			+	-		-	-	
69DTU										
72XCE	+	+	-		+	-		+	-	
76KFL	-				-	-		-	-	
77DLO										
78BCA	+	+			-	-		-	-	
79BCO	+	+	-		-	-		-	-	
83BAN	+	-			-	-		-	-	
84BPS										
86BIN										
87BPL										
88BEG	-	-			+	+	+			
89PJO										
90BCO	-	-			+	+	+	-	-	
91BDO	+	+			+	-	-	-	-	
92VPA	-	-			+	+	-	-	-	

Homolog	pBXC3GH				pBC3H			pBNH3		
	exp.	ext.	FSEC	SEC	exp.	ext.	SEC	exp.	ext.	SEC
93AUR	-	-			+	-		+	-	
94CLI	+	-			+	+	-	-	-	
97CLI	-	-			-	-	-	+	-	
98ELE	-	-			+	+	+			
99CCU	-	-			++	++	+	-	-	
100SWA										
101FJO	++	+		-	++	+	-			
103LIN	-	-			-	-		-	-	
106SSP	+	+		-	+	+	-	+	-	
107SCA	-	-			+	+	-	-	-	
112DAC	-	-			+	+	-	-	-	
113LPL	+	+	-		+	-		-	-	
118OCA	+	-			+	-		+	-	
119RET	+	-			+	-		++	++	-
125DMA										
126DVU	-	-			-	-		-	-	
128SWO	-	-			-	-		-	-	
129ECO	-	-			-	-		-	-	
130MTU	-	-			-	-		-	-	
135SCA	-	-			+	+	+++	+	-	-
137LWE	-	-			++	+	-	-		
138CGL										
141CSE	-	-			-	-		-	-	
142GAD	-	-			+	+	-	-	-	
146NHA	-	-			+	+	-	-	-	
147BIN	-	-			-	-		-	-	
148LME	-	-			+	+		+	+	
149GOX	-	-			+	-		+	-	
153WPA	+	-			-	-		+	-	
155BPU	+	+	-		+	+	-	+	-	
156BXE	-	-			+	-		-	-	
157MLU	-	-			-	-		-	-	
162HTU	-	-			+	-		-	-	
164ACH	+	+	-		-	-		+	+	
165BLO	+	+	-		+	+		+	-	
167RER	-	-			+	-		+	-	
168ESI	-	-			+	+	-	+	-	
169AAC	-	-			++	+	-	-	-	
172SSA	-	-			+	+		-	-	
178BTH	-	-			-	-		-	-	
179BFR	-	-			-	-		-	-	
180POR	-	-			-	-		-	-	
184HVO	-	-			-	-		-	-	

Table 3 Overview of the 86 homologs selected for cloning and expression tests.

Homologs that could not be amplified are marked in grey. Minus (-) indicates that the sample was either not expressed (exp.) or extracted (ext.). Expression, extraction and stability properties on FSEC/SEC were ranked between medium (+) to very good (+++). Plus signs marked in orange indicated cases where, although detectable in in-gel fluorescence experiments or on western blots, degradation of the protein was observed. 88BEG and 98ELE were not monodisperse on SEC and degraded over a period of 1-2 days after SEC.

The expression screening was carried out in 24-well plates in 4 ml cultures. For each homolog three different constructs (NH3, C3H, C3GH) were combined with up to three different arabinose concentrations. Cells were lysed by bead beating and the supernatant was recovered after low spin centrifugation. In all cases membrane proteins were extracted by the addition of DDM (n-dodecyl- β -D-maltopyranosid). Samples for western blot analysis were taken before and after ultracentrifugation to compare the total expression levels with the amount of extracted proteins that remains in the supernatant

(after ultracentrifugation). In case of GFP-tagged proteins, SDS-PAGE samples were analyzed by measurement of in-gel fluorescence followed by western blot analysis. The results of this screen are summarized in Table 3.

For round one the number of genes that could not be amplified from genomic DNA is comparably high. A likely cause is that in most cases gDNA was isolated from dried cell pellets of probably low cell density, which might explain the poor success rate of PCR. Additionally some of the bacterial strains needed very harsh conditions to break their cell wall (e.g. several hours of incubation at max. 80 °C). In these cases lysis was not complete and the integrity of the gDNA might have suffered from the incubation. In round two all bacterial genomes were obtained as pre-purified gDNA from DSMZ. In this case only two out of 51 genes were not successfully amplified (Table 3).

In summary, 49 different genes could be expressed in at least one of three investigated expression constructs. Six homologs (66CAG, 78BCA, 91BDO, 148LME, 164ACH, 165BLO) were expressed and extracted but showed significant degradation as observed by in-gel fluorescence and western blot analysis. Out of the 33 genes that were extractable in detergent solution, only six genes were sufficiently stable for large-scale expression, protein purification and crystallization screening. Three of these genes (88BEG, 90BCO, 98ELE) were significantly degrading during and after purification, which was also reflected in the heavy precipitate visible in the crystallization setups (data not shown).

The results of the three most promising candidates (29LLA, 99CCU, 135SCA) are depicted in Figure 8. 29LLA was expressed as GFP-fusion construct and subjected to FSEC (Figure 8a, c). 29LLA-GFP eluted at 7.6 ml, which corresponds to an apparent molecular weight of ~80-90 kDa on this column. Calculated from the amino acid sequence, the molecular weight of 29LLA-GFP is 82.9 kDA (29LLA 55.9 kDa, GFP 27 kDA). The positive control LacS-GFP, which is 3.3 kDa smaller, elutes at slightly higher elution volume. Due to the detergent surrounding the solubilized membrane protein, the apparent molecular weight estimated from the elution volume on SEC is generally larger than its theoretical mass derived from the amino acid composition. The absolute fluorescence measured for the peak of 29LLA-GFP is by 1/3 smaller (3.4 FU) compared to LacS-GFP (5.1 FU) indicating lower expression levels or extraction efficiency. There is another peak towards lower molecular weight, indicating that 29LLA-GFP is not fully monodisperse.

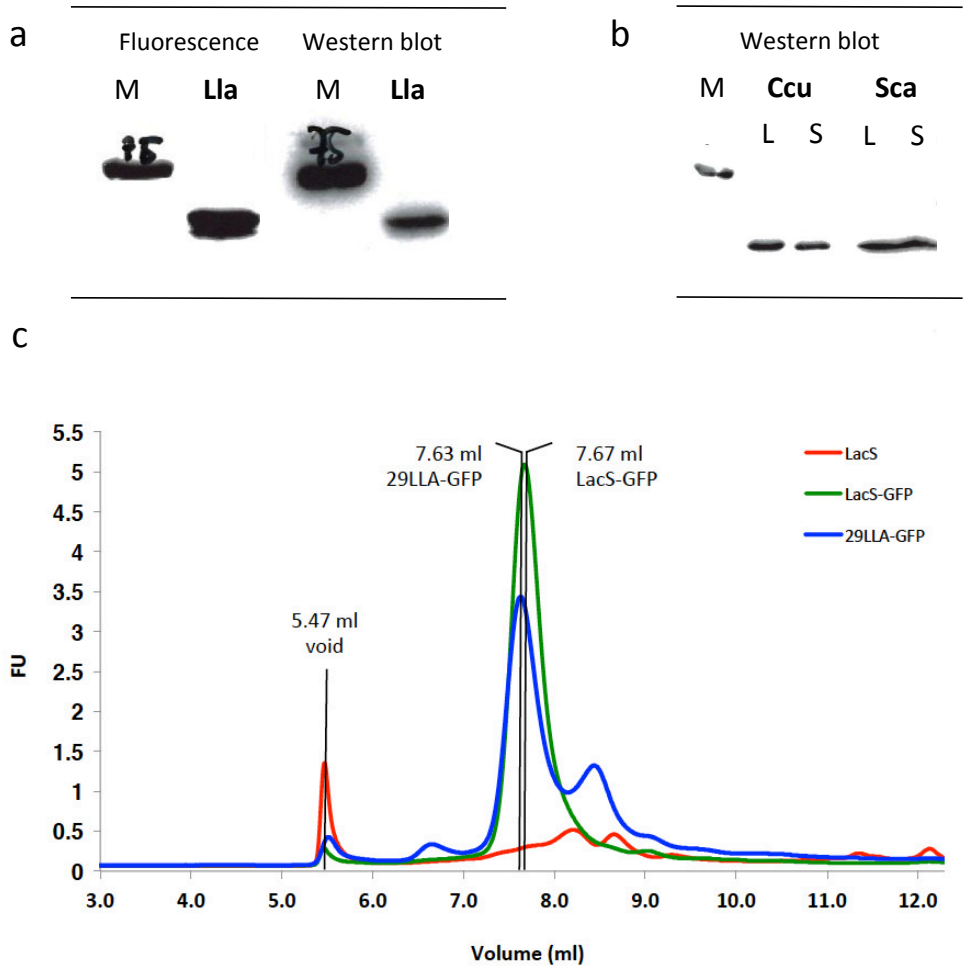

Figure 8 Candidate selection by western blot and FSEC analysis.

29LLA, 99CCU and 135SCA were identified as candidates with superior expression and extraction properties. (a) The GFP fluorescence of the extracted protein was detected for 29LLA in an SDS-PAGE gel (left), which was subsequently used for western blot analysis (right). (b) Samples of 99CCU and 135SCA after lysis (L) and after extraction (S) were analyzed by western blot analysis. All three proteins are visible as single bands after extraction. (c) FSEC analysis of 29LLA-GFP. The positive control LacS-GFP (green) and the fluorescence negative control LacS (red) are represented in an overlay with the elution profile of 29LLA-GFP (blue). Elution volumes of the main peaks are indicated in volume (ml) and fluorescence units (FU).

No significant fluorescence signal is detected for LacS expressed without GFP. Homolog 99CCU and 135SCA are both expressed and appear as single band on SDS-PAGE before and after extraction. Judging from western blot analysis it appears that most but not all of 99CCU is extracted (Figure 8b). Since both proteins were expressed without GFP their stability and aggregation behavior was investigated after purification from a large-scale expression culture (see next chapter).

A summary of the screening results is shown in Figure 9. The majority of genes (73%) could be overexpressed and detected by western blot analysis. At least 50% of the C3H and C3GH constructs but only three out of 20 proteins expressed as NH3 fusion could be extracted in DDM. The majority of the GFP fusion constructs (C3GH) were not stable when tested on FSEC. The behavior during scale-up and purification of the three best-behaved candidates (29LLA, 99CCU, 135SCA) will be described in the following chapter.

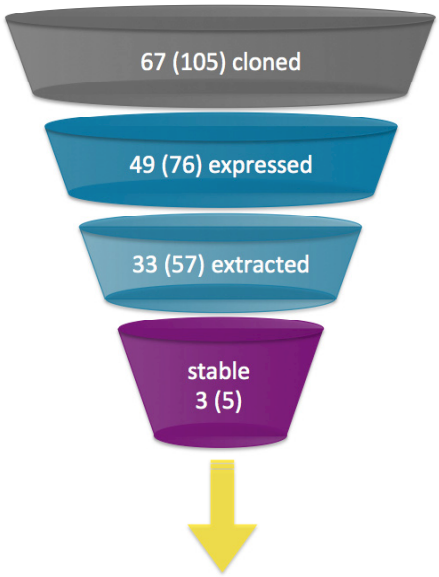

	I + II	III	total
selected	86	50	136
cloned	67	38	105
expressed			
NH3	20	n.a.	20
C3H	39	17	31
C3GH	24	19	43
extracted			
NH3	3	n.a.	3
C3H	21	15	36
C3GH	16	16	32
FSEC			
C3GH	1	10	11
NH3, C3H	n.a.	n.a.	n.a.
SEC			
NH3	0	n.a.	0
C3H	2	0	2
C3GH	1	2	3

Figure 9 Screening funnel of tested prokaryotic DMT homologs.

The figure summarizes the screening results obtained for the 105 investigated homologs Numbers in the funnel refer to individual homologs described in this study, values in brackets refer to the total number of tested homologs. In the table all homologs are listed as individual constructs (from left to right: round I+II, round III, total including all three rounds). NH3-constructs were only prepared for round 1 and 2.

2.2. Biochemical characterization of selected prokaryotic SLC11 homologs

For crystallization the target protein needs to be pure, stable and monodisperse in a detergent solubilized state. In order to achieve this, affinity purification on metal chelate resin via the His_{10}-tag attached to the protein was followed by size exclusion chromatography. IMAC was used as main purification step. This technique is based on the metal chelating properties of imidazole groups which form complexes with divalent metal ions such as Ni^{2+}, Co^{2+}, Fe^{2+} and Zn^{2+} (Block et al., 2009; Porath et al., 1975). Recombinant proteins fused to a polyhistidine-tag selectively bind to a metal loaded nitrilo-tri-acetic acid resin whereas untagged protein will not bind and is thus efficiently removed. Excess imidazole is added to elute the bound protein by competing for the metal ion. The second critical purification step is SEC, which separates proteins based on their shape and their molecular weight (Mori and Barth, 1999; Porath and Flodin, 1959). In that way high molecular weight aggregates can be efficiently separated from the target protein. SEC is a frequently used tool to monitor stability, oligomeric state and monodispersity of a protein, as these biochemical parameters determine the selection of suitable targets for crystallization studies. A stable and monodisperse protein typically elutes as single symmetrical peak at an elution volume corresponding to its size. Unstable or impure protein will result in a chromatogram containing multiple peaks with significant amount of the target protein in the void fraction. In case of a well-behaved protein a purity of 95 % should be reached with this protocol. After SEC, all fractions were analyzed by SDS-PAGE.

This two-step purification protocol was used for further characterization of promising candidates selected during the expression and extraction screening. Well-expressed bacterial homologs that could be extracted in DDM, and were detected as single band on a western blot were selected for this thorough investigation. For protein expression, *E.coli* cells carrying the respective expression vector were cultivated in TB medium in shaker flasks and grown o/n after induction with arabinose. The same temperature profile as for the test-expressions was used. The next day, the cells were lysed and membrane vesicles were prepared. At harvest, the optical density (OD_{600}) of the culture was typically 1.5-2.0, which is low compared to the overexpression of other membrane proteins under similar conditions. This resulted in 3-4.5 g vesicles from 2.4 l of culture (1.6 g vesicles/l culture), which were usually enough for initial protein

purification. Variation of the expression conditions (temperature, OD_{600} at induction, duration of expression) did not change the yield significantly. The large-scale cultures used for crystallization screening were grown in a fermenter to yield a higher cell mass per liter of culture. The OD_{600} at harvest was reproducible and did marginally vary depending on the DMT homolog, The OD_{600} was ~10-11 for 29LLA, ~11-12 for 99CCU and ~12-14 for 135SCA. One 9 l fermenter typically yielded between 45 and 100 g membrane vesicles, which was sufficient for 1-3 large-scale protein purifications to set-up ten 96-well crystallization plates (with 100 nl drops). For membrane protein extraction the vesicles were incubated with the mild non-ionic detergent DDM. Insoluble material was removed by high-spin centrifugation and the supernatant was incubated with Ni-NTA resin to bind the His-tagged target protein to the matrix. To remove unspecific bound proteins, the resin was washed with buffer containing intermediate amounts of imidazole. After elution of the bound protein with high amounts of imidazole the sample was incubated with 3C protease to cleave off the fusion-tag. The cleavage was combined with a dialysis step to lower the imidazole concentration. The protease is His-tagged and can therefore be removed together with the cleaved tag by rebinding to fresh Ni-NTA resin. The flow-through, containing the cleaved target protein was concentrated and subjected to SEC on a Superdex S200 column equilibrated in running buffer containing DDM 5x above its critical micelle concentration (CMC). The S200 column is capable of separating proteins with a mass range of 10-500 kDa. The void volume of the column is 8.4-8.6 ml. Due to the detergent micelle surrounding the membrane protein; the apparent size can be significantly higher than its calculated molecular weight. The prokaryotic DMT homologs elute at about 13 ml on an S200 column, which corresponds to an apparent molecular weight of 120-140 kDa. Since these proteins are on average 45-55 kDa in size, the detergent contributes to >50 % of the (apparent) molecular weight.

The sequence alignment of the three stable homologs and human DMT1 underlines general properties of these transporters (Figure 10). From the alignment it is apparent that the amino acid composition of the transmembrane regions is fairly conserved. 29LLA and 135SCA (ScaDMT) share a sequence identity to hDMT1 of 28% and 36% respectively, and a similarity of ~40%. Whereas 99CCU shares a high sequence similarity to 29LLA (43%) and ScaDMT (52%), its homology to hDMT1 is lower (28%) compared to the two other prokaryotic homologues.

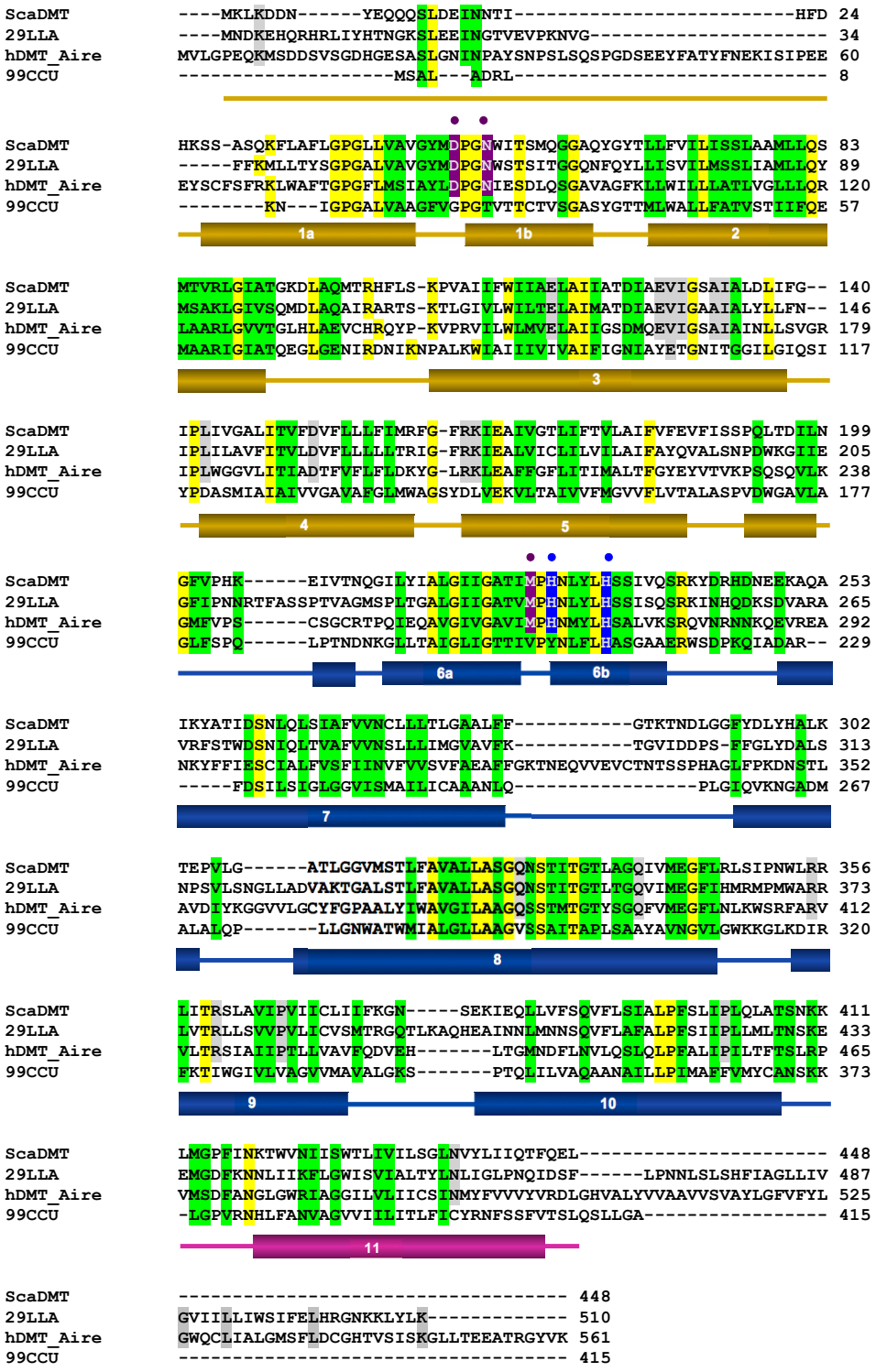

Figure 10 Sequence alignment.

The three stable bacterial DMT homologs and human DMT1 (isoform 3) are aligned with ClustalW2 (Larkin et al., 2007). Secondary structure elements are shown below. Labels indicate: (violet circle) residues of the transition metal binding site, (blue circle) residues involved in pH dependence and H^+ transport of hDMT1.

The N terminus of all three bacterial homologs is, on average $^{2}/_{3}$ shorter than the N terminus of hDMT1 (23 amino acids compared to 62 amino acids). Additionally their extracytoplasmic loops L5, L7, L9 (between TM5-6, TM7-8 and TM9-10) are more compact. Whereas 99CCU is the most compact protein with only 415 amino acid residues with the shortest loop regions, none of the metal binding site motifs is fully preserved. Instead of the highly conserved DPGN motif in helix 1 the residues in 99CCU are GPGT with a glycine replacing the aspartate and a threonine the asparagine residue. Additionally there is a valine instead of the methionine located in the unwound region of helix 6. Furthermore in 99CCU only one of the two highly conserved histidine residues is present (a tyrosine replaces the histidine that is usually located two residues after the binding site methionine). It is unclear how the altered binding site in 99CCU affects transport, but due to the importance of the residues for metal ion recognition, a different substrate-specificity can be expected. An experiment that investigates the transport properties of 99CCU, and a mutant of ScaDMT with equivalent replacements (i.e. D49G, N52T, M226V and H228Y) would reveal the altered transport properties. The prokaryotic homolog 29LLA is with 510 amino acids the longest of the three prokaryotic transporters. This can be explained by the long C terminus, which is predicted to encode for an additional transmembrane helix. However, the residues encoding the putative 12th transmembrane helix do not share strong homology with hDMT1.

In the following chapters the three selected homologs (29LLA, 99CCU and ScaDMT) are discussed with respect to their biochemical properties observed during large-scale expression and purification in maltoside detergents.

2.2.1. Purification of 29LLA

The first homolog selected for large-scale purification was 29LLA from the bacterium *Lactococcus lactis*. 29LLA was expressed as GFP fusion protein, which is in agreement with its predicted 12 transmembrane spanning segments. When expressed as fermentation culture the cell density was reproducibly around an OD_{600} of 10-11, at harvest. From 1 l fermenter culture I typically obtained ~5 g membrane vesicles. For 1 mg of purified protein (after SEC), 3 l of fermentation culture (corresponding to 15 g membrane vesicles) were required, which is improved compared to 20 l of shaker flask culture that

would be necessary for the same amount of protein (despite using the same medium, inoculum, temperature profile). Due to the comparably low binding efficiency of 29LLA to IMAC resin, 1.2 ml of 50 % Ni-NTA slurry were necessary per 1 g of vesicles. Consequently the protein was more diluted after elution and needed extensive concentration before size exclusion chromatography. Compared to 99CCU and 135SCA, 29LLA was the least stable homolog during the two concentrating steps (before SEC and before crystallization), as usually 20-30% of 29LLA was lost during each concentration step. In Figure 11 the size exclusion profile of 29LLA together with its corresponding SDS-PAGE and in-gel fluorescence images is shown. The protein was still fused to GFP and loaded onto the SEC column directly after the IMAC. The calculated size of this construct is 82.9 kDa.

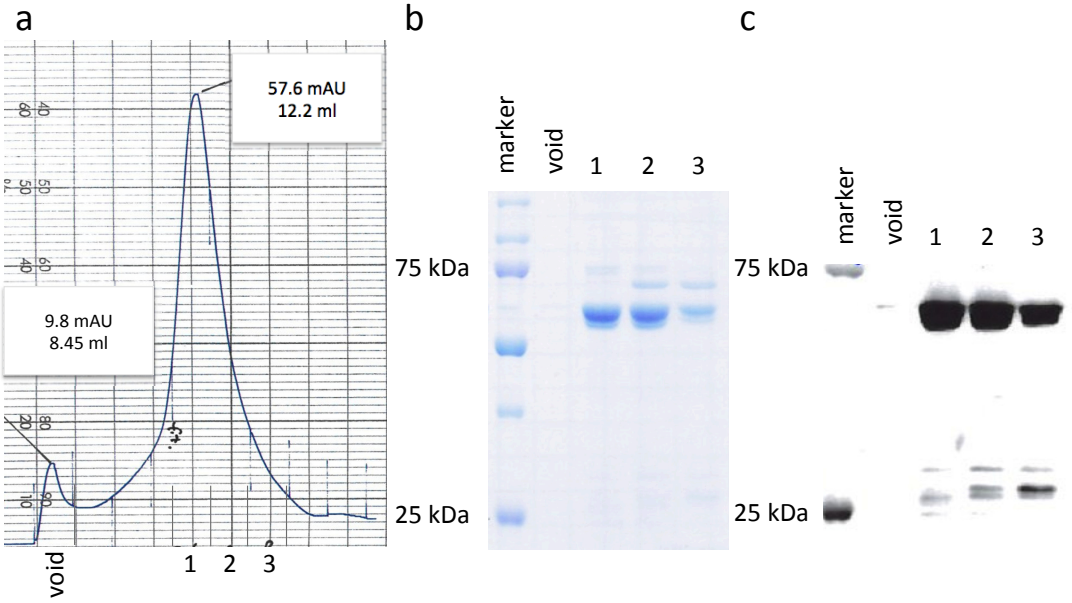

Figure 11 Size exclusion chromatography of 29LLA.

29LLA was expressed as C-terminal His_{10}-GFP-fusion protein and purified in DDM. (a) Size exclusion profile detected by UV absorption at 280 nm. Elution volume and peak height of the void peak (8.45 ml, 9.8 mAU) and main peak (12.2 ml, 57.6 mAU) are labeled. The protein elutes as a single peak that is, although slightly tailing, well separated from the void peak. (b) SDS-PAGE gel of the void fraction and the three main peak fractions 1-3. The target protein is the main band at 65 kDa and there is no protein detectable in the void peak. (c) In-gel fluorescence measurement of the gel shown in (b) confirms that there is little fluorescence signal in the void peak thus underlining that the fraction of aggregated protein is not significant. Whereas the main band corresponds to the target protein fused to GFP, smaller bands around 28 kDa found in fractions 1-3, most probably come from degradation products that still include the GFP moiety.

On SDS-PAGE the protein is found close to the 65 kDa MW marker. The higher molecular weight band, which as it is not fluorescent, might probably be an impurity. The 4 bands at ~28 kDa are fluorescent, and thus probably correspond to proteolytic cleavage of the C-terminal GFP. The small void peak does not contain a significant amount of the target protein. The main band in fractions 1-3 contains a small fraction with apparent smaller molecular weight, which could be due to the loss of few amino acids on the N terminus. Figure 12 shows the chromatogram of the same protein after incubation with 3C protease. The sample was subjected to SEC without prior removal of the GFP. There is uncut protein detectable in the main peak at 12.9 ml as visible in the SDS-PAGE and the corresponding in-gel fluorescence image of the gel.

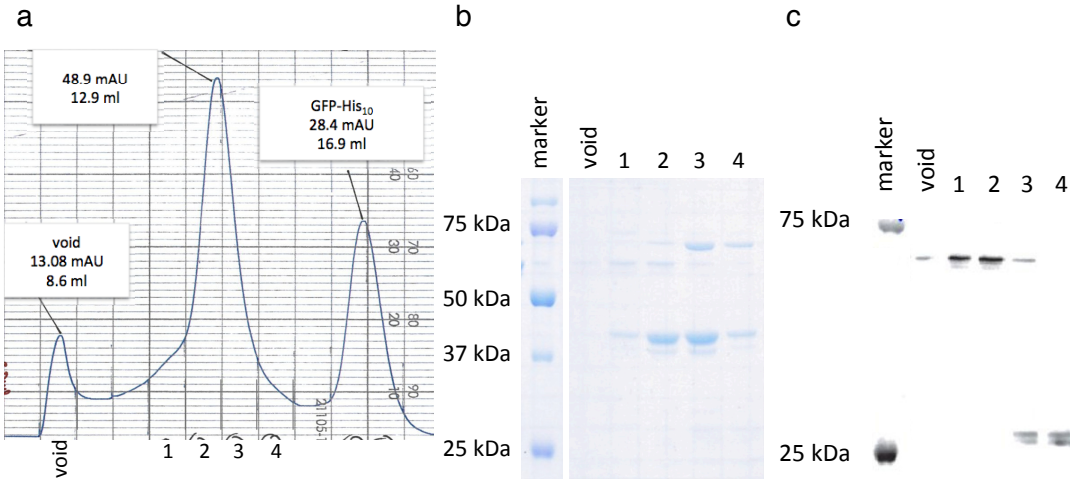

Figure 12 Size exclusion chromatography of 29LLA after cleavage of the fusion protein.
(a) Size exclusion profile of 29LLA and GFP detected by measurement of the UV absorption at 280 nm. Elution volume and peak height of the void peak (8.6 ml, 13.08 mAU) and main peak (12.9 ml, 48.9 mAU) are labelled in the figure. The target protein elutes as a single peak well separated from the void. (b) SDS-PAGE gel of the void fraction and the four main peak fractions 1-4. The cleaved target protein corresponds to the main band at ~40 kDa. There is no protein detectable in the void peak. (c) In-gel fluorescence measurement of the gel shown in (b). There is very little fluorescence in the void peak. The size corresponds to the target protein fused to GFP. In fractions 1-3 residual 29LLA still fused to GFP is detectable. In fraction 3 and 4 the GFP of the second peak at 16.9 ml with 28.4 mAU is already visible.

A second IMAC step was introduced after cleavage, to remove the fusion-tag and the His-tagged 3C protease prior to SEC. In this purification, the protein eluted at the same volume as in the medium-scale purification experiment, although with a shoulder at higher molecular weight. On SDS-PAGE the fractions show a double band containing a

minor fraction with apparent smaller molecular weight (Figure 13). Despite this heterogeneity, 29LLA was concentrated to 7.5 mg/ml and subjected to crystallization screening. These setups did not show any crystals, instead the protein heavily precipitated in most of the wells.

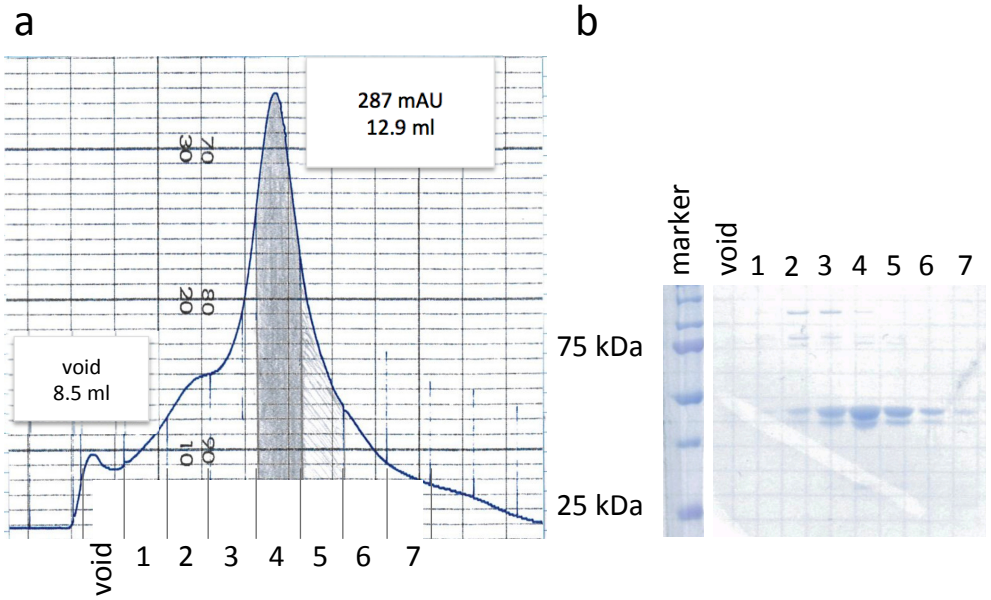

Figure 13 Large-scale purification of 29LLA and initial crystallization trials.

(a) SEC chromatogram of the large-scale purification of 29LLA. (b) SDS-PAGE analysis of the peak fractions.

Taken together, 29LLA could be purified in the mild maltoside detergent DDM. A double band detected on SDS-PAGE could come from proteolytic cleavage. In order to determine if proteolytic digest occurs during purification each gel band could be analyzed by mass spectrometry. Investigating freshly purified protein in a limited proteolysis experiment, followed by SDS-PAGE and mass spectrometry, might additionally help to identify a stable core of 29LLA. Systematic N- and C-terminal truncations of 29LLA have been investigated during this study (data not shown) but did neither result in compelling stability improvements nor in improved crystallization properties of the protein.

2.2.2. Purification of 99CCU

The prokaryotic SLC11 homolog of *Cryptobacterium curtum* (99CCU) was identified in the expression screening as promising candidate, fused to a C-terminal His_{10}-tag. For 99CCU eleven transmembrane segments are predicted. The protein has very compact loops even compared to other bacterial homologs. The expression yields are comparable to 29LLA. With 20 g membrane vesicles approximately 6 mg of protein was eluted from an IMAC column. Compared to 29LLA the losses after size exclusion chromatography were lower. Typically 15-20% of protein was lost at the final concentration step, resulting in 1.8 mg pure 99CCU, that were used for crystallization experiments. In Figure 14a the chromatogram of the protein purified in the detergent DDM is shown. The protein elutes at 13.1 ml, similar as observed for 29LLA and is well separated from the small void peak. In this chromatogram there is also a small shoulder found at higher elution volume. In Figure 14b the corresponding fractions were loaded on a SDS-PAGE gel and stained with Coomassie blue dye. As for 29LLA there is no target protein detected in the void fraction.

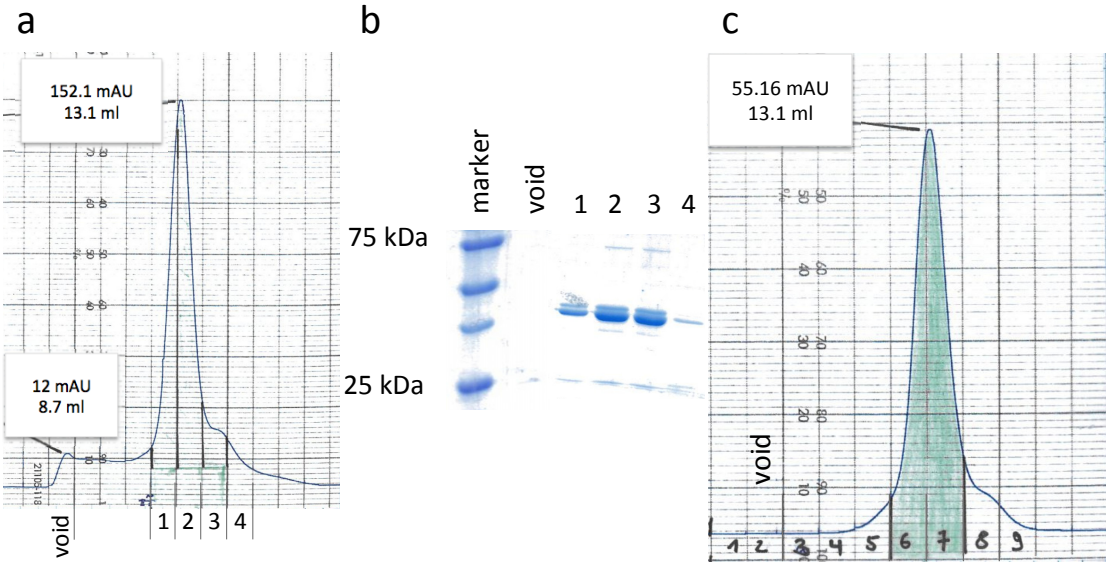

Figure 14 Size exclusion chromatography of 99CCU purified with DDM.

(a) The protein elutes at 13.1 ml as symmetrical peak with a small shoulder towards the lower molecular weight. The void peak, corresponding to higher molecular weight aggregates, is very small. (b) SDS-PAGE gel of the void and the four peak fractions. The protein runs as double band indicating heterogeneity. This double band behavior was not observed in subsequent purifications. (c) Reinjection of the protein three days after the first SEC.

The Protein migrates with an apparent molecular weight of 45 kDa. The faint band at 25 kDa might originate from degradation products. The peak fractions were stored at 4 °C and subjected to a second size exclusion run three days later. The chromatogram is shown in Figure 14c. Also in the second run the small shoulder at higher elution volume is found, but there is no void peak and no shift in the elution volume of the main protein peak, thus indicating that the protein is stable in the detergent DDM.

For crystallization screening, the expression was scaled-up, the protein was purified by the same procedure and concentrated to 5.0 and 7.5 mg/ml. Crystallization was broadly screened (>2000 conditions in different full and sparse matrix screens), with the help of the crystallization facility of the Dept. of Biochemistry, in 100 nl volume by vapour diffusion in sitting drops. Despite its purity and apparent stability, 99CCU did not crystallize when purified in the detergent DDM. In a next attempt the crystallization behavior of the protein in shorter chain detergents of the same class was investigated. The protein was purified in the detergent DM, which is two methyl groups shorter as DDM resulting in a smaller micelle size: An empty detergent micelle of DDM in aqueous buffer is ~64 kDa compared to 37 kDa of an empty DM micelle (Kunji et al., 2008). In Figure 15 the SEC profile and its corresponding SDS-PAGE analysis is shown. 99CCU is monodisperse and elutes at 13.7 ml with a small shoulder at higher elution volume. The protein is pure as confirmed by SDS-PAGE.

Whereas the protein appears to be stable in the detergents DM and DDM, there are first signs of reduced stability in the shorter chain maltopyranoside NM. In Figure 15 the SEC profile and the corresponding SDS-PAGE analysis is depicted. For purification in NM, protein extraction and IMAC were performed in DM and the detergent was exchanged to NM on the S200 column. This procedure is gentle but may result in an incomplete detergent exchange. Still in several cases detergent exchange by this protocol has been shown to significantly improve crystallization behavior of the protein. For crystallization of 99CCU in DM and NM (n-nonyl-β-D-maltopyranosid) solution, the protein was concentrated to 5, 7.5 and 10 mg/ml and used for broad crystallization screening, but in no case any crystals were observed. In summary 99CCU, showed promising biochemical properties and was successfully purified in different maltosides. However, despite its promising behavior and a broad screening of conditions, the protein did not crystallize in any of the three detergents. Crystallization is a complex process that is sensitive to biochemical, chemical and physical properties of the sample such as purity,

stability, proteolysis that might occur, its isoelectric point (pI), and conformational heterogeneity.

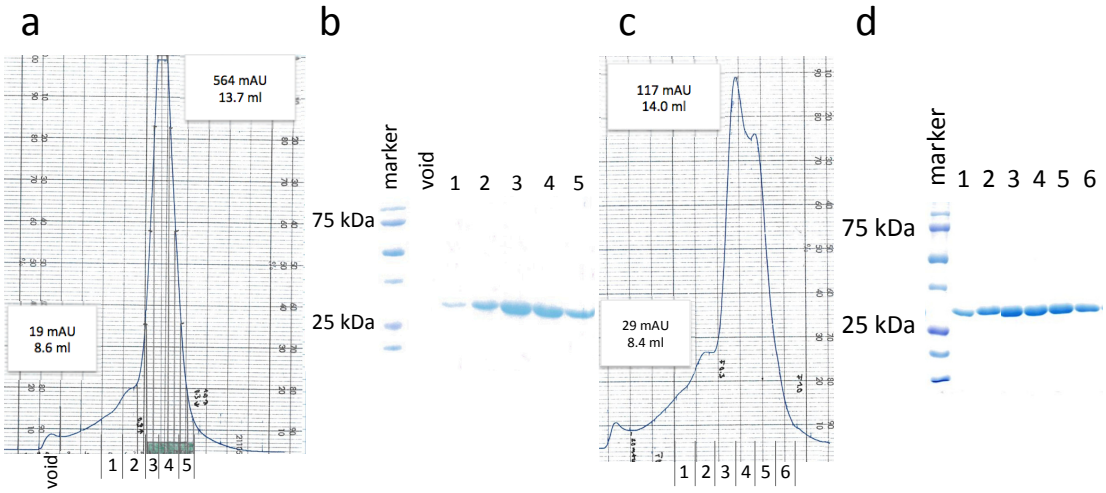

Figure 15 Purification of 99CCU in the detergent DM and NM.

(a) Size exclusion profile in DM. The protein elutes as one symmetric peak with a small peak at lower and a slight shoulder at higher elution volume. The void peak is small. (b) SDS PAGE gel showing a single band corresponding to 99CCU in the elution peak and no protein in the void fraction. (c) Size exclusion chromatogram of 99CCU purified in NM. The protein is well separated from the void. A detector problem caused the double peak. The elution volume is shifted to 14 ml, which can be explained by the smaller micelle of NM. (d) The SDS PAGE gel shows a single band, indicating that the protein is pure.

Successful crystallization also depends on the properties of the surrounding solution including precipitant type and concentration, salt type and concentration, pH and buffer, detergent, lipids, temperature, crystallization volume, and the crystallization technique (eg. vapor diffusion, the use of bicelles or lipidic cubic phase). Judging from size exclusion and SDS-PAGE analysis the protein was sufficiently stable and pure after purification. Despite these promising starting condition, the process of crystallization remains still an empirical process and requires extensive screening. While a large set of different conditions were tested (>3800), they cover only a small fraction of the possible experimental space. Conformational heterogeneity or a disadvantageous net surface charge of the protein at certain pH values may prevent crystallization. For 99CCU other detergents apart from maltosides were not thoroughly investigated. In addition to that it may have been worth to investigate other crystallization techniques such as crystallization in bicelles (Ujwal and Bowie, 2011) or in lipidic cubic phases (Landau and Rosenbusch, 1996). It can also not be excluded that lipids might have had a significant impact on the

crystallization properties of the protein. In such a case it might be worthwhile to add lipids during purification, before crystallization (e.g. by the HILIDE method (Gourdon et al., 2011)) or as additive together with the mother liquor during crystallization. Since ScaDMT, the homolog presented in the next chapter, was better behaved and crystallized, I decided not to explore all possibilities for crystallization of 99CCU and instead focused my efforts on improving the ScaDMT crystals.

2.2.3. Purification and crystallization of ScaDMT

The third bacterial homolog identified as promising candidate for further biochemical characterization, ScaDMT (135SCA), was cloned form the bacterium *Staphylococcus capitis*. Although phylogenetic distances between 29LLA and 135SCA are small, 11 transmembrane segments were predicted for ScaDMT, in contrast to the 12 TMs predicted for 29LLA. The protein was expressed as C-terminal His_{10}-tag construct and scale-up to fermenter cultures yielded on average 10 g membrane vesicles per 1l medium (OD_{600} at harvest 12-14). After purification, following similar procedures as described for 99CCU, ScaDMT was stable in the longer chain detergent DDM and the shorter detergent DM. In Figure 16 SEC profiles of the protein purified in DDM (left) and in DM (right) are shown.

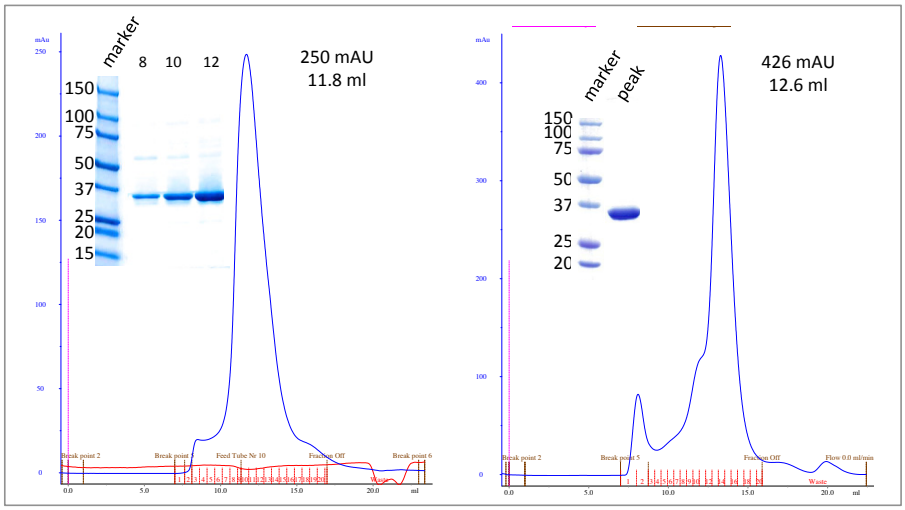

Figure 16 Size exclusion chromatogram of ScaDMT.

(left) Purification of ScaDMT in DDM. The protein elutes as single peak. The purity was confirmed by SDS-PAGE, which shows one major band with traces of impurity at 60 kDa. (right) ScaDMT purified in DM. The protein elutes as sharp main peak with a small second peak towards higher molecular weight. Peak fractions were pooled and loaded on SDS-PAGE (peak).

The protein elutes as single narrow and symmetric peak and is pure as judged from SDS-PAGE analysis. Both samples were concentrated to 7.5 mg/ml and subjected to crystallization screening. Expression levels of ScaDMT were significantly higher as those of 29LLA and 99CCU. From 10 g vesicles on average 10 mg protein eluted from the IMAC column and after size exclusion ~2.0 mg pure ScaDMT was available for further experiments (1.7 mg pure protein/l culture). In contrast to DM the protein was not stable when purified in the detergent NM) which is one methyl group shorter than DM, and instead showed time-dependent aggregation (data not shown).

In contrast to 29LLA and 99CCU, I have succeeded with crystallization of ScaDMT. When purified in DDM, ScaDMT did not crystallize despite the broad range of investigated conditions (>2400). Contrary to DDM, crystals of ScaDMT purified in DM were observed in a single well of a screen containing more than 2400 conditions. The precipitant solution leading to successful crystallization contained 200 mM $CaCl_2$, 90 mM NaCl, 90 mM MES, pH 6.0, 26-30% PEG400 (Note: $MgCl_2$ instead of $CaCl_2$ as well as PEG300 instead of PEG400 were tolerated). Micro-crystals appeared three weeks after the drops were set up and grew over a period of 6 weeks to needles with a maximal dimension of about 10 µm (Figure 17). For the investigation of their diffraction properties the crystals were cryo-protected by stepwise increase of the PEG concentration to 35% and frozen in liquid propane.

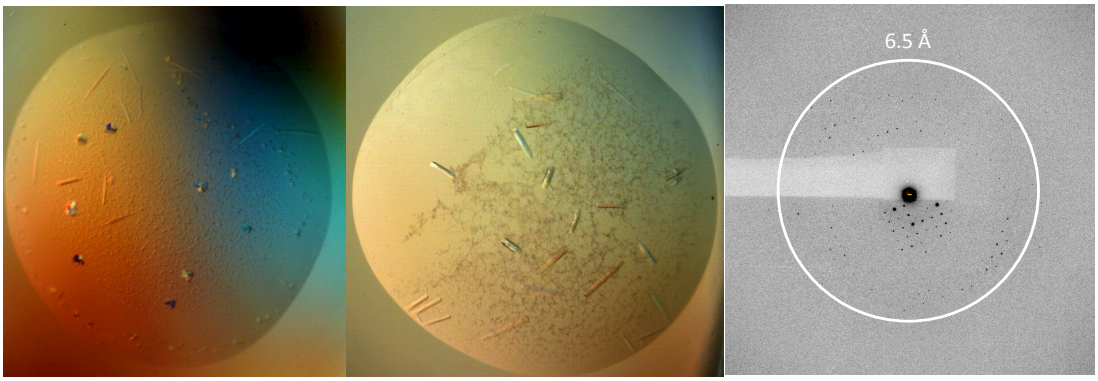

Figure 17 Crystals of ScaDMT.

(a) Initial crystal hit. (b) Crystals after fine screening. (a, b) The drops were both imaged 7 weeks after the experimental set-up. Images taken under a polarization filter. (c) Diffraction pattern collected at PXI. Resolution limit 6.5 Å.

Diffraction experiments were carried out at the X06SA (PXI) beamline at the Swiss Light Source. Initial crystals diffracted up to 7.5 Å. After refinement of crystallization conditions larger crystals were obtained but the diffraction did not improve significantly. The best crystal diffracted to ~6.5 Å and allowed data collection (Table 4), which was processed with XDS. The data is 92.7% complete and extends up to 6.5 Å. The crystals are of space group $P3_221$ with cell dimensions of a=b=150.9 Å, c=157.3 Å, α=β=90°, γ=120°. The Matthews parameter was calculated to estimate the number of protein molecules per asymmetric unit (Kantardjieff and Rupp, 2003). For these crystals two molecules per asymmetric unit would results in a solvent-content of 75%, which is not unusual for membrane protein crystals. These crystals were later used to determine the structure of full-length ScaDMT by molecular replacement (see chapter 2.7).

ehr38_4, ScaDMT alone

SUBSET OF INTENSITY DATA WITH SIGNAL/NOISE >= -3.0 AS FUNCTION OF RESOLUTION

RESOLUTION LIMIT	NUMBER OF REFLECTIONS OBSERVED	UNIQUE	POSSIBLE	COMPLETENESS OF DATA	R-FACTOR observed	R-FACTOR COMPARED expected	I/SIGMA	R-meas	CC(1/2)
18.16	2644	214	231	92.6%	10.1%	10.1%	2644	24.94	10.6%	98.6*
13.31	4457	320	320	100.0%	9.2%	10.4%	4457	24.66	9.5%	99.7*
11.01	5485	395	397	99.5%	11.3%	11.0%	5485	21.86	11.7%	99.6*
9.59	5874	456	462	98.7%	12.4%	11.5%	5874	18.42	12.9%	99.6*
8.61	6596	507	518	97.9%	16.5%	13.7%	6596	14.81	17.2%	99.6*
7.88	7047	535	552	96.9%	23.8%	18.6%	7047	10.78	24.8%	99.7*
7.31	6480	547	606	90.3%	41.9%	29.7%	6480	7.01	43.8%	98.8*
6.85	6396	555	639	86.9%	90.5%	60.8%	6396	4.34	94.8%	95.4*
6.47	5971	572	701	81.6%	135.5%	90.1%	5961	2.90	142.5%	87.4*
total	50950	4101	4426	92.7%	13.0%	12.0%	50940	12.54	13.6%	98.8*

Table 4 Data collection statistics of ScaDMT

The number of reflection, the completeness of the data set, its calculated R-factor and the I/sigma are displayed for different resolution shells.

2.2.4. Summary

I have started my work towards the structure determination of a DMT transporter by selecting stable proteins from a large set of prokaryotic homologs. For that purpose I have cloned 86 homologs from genomic DNA of different bacteria. From this set three proteins were sufficiently stable for scale-up purification and screen for crystallization.

Figure 18 summarizes the progress of this project, from expression screening to crystallization, in percent of all successfully cloned homologs. Exact numbers are listed in Figure 9. Among the investigated proteins the homolog 29LLA from the bacterium *Lactococcus lactis* was the least stable transporter, which yielded heavy precipitate in

crystallization experiments. The homolog 99CCU from the bacterium *Cryptobacterium curtum* was better behaved as it was stable in DDM, DM and NM but it did not crystallize either. ScaDMT from the bacterium *Staphylococcus capitis* was stable when purified in the detergent DDM and DM. While no crystals were obtained in DDM, ScaDMT was successfully crystallized in the detergent DM. The diffraction of these crystals was limited to 6.5 Å and could not be improved further.

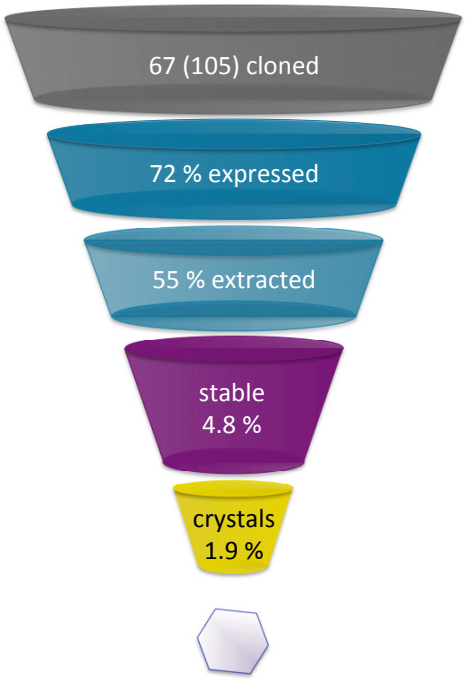

Figure 18 Summery of the screening of prokaryotic DMT homologs.
In total 67/105 genes could be amplified and screened for expression. 72 % (49/76) of these proteins could be expressed in at least one of the three vectors used. Around 25 % were not extractable. Only one tenth of the extractable proteins were stable and monodisperse (3/5). On average one out of 50 investigated homologs yielded protein crystals (1/2). Numbers in parentheses indicate the number of proteins described in this study/total number of homologs investigated in this project.

2.3. Biochemical characterization of ScaDMT

2.3.1. Biochemical characterization of truncated ScaDMT constructs

Flexible parts of a folded protein such as disordered termini or loops might interfere with the formation of an ordered crystal lattice and as a consequence prevent crystallization or lead to poor diffraction properties of the crystals (Rupp, 2010). The removal of flexible parts has been successfully applied in several cases to improve the packing properties of proteins in crystals and thus increase the resolution of the diffraction data (De Kerpel et al., 2006).

In an attempt to improve the crystal packing of ScaDMT, its N and C terminus were systematically shortened and new constructs were tested for their stability in detergent solution. While homologues of the SLC11 family are highly conserved, particularly in their predicted trans-membrane regions, their N terminus is poorly conserved and predicted to be flexible. By analyzing the sequence with respect to its probability not to fold into defined structures with the program DRIPPRED (MacCallum, 2004), the first 30 residues of the N-terminal region of ScaDMT were predicted to be unstructured (Figure 19).

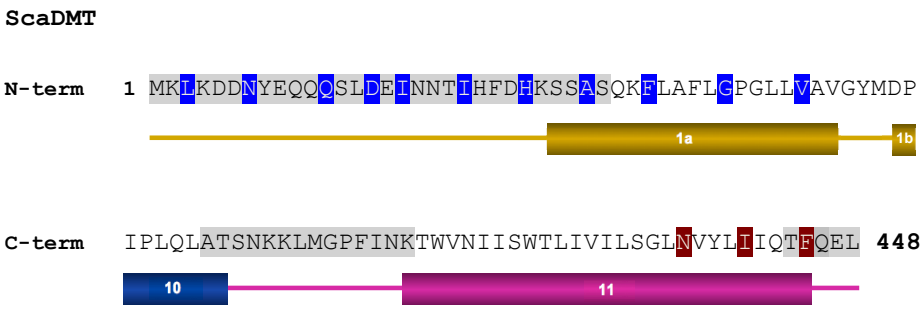

Figure 19 Disorder prediction of ScaDMTs termini.

The upper panel shows the first 50 residues of ScaDMT, the lower panel the 48 residues of the C-terminal region. The amino acids that were predicted to be disordered (DRIPPRED, MacCallum, 2004) are highlighted in grey. The start of the respective truncations is indicated in blue. The last amino acid of the respective C-terminal truncation is highlighted in red. Secondary structure elements are shown below.

Several constructs were thus prepared with part of these residues removed. As predictions contain a certain degree of uncertainty, also two constructs removing half of the first predicted transmembrane segment were included. As any removal of a part of a transmembrane segment was expected to result in unstable protein, these constructs should serve as upper boundaries of how many residues of the N terminus can be removed without interfering with protein folding and stability. Although on the C terminus no disorder was predicted, the removal of amino acids was also investigated in this case.

2.3.2. Expression test and western blot analysis of truncated ScaDMT constructs

Fourteen truncated constructs of ScaDMT were prepared with the FX-cloning method. For expression, the genes were cloned into the same vector as used for the expression of full length ScaDMT. Test-expressions and western blot analysis were performed as described earlier. ScaDMTΔ17-448 gave the strongest signal on the western blot, indicating good expression and extraction properties. ScaDMTΔ25 and ScaDMTΔ29, two constructs starting close to the first predicted transmembrane helix were as well detected in the total lysate as well as in the extracted fraction. In contrast no expression could be detected for the shorter construct ScaDMTΔ32. Similarly ScaDMTΔ37 was poorly expressed and not extractable in detergent solution. Unexpectedly ScaDMTΔ42, a shorter construct in which part of the first transmembrane helix was removed was well expressed and extractable in DM. Constructs with shortened C terminus such as ScaDMT1-Δ437 and ScaDMT1-Δ441 were expressed but only poorly extractable in mild detergent, which indicates that they are not probably folded. Among the C-terminal truncations, only the longest construct ScaDMT1-Δ445 with three residues on the C-terminus removed was the construct that was fully extractable in DM (Figure 20). In summary the removal of residues of the putatively disordered N terminus of ScaDMT was well tolerated and provided stable shortened protein constructs that are potentially suitable for crystallization experiments. Remarkably, in the shortest stable construct ScaDMTΔ42 a part of the predicted first transmembrane helix was removed.

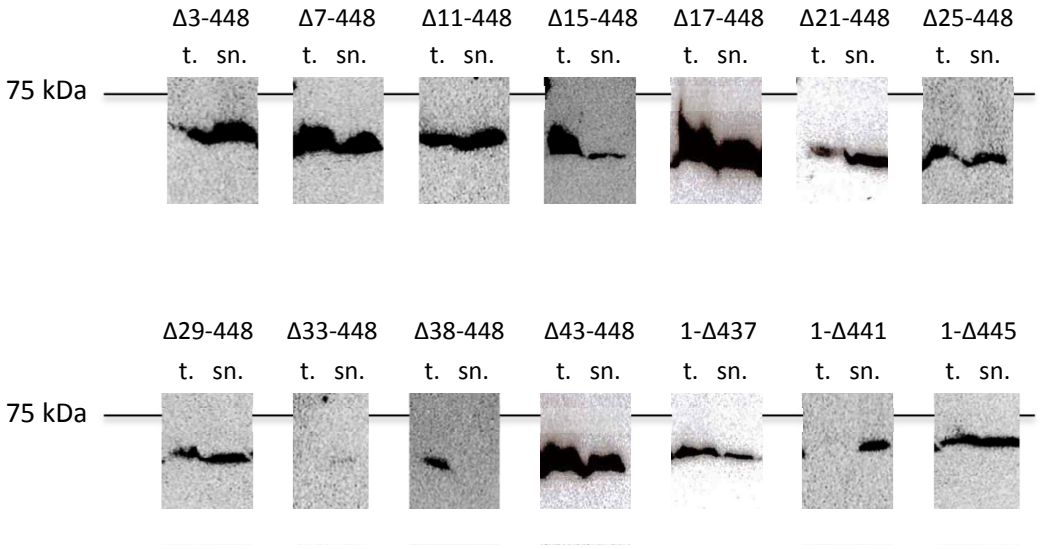

Figure 20 Western blot analysis of ScaDMT truncations.

Expression and extraction analysis of N- and C-terminal truncation constructs. The constructs are labeled on top. t. indicates the total sample loaded after cell lysis, sn. the supernatant after extraction with detergent and ultracentrifugation. The size of the molecular weight marker (75 kDa) is indicated by the black line.

2.3.3. Purification of selected ScaDMT truncation constructs

As result of the expression screening, the shortened constructs ScaDMTΔ16 and ScaDMTΔ42 were selected as most promising candidates for scale-up and purification in DM due to their strong expression properties. In addition ScaDMTΔ24 and ScaDMTΔ28 were selected because of the proximity of the N-terminus to the first predicted trans membrane segment. Among the C-terminal truncations ScaDMT1-Δ445 was selected as only construct with suitable expression and extraction properties. All constructs were expressed in shaker flask cultures (each 4 x 0.6 l TB) according to the protocol described previously. The OD_{600} at harvest was between 1.0 and 1.8, which is on average lower than for the full length ScaDMT protein (when expressed in shaker flask cultures the OD_{600} in this case was 1.6-2.0). Nevertheless, despite the small amount of membrane vesicles (1.5-2.8 g), the amount of protein was sufficient for purification and size exclusion chromatography. Fermenter cultures of the two most promising truncated ScaDMT constructs (ScaDMTΔ28 and ScaDMTΔ42) were grown in the same way as described for full-length ScaDMT. The OD_{600} at harvest was reduced for both proteins, although for ScaDMTΔ28 (OD_{600} 3.5) the effect was more pronounced than

for ScaDMTΔ42 (OD_{600} 10 compared to 12-14 for ScaDMT full-length). The proteins were efficiently extracted with the detergent DM and purified by the standard two-step protocol described earlier. The amount of protein eluted from the Ni-NTA column was very similar to what I observed for full-length ScaDMT. Only ScaDMTΔ42 eluted less than 0.8 mg protein per g of membrane vesicles. After proteolysis and concentration all proteins were subjected to size exclusion chromatography. When applied to SEC, ScaDMTΔ16 purified in DM eluted as peak at ~13.3 ml, which is shifted by 0.7 ml compared to WT (which in DM elutes at ~12.6 ml) but with a shoulder towards higher molecular weight and a second peak at the void volume (left). The void peak did contain aggregated target protein and no void peak was observed when injecting the main peak fractions three days later, thus indicating that the largest part of the protein was stable for several days at 4 °C (Figure 21 right). Some higher molecular weight impurities (observed in Fraction 11 and 13 around 75 kDa) could contribute to the shoulder seen in the chromatogram (Figure 21 left, small panel).

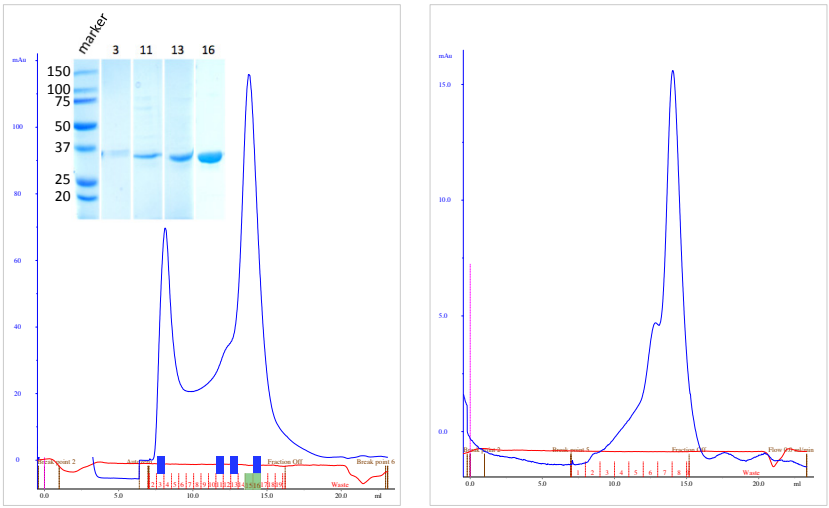

Figure 21 Size exclusion profile of ScaDMTΔ16.

(left) ScaDMTΔ16-448 was purified in DM and injected on a Superdex S200 column. The fractions 3, 11, 13 and 16 highlighted in blue were analyzed by SDS-PAGE (inset). Molecular weights are indicated in kDa. The fractions 15 and 16 were pooled and subjected to a second SEC three days after the initial purification (highlighted in green). (right) SEC run of the peak fractions three days after purification. There is no void peak detectable. The shoulder towards higher molecular weight is seen in both SEC runs.

While comparably pure (see fraction 16 on SDS-PAGE) with the bulk of the protein eluting as sharp peak at corresponding elution volumes, ScaDMTΔ16 is not fully monodisperse as indicated by the shoulder observed in both SEC chromatograms. ScaDMTΔ16 yielded 0.3 mg of SEC purified protein per liter of culture.

The SEC profile of the seven amino acids shorter construct ScaDMTΔ24 is shown in Figure 22. Also in this case a void peak is detected that contains small amounts of aggregated target protein. However, the main peak eluting at 13.5 ml is sharp and symmetrical. In this chromatogram the shoulder observed in construct ScaDMTΔ16 is less pronounced in ScaDMTΔ24. Again the elution profile of the second SEC run upon reinjection of the protein after an incubation time of three days is promising, as there is no void peak and only a small shoulder observed. The behavior of ScaDMT Δ 24 thus suggests that the protein construct is stable in the detergent DM after storage at 4 °C for several days. The purification of ScaDMTΔ24 resulted in 0.45 mg sufficiently pure protein per liter of culture.

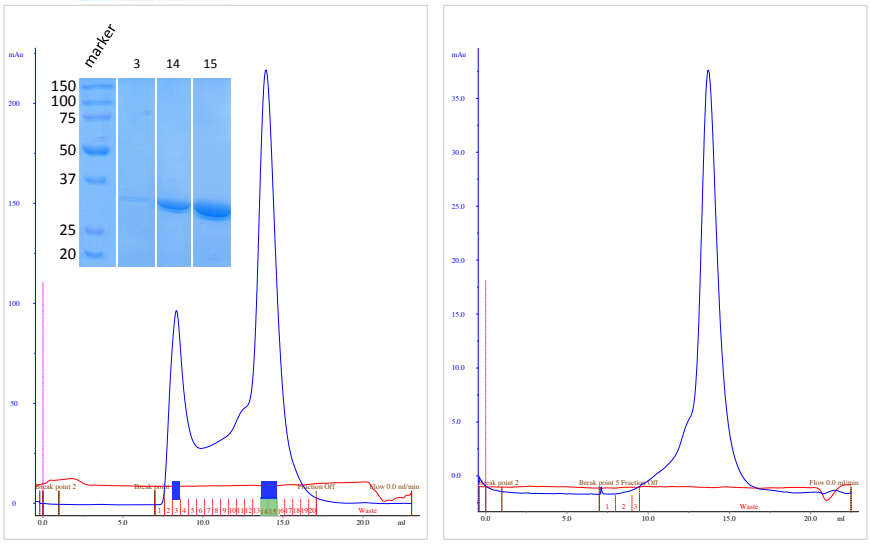

Figure 22 Size exclusion profile of ScaDMTΔ24.

(left) SEC profile of ScaDMTΔ24 purified in DM. Fractions 3, 14 and 15 (blue bars) were loaded on a SDS-PAGE gel shown in the upper left of this figure. Molecular weights (kDa) are indicated. Fractions 14 and 15 (green) were subjected to a second round of SEC three days after the initial purification. (right) Size exclusion profile of the peak fractions, three days after purification. There is no void peak detectable. The shoulder towards higher molecular weight has almost vanished.

ScaDMTΔ28, which is only four amino acids shorter than ScaDMTΔ24, shows a comparable behavior on SEC (elution volume of main peak at ~13.5 ml). The protein is stable for several days at 4 °C although the small shoulder on the second SEC chromatogram is somewhat broader compared to the longer construct (Figure 23). The yield for ScaDMTΔ28 was, with 0.6 mg/l culture, the highest amongst the tested ScaDMT truncation constructs but this still only corresponds to one third of the yield usually observed for full-length ScaDMT (~2 mg/l culture).

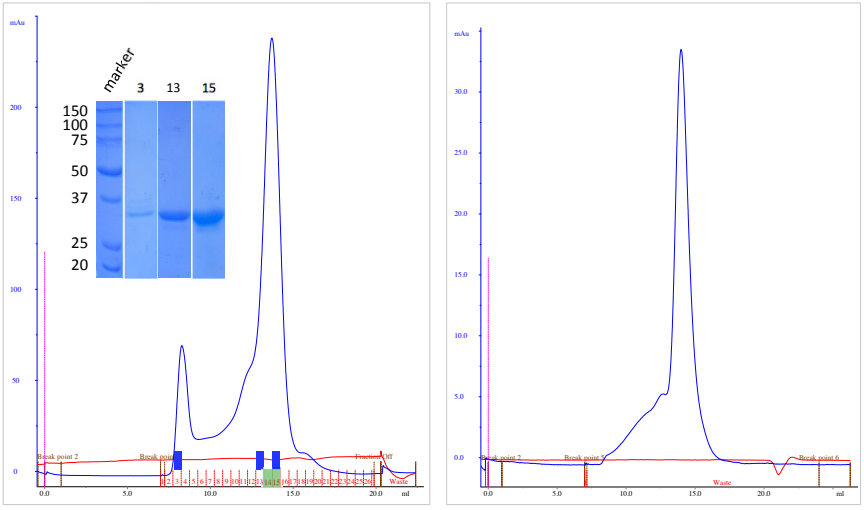

Figure 23 Size exclusion profile of ScaDMT Δ 28.

(left) SEC profile of ScaDMTΔ28 purified in DM. Fractions 3, 13 and 15 (blue bars) were loaded on a SDS-PAGE gel shown in the upper left of this figure. Molecular weights are indicated in kDa. Fractions 14 and 15 (green) were subjected to a second SEC run three days after the initial purification. (right) Profile of the second SEC run. There is no void peak detectable but the shoulder towards higher molecular weight has become broader.

Unexpectedly, but consistent with previous experiments, the shortest construct ScaDMTΔ42, which removes parts of the first predicted transmembrane helix is stable in detergent solution (Figure 24). Consistent with being the shortest of the tested constructs, the main peak elutes at 13.7 ml. Even if the protein peak is somewhat asymmetric, the SDS-PAGE of the corresponding fractions shows a single species at the expected size. When subjected to a second round of SEC after incubation at 4 °C for three days the protein elutes as a single sharp peak with a small shoulder at lower elution volume. Although the protein was well behaved, the yield of purified protein (0.4 mg/l culture) was reduced by 80% compared to full-length ScaDMT.

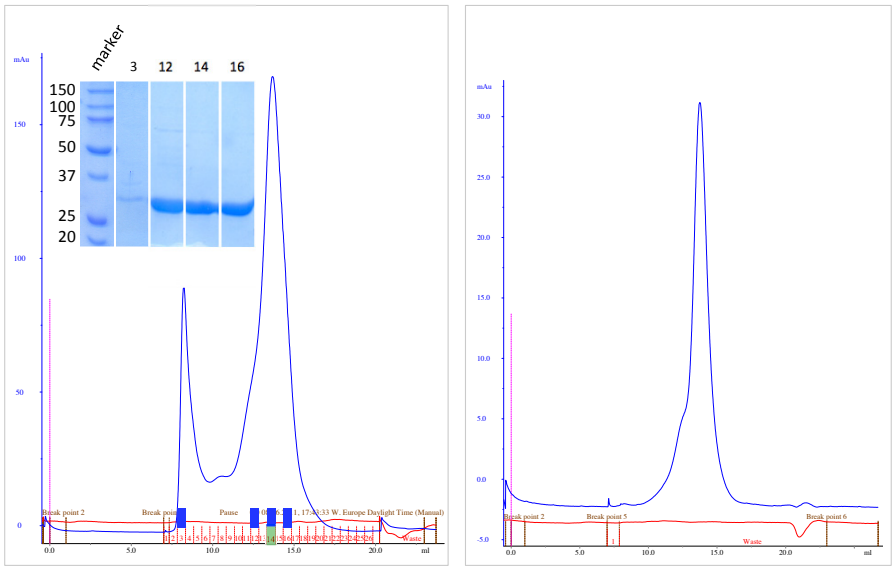

Figure 24 Size exclusion profile of ScaDMTΔ42.

(left) SEC profile of ScaDMTΔ42 purified in DM. Fractions 3, 12, 14 and 16 (blue bars) were loaded on a SDS-PAGE gel shown on the upper left. Molecular weights in kDa are indicated. Fraction 14 (green) was subjected to a second SEC three days after the initial purification. (right) SEC profile of the second size exclusion run. There is no void peak detectable. In the second chromatogram, the peak is more symmetric that in the first SEC profile.

ScaDMT1-Δ445 was the only C-terminally truncated construct tested for purification in DM. The protein was not stable during purification (Figure 25). The void peak obtained during SEC contains the target protein indicating the formation of high molecular aggregates.

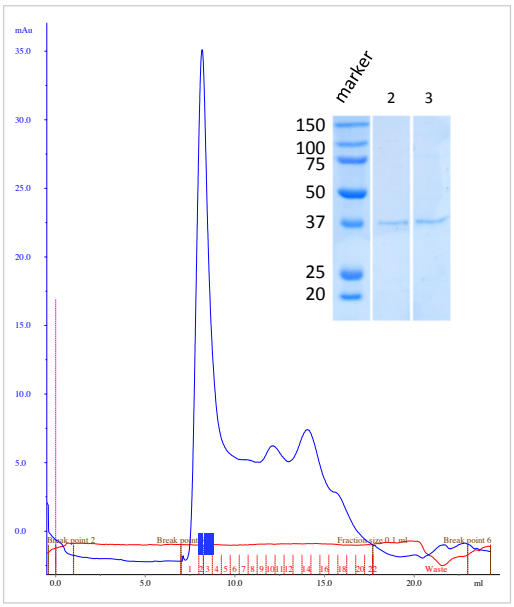

Figure 25 Size exclusion profile of ScaDMT1-Δ445.

ScaDMT1-Δ445 was purified in DM. Fractions 2 and 3 (blue bars) were loaded on a SDS-PAGE gel. Molecular weights are indicated in kDa.

The results from scale-up and purification demonstrate that constructs of ScaDMT that were shortened at the N terminus are stable and well behaved. This includes a construct where the first 41 amino acids were removed, which is proposed to lack part of the first transmembrane helix. In contrast C-terminal truncations had a strong effect on the stability of the protein. ScaDMT1-Δ445, the only construct that could be extracted in mild non-ionic detergents heavily aggregated during purification in DM.

2.3.4. Crystallization of ScaDMT Δ42-448

Due to their promising biochemical behavior, the protein constructs ScaDMTΔ28 and ScaDMTΔ42 were purified in DM, concentrated (5.0, 7.5 and 10 mg/ml) and used for broad crystallization screening. No crystals were obtained for ScaDMTΔ28 and crystals of ScaDMTΔ42 only grew in the same condition already identified for WT ScaDMT. For the truncated protein the crystals grew faster and were less fragile compared to WT (Figure 26 left). However, despite their larger size, the diffraction limit improved only slightly compared to full-length ScaDMT. The best crystal of the construct ScaDMTΔ42, hereafter referred to as ScaDMT^{tru}, was tested at the X06SA beamline of the SLS and diffracted to 5.7-6.0 Å resolution. An example diffraction pattern is depicted in Figure 26 on the right panel.

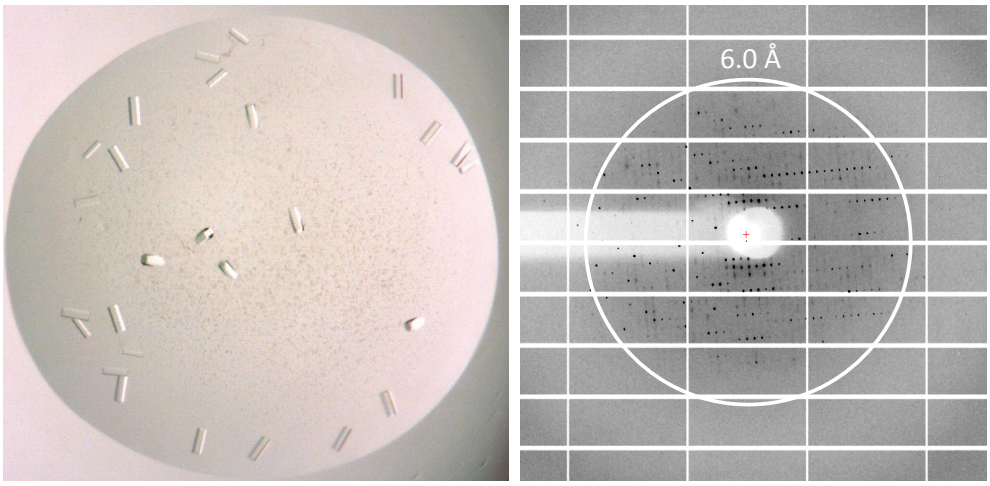

Figure 26 Crystals of ScaDMT Δ42-448.

(left) ScaDMTΔ42 was purified in the detergent DM and used for crystallization screening. Crystals appeared after 1 week of incubation at 4 °C. (right) Diffraction pattern of crystal frozen in liquid propane and exposed at the X06SA beamline of the SLS.

From the best crystal 137° of data were collected (at 1.0° increments, λ=1.0 Å) at the X06SA beamline of the SLS. The reflections were integrated and scaled with XDS (Kabsch, 1993). The crystals of the truncated protein are of the same space group as full-length ScaDMT: P321 (a=b=151.9 Å, c= 157.6 Å, α=β=90°, γ=120°). Judging from the data statistics (Table 5), the resolution of the dataset is limited to 5.7-6.0 Å, with an I/sigma of 1.97 in the highest resolution shell (6.02-5.68 Å). The data is complete to ~6.0 Å. Although in the highest resolution shell the R-factor is high, it is in an appropriate range for the complete data set ("total", 6%). Although there was a slight improvement in the maximal resolution compared to WT, the crystals of ScaDMT^{tru} did not diffract sufficiently well to embark on the next step for structure solution.

ehr520A_1, ScaDMTtru alone

SUBSET OF INTENSITY DATA WITH SIGNAL/NOISE >= -3.0 AS FUNCTION OF RESOLUTION

RESOLUTION LIMIT	NUMBER OF REFLECTIONS OBSERVED	UNIQUE	POSSIBLE	COMPLETENESS OF DATA	R-FACTOR observed	R-FACTOR COMPARED expected	I/SIGMA	R-meas	CC(1/2)
16.18	1671	298	322	92.5%	4.2%	3.9%	1666	40.15	4.6%	99.6*
11.77	3031	473	474	99.8%	4.3%	4.2%	3028	38.58	4.6%	99.9*
9.70	3756	594	596	99.7%	4.6%	4.4%	3756	33.76	5.0%	99.8*
8.44	4698	669	667	100.3%	5.5%	5.2%	4697	26.94	6.0%	99.9*
7.58	5670	764	766	99.7%	7.6%	8.2%	5670	17.37	8.2%	99.9*
6.93	6236	844	844	100.0%	14.1%	16.9%	6236	10.05	15.2%	99.8*
6.42	6754	905	905	100.0%	35.5%	45.5%	6754	5.18	38.2%	99.2*
6.02	7465	961	961	100.0%	79.1%	102.2%	7465	2.79	84.7%	96.5*
5.68	6985	966	1027	94.1%	106.1%	138.1%	6966	1.97	114.2%	94.8*
total	46266	6474	6562	98.7%	5.8%	6.0%	46238	15.34	6.3%	99.7*

Table 5 Statistics of the best data set of ScaDMT^{tru} after integration and scaling.
The number of reflections, the completeness of the data set, R-factor and I/σI are plotted for different resolution shells.

2.3.5. Summary

In an attempt to improve the diffraction propertied of ScaDMT crystals, I have investigated shorter versions of the protein. N-terminal truncations of residues, predicted to be disordered, in ScaDMT, have allowed me to identify constructs that were stable and well behaved in detergent solution. ScaDMTΔ42, a minimal construct that lacks 41 residues on the N terminus, could be purified and crystallized. Crystals of ScaDMTΔ42 were obtained from the same condition as the full-length protein. Although these crystals grew much faster compared to ScaDMT, they are of the same crystal form and their resolution could not be sufficiently improved for structure determination by this approach. The construct ScaDMTΔ42 is following referred to as ScaDMT^{tru}.

2.4. Nanobodies as crystallization chaperones

Crystallization chaperones are auxiliary proteins that can be used for the co-crystallization with the membrane protein of interest and that potentially improve the diffraction properties of crystals. They can either be covalently inserted into a loop of the target protein, as done in case of the human beta 2-adrenergic receptor where T4-lysozyme was fused to the receptor protein (Rosenbaum et al., 2007), or used as non-covalent binders recognizing a structured epitope of the target protein. The second strategy is more widely exploited with a variety of different protein scaffolds: Binding epitopes of antibodies are usually used as F_{ab} fragments or as scFv's (single chain variable fragments), variable domains fused into one single protein chain. Alternative scaffolds are designed ankyrin repeat proteins (darpins), fibronectin derived monobodies and camelid derived nanobodies (Koide, 2009; Lieberman et al., 2011; Tereshko et al., 2008).

Certain binding proteins such as darpins, monobodies and scFv's are usually selected from a naïve, synthetic library via ribosome-, phage- or yeast-surface display (Gera et al., 2013; Lipovsek and Plückthun, 2004; Winter et al., 1994). Antibodies and nanobodies in contrast are commonly generated by the immunization of animals (mice in the case of antibodies, and camelids in the case of nanobodies). This latter approach exploits the high variability of the animal immune system which contains around 10^{11} different binders (Janeway, 2001; Schroeder, 2006). Furthermore, upon repetitive stimulation, selected immunoglobulins undergo a process termed affinity maturation (Eisen and Siskind, 1964), which is used in nature to increase the potency of an antibody and which can be exploited for the generation of highly specific and affine binders against a target protein.

In 1993 it was discovered, that the camelid immune system contains, additionally to their conventional antibodies, special immuoglobulines that consist of heavy chains only (Hamers-Casterman et al., 1993). The binding domains of such V_{HH} antibodies, also called single-domain V_H antibody fragments or nanobodies, are usually less than 15 kDa in size and they have become popular tools for various biological and biochemical problems. In Figure 27 a schematic comparison of conventional antibodies and heavy chain-only antibodies is depicted. As representation of a conventional hetero-tetrameric antibody, an IgG (150 kDa), consisting of four protein chains connected to each other by disulfide bonds, is shown. For different biochemical purposes antibodies can be partially digested and F_{ab} fragments (~50 kDa) that do no longer contain the F_c part can be used

as monomeric binding proteins. In contrast to IgG antibodies, camelid heavy chain-only antibodies do not have light chains (~90 kDa). The parts, which recognize the epitope, are two V_H domains. ScFv's (~25 kDa) are engineered antibody fragments that contain two variable domains, one derived form the heavy chain and the other from the light chain of a conventional antibody. Both chains are tethered to each other via a flexible peptide linker. Each variable region of an antibody or antibody fragment, includes three complementarity determining regions (CDR), loops in the protein domain that are highly variable in their sequence and flexible, so they can be used to optimize the binding interactions.

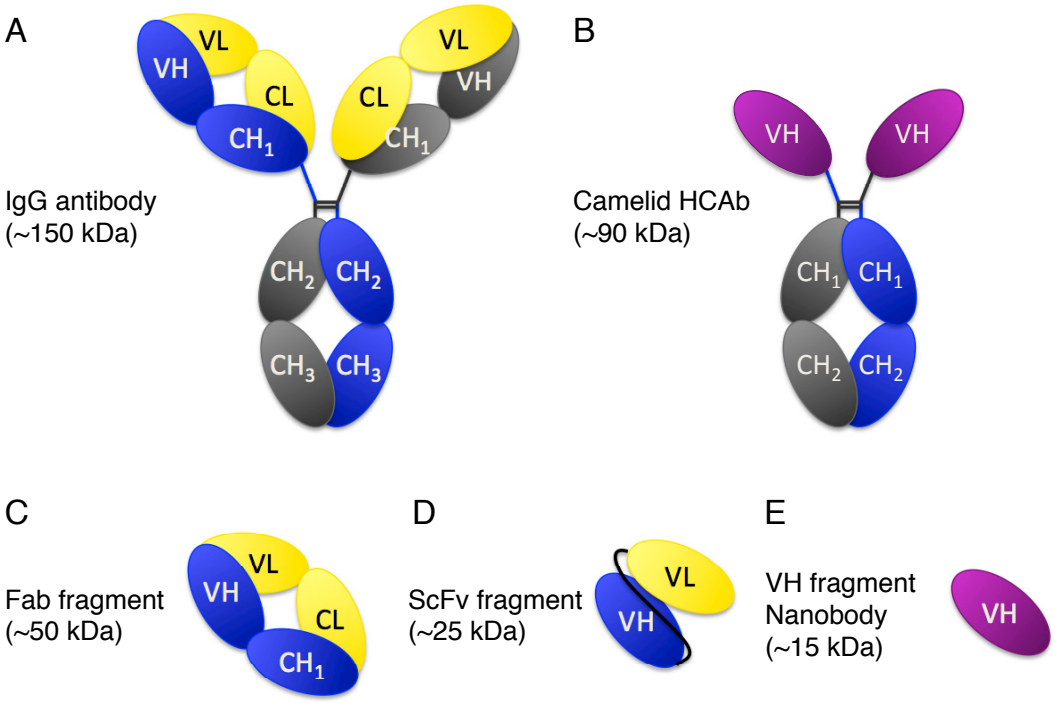

Figure 27 Schematic representation of different antibody types.

(A) A Conventional IgG antibody with its constant and variable parts is shown. (B) A camelid heavy chain antibody is comprised of a doublet of two constant and one variable heavy (VH) domain. (C) F_{ab} fragments can be generated by proteolytic digest of IgG antibodies. (D) ScFv's are fragments where two variable domains are connected via a flexible linker. (E) The V_H fragment, or nanobody, is the epitope binding entity of heavy-chain only antibodies that is used in various applications.

One of the proposed advantages of nanobodies is their unusually long CDR3 region, consisting of a typically 16-18 amino acid long variable loop, which is generally longer

than in conventional antibodies (in mouse antibodies this loop is ~9 amino acids, in human ~12 amino acids). This loop is ideally suited for the binding into cavities (De Genst et al., 2006; Saerens and Muyldermans, 2012). The use of nanobodies as crystallization chaperones has already been successfully applied for the structure determination of different membrane proteins (Löw et al., 2013; Pardon et al., 2014; Rasmussen et al., 2011).

2.4.1. Generation of ScaDMT specific nanobodies

The nanobodies used in this study were generated in collaboration with the lab of Prof. Jan Steyaert at the Free University of Brussels, Belgium that is specialized in the generation of highly specific nanobodies against different target proteins by the immunization of Llamas (*Lama glama*) and the subsequent selection of suitable binders by display techniques (Pardon et al., 2014).

To generate nanobodies recognizing structured epitopes of ScaDMT, Llamas were immunized with the protein on a weekly basis for six consecutive weeks. For this purpose ScaDMT was freshly purified each time shortly before the immunization and sent on ice to our colleagues in Brussels. After an incubation period, following the last injection of target protein, blood was taken to collect the B-lymphocytes for the subsequent amplification of nanobody-encoding mRNA. For that purposed the entire population of encoded antibodies and nanobodies was amplified by RT-PCR and the nanobody fraction was subsequently cloned into a phage-display library after separation by agarose-gel electrophoresis. As for each immunization several different targets were injected, the selection of binders by phage display was performed in the laboratory of Prof. Jan Steyaert to ensure the protection of intellectual property (Pardon et al., 2014). In case of ScaDMT, two rounds of phage display were performed with biotinylated versions of the target proteins ScaDMT and ScaDMT^{tru}. For expression, both constructs were cloned into an expression vector as fusion proteins with a C-terminal AVI-tag followed by a 3C protease site. The AVI-tagged proteins were purified in DM and subjected to SEC. The peak fractions were pooled and the biotinylation proceeded by incubating the protein with the biotin ligase BirA, the substrate biotin and cofactors such as ATP and magnesium. His-tagged BirA was removed by binding to Ni-NTA resin and the target proteins were subjected to a second SEC run to remove the remaining buffer components and to confirm the monodispersity of the protein (Figure 28).

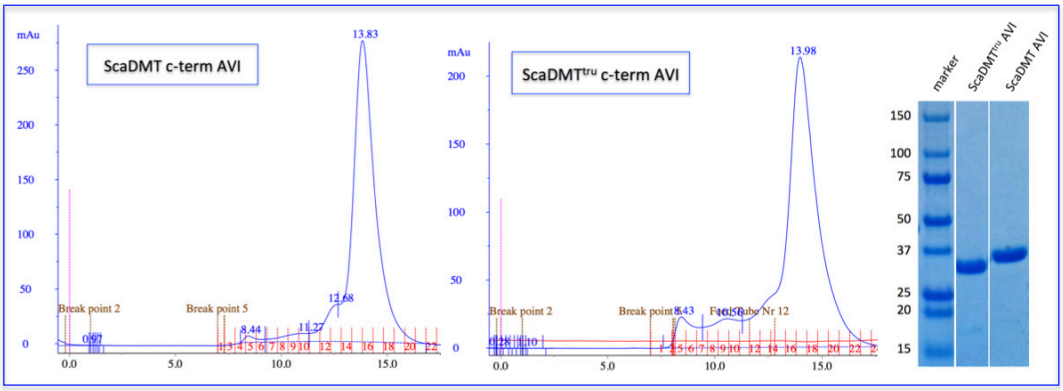

Figure 28 Size exclusion profile of avi-tagged and biotinylated ScaDMT and ScaDMT^{tru}. ScaDMT and ScaDMT^{tru} were expressed with an AVI-tag fused to their C-terminus. After biotinylation with BirA the proteins were subjected to a second SEC run. The chromatogram on the left hand side corresponds to the elution profile of ScaDMT, the chromatogram on the right to ScaDMT^{tru}. Both protein peaks were pooled and loaded on a SDS-PAGE gel. ScaDMT and ScaDMT^{tru} are both monodisperse and pure.

The biotinylated proteins were shipped on ice to our collaborators in Brussels where they performed phage-display and single-clone ELISA to detect the signal of individual nanobodies. 16 different nanobodies, binding either of the two constructs, were in that way identified in the lab of Jan Steyaert, from whom we obtained plasmids encoding the corresponding anti-ScaDMT nanobodies. Figure 29 displays a sequence comparison of the 16 different nanobody sequences aligned with ClustalW2 (Goujon et al., 2010; Larkin et al., 2007). The phylogenetic tree visualizes the three main clusters into which 13 of the nanobodies can be categorized. Three nanobodies (nb) are more distant to the other nanobody sequences but they can still be assigned to be closer related to one group. Nb08 is closest to group I, nb98 closest to group II and nb94 can be associated with group III. Based on the sequence alignment, the overall variability of the three CRD regions is evident. Group I nanobodies have the largest sequence differences in CDR1 and are rather uniform in CDR3, which fits the criteria suggested in Pardon et al., 2014 to define a nanobody family (>80% sequence identity in CDR3, identical length). In contrast to group I, group II and III nanobodies have differences in CDR3. On average the CDR3 of the 16 nanobodies is 15 amino acids long. Nanobodies nb94 (18 residues), nb98 (20 residues) and nb06 (21 residues) possess the longest CDR3 loops. The CDR3 of nb18 is with 7 residues comparably short.

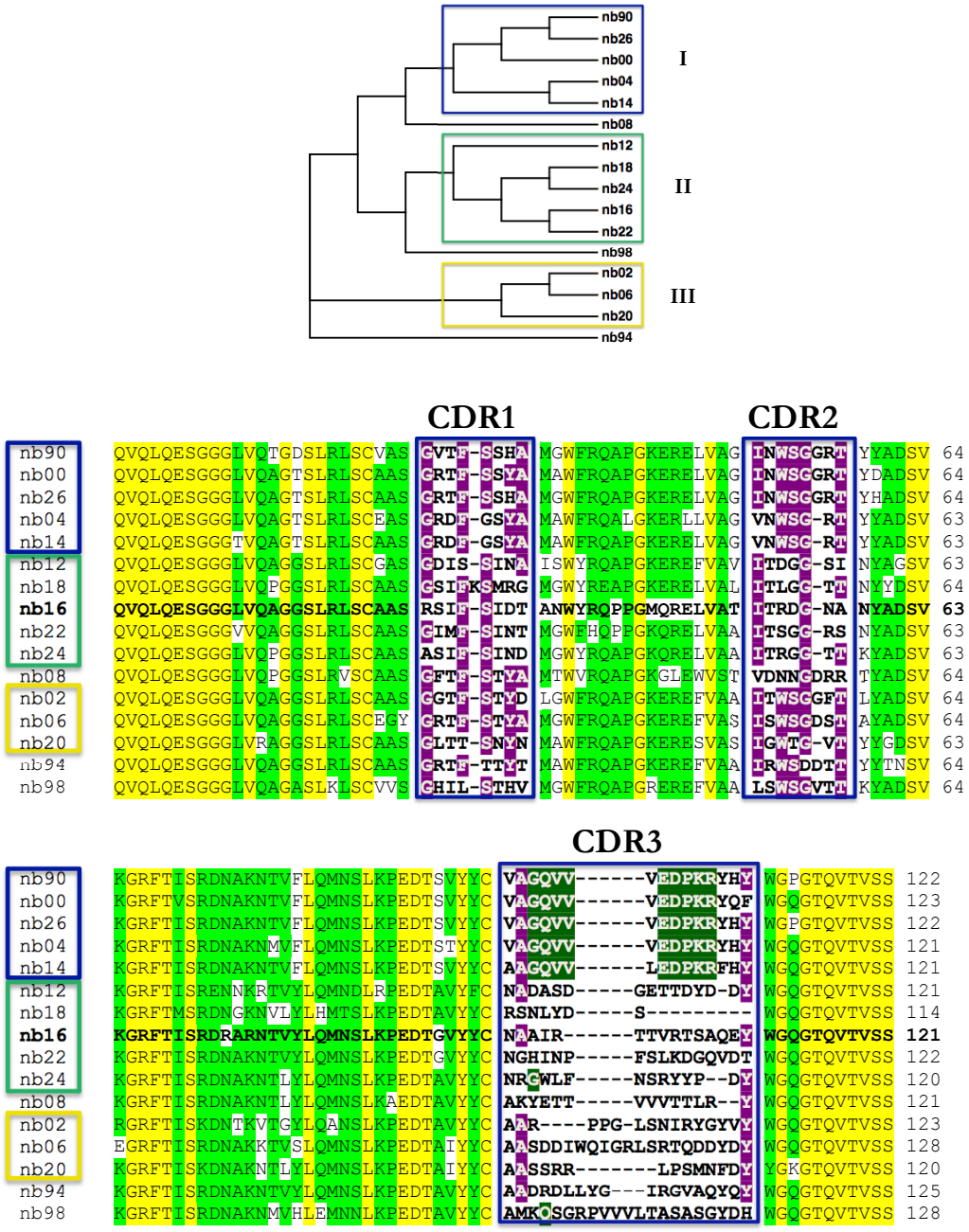

Figure 29 Sequence alignment and phylogenetic tree of the 16 selected nanobodies.

A phylogenetic tree of the 16 nanobodies selected against ScaDMT/ScaDMT^{tru} is shown on the top; a residue-by-residue comparison of the nanobodies is depicted at the bottom. The three groups that cluster together are highlighted by rectangles: Group I (blue), group II (green) and group III (yellow). Identical amino acids are marked in yellow, residues identical in most of the nanobody sequences are marked in green. CDR regions 1-3 are marked by a rectangles (blue) and labeled. Residues shared by more than half of the nanobodies are depicted in violet. Identical residues found in CDR3 within group I are highlighted in green.

2.4.2. Characterization of ScaDMT specific nanobodies

To investigate the suitability of the selected nanobodies for co-crystallization experiments they were characterized with respect to capability to form stable complexes with ScaDMT constructs, in conditions that are close to the ones used during crystallization. The complex was prepared by incubation of the membrane protein with 1.5 molar excess of the nanobody for 20 min at 4 °C. The stability of the complex was tested on SEC. Co-migration of both proteins was assayed either on an analytical SEC column on a HPLC system or with a preparative Superdex S200 column. In both cases the proteins were detected by their absorbance at 280 nm. In these experiments the peak containing ScaDMT shows a clear shift in the elution volume towards higher molecular weight when injected together with nanobody 04 (nb04) and nanobody 16 (nb16), which suggests that both protein form stable complexes that do not dissociate during SEC (Figure 30 right panel and SDS-PAGE analysis (data not shown)).

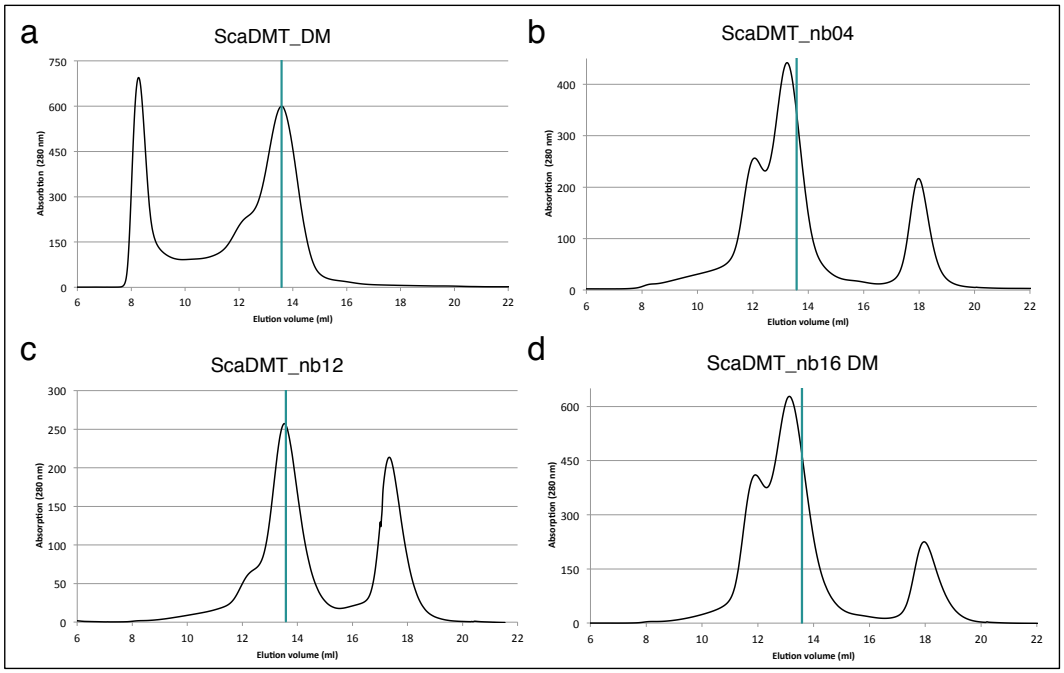

Figure 30 Size exclusion chromatography analysis of ScaDMT nanobody complexes.
Comparison of the elution volumes of ScaDMT and ScaDMT-nanobody complexes on a S200 column. (a) ScaDMT, purified in the detergent DM elutes at 13.6 ml. (b, d) Nb04 and nb16 bind to ScaDMT as indicated by the shift in elution volume. Interestingly both nanobodies appear to promote dimerization of the ScaDMT nanobody complex in solution. (c) Nanobody 12 does not bind to ScaDMT strong enough to co-migrate during the SEC run. The green line indicates the reference elution volume of ScaDMT alone.

In contrast no co-elution with ScaDMT was found for nanobody 12 (nb12) in SEC (Figure 30 lower left panel) and the corresponding SDS-PAGE analysis (data not shown), thus indicating that this nanobody did not form stable complexes with the membrane protein.

For analysis on HPLC, purified ScaDMT was used as reference for the un-complexed transporter and nb16 was used as reference for the nanobody. Two indicatures were used to judge whether a stable nanobody transporter complex was formed: A shift in the retention volume was observed due to the increased size of the complex. In addition the absorption of the complex was increased as all nanobodies selected against ScaDMT/ScaDMT^{tru} have a comparably high extinction coefficient (1.3-1.5), therefore the complex peak absorbs stronger at 280 nm compared to the transporter alone (Table 6).

		peak 1 min	mAU	peak 2 min	mAU	Shift of elution time (min)	Shift of Abs_{280} (mAU)	Complex formation
ScaDMT		22.370	40.0			n/a	n/a	n/a
	nb16			30.700	25	n/a	n/a	n/a
ScaDMT	nb00	22.355	40.2	30.580	46	0.015	0.2	no
ScaDMT	nb02	22.079	57.8	30.505	20	0.291	17.8	**yes**
ScaDMT	nb06	22.040	72.1	30.042	41	0.33	32.1	**yes**
ScaDMT	nb08	22.162	50.0	30.066	15	0.208	10.0	**yes**
ScaDMT	nb14	22.074	53.9	30.219	20	0.296	13.9	**yes**
ScaDMT	nb18	22.378	36.0	30.037	38	-0.008	-4.0	no
ScaDMT	nb20	22.299	42.0	30.900	16	0.071	2.0	no
ScaDMT	nb22	22.146	51.5	29.770	5	0.224	11.5	**yes**
ScaDMT	nb24	22.244	52.3	31.059	12	0.126	12.3	**yes**
ScaDMT	nb90	22.145	48.8	30.147	3	0.225	8.8	**yes**
ScaDMT	nb94	22.046	55.7	30.002	44	0.324	15.7	**yes**
ScaDMT	nb98	22.107	56.3	30.257	25	0.263	16.3	**yes**

		peak ml	Shift of elution volume (ml)	Complex formation
ScaDMT		13.58	n/a	n/a
ScaDMT	nb04	13.24	0.34	**yes**
ScaDMT	nb12	13.52	0.06	no
ScaDMT	nb16	13.13	0.45	**yes**
	nb26	not well expressed/ not stable		n/a

Table 6 HPLC analysis of nanobody ScaDMT complexes.

Nanobodies were injected together with ScaDMT onto an analytical size-exclusion column (PC3.2/300, GE Healthcare) connected to a HPLC system. The elution volume and the absorption maximum at 280 nm of potential complexes were compared to the ScaDMT elution profile. Peak 1 corresponds to ScaDMT or the ScaDMT-nb complex, peak 2 to the elution of the free nanobody. A shift towards shorter elution time and an increase of the absorption maximum of peak 1 indicates the co-migration of the nanobody with ScaDMT.

Both indicators were positive for nb00, nb06, nb08, nb14, nb22, nb24, nb90, nb94 and nb98, thus indicating that a stable complex is formed. In the case of nb02, nb18 and nb20 no significant shift in both the elution volume and the AU_{280} was detected and these nanobodies were thus considered as weak binders. Nb26 could not be investigated since the protein was not well behaved during expression and purification.

In summary, from the 16 different nanobodies selected against ScaDMT 11 nanobodies (69%) form a stable complex that co-migrates during size exclusion chromatography, 4 nanobodies (25%) that gave a signal on ELISA, which indicates binding, do not co-migrate on SEC, thus suggesting that the affinity of the complex is low. One nanobody (6%) was not well behaved and thus excluded from further analysis.

2.4.3. Co-crystallization of ScaDMT-nanobody complexes

Before they were used for co-crystallization, the expression of nanobodies had to be scaled-up. As the expression levels varied significantly in the originally used pMESy4 vector, the genes encoding for different nanobodies were sub-cloned into pBXNPHM3, an arabinose inducible expression vector. In this vector all nanobodies were expressed as fusion proteins containing a His_{10}-MBP-3C tag following the PelB signal sequence at their N terminus, which targets the protein to the periplasm that is required for the formation of disulfide bonds. The fusion to maltose binding protein (MBP) was found to increase the expression level of the nanobodies in *E. coli*. After incubation with 3C protease this tag only adds two additional amino acids (Glycine-Proline) from the cleavage site to the proteins N terminus. Large-scale expression was carried out either in shaker flasks or in fermenter cultures. After purification using IMAC and SEC, the nanobodies were concentrated and mixed with SEC purified and concentrated ScaDMT (nb in 1.5 times molar excess). After incubation on ice, the complex was subjected to SEC, which allowed the removal of free nanobody. Peak fractions of the ScaDMT-nb complex were concentrated (12 mg/ml) and used for crystallization screening (Figure 31).

A high affine, SEC positive binder is a preferred tool for co-crystallization but it cannot be excluded that a weak binder might also be suitable. The high protein concentrations present in a vapor diffusion experiment can in principle shift the equilibrium towards the nanobody-transporter complex even in cases where the nanobody would not bind strong enough to co-migrate on SEC. To rule out to miss a

weak binder that may still improve crystallization, nanobodies nb12, nb18 and nb00 were included in crystallization screening. In this case the purified nanobodies were mixed with ScaDMT in slight stoichiometric excess (i.e. 1.2:1) and used for crystallization experiments without SEC of the complex .

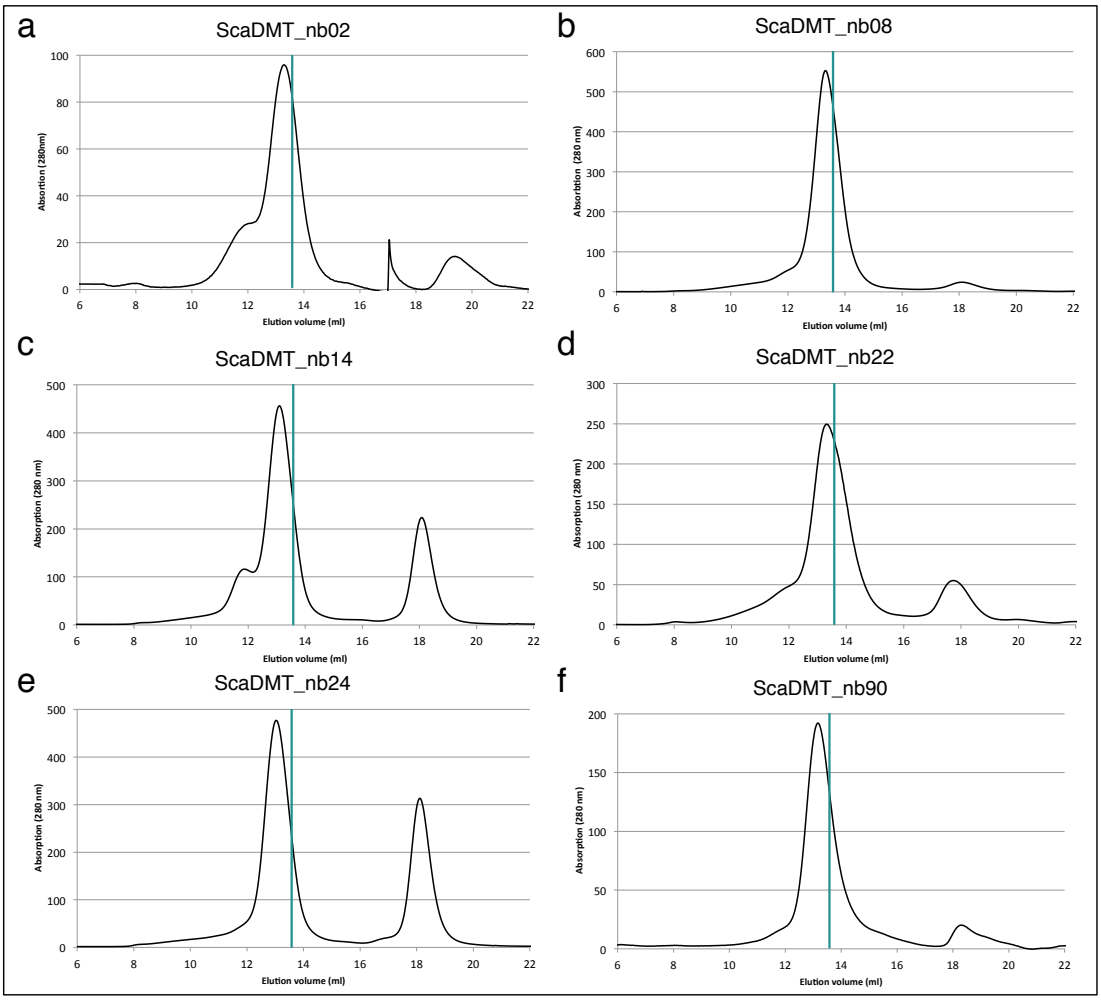

Figure 31 Size exclusion analysis of ScaDMT-nanobody complexes.

Purified ScaDMT was injected together with molar excess of the respective nanobody on a SEC column equilibrated in buffer containing DM. (a-f) SEC runs of samples used for crystallization screening. The green line marks the reference elution volume of ScaDMT alone.

All nanobody complexes were subjected to broad crystallization screening covering about 1000 different conditions (i.e. 10 screens in 96-well format). As the nanobodies influence the stability, solubility and crystal packing of the transporter the crystallization conditions were expected to change. Indeed crystals were observed in several new conditions for different nanobody complexes. Crystallization experiments with nb06 and nb08 yielded small crystals growing in the presence of alkaline earth metal ions.

ScaDMT-nb06 yielded needle-shaped crystals in a condition similar to the original high calcium chloride condition of WT (Figure 32 A). ScaDMT-nb08 crystallized in two conditions, one in the presence of calcium chloride and a second one in magnesium chloride (Figure 32 b, c). When tested at the X-06SA beamline at the SLS these crystals showed poor diffraction properties (Table 7). Nanobody 22 and nb24 crystallized each in one condition but crystals were fragile and their diffraction could thus not be investigated.

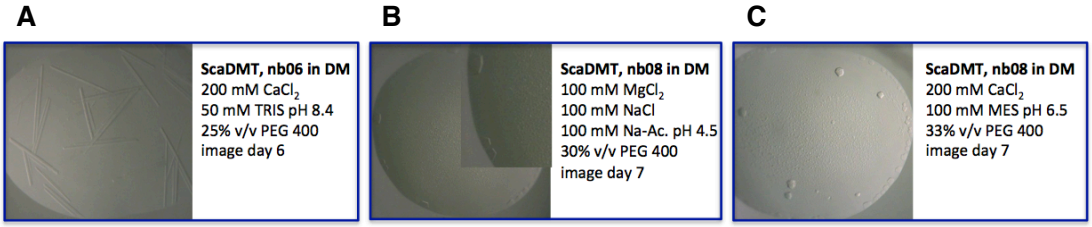

Figure 32 Crystallization conditions and images of selected ScaDMT nb complexes.
(A) ScaDMT-nb06 crystallized in a high calcium condition at pH 8.4. (B, C) ScaDMT-nb08 crystals were very fragile and soft. They grew either in high magnesium concentrations at pH 4.5 or in high calcium concentrations.

The complex of ScaDMT-nb16 crystallized in several different conditions in low and high molecular PEGs (PEG 400-8000). Several conditions contained calcium but there were also crystals growing in conditions containing either lithium sulfate, ammonium sulfate or zinc acetate as salt additive. Crystals grew in a broad pH range (pH 4.5- pH 9.4). Despite the large number of conditions, crystals of the complex did generally not diffract to higher resolution than crystals of ScaDMT alone (Table 7). Among the investigated crystals, a crystal form growing in an ammonium sulfate condition at pH 4.6 was identified that diffracted to 6 Å and which had an unusually long c-axis as manifested in the close spacing between adjacent reflections on a diffraction image (Figure 33).

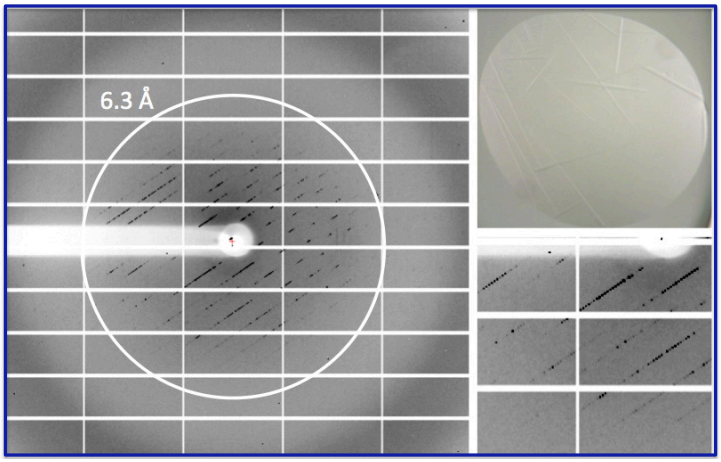

Figure 33 Diffraction image of ScaDMT-nb16 complex in a crystal form with a large unit cell dimension.

Crystals of ScaDMT-nb16 were grown in 200 mM ammonium sulfate, 100mM sodium acetate pH 4.6 and 12% w/v PEG 4000. Their diffraction was anisotropic and extended in the best direction to 6.3 Å resolution. The crystal has a very long c-axis, as already visible from the diffraction pattern.

Interestingly, nb16 was found to stabilize ScaDMT, which allowed the exchange from DM to the shorter detergent NM in the last purification step (Figure 34). A pronounced double peak, with the first peak corresponding to a dimer of the ScaDMT-nb16 complex was observed in gel filtration. The molecular weight of these peaks as monomers and dimers was verified by MALS experiments (Figure 35).

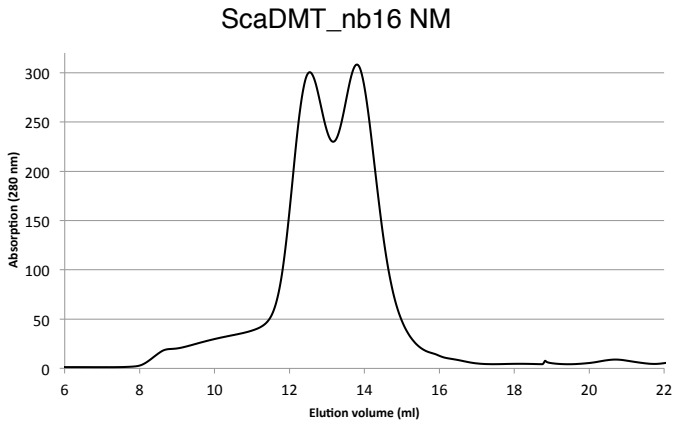

Figure 34 Size exclusion profile of ScaDMT in complex with nb16 in the detergent NM.

The nanobody-ScaDMT complex elutes as a double peak corresponding to a monomeric and dimeric form of the complex.

ScaDMT elutes with an apparent molecular weight of ~122 kDa of which more than 56% are contributed form the detergent DM surrounding the protein. The ScaDMT–nb complex elutes in two peaks: The monomer-complex elutes with an apparent molecular weight of ~133 kDa of which >52% of the weight is contributed by the detergent DM. The dimer-complex elutes at ~271 kDa with a remarkably reduced weight contribution from the detergent of ~37%. This can be explained by the protein-protein interaction, excluding detergent molecules from the area of the dimer-interface.

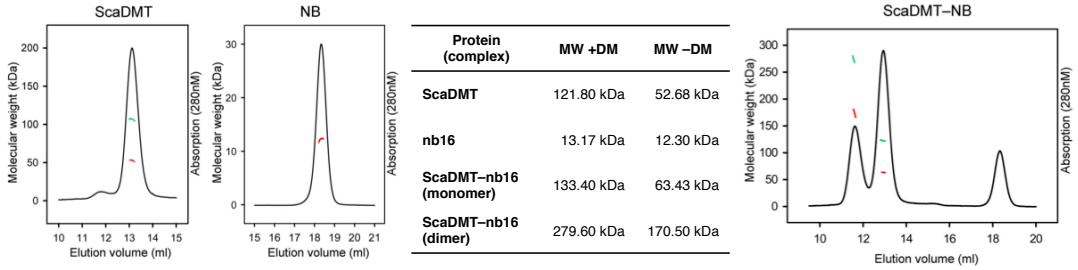

Protein (complex)	MW +DM	MW –DM
ScaDMT	121.80 kDa	52.68 kDa
nb16	13.17 kDa	12.30 kDa
ScaDMT–nb16 (monomer)	133.40 kDa	63.43 kDa
ScaDMT–nb16 (dimer)	279.60 kDa	170.50 kDa

Figure 35 Multi angle light scattering.

Gel filtration and light scattering results of ScaDMT, nb16 and the ScaDMT–nb16 complex in the detergent DM. The respective molecular weight of the protein-detergent complex obtained from light scattering is shown in the chromatogram in green, the molecular weight of the protein complex alone in red. The corresponding values with and without the detergent component are depicted in the table.

Crystals of the complex grown in NM showed anisotropic diffraction up to 4.5 Å in the best direction (Table 7). Crystals grew also after exchanging into the shorter chain detergent octyl-maltoside (OM), but in this case fewer crystals and more precipitate indicated that the protein might be less stable in OM. In this case also the diffraction properties were deteriorated with crystals showing anisotropic diffraction up to 6.5 Å (Table 7).

In summary, four nanobody complexes of ScaDMT (nb04, nb06, nb08 and nb16) were successfully crystallized. In four cases no co-migration on SEC was observed (i.e for nb00, nb12, nb18 and nb20) thus indicating weak affinity. No apparent correlation between sequence-based group assignment of nanobodies (I, II or III) and their biochemical behavior was observed (Figure 36). Nanobody 16 had the most drastic impact on the crystallization behavior of ScaDMT. In this case highly anisotropic diffraction up to a maximum resolution of 4.5 Å was observed.

Construct	nb	Detergent	Crystallization condition			Diffraction properties
ScaDMT	nb04	DM	200 mM Potassium phosphate	10 % PEG 4000	50 mM Sodium Cacodylate pH 5.5	Max to 9 Å
		DM	100 mM NaCl	18 % PEG 400	100 mM Sodium citrate pH 5.6	anisotropic diffraction 7.5 Å good direction 10 Å bad direction
	nb06	DM	200 mM $CaCl_2$	25 % PEG 400	50 mM Tris pH 8.4	Max to 9 Å
		DM	100 mM Potassium Sodium tartrate	25 % PEG 400	50 mM ADA pH 6.5	Max to 8 Å
	nb16	DM	100 mM Li_2SO_4, 100 mM Na_2SO_4	10 % PEG 4000	50 mM ADA pH 6.5	Max to 9 Å
		DM	200 mM $CaCl_2$	25 % PEG 400	100 mM MES pH 6.4	Max to 7 Å
		NM	200 mM $CaCl_2$	10 % PEG 4000	50 mM Glycine pH 9.4	Max to 9 Å
		NM	100 mM NaCl	18 % PEG 400	100 mM Sodium citrate pH 5.6	Max to 7.5 Å
		NM	200 mM Ammonium sulfate	12 % PEG 4000	100 mM Sodium citrate pH 4.6	Max to 6.3 Å long unit cell axis
		NM	200 mM Zinc Acetate	10 % PEG 8000	100 mM Imidazol pH 6.5	Max to 7 Å long unit cell axis
		NM	200 mM Zinc Acetate	10 % PEG 3000	100 mM Sodium acetate pH 4.5	Max to 9 Å
		NM	200 mM $CaCl_2$, 0.11 % w/v Maleic acid	25 % PEG 400	50 mM HEPES pH 7.4	Max to 7.5 Å
		NM	200 mM $CaCl_2$, 100 mM Glycine	25 % PEG 400	50 mM HEPES pH 7.4	anisotropic diffraction 4.5 Å good direction 7 Å bad direction
		NM	200 mM $CaCl_2$, 20 mM Taurine	25 % PEG 400	50 mM HEPES pH 7.4	anisotropic diffraction 4.8 Å good direction 7.5 Å bad direction
		NM	200 mM $CaCl_2$, 200 mM RbCl	25 % PEG 400	50 mM HEPES pH 7.4	anisotropic diffraction 5 Å good direction 7 Å bad direction
		NM	200 mM $CaCl_2$, 400 mM Dimetylformamide	25 % PEG 400	50 mM HEPES pH 7.4	Max to 6.5 Å
		NM	200 mM $CaCl_2$, 200 mM Ammonium nitrate	25 % PEG 400	50 mM HEPES pH 7.4	anisotropic diffraction 4.5 Å good direction 7 Å bad direction
		OM	100 mM Li_2SO_4, 100 mM Na_2SO_4	10 % PEG 4000	50 mM Sodium Acetate pH 4.5	anisotropic diffraction 6.5 Å good direction 8 Å bad direction
		OM	200 mM Potassium phosphate	10 % PEG 4000	50 mM ADA pH 6.5	Max to 8 Å
		OM	-	5 % PEG 4000	50 mM Glycine pH 9.4	Max to 7 Å

Table 7 Summary of ScaDMT-nanobody complex crystals.

ScaDMT was co-crystallized with different nanobodies in vapor-diffusion experiments. In all experiments ScaDMT was initially purified in the detergent DM and mixed with purified nanobody. The complex was subsequently subjected to another SEC chromatography. In specified cases the detergent was changed to NM or OM during that step. The crystallization conditions and the diffraction properties are specified for each crystal form.

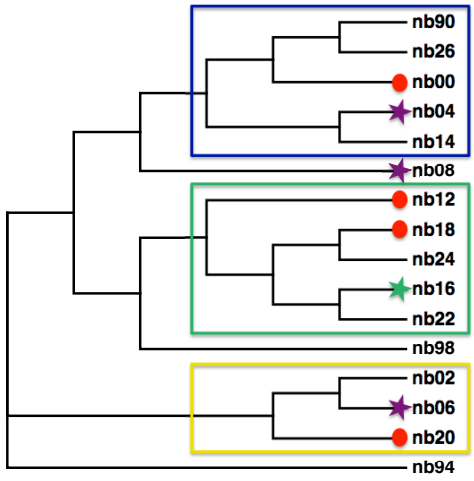

Figure 36 Phylogenetic tree of the nanobodies selected against ScaDMT/ScaDMT^{tru}.

The three families classified by sequence analysis are marked in rectangles (group I in blue, group II in green and group III in yellow). Nanobodies marked with a red dot did not co-migrate with ScaDMT on SEC. Nanobodies marked with a violet star did co-crystallize. Nb16, which was successfully used for structure determination, is highlighted by a green star.

2.4.4. Crystallization of the ScaDMT^{tru}-nb16 complex

Besides the full-length protein, nb16 was also found to bind to the truncated version ScaDMT^{tru} as confirmed by SEC (Figure 37). Crystals of the ScaDMT^{tru}-nb16 complex grew in similar conditions as the WT ScaDMT-nb16 complex but also after replacing calcium by potassium or magnesium ions. The condition in high potassium chloride was the first crystal that was found to diffract close to 4 Å (Table 8). Crystals growing in magnesium chloride showed anisotropic diffraction to 4.5-5.5 Å. Crystals growing in high calcium with PEG 4000 as precipitant diffracted anisotropically to 4.5-7.5 Å as well. The replacement of PEG 4000 by PEG 400 improved the diffraction significantly and isotropic data to 4 Å could be collected.

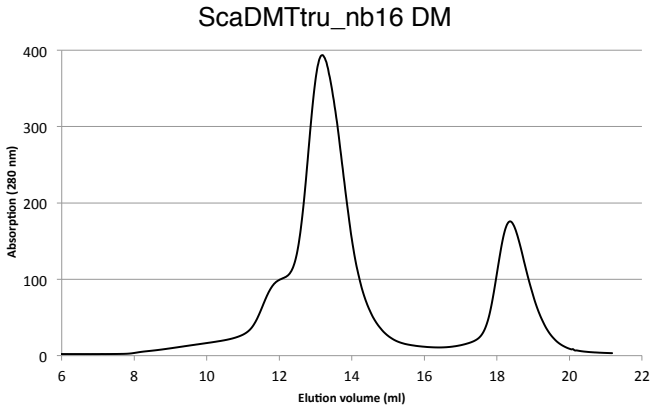

Figure 37 Size exclusion profile of ScaDMT^{tru} in complex with nb16.
ScaDMT^{tru} purified in DM was incubated with nb16 and loaded onto a S200 column. The complex elutes at 13.2 ml as one major peak with a small shoulder towards higher molecular weight.

As for ScaDMT also the ScaDMT^{tru} -nb16 complex showed increased stability in shorter chain detergents and therefore tolerated detergent exchange into NM on SEC (Figure 38). In NM, ScaDMT^{tru}-nb16 crystals grew at high calcium concentrations in PEG 400 in a broad pH range. They were of hexagonal shape and grew in drops of 150 nl volume, after equilibration to a maximal size of 250-300 µm. These crystals diffracted reproducibly beyond 4 Å, a striking improvement reached by the use of a shorter chain detergent.

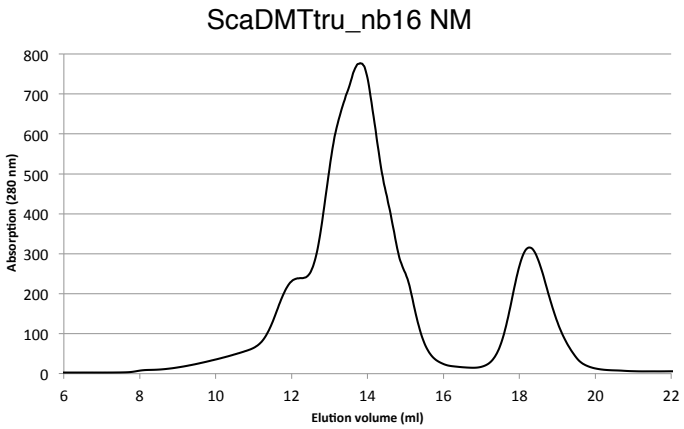

Figure 38 Size exclusion profile of ScaDMT^{tru} in complex with nb16 in NM.

ScaDMT^{tru} was purified in DM, incubated with nb16 and loaded onto a S200 column equilibrated in buffer containing NM. The main peak elutes at 13.8 ml. The asymmetry of the peak was frequently observed when loading large amounts of protein, which may exceed the capacity of the column.

Construct	nb	Detergent	Crystallization condition			Diffraction properties
ScaDMT^{tru}	nb16	DM	500 mM KCl	15 % PEG 400	50 mM HEPES pH 7.4	Max to 4.2 Å
		DM	500 mM KCl	25 % PEG 400	50 mM Glycine pH 9.4	Max to 7.5 Å
		NM	100 mM NaCl	12 % PEG 4000	100 mM Sodium citrate pH 5.6	Max to 7 Å
		DM	50 mM NaCl, 20 mM $MgCl_2$	22 % PEG 400	100 mM Sodium citrate pH 6.0	anisotropic diffraction 4.5 Å good direction 7.2 Å bad direction
		DM	100 mM $MgCl_2$	12 % PEG 6000	100 mM Sodium acetate pH 4.6	anisotropic diffraction 5 Å good direction 7 Å bad direction
		DM	100 mM $MgCl_2$	12 % PEG 6000	100 mM Sodium acetate pH 4.6	anisotropic diffraction 4.5 Å good direction 5.5 Å bad direction
		NM	1 M Ammonium Formate	10 % PEG 4000	50 mM Sodium Cacodylate pH 5.5	Max to 7 Å long unit cell axis
		DM	100 mM Li_2SO_4, 100 mM Na_2SO_4	25 % PEG 400	50 mM Sodium Acetate pH 4.5	Max to 8 Å
		NM	100 mM Li_2SO_4, 100 mM Na_2SO_4	10 % PEG 4000	50 mM Sodium Cacodylate pH 5.5	anisotropic diffraction 4.1 Å good direction 5.5 Å bad direction
		NM	100 mM Li_2SO_4, 100 mM Na_2SO_4	10 % PEG 4000	50 mM Sodium Cacodylate pH 5.5	anisotropic diffraction 4.5 Å good direction 7.5 Å bad direction
		DM	200 mM $CaCl_2$	10 % PEG 4000	50 mM Sodium Cacodylate pH 5.5	anisotropic diffraction 5 Å good direction 7.5 Å bad direction
		DM	200 mM $CaCl_2$	25 % PEG 400	50 mM HEPES pH 7.4	Max to 4 Å
		NM	200 mM $CaCl_2$	25 % PEG 400	50 mM Sodium Cacodylate pH 5.5	Max to 4 Å
		NM	200 mM $CaCl_2$	25 % PEG 400	100 mM MES pH 6.4	Max to 3.8 Å
		NM	200 mM $CaCl_2$	25 % PEG 400	50 mM Glycine pH 9.4	Max to 3.4 Å
		NM	200 mM $CaCl_2$	25 % PEG 400	50 mM HEPES pH 7.4	Data set to 3.1 Å

Table 8 Summary of crystallized ScaDMT^{tru}-nanobody complexes

ScaDMT^{tru}–nb16 complex crystallized by vapor diffusion in sitting drops. ScaDMT^{tru} was purified in the detergent DM incubated with purified nanobody and purified on SEC. Detergent was exchanged into NM on SEC if indicated. Crystallization conditions and the diffraction properties are specified.

As scale-up of the crystallization experiments to 250 nl in 96-well plates and 1 µl in 24-well plates yielded crystals of decreased size and quality, all further crystallization experiments were carried out at 150 nl. A second crystal form appearing in the same condition of large volume crystallization setups grew in clusters of small needles that were not suitable for data collection. The increase in the crystallization volume thus favored growth of an unsuitable crystal form and was thus no pursued.

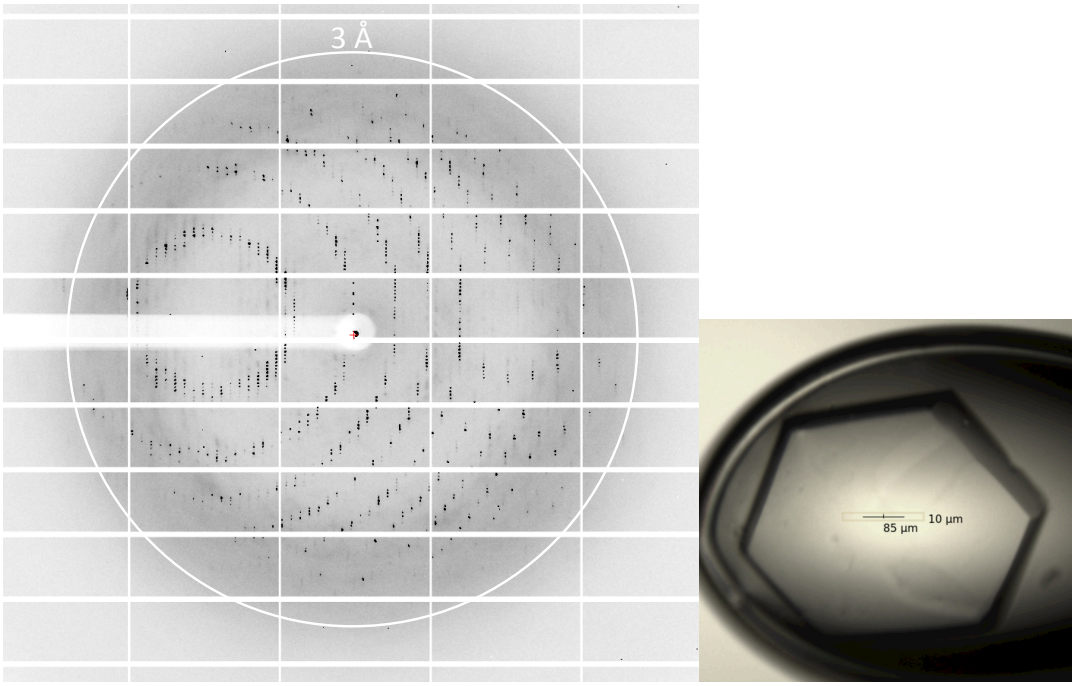

Figure 39 Diffraction of ScaDM^{tru}-nb16.

(left) Diffraction image of a ScaDMT^{tru}-nb16 crystal, which diffracted X-rays to 3.1 Å. (right) Image of the crystal used for the diffraction experiment, which was grown in 200 mM $CaCl_2$, 50 mM Hepes pH 7.4, 25% PEG400, cryo-protected and flash frozen in liquid propane.

The best crystal observed after an extensive screen, allowed data collection to 3.1 Å (Figure 39). The protein crystallized in the space group $P3_121$ with unit cell parameters of a=b=114.4 Å, c= 257.9 Å, $\alpha = \beta = 90°$, $\gamma = 120°$ (Table 9). The number of molecules per asymmetric unit was estimated by calculation of the Matthews coefficient and the corresponding solvent content (Kantardjieff and Rupp, 2003; Matthews, 1968). With two ScaDMT^{tru}-nb16 complexes per asymmetric unit the solvent content would be 69 %, which is in the expected range for a membrane protein.

ScaDMT^{tru}–nb16	Data collection
Wavelength (Å)	1.0
Space group	$P3_121$
Cell dimensions	
a, *b*, *c* (Å)	114.4, 114.4, 257.9
α, β, γ (°)	90.0, 90.0, 120.0
Resolution (Å)	50–3.1 (3.3–3.1)
R_{merge}	6.0 (120.)
$I / \sigma I$	21.0 (2.1)
Completeness (%)	99.6 (98.2)
Redundancy	9.5 (15.2)

Table 9 Data collection statistics for ScaDMT^{tru}–nb16

Statistics for the best native dataset collected from a ScaDMT^{tru}–nb16 crystal grown in NM.

2.4.5. Summary

Crystallization chaperones have been successfully used to improve the crystallization properties of difficult targets, such as membrane proteins. They stabilize the protein in a specific conformation, reduce the flexibility of loop regions, and in the case of membrane proteins increase the hydrophilic surface available for crystal contacts. In collaboration with the group of Prof. Jan Steyaert, nanobodies targeting ScaDMT, were raised in Llamas by immunization of the animal with purified, detergent solubilized protein. For selection purposes, the entire repertoire of nanobodies was cloned into a phage-display library, which was subsequently used to enrich ScaDMT specific binders via phage display technology. In that way, 16 different nanobodies that recognize ScaDMT in ELISA assays were obtained. Complex formation of identified binders with ScaDMT was subsequently analyzed by SEC. Eleven out of 16 nanobodies were found to form tight complexes and were thus used for co-crystallization experiments with the transport protein. For four complexes crystals were obtained, although most of these crystal forms diffracted to low resolution. One nanobody, nb16, has stabilized the membrane protein in detergent solution. The complex with ScaDMT crystallized in several different conditions, but the diffraction was usually anisotropic and limited to 4.5 Å in the best direction. The exchange of the complex into the shorter chain maltoside detergents NM or OM did not improve the diffraction properties. In contrast, crystals grown from nb16 in complex with, ScaDMT^{tru}, a truncated version of the transporter, diffracted up to 4 Å in the detergent DM. By exchanging the detergent to NM, the

diffraction was successfully improved to 3.1 Å, which is of suitable resolution for structure determination in case phases can be obtained.

2.5. Seleno-methionine derivatization of ScaDMT^{tru} and structure-determination of the ScaDMT^{tru}-nb16 complex by SAD phasing

An electron density map is calculated by the fourier transformation of the structure factors, which contain for each reflection amplitude and a phase angle. The diffraction data collected from a crystal reveals the amplitude of each reflection whereas the phase information is lost. In order to retrieve the phase information, different methods are available: In Molecular Replacement the structure of a closely related protein, can be used as a search model, which is then positioned in the crystal structure to reconstruct the packing in the crystal form who's structure needs to be determined. This reconstructed crystal structure can be used to calculate a set of initial phases that are combined with the measured structure factor amplitudes to calculate an electron density map. However, in cases where no similar structure is available, phases need to be determined experimentally either by isomorphous replacement or anomalous diffraction techniques. Direct methods (ab initio) are successfully applied in small-molecule crystallography but are usually not feasible for macromolecular crystallography.

Experimental phasing methods rely on the presence of a small subset of heavy atoms that have recognizable features in the diffraction pattern. In both cases the substructure of the heavy atom components is determined first. Isomorphous replacement methods require the preparation of a heavy atom derivative that is usually prepared by soaking of native crystals and collection of a heavy atom derivative data set. The difference in the diffraction due to bound heavy atoms can then be calculated by subtracting the amplitudes of the heavy atom derivative data set from the native data set, and by determination of the substructure with Patterson methods. This method relies on the assumption that the heavy atom and the native data sets are isomorphous, which means that the protein components in both, the native and the heavy atom derivative data set needs to be the same. In membrane protein crystals, heavy-atom binding frequently decreases the resolution and changes the crystal packing, resulting in non-isomorphism, which prevents structure determination by isomorphous replacement. Furthermore it can be difficult to identify a suitable heavy atom derivative that incorporates a sufficient number of heavy atoms within the asymmetric unit, to obtain phases with low error.

Single anomalous diffraction experiments do not rely on isomorphism between different crystals, since all data used for phase calculation, are collected from the same crystal. Data is collected close to the absorption edge of certain elements, at which the absorption of a small fraction of the incident beam is maximized and photons are re-emitted with a phase shift (of 90°). This effect is generally stronger for heavier atoms, e.g. the anomalous scattering of selenium is stronger than of sulfur. Anomalous scattering causes a breakdown of Friedel's law, which describes the symmetry in the structure factor amplitudes between reflections with indices hkl and –h-k-l. In case of anomalous scattering the differences in the intensity between the Friedel pairs can be quantified. As these differences are generally small, a high redundancy of the data is essential whereas radiation damage due to overexposure of the crystals should be avoided. This can be accomplished by a reduction of the beam intensity to minimize radiation damage and the collection of several complete datasets of one crystal. As most commonly used method to introduce anomalous scatterers into the crystal, the heavy atom selenium is incorporated into the protein during expression, by replacing the amino-acid methionine with Se-methionine.

In 1990 the first time Se-methionine (Se-Met) labeled protein was used for phasing by Hendrickson, Horton and LeMaster (Hendrickson et al., 1990). Since then several modified versions of the protocol to generate Se-Met derivatives have been applied (Doublié, 2007). An important concept of this strategy is that prokaryotic and eukaryotic cells can incorporate seleno-methionine instead of the naturally occurring methionine during protein synthesis. Two main approaches have been used to increase the incorporation efficiency of seleno-methionine. BL21(DE3) derived methionine auxotroph *E. coli* strains have been used successfully for the T7/ IPTG based expression system (Doherty et al., 1995). These strains can metabolize arabinose and are therefore not suitable for arabinose-inducible expression systems. In an alternative approach compatible with expression controlled by the arabinose promoter the methionine synthesis can be inhibited by the addition of L-Lysine, L-Threonine, L-Phenylalanine, L-Leucine, L-Isoleucine and L-Valine to the medium. These amino acids are known to inhibit the enzyme aspartokinase, which is necessary for methionine synthesis, in a synergistic way (Truffa-Bachi and Cohen, 1968). In both cases either minimal medium or a medium with a defined amino acid composition is used and sufficient amounts of Se-Met have to be added to the medium. For MC1061, the *E. coli* strain used in this study, the medium has also to be supplemented with Thiamine (Vitamin B1). The protein yield

is generally lower for expression cultures growing in seleno-methionine containing medium and it can depend on the media composition. Therefore it is generally advisable to test different media suitable for seleno-methionine incorporation for their effect on the target protein expression.

2.5.1. Expression screening of seleno-methionine labeled ScaDMT^{tru}

ScaDMT^{tru} contains 9 endogenous methionines (i.e. 1 methionine per 50 amino acids), which is sufficient for Se-Met SAD (single anomalous dispersion) phasing (18 methionine per asymmetric unit). In order to produce sufficient amounts of the labeled transporter, expression tests were performed in *E. coli* MC1061 cells. Three media containing all amino acids (with Se-Met replacing Met, MMAA) were compared with three minimal media (MM) containing, except Se-Met, only the amino acids needed to inhibit the methionine biosynthesis of the host strain (Table 10). Two different approaches were tested for each of the media conditions. In all cases the cultures were directly inoculated 1/100 from an o/n culture grown in Terrific Broth (without washing the cells).

Strategy "Methionine first": Methionine was available during initial growth by either the addition of methionine in the case of MMAA medium or by not repressing the methionine biosynthesis if MM was used. Prior to induction cells were harvested under sterile conditions and resuspended in the corresponding medium not containing methionine. The amino acid cocktail, which inhibits the methionine biosynthesis, was added to the cultures in MM. After a growth period to deplete cells from free methionine Seleno-methionine was added. Before expression was induced by the addition of arabinose, cells were allowed to adapt to Seleno-methionine for one hour.

Strategy "Se-methionine": All cultures were inoculated in the respective medium with Seleno-methionine added from the beginning. The media also included the Methionine biosynthesis inhibition cocktail for MM cultures. Prior to induction a second aliquot of the Met-inhibition cocktail was added to these cultures. Induction and o/n expression were carried out corresponding to the standard expression protocol.

	Nitrogen source/ buffer	Amino acids and nucleotides	Vitamins, Trace elements
MMAA 1	M63 medium $(NH_4)_2SO_4$, KP_i	0.2 g/l Cys, His; 0.3 g/l Ala, Arg, Asp, Asn, Gln, Glu, Gly, Ile, Leu, Lys, Pro, Ser, Trp, Tyr, Thr, Phe, Val; 0.5 g/l Adenine, Cytidine, Guanine, Thymine, Uracil	$MgSO_4$, $CaCl_2$, $ZnSO_4$, $MnCl_2$, $(NH_4)_6Mo_7O_{24}$, $CuSO_4$, $FeSO_4$, $CoCl_2$, H_3BO_4, Kao-Michayluk Vitamin solution and additionally Biotin and Thiamine
MMAA 2	M63 medium $(NH_4)_2SO_4$, KP_i	2 mg/l Ala, Arg, Asn, Asp, Cys, Gln, Glu, Gly, His, Ile, Leu, Lys, Phe, Pro, Ser, Thr, Tyr, Val, 1mg/L Trp; 2mg/l uracil	$MgSO_4$, $CaCl_2$, $FeSO_4$, Biotin, Nicotinamide, Riboflavin, Thiamine
MMAA 3	M63 medium $(NH_4)_2SO_4$, KP_i	20 mg /l Ala, Arg, Asn, Asp, Cys, Gln, Glu, Gly, His, Ile, Leu, Lys, Phe, Pro, Ser, Thr, Tyr, Val, 1mg/L Trp	$MgSO_4$, $CaCl_2$, $FeSO_4$, Thiamine
MM 1	M63 medium $(NH_4)_2SO_4$, KP_i	-	$MgSO_4$, $CaCl_2$, $FeSO_4$, Thiamine
MM 2	M9 medium NH_4Cl Na/KP_i	-	$MgSO_4$, $CaCl_2$, $FeSO_4$, Thiamine
MM 3	M9 medium NH_4Cl Na/KP_i		$MgSO_4$, $CaCl_2$, $ZnSO_4$, $MnCl_2$, $CuSO_4$, $FeSO_4$, $CoCl_2$, H_3BO_4, Kao-Michayluk Vitamin solution

Table 10 Overview of the different growth media used for the small-scale expression test. Medium MMAA 1 is based on a protocol by A. Evdokimov which is itself a modification of the original protocol published by S. Doublié (Doublié, 2007; Evdokimov). The carbon source was in all cases 0.75% glycerol.

Cells were lysed by bead-beating and membrane proteins were extracted by addition of DM. After removal of aggregates by ultra centrifugation the supernatant was used for western blot analysis. ScaDMT^{tru} was detected with an anti-His HRP conjugated antibody (Figure 40). The difference between the MMAA and MM strategy with respect to ScaDMT^{tru} expression was striking. Independent of the time point for the addition of Seleno-methionine all three MM cultures expressed significantly more protein than the MMAA cultures. As shown in Figure 40, only for one MMAA culture a protein band at the right molecular weight was detectable when seleno-methionine was added one hour before induction.

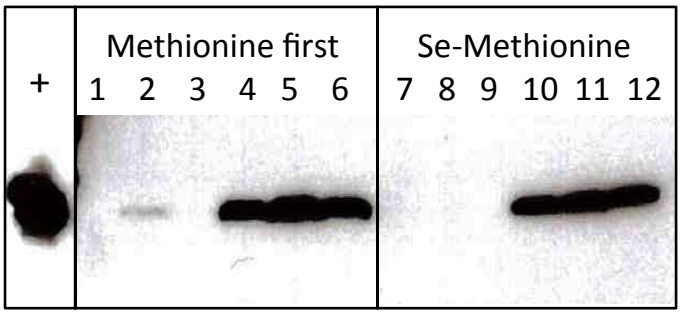

Figure 40 ScaDMT expression analysis for seleno-methionine labelled protein.
The extracted membrane protein fraction was separated by SDS-PAGE and then transferred onto a PVDF membrane. The western blot analysis was performed with an anti-his HRP conjugated antibody. Lane (+) ScaDMT^{tru} expressed in standard TB was loaded as a reference. Lanes 1-3 correspond to MMAA media where the cells were exposed to seleno-methionine only one hour prior to induction Lane 1-2 no protein is detectable. Lane 2 a faint band of ScaDMT^{tru} is visible. Lane 4-5 Significantly more expression of ScaDMT^{tru} is detected in all three cases where medium without addition of all amino acids is used. Lane 7-8 No protein is detected for all three media containing amino acids when Seleno-Methionine is added from the beginning. Lane 10-12 Comparable amounts of ScaDMT^{tru} where detected for the cultures grown in minimal medium with addition of Seleno-Methionine.

From these results it can be concluded that a sufficient amount of protein was produced with the MM but not the MMAA expression strategy. Cultures that were treated with the methionine-biosynthesis inhibition cocktail for one hour, followed by a one-hour adaptation to seleno-methionine prior induction, gave double the amount of biomass at harvest. As also this strategy, which includes additionally trace elements and the Kao-Michayluk Vitamin solution (MM3), has yielded the higher expression levels (see Figure 40, lane 5), it was used for scale-up. In total 50 flasks, with a volume of 0.6 l each, were grown according to the protocol and induced with arabinose at an OD_{600} of 0.6. Three hours post induction the culture was supplemented with an additional aliquot of the methionine-biosynthesis inhibition cocktail. Cells were harvested fourteen hours after induction at an OD_{600} of ~3.0. The resuspended cells were lysed by sonication, and membrane protein extraction was started directly after a low-spin centrifugation step, to remove unbroken cells and debris. The protein was purified by IMAC, only half of the Ni-NTA resin was used compared to the standard protocol for the unlabeled transporter, to compensate for the lower expression levels. Efficient incorporation of seleno-methionine into ScaDMT^{tru} was confirmed by MALDI-MS (Data not shown), which revealed an incorporation of 7-8 seleno-methionines per transporter corresponding to an

incorporation efficiency of 83%. After SEC in the detergent DM the seleno-methionine labeled transporter ScaDMT^{tru} was combined with the purified, unlabeled nanobody and subjected to an additional SEC run on a S200 column, equilibrated in a buffer containing the detergent NM. The protein complex was concentrated to 11 mg/ml and set-up in sitting-drop vapor diffusion experiments, screening in a constricted range around the ideal condition used for the native crystals. Overall the protein behaved comparable to unlabeled ScaDMT^{tru} during purification, despite the low yield of 37 µg/l culture. The protein did crystallize, although the crystals were thinner and nucleation was less frequently observed, which can be partly explained by the slightly lower protein concentration (11 instead of 12 mg/ml) used to set up the crystallization experiments.

2.5.2. Structure determination of the ScaDMT^{tru}-nb16 complex

Diffraction data of the seleno-methionine derivatized crystals was collected close to the absorption edge for selenium, at λ = 0.9795 Å at low beam intensity with an oscillation range 0.5° per image. In order to obtain high redundancy 1500 frames were collected, which results in a total oscillation range of 750°. The data was indexed, integrated and scaled with XDS (Kabsch, 1993). A summary of the data statistics is shown in Table 11. The data is 22.0-fold redundant and 99.2% complete (with a 22.5-fold redundancy and a completeness of 95.4 % in the highest resolution shell (3.8-3.6 Å). An I/σI of 2.94 in the highest resolution shell indicates a diffraction limit close to 3.6 Å. The anomalous signal of selenium is detectable up to ~4.6 Å (F"/σI of 1.127 at 4.8 Å and 0.933 at 4.4 Å).

ehr25_2, ScaDMTtru-nb16, Se-Met, SAD

SUBSET OF INTENSITY DATA WITH SIGNAL/NOISE >= -3.0 AS FUNCTION OF RESOLUTION

RESOLUTION LIMIT	NUMBER OF REFLECTIONS OBSERVED	UNIQUE	POSSIBLE	COMPLETENESS OF DATA	R-FACTOR observed	R-FACTOR expected	COMPARED	I/SIGMA	R-meas	CC(1/2)	Anomal Corr	SigAno	Nano
10.56	35501	1725	1741	99.1%	4.4%	4.4%	35501	72.12	4.5%	100.0*	93*	4.067	695
7.55	63544	3013	3013	100.0%	5.0%	4.9%	63544	60.10	5.1%	100.0*	85*	3.186	1338
6.19	85836	3887	3887	100.0%	9.2%	8.7%	85836	35.88	9.4%	99.9*	73*	2.276	1775
5.37	101907	4550	4550	100.0%	15.0%	15.1%	101907	23.80	15.3%	99.7*	54*	1.529	2105
4.81	112287	5174	5174	100.0%	16.1%	16.4%	112287	21.96	16.5%	99.7*	30*	1.127	2417
4.40	128792	5674	5674	100.0%	20.2%	20.9%	128792	18.29	20.7%	99.6*	15*	0.933	2667
4.07	137863	6248	6248	100.0%	32.7%	34.4%	137863	12.01	33.5%	99.0*	4	0.807	2953
3.81	142284	6661	6661	100.0%	69.3%	72.8%	142284	5.95	71.0%	95.9*	-4	0.762	3160
3.59	135905	6775	7100	95.4%	126.2%	137.5%	135799	2.94	129.4%	79.4*	-3	0.719	3160
total	943919	43707	44048	99.2%	10.9%	11.1%	943813	20.71	11.1%	100.0*	40*	1.313	20270

Table 11 Data collection statistics of the ScaDMT^{tru}-nb16 data set used for SAD phasing.
The number of reflection, the completeness of the data set, its calculated R-factor, I/σI and the anomalous signal are displayed for different resolution shells.

SHELX C and D (Schneider and Sheldrick, 2002) were used to identify the 18 selenium sites present in each asymmetric unit. In Figure 41 the signal-to-noise ratio (I/σI) is plotted in dependence of the resolution, which defines the high-resolution limit of the dataset as 3.5 Å. In the same figure on the right, the ratio of anomalous differences over background is shown against resolution, indicating an anomalous signal over-noise of up to 4.4 Å. The selenium sites were determined from the anomalous difference Patterson map by Patterson superposition methods. Whereas incorrect solutions have a correlation coefficient (CC) below 20%, a value above 35% is indicative for a correct substructure solution. The histogram depicted in Figure 42 illustrates the distribution of all calculated solutions. In combination with the CC the Patterson figure of merit (PATFOM) for each trial is useful to distinguish correct from wrong solutions (Figure 42 right panel). The highest CC and PATFOM values indicate the correct solution of the substructure search.

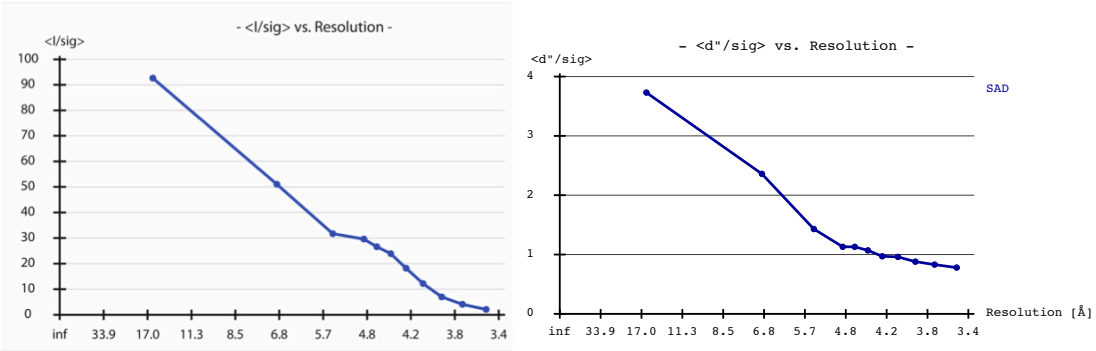

Figure 41 SHELXC: I/σI vs. resolution and f''/ σI vs. resolution.

(left) I/σI is plotted against the resolution (Å). With higher resolution the signal-to-noise ratio drops to a value where the signal is no longer distinguishable form the background (I/σI < 2.0). (right) The ratio of anomalous differences over background is shown against resolution.

SHELXD ranks the selenium sites based on their relative occupancies (with a maximum occupancy of 1.0). This graph allows estimating the number of sites reliably identified. A steep decrease of the occupancy usually indicates the boundary between heavy atoms of the substructure and noise. Sites with an occupancy of less than ~20-25% are usually considered insignificant. The corresponding graph for the ScaDMT^{tru}-nb16 data is presented in Figure 43. The site occupancies gradually decrease with increasing site number but there is no distinct drop observed. Since the occupancy of the first 18 sites is above 25%, all sites present in the asymmetric unit have been correctly identified.

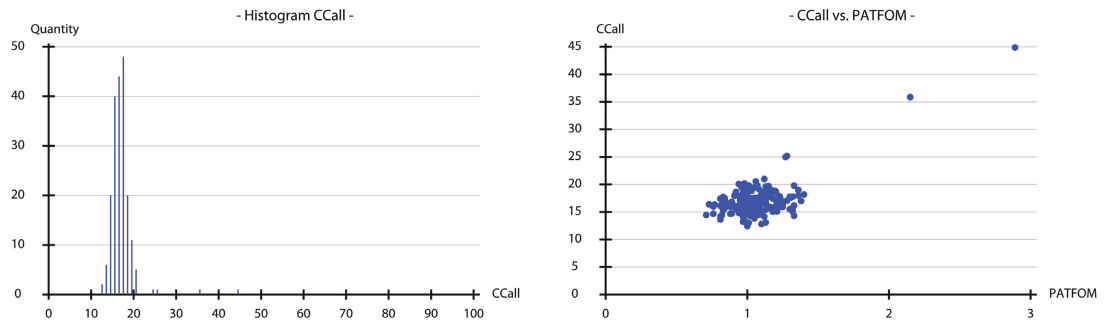

Figure 42 Graphical output of SHELXD.

(left) Histogram of the calculated solutions (quantity) plotted against the weighted correlation coefficient between E_{obs} and E_{calc} weighted by $1/\sigma E$ (CC_{all} in %). (right) For each trial CC_{all} is plotted against the PATFOM value.

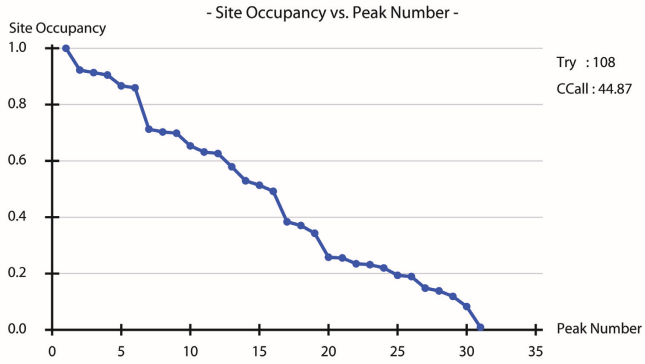

Figure 43 SHELXD statistics: Selenium site occupancies vs. peak number.

Site occupancies are normalized to the highest value. The number of significant peaks in the substructure can be estimated by plotting the peak height (site occupancy) in descending order.

During the Patterson calculations the direction of the anomalous signal that allows distinguishing the two enantiomers is lost. Both hands of the atomic substructure thus give rise to the same anomalous differences. To resolve this ambiguity SHELXE applies density modification to both enantiomorph solutions (original and inverted), which permits identification of the correct hand by a stronger increase in contrast (non-solvent/solvent) in the right solution over the wrong hand. The graphical output of the SHELXE statistics is displayed in Figure 44. Over the course of 150 cycles the contrast of the original solution increases stronger than the one of the inverted solution. The CC_{map} of the correct solution is higher compared to the inverted solution over the entire resolution range.

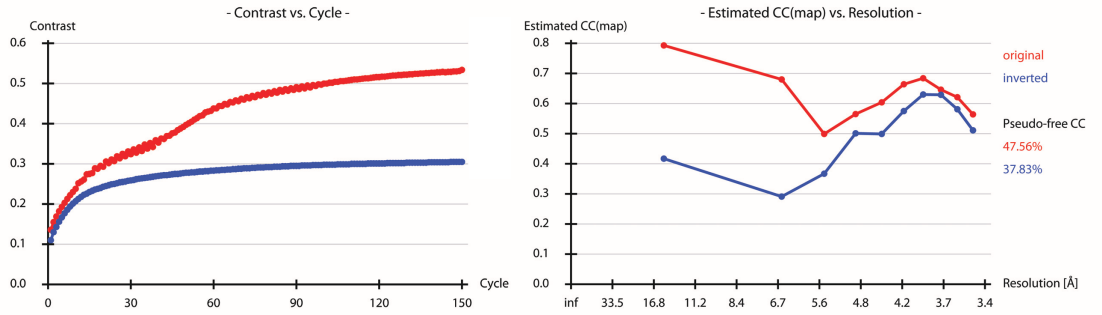

Figure 44 Solving the enantiomorphism problem with SHELXE.

(left) The contrast for each cycle is shown. The correct solution, (red) shows a stronger increase in contrast compared to the inverted solution (blue). (right) The CC of both maps is plotted against the resolution (Å).

The heavy atom coordinates identified in SHELXD were refined, and a first set of single anomalous dispersion phases was calculated in SHARP (De La Fortelle and Bricogne, 1997). During refinement the xyz coordinates, occupancies and B-factors of the selenium sites were optimized. The phasing power of the anomalous component gives an indication of the quality of the phases in dependence of the resolution (Figure 45). The phasing power decreases towards higher resolution and drops below 1 at around 5 Å (Figure 45 top graph). The FOM_{cen} is a quality measure of the phases of the centric reflections. As shown in Figure 45 (lower graph) the phase probabilities are decent up to 5 Å resolution. The initial SAD phases were subsequently improved and extended in DM (Cowtan, 1994), by solvent flattening, histogram matching and non-crystallographic symmetry (NCS) averaging between the two copies of the ScaDMT^{tru}–nb16 complex, present in the asymmetric unit of the crystals. Initial NCS symmetry operators were determined from the heavy atom positions and a monomer mask was generated based on the low-resolution boundaries of the electron density. In that way the phases were extended to 3.1 Å, the resolution limit of the best native data set.

The improved phases were of sufficient quality for interpretation by an atomic model. The structure was built in COOT (Emsley and Cowtan, 2004) and refined in PHENIX (Adams et al., 2002). Figure 46 displays electron density calculated with experimental phases that were improved by NCS averaging, next to the $2F_o$-F_c density calculated with phases of the refined model at 3.1 Å. The R/R_{free} values of the final model are 25.0% and 28.5%. R_{free} values were calculated from 5 % of the reflections that were excluded from refinement.

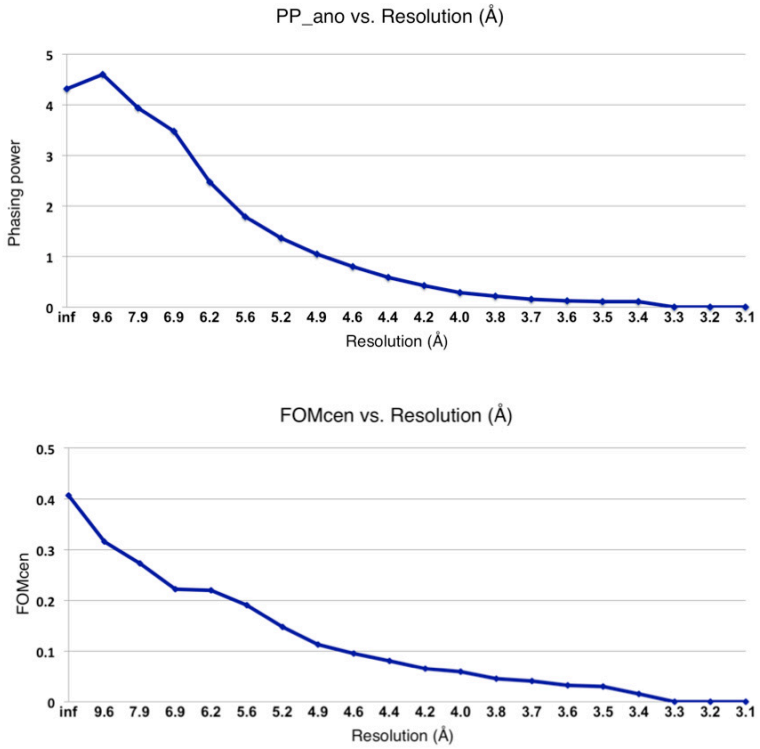

Figure 45 SHARP statistics: Phasing power and FOM_{cen} vs. resolution.

(top) The Phasing power of the anomalous data set is plotted against the resolution (Å). (bottom) The figure of merit of the centric reflections (FOM_{cen}) is shown in dependence of the resolution (Å).

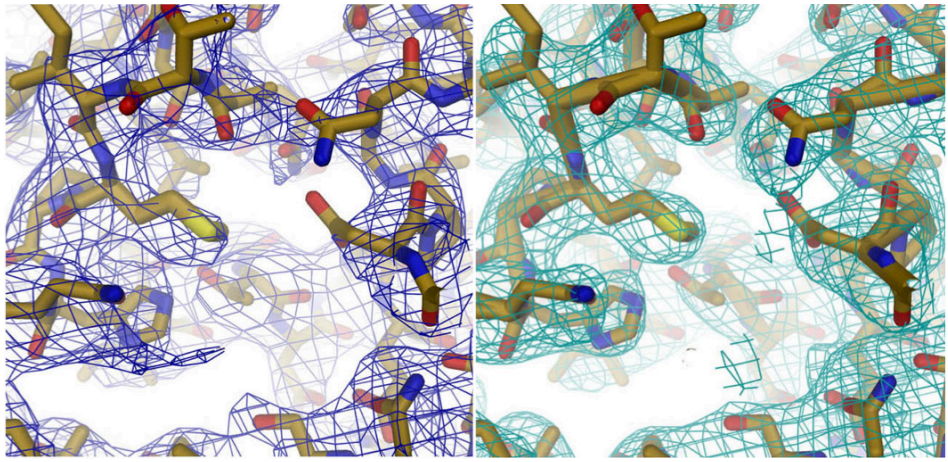

Figure 46 Electron density after SAD-phasing and after structure refinement.

(left) Elecron density at 3.5 Å that was calculated from experimental phases that were improved by NCS averaging. The density, contoured at 1 σ and superimposed on the final model, is shown in blue. (right) $2F_o$-F_c density at 3.1 Å calculated with the phases of the refined model and contoured at 1 σ, is shown in cyan.

2.5.3. Summary

For SAD phasing crystals of seleno-methionine labelled protein were prepared. In order to produce Se-Met labelled protein, cells were grown under defined conditions with the endogenous methionine synthesis inhibited by the addition of the amino acids L-Lysine, L-Threonine, L-Phenylalanine, L-Leucine, L-Isoleucine and L-Valine. During initial expression screening, a large difference in protein yield was detected depending on the media and growth conditions. The results of this initial screen allowed to identify conditions with high expression levels. These improved expression conditions permitted scale-up and purification with a protein yield of 1.1 mg from a 30 l culture and an incorporation efficiency of seleno-methionine of >80 %. The crystals of Se-Met-derivatized protein grew in space group $P3_121$ with two proteins per asymmetric unit, and were isomorphous to the native protein complex.

Anomalous data collection of Se-Met crystals has provided an initial set of phases by the SAD method, which has subsequently led to the structure determination of the ScaDMT^{tru}-nb16 complex at 3.1 Å resolution. The workflow during phasing is summarized in Figure 47. After data reduction in XDS, the SHELX suite (C/D/E) was used to solve the selenium substructure. SHARP was used to refine the selenium sites and calculate phases to 4.5 Å (SAD data set). Solvent flattening, histogram matching and 2-fold NCS symmetry averaging in DM improved the phases and allowed phase extension to 3.5 Å. This map was used to build an initial atomic model in COOT. The model was improved by refinement with PHENIX using a native dataset at 3.1 Å.

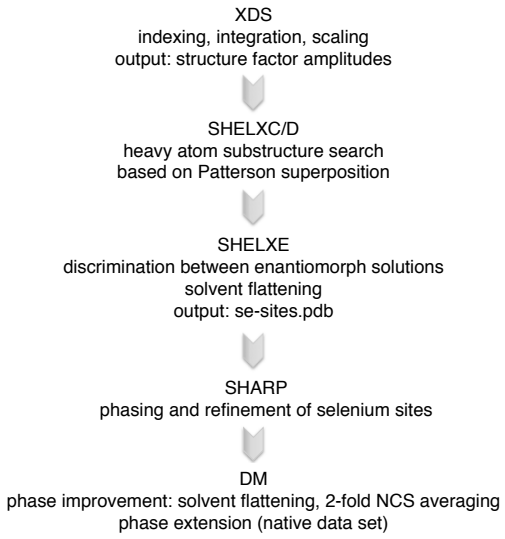

Figure 47 Workflow of the SAD phasing process for the ScaDMT^{tru}-nb16 complex
Schematic representation of the workflow applied for the ScaDMT^{tru}-nb16 complex solved by the SAD method.

2.6. Functional characterization of ScaDMT

2.6.1. Isothermal titration calorimetry of ScaDMT wild type, binding site mutants and ScaDMT^{tru}

Isothermal titration calorimetry (ITC) is a powerful biophysical tool to determine the thermodynamic parameters of interactions between biological molecules and their ligands. In ITC measurements the small enthalpy differences that occur upon binding of a ligand to a receptor molecule (e.g. binding of an ion to a protein in solution) are detected. For this purpose, ITC devices have two compartments, one cell containing the sample in solution (e.g. protein) and one reference cell filled with buffer (or water). These cells are set to a fixed reference power and the instrument tries to maintain equal power between them. Upon injection of the ligand to the sample cell, heat is released or taken up by the system, depending on the enthalpy of the chemical reaction. In response, the sample cell is either heated or cooled to compensate for the temperature difference between sample and reference cell. These power changes are recorded over time. In an exothermic reaction heat will be released upon ligand binding, and the power will be down regulated (by cooling) to keep the sample cell at the reference power. An endothermic reaction will take up heat upon ligand binding, and therefore the system needs to be heated. For every injection the total energy is integrated and plotted against the ligand concentration. For analysis the integrated heat exchange values are fitted to a suitable binding isotherm, which allows the calculation of the binding affinity (K_a) and other thermodynamic parameters (enthalpy changes ΔH, Gibbs free energy changes ΔG, entropy changes ΔS and binding stoichiometry n). In that way, affinities in the nanomolar to sub-millimolar range can be detected reliably. As ITC experiments measure the energy changes of the system, they are independent of the ligand size, which is an advantage over similar label-free techniques (e.g. surface plasmon resonance or microscale thermophoresis), where most ions are not detectable. Large quantities of pure and stable protein, as well as ligand, supplied in the same buffer composition are needed for ITC measurements. The temperature used during the experiments, is chosen to ensure measureable enthalpy differences. A high protein concentration is advantageous, not only to improve the signal-to-noise ratio, but more importantly to measure the entire

range from sub-stoichiometric binding to ligand saturation. Because the stability of the protein during the measurement is of high importance, lower protein concentrations may have to be used, which may not permit the reliable measurement of all thermodynamic quantities. Despite this limitation, K_a values can be determined with satisfying precision to answer biochemical questions.

In the case of ScaDMT, we were interested in the binding affinity of a transported ion to the protein, and thereby compare the binding affinities of binding site mutants to the wild type protein. ITC measurements also allowed us to show that the truncated version of ScaDMT, ScaDMT^{tru}, binds cadmium with similar affinity as the wild type transporter. For these measurements, cadmium (as $CdCl_2$) was preferred over manganese or other divalent transition-metal substrates, because it is stable in aqueous solution (under the conditions used) and therefore would allow us to measure affinities with higher reliability/precision than with less stable divalent metal ions. Manganese was tested as well, but noise levels were higher, and K_d values were thus determined less accurately (data not shown). Cadmium was advantageous for a second reason: In our competition transport assays (see next chapter) cadmium is preferably transported over manganese, indicating a higher affinity for cadmium in ScaDMT, which has also been shown for hDMT1 (Mackenzie et al., 2007).

For ITC analysis, ScaDMT was purified with the same protocol used for crystallization, in the detergent DM. After SEC the protein fractions were pooled (concentration ~1 mg/ml) and dialyzed 1/100 against the ITC buffer containing 2.8x CMC DM. This is necessary because slight differences of the sample buffer and the titration buffer can cause large background signals (heat absorbed or released upon solvation), thereby perturbing accurate measurements of the ligand binding reaction. The next day, ScaDMT was concentrated with a centrifugal filter device with a MWCO large enough to allow the passage of empty DM micelles. Just before the ITC experiment, the protein was filtered trough a 0.1 µm centrifugal filtration device, and the concentration was determined by spectrophotometry. The ITC measurements were carried out with protein concentrations between 5.5-6 mg/ml (110-180 µM). An ITC200 (GE, Microcal) instrument was used, which has a small sample cell of ~230 µl (a bit more sample is needed to ensure there are no air bubbles left that would cause the detergent to foam when stirring starts). One run, thus consumed around 1.5 mg of purified protein. As ScaDMT is more stable at low temperatures, 6 °C was found to be the temperature where ScaDMT is stable, and the heat differences are well enough detectable. The

cadmium chloride solution was prepared in the buffer the protein was dialyzed into. For ScaDMT and ScaDMT^{tru} ITC measurements, the cadmium concentration in the syringe was 4 mM and titrated in aliquots of 2 µl. The raw data of the absorbed heat upon cadmium injection is shown in Figure 48 (top). All measurements were background-corrected. For every run, cadmium was titrated into the respective buffer (no protein) and the signal was subtracted from the sample run (with protein). ScaDMT binds cadmium, with an affinity of 29 ±10 µM and ScaDMT^{tru} was found to bind cadmium with comparable affinity of 37 ±8 µM. After the ITC run, the integrity of the protein-Cd^{2+} samples was analyzed by SEC. All constructs were eluting as one single peak at the expected molecular weight, with no detected aggregation peak (data not shown).

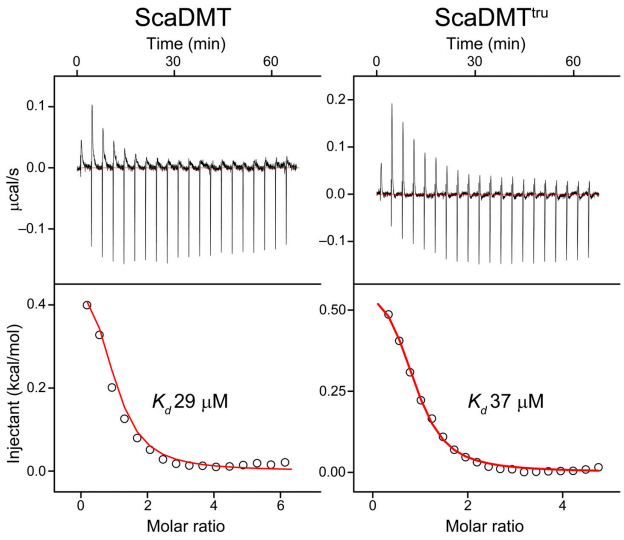

Figure 48 ITC measurements of Cd^{2+} binding to ScaDMT and ScaDMT^{tru}

(Top graphs) Heat absorbed upon injection of Cd^{2+} into the cell, containing the respective protein. (Bottom graphs) Fit of the integrated and buffer corrected heat to a single-site binding isotherm (red line). The exponent *n* was constrained between 0.9 and 1.1.

Alanine mutants of binding site residues of ScaDMT were constructed by mutagenesis, expressed and purified in DM with the same protocols as used for the wild type protein. Expression levels of D49A and N52A mutants were lower, yielding 12 % and 35 % less protein than for wild type ScaDMT (1.56 mg/l culture and 1.13 mg/l culture respectively). The mutant M226A yielded about 90 % more protein compared to wild type (M226A 3.4 mg/l culture compared to 1.77 mg/l for ScaDMT). For ITC measurements of two binding site mutants (D49A and N52A) a higher cadmium concentration (up to 25 mM) and the concatenation of two runs (of twice 20 times 2µl injections) was needed to measure saturated binding. Background was measured and subtracted as described before. The heat release and the integrated and fitted data are depicted in Figure 49. In all three mutants the binding of cadmium to the protein is exothermic (at 6°C with the specified buffer and detergent), whereas it is endothermic

for wild type and truncated ScaDMT. Similar changes were reported in the literature for another protein (Grenha et al., 2013). The exact cause of such a change from an endo- to exothermic process is unknown. One could speculate that the preferred conformation of the mutant is not the same as for the wild type protein, which might have an impact on the energy status of the system. The mutation of single residues of the binding site was found to have a strong effect on cadmium binding. The affinity for cadmium shifted by more than an order of magnitude, towards higher cadmium concentration. K_d values are: 475 ±38 µM for D49A, 929 ±151 µM for N52A and 769 ±27 µM for M226A. All three mutants were subjected to SEC after the ITC experiments to confirm their stability. No void peaks were detected and the proteins eluted as single peaks at their expected elution volume (data not shown).

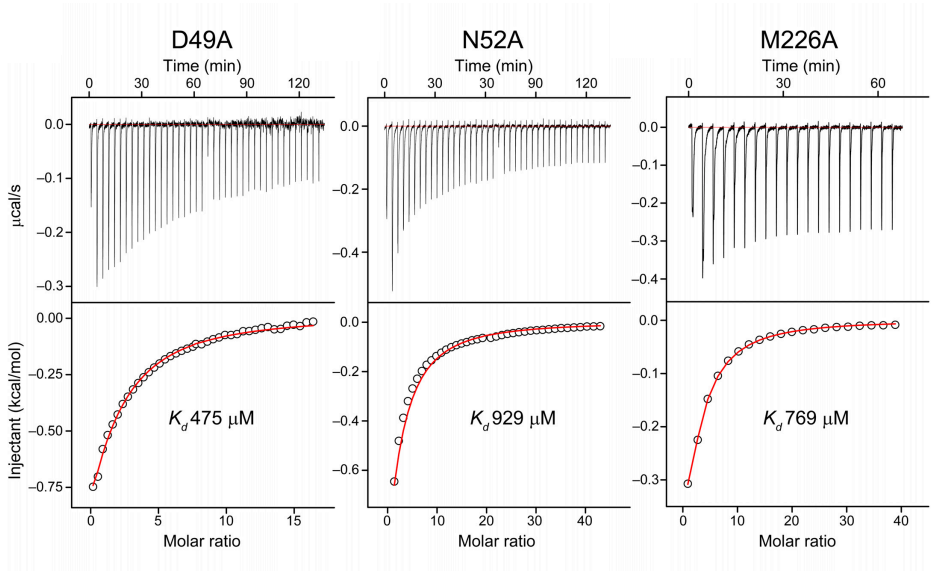

Figure 49 Binding of Cd^{2+} to ScaDMT binding site mutants

From left to right: D49A, N52A and M226A. (Top graphs) Heat absorbed upon injection of Cd^{2+} into the cell containing the respective protein. (Bottom graphs) Fit of the integrated and buffer corrected heat to a one-site binding isotherm (red line). The exponent *n* was constrained between 0.9 and 1.1.

In summary, the ITC experiments have allowed me to determine the affinity of cadmium to a single binding site in ScaDMT (K_d 29 µM). I could show that the truncation of N-terminal residues in the construct $ScaDMT^{tru}$ does not have strong effects on the binding affinity of cadmium (K_d 37 µM), thus confirming that its binding site remained intact. Furthermore, ITC measurements of the binding site mutants revealed drastic shifts in the

ion binding affinities compared to the wild type protein (D49A K_d 475 µM, N52A K_d 929 µM and M226A K_d 769 µM). ITC can precisely measure affinities and reveal thermodynamic parameters, but it does not assess transport properties. To measure the transport of various divalent metal ions, I have established a fluorescence-based proteoliposomal assay, described in the following chapter.

2.6.2. Transport assays of ScaDMT and ScaDMT^{tru}

Methods to reconstitute membrane proteins into liposomes have been used since more than 35 years, for the development of cell-free transport assay (Darszon, 1979). Yet successful incorporation of detergent solubilized (active) protein into lipid vesicles can be highly dependent on the lipid composition, the protein and the detergents used. Therefore, different reconstitution methods are described in the literature. They mostly differ in two steps, the preparation of lipids (e.g. by the use of pre-formed liposomes or detergent solubilized lipids) and the strategy of lipid-removal (e.g. by dialysis, rapid dilution, bio-bead addition or sucrose density centrifugation).

For the reconstitution of ScaDMT, a protocol based on the preparation of preformed liposomes, destabilized with Triton-X-100 was applied (Geertsma et al., 2008b). *E. coli* polar lipid extract and phosphytidylcholine from egg-yolk were mixed in a 3:1 ratio and washed with chloroform and diethylether. Diethylether was removed under vacuum or a nitrogen gas stream. The lipids were resuspended in the reconstitution buffer and homogeneous unilamellar liposomes were prepared by extrusion trough a polycarbonate filter. The vesicles were destabilized with Triton-X-100 beyond saturating concentrations, and then combined with the freshly purified transporter (in the detergent DM). Polystyrene beads (Bio-Beads) were used to remove the detergent, and to allow proteoliposome formation. Bio-Beads were removed by filtration. Proteoliposomes were harvested by centrifugation, flash frozen and stored in liquid nitrogen until use. Efficient incorporation of ScaDMT was assessed by freeze-fracture electron microscopy shown in Figure 50. The protein was reconstituted at a protein-to-lipid ratio of 1:40 (w/w) (= LPR 40).

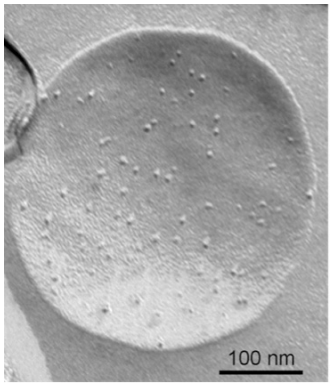

Figure 50 Freeze-fracture electron micrograph of proteoliposomes with incorporated ScaDMT.
The protein was reconstituted into liposomes at an LPR of 40. Proteoliposomes were frozen under high-pressure in liquid nitrogen, fractured under vacuum, subsequently shaded with a carbon-platinum layer at 45° and coated with carbon at an angle of 90°. The image was taken with a Philips CM100 transmission electron microscope.

Transport of the reconstituted protein can be measured with fluorescence dyes. These dyes need to be metal sensitive; their fluorescence is either quenched or increased when the divalent metal ion is present. Additionally the dye needs to be efficiently trapped in the liposome, which can be achieved by extrusion of the proteoliposomes together with the dye and subsequent removal of the untrapped dye. It is critical that the dye is sufficiently hydrophilic to be membrane impermeable. To my knowledge, there are no commercially available fluorescence dyes that are equally sensitive to all the divalent metal ions. Often these dyes are engineered for maximum calcium sensitivity (an earth alkaline metal ion) or zinc sensitivity (a transition metal ion). The two fluorophores used in this study are calcein and fura-2. Their signal in response to different metal ions was assessed in aqueous solution to have an estimate of their sensitivity under conditions close to the experimental set-up. Table 12 summarizes the fluorescence response of calcein to different metal ions and the fluorescence change of fura-2 observed in the presence of cadmium and calcium. Signals were measured with a plate reader at the optimal excitation and emission wavelength for the respective fluorophore. Calcein is efficiently quenched by Mn^{2+}, Co^{2+} and Ni^{2+} but not by Cd^{2+}, Zn^{2+}, Ca^{2+}, Sr^{2+} and Ba^{2+}.

Although calcein was designed as an indicator for calcium it is only sensitive to calcium at strongly alkaline pH (Lewin et al., 1969). The sensitivity of calcein for Mn^{2+} is lower than for Co^{2+} and Ni^{2+}. The fluorescence of fura-2 is strongly increased upon addition of cadmium. Fura-2 is a highly sensitive fluorophore designed to detect small changes (nM range) in calcium concentration but at calcium concentration above 1 µM its fluorescence is basically calcium independent (Kong and Lee, 1995). Besides calcein and fura-2, phengreen and fluozin-3 were tested as well, but they were both leaking out of the liposomes (since they are probably too lipophilic), and were as a consequence not suitable for the transport measurements. Additionally no fluorescence changes of

phengreen in response to cadmium and manganese were observed under the investigated conditions (aqueous buffer, ion concentrations between 5 nM and 1mM).

Fluorophor			molar ratio	1:1
Calcein	λ_{ex}	492 nm	Mn^{2+}	70%
	λ_{em}	518 nm	Co^{2+}	18%
			Ni^{2+}	20%
			Ca^{2+}	105%
		insensitive	Cd^{2+}, Zn^{2+}, Sr^{2+}, Ba^{2+}	
Fura-2	λ_{ex}	335 nm	Cd^{2+}	173%
	λ_{em}	505 nm	Ca^{2+}	100%

Table 12 Ion selectivity of calcein and fura-2.

The fluorescence signal of calcein (0.5 µM) and fura-2 (0.5 µM) in response to different divalent metal ions (molar ratio of fluorophore to ion is 1:1) is presented as percentage of the maximum fluorescence measured in buffer without the addition of divalent metal ions (100%). Calcein was excited at 492 nm and emission was detected at 518 nm. Fluorescence changes of calcein in response to Cd^{2+}, Zn^{2+}, Sr^{2+} and Ba^{2+} were less than 10% at all tested concentrations. Fura-2 was exited at 335 nm and emission was detected at 505 nm. Both fluorophores are insensitive to calcium (under the investigated conditions).

Calcein is very light sensitive (upon light exposure the fluorescence will increase by ~10% and then decrease back to starting levels within 2-3 min). To exclude this effect during time-dependent measurements, the measurement and the pipetting steps were carried out in the dark. Fura-2 does not show this effect but generally the baseline fluorescence showed a higher fluctuation. Calcein-trapped proteoliposomes were used to detect ScaDMT and ScaDMT^{tru} mediated import of manganese (Figure 51). For that purpose, Mn^{2+} was added to the outside medium and the fluorescence change of the trapped calcein was measured every 20 seconds over a time course of 30 minutes. Towards the end of the experiment, the divalent metal ion selective ionophor calcimycin was added to measure maximal quenching in both, the proteoliposomes and the control liposomes devoid of protein. The assay as such is not strictly quantitative, but it allows a qualitative comparison between the different traces of the same metal ion. Interestingly ScaDMT^{tru} does still transport manganese into the vesicles, although clearly at a lower rate than ScaDMT.

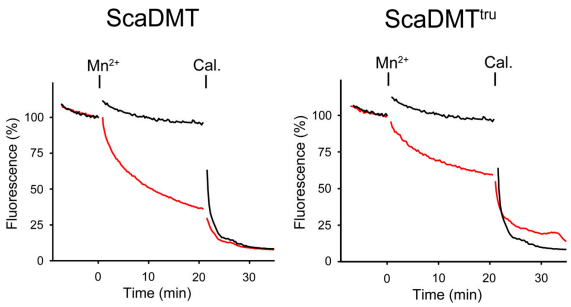

Figure 51 Transport of manganese.

ScaDMT and ScaDMT^{tru} mediated uptake of manganese. Calcein is quenched inside the vesicles when manganese (300 µM) is added to the external medium (red). A control trace of liposomes devoid of protein is shown in black.

To measure cadmium transport, fura-2 was trapped inside the vesicles and the fluorescence increase of the fluorophore in response to cadmium supplied to the external medium, was assayed. In Figure 52 the traces for ScaDMT and ScaDMT^{tru} are displayed. For ScaDMT^{tru} the picture is similar to the uptake of manganese: ScaDMT^{tru} does still transport cadmium but the curve is not as steep as the one for ScaDMT, indicating lower transport levels for cadmium in case of the truncated protein.

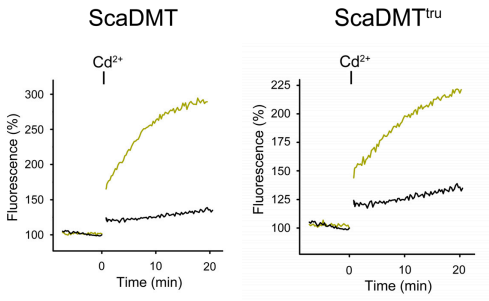

Figure 52 ScaDMT and ScaDMT^{tru} mediated uptake of cadmium.

The fluorescence of fura-2, trapped inside the vesicle, increases upon addition of cadmium (200 µM) to the external medium (yellow). A control trace of liposomes devoid of protein is shown in black.

In all transport assays the transport was triggered by the addition of the divalent metal ion to the external medium. The pH of the inside and the outside solution was kept at 7.5. The transport of the divalent metal ion was driven by its concentration gradient and independent of sodium or potassium gradients applied (data not shown). The fact that the presumably electrogenic transport proceeds without dissipation of the membrane

potential is probably due to the leakiness of the liposomes for protons. Tests with the pH-sensitive fluorophore pyranine revealed that the liposomes were leaky to protons over the timescale used in the assays. Optimization of the liposome preparation and reconstitution procedure is required to improve the tightness of the liposomes. Future experiments with proton-tight liposomes might allow us to reveal if the transport of divalent metal ions by ScaDMT is coupled to protons.

2.6.1. Summary of the functional characterization of ScaDMT

The binding and transport properties of ScaDMT wer characterized by the application of biophysical and functional methods. With ITC the binding affinity of detergent solubilized ScaDMT for cadmium could be determined (K_d 29 µM). The affinity of the truncated protein ScaDMT^{tru} (K_d 37 µM) was only slightly shifted compared to the full-length protein indicating that the truncation did not alter the conformation of the ion-binding site. K_d values of the three individual binding site mutants were strongly shifted towards higher concentrations, thus underlining the importance of the three residues (D49, N52 and M226) for ion binding.

An initial transport assay was successfully established, which allowed me to investigate divalent metal ion transport into proteoliposomes containing purified and reconstituted ScaDMT. ScaDMT dependent manganese and cadmium import was measured by metal sensitive fluorophores. Interestingly the truncated transporter ScaDMT^{tru} that we used for structure determination is still capable of transporting manganese and cadmium, although with slower kinetics. In ion-competition experiments, (see chapter 2.7) we saw that the earth alkaline metal ions calcium, barium and strontium are not transported by ScaDMT, even at concentrations up to 1 mM. A potential coupling of metal ion transport in ScaDMT to protons, which was found for eukaryotic SLC11 members, remains to be investigated. Future experiments with an improved experimental set-up might allow us to address this important question.

2.7. Crystal structure of a SLC11 (NRAMP) transporter reveals the basis for transition-metal ion transport

Ines A. Ehrnstorfer[1], Eric R. Geertsma[1,4], Els Pardon[2,3], Jan Steyaert[2,3] & Raimund Dutzler[1]

[1]Department of Biochemistry, University of Zurich, Zurich, Switzerland

[2]Structural Biology Research Center, Flanders Institute for Biotechnology, Brussels, Belgium

[3]Structural Biology Brussels, Vrije Universiteit Brussel, Brussels, Belgium

[4]Present address: Institute of Biochemistry, Biocenter, Goethe-University Frankfurt, Frankfurt am Main

Author contributions

I.A.E. carried out all experiments except for the initial nanobody selection. E.R.G. supported the high-throughput expression screening and transport assays and initiated nanobody selection by phage display. E.P. performed immunization, cloned and expressed nanobodies and performed the initial selection. J.S. supervised nanobody production. R.D. assisted I.A.E. in structure determination. I.A.E. and R.D. jointly planned the experiments, analysed the data and wrote the manuscript.

Nature Structural & Molecular Biology, Volume 21, Number 11, November 2014,
doi: 10.1038/nsmb.2904

nature structural & molecular biology

Crystal structure of a SLC11 (NRAMP) transporter reveals the basis for transition-metal ion transport

Ines A Ehrnstorfer[1], Eric R Geertsma[1,4], Els Pardon[2,3], Jan Steyaert[2,3] & Raimund Dutzler[1]

Members of the SLC11 (NRAMP) family transport iron and other transition-metal ions across cellular membranes. These membrane proteins are present in all kingdoms of life with a high degree of sequence conservation. To gain insight into the determinants of ion selectivity, we have determined the crystal structure of *Staphylococcus capitis* DMT (ScaDMT), a close prokaryotic homolog of the family. ScaDMT shows a familiar architecture that was previously identified in the amino acid permease LeuT. The protein adopts an inward-facing conformation with a substrate-binding site located in the center of the transporter. This site is composed of conserved residues, which coordinate Mn^{2+}, Fe^{2+} and Cd^{2+} but not Ca^{2+}. Mutations of interacting residues affect ion binding and transport in both ScaDMT and human DMT1. Our study thus reveals a conserved mechanism for transition-metal ion selectivity within the SLC11 family.

Iron is the most abundant trace element in mammals. As a cofactor of proteins, it plays an important part in different processes ranging from oxygen transport to the catalysis of redox reactions. Owing to the essential role of iron in metabolism and the harm caused by its uncontrolled accumulation in the body, uptake and storage of iron is tightly regulated. In vertebrates, the transport of free iron into the cytoplasm is catalyzed by members of the solute carrier 11 (SLC11) family[1,2]. These secondary active transporters are found in all kingdoms of life, with a high degree of sequence conservation[3]. The human genome encodes two SLC11 transporters (also known as natural resistance–associated macrophage proteins (NRAMPs)): SLC11A1 (NRAMP1)[4] and SLC11A2 (NRAMP2 or DMT1)[5]. Whereas NRAMP1 is expressed in the phagosomes of macrophages, where it has an essential role in host defense against pathogens[6], the divalent metal-ion transporter DMT1 is broadly expressed in the duodenum, kidney, brain, testis and placenta[7]. Malfunction of either protein is associated with iron storage diseases[8] and a decreased resistance against bacterial infections[9]. With respect to function, DMT1 is the most thoroughly characterized family member[10]. The protein catalyzes the cotransport of protons and divalent transition-metal ions such as Fe^{2+}, Mn^{2+} and Cd^{2+}, whereas Zn^{2+} is a poor substrate[5,11]. The alkaline earth metal ions Ca^{2+} and Mg^{2+} are not transported[12]; this is important because their high concentration in the duodenum would interfere with the absorption of Fe^{2+}. DMT1 is the main route for import of Fe^{2+} and potentially also of Mn^{2+} into the human body, but it is also responsible for the uptake of toxic metals such as Cd^{2+} (refs. 13,14).

In bacteria, SLC11 transporters catalyze the import of Mn^{2+} because iron is usually transported either as complex with siderophores or porphyrins[15,16]. Functional characterization and the high sequence homology suggest that bacterial SLC11 homologs share architecture and substrate specificity with their eukaryotic counterparts and thus work by similar transport mechanisms. On the basis of hydropathy analysis, SLC11 transporters are supposed to contain 11 or 12 transmembrane helices with the N terminus located in the cytoplasm[17]. Although SLC11 proteins were recently predicted to share features with a class of transporters including the amino acid transporter LeuT[18–20], detailed structural information on the family has been absent so far.

We were interested in the mechanism of how divalent transition-metal ions are selectively transported across the membrane, whereas other divalent ions, such as Ca^{2+}, are excluded. To address this question, we have determined the structure of a prokaryotic SLC11 transporter, ScaDMT, by X-ray crystallography and have studied its functional properties by isothermal titration calorimetry (ITC) and transport assays. We have also exploited ScaDMT's homology to mammalian family members in our characterization of site-directed mutants of human DMT1 by two-electrode voltage-clamp electrophysiology. Our study reveals a framework for an important class of membrane transporters, and it provides insight into the structural basis of the transition-metal ion selectivity that is conserved within the family.

RESULTS

Functional characterization of ScaDMT

To identify a SLC11 transporter with suitable properties for structural studies, we cloned 105 close prokaryotic homologs with the fragment-exchange (FX) cloning technique[21] and investigated their expression properties in small-volume cultures. Our broad screen allowed us to single out a transporter from the bacterium *S. capitis* (ScaDMT) as a protein with superior expression levels and high stability. ScaDMT is

[1]Department of Biochemistry, University of Zurich, Zurich, Switzerland. [2]Structural Biology Research Center, Vlaams Instituut voor Biotechnologie (VIB), Brussels, Belgium. [3]Structural Biology Brussels, Vrije Universiteit Brussel, Brussels, Belgium. [4]Present address: Institute of Biochemistry, Biocenter, Goethe-University Frankfurt, Frankfurt am Main, Germany. Correspondence should be addressed to R.D. (dutzler@bioc.uzh.ch).

Received 1 May; accepted 19 September; published online 19 October 2014; doi:10.1038/nsmb.2904

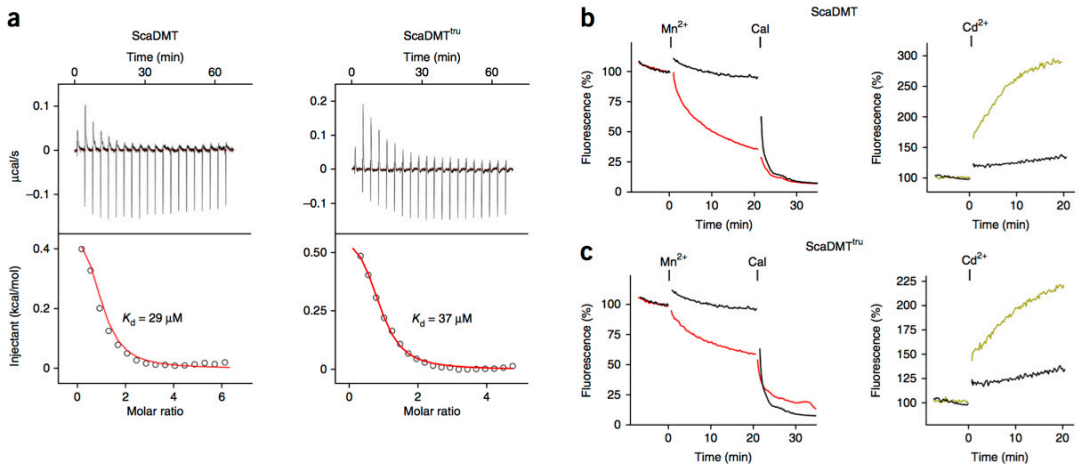

Figure 1 Transition-metal ion binding and transport. (**a**) Cd^{2+} binding to ScaDMT (left) and ScaDMT^{tru} (right), as determined by ITC. Top graphs, heat absorbed upon injection of Cd^{2+} to the experimental chamber containing the respective protein. Bottom graphs, fit of the integrated and corrected heat to a binding isotherm (red line). The exponent *n* was constrained between 0.9 and 1.1. (**b**) Left, ScaDMT-mediated transport of Mn^{2+} into proteoliposomes, showing time-dependent quenching of calcein inside the vesicle, in response to the application of 300 µM Mn^{2+} to the external medium. Addition of Mn^{2+} and the ionophore calcimycin (Cal) is indicated at top. A control trace from liposomes devoid of protein is shown in black. Right, ScaDMT-mediated transport of Cd^{2+} into proteoliposomes, showing time-dependent increase of the fluorescence of fura-2 inside the vesicle, upon addition of 200 µM Cd^{2+} to the external medium. A control trace from liposomes devoid of protein is shown in black. (**c**) ScaDMT^{tru}-mediated transport of Mn^{2+} (left) and Cd^{2+} (right) into proteoliposomes. Procedures are as in **b**.

highly homologous to human DMT1. The protein contains 448 amino acids, of which 37% are identical and 59% are homologous to those in its human counterpart (**Supplementary Fig. 1**). The biggest differences between the two proteins are found in their termini, which are both longer in DMT1. Whereas the 36–amino acid extension on the N terminus of DMT1 is predicted to be unstructured, the 59 additional residues on the C terminus encode an additional transmembrane helix. When purified in the detergent *n*-decyl-β-D-maltoside (DM), ScaDMT is monomeric as determined by multiangle light scattering (MALS; **Supplementary Fig. 2a–e**).

To characterize the interaction of the transporter with divalent cations, we investigated ion binding to the detergent-solubilized protein by ITC. ScaDMT binds the divalent transition-metal ion Cd^{2+}, which has previously been shown to be transported by different pro- and eukaryotic family members[5,16], with micromolar affinity ($K_d = 29 \pm 10$ µM error of fit; **Fig. 1a**). We assayed transport with ion-selective fluorophores after reconstitution of the transporter into liposomes (**Supplementary Fig. 2f**). The time-dependent decrease of the fluorescence after the addition of Mn^{2+} and the fluorescence increase upon addition of Cd^{2+} indicates transport of these ions into proteoliposomes, whereas we observed no fluorescence change for liposomes devoid of protein (**Fig. 1b**). When taken together, our results demonstrate that ScaDMT binds and transports Cd^{2+} and Mn^{2+}. This functional resemblance to mammalian DMT1 underlines the close relationships within the SLC11 family and distinguishes ScaDMT as a valuable model system for understanding transition-metal ion transport.

ScaDMT structure

To learn more about the structural basis of transport, we determined the structure of ScaDMT by X-ray crystallography. Crystallization experiments on the full-length protein allowed us to obtain crystals diffracting to a resolution of 6.5 Å (**Table 1**), which we could not further improve. In an attempt to obtain better-diffracting crystals, we systematically screened shorter constructs of the transporter and generated nanobodies[22] by immunization of llamas and used the nanobodies for cocrystallization with the membrane protein. In the shortest construct, termed ScaDMT^{tru}, we removed 41 amino acids from the N terminus, including 17 residues of the first predicted transmembrane helix (**Supplementary Fig. 1**). This construct was stable, and it transported Cd^{2+} and Mn^{2+} and bound Cd^{2+} with similar affinity ($K_d = 37 \pm 8$ µM) to that of wild type, thus ensuring that the functional properties of the truncated protein were retained (**Fig. 1a,c**). A complex of ScaDMT^{tru} with a nanobody, which recognizes both the full-length and the truncated membrane protein and which promotes dimerization in solution, allowed us to identify crystals with superior diffraction properties that permitted structure determination at 3.1 Å by the selenomethionine single-wavelength anomalous dispersion (SAD) method (**Supplementary Figs. 2** and **3** and **Table 1**). Crystals were of space group $P3_121$ with two copies of the ScaDMT^{tru}–nanobody complex in the asymmetric unit (**Fig. 2a**). Both copies were related by two-fold noncrystallographic symmetry (NCS) and buried 1,190 Å^2 of the combined molecular surface of the membrane protein and 960 Å^2 of the nanobody. Despite the comparably large interaction interface, the two-fold relationship is not likely to represent the oligomeric state of the protein in the membrane because both transporters are tilted with respect to the NCS axis. The nanobody binds to a region exposed to the periplasmic side of the transporter, where it is involved in extensive intermolecular contacts (**Supplementary Fig. 4 a,b**).

ScaDMT contains 11 transmembrane helices, some of which are bent or interrupted by short loops (structure and topology in **Fig. 2**). Its N terminus is located in the cytoplasm, and its C terminus is located on the periplasmic side. The first five α-helices are structurally related to the following five α-helices by an approximate two-fold rotation around an axis located in the center of the membrane and

Table 1 Data collection and refinement statistics

	ScaDMT^{tru}–nanobody	SeMet	ScaDMT^{tru}–nanobody Mn^{2+}	ScaDMT
Data collection				
Wavelength (Å)	1.0	0.9795	1.8940	1.0
Space group	$P3_121$	$P3_121$	$P3_121$	$P3_221$
Cell dimensions				
a, *b*, *c* (Å)	114.4, 114.4, 257.9	114.6, 114.6, 257.6	114.1, 114.1, 257.4	151.8, 151.8, 157.3
α, β, γ (°)	90.0, 90.0, 120.0	90.0, 90.0, 120.0	90.0, 90.0, 120.0	90.0, 90.0, 120.0
Resolution (Å)	50–3.1 (3.3–3.1)	50–3.6 (3.8–3.6)	50–3.4 (3.6–3.4)	50–6.5 (6.7–6.5)
R_{merge}	6.0 (120)	11.2 (142)	8.1 (127)	11.7 (169)
$I / \sigma I$	21.0 (2.1)	19.3 (3.2)	19.0 (2.4)	11.1 (2.1)
Completeness (%)	99.6 (98.2)	100.0 (100.0)	99.9 (100.0)	94.9 (89.5)
Redundancy	9.5 (15.2)	22.0 (22.5)	9.6 (9.4)	12.9 (12.3)
Refinement				
Resolution (Å)	20–3.1		20–3.4	20–6.5
No. reflections	35,850		27,349	3,803
R_{work} / R_{free}	25.0 / 28.5		26.0 / 28.5	27.20 / 33.4
No. atoms				
Protein	7,948		7,948	
Ligand/ion			2	
B factors				
Protein	139		148	
Ligand/ion			194	
r.m.s. deviations				
Bond lengths (Å)	0.003		0.003	
Bond angles (°)	0.75		0.69	

Values in parentheses are for highest-resolution shell. SeMet, selenomethionine.

close to the substrate-binding site are well defined (**Supplementary Fig. 3**). It is noteworthy that in the inward-facing conformation of LeuT, this part of the helix interacts only loosely with the rest of the protein[29]. Electron density of full-length ScaDMT crystallized in the absence of a nanobody at 6.5 Å shows an unaltered conformation with residual electron density for α-helix 1a located at the equivalent position as found in LeuT; this underlines that neither the truncation of the N terminus nor the binding of the nanobody perturbed the ScaDMT^{tru} structure (**Supplementary Fig. 5** and **Table 1**). Although we grew the crystals in conditions containing a high (200 mM) concentration of Ca^{2+}, we did not observe specific binding of this ion in the $2F_o - F_c$ electron density of the refined model and in anomalous difference electron density maps collected at appropriate wavelengths, results suggesting that the protein shows a substrate-free conformation (**Fig. 3c** and **Supplementary Fig. 3d**). The structure of ScaDMT reveals the detailed architecture of SLC11 transporters, and it confirms the relationship between family members and a diverse class of secondary active transporters, as previously postulated from sequence analysis[19,20].

running parallel to its plane (**Fig. 2b,c**). The organization of subdomains as inverted repeats of five transmembrane helices places SLC11 proteins among transporters sharing a conserved protein fold that was initially observed in the amino acid transporter LeuT[18] and was later found in several other transporter families[23–28]. As in these transporters, the first helix of each repeat (i.e., α-helices 1 and 6 in ScaDMT) is unwound in the center of the membrane, thus providing residues for the coordination of the transported substrates. In the crystal structure, the protein adopts an inward-facing conformation that is similar to the corresponding conformations observed for LeuT[29] and the sodium/galactose transporter vSGLT[26] (with r.m.s. deviations of transmembrane helices of 3.2 Å and 3.9 Å respectively; **Supplementary Fig. 4c,d**). Pronounced structural differences are present in the ion-binding region, where the small size of the transported substrate of ScaDMT requires the proximity of coordinating residues. Owing to the truncation at the N terminus, the first half of α-helix 1 is absent, whereas the residues

Ion-binding site

Because the ion binding properties of ScaDMT^{tru} are fully preserved, we used the structure to investigate the interaction with different mono- and divalent cations by X-ray crystallography. Strong anomalous difference density in a data set of a crystal soaked in Mn^{2+} shows binding of the ion to a single site that is accessible from the cytoplasm and located at the unwound parts of α-helices 1 and 6 in the center of the membrane (**Fig. 3a**). Whereas the bound metal ion is well defined, the present resolution of the data does not allow conclusions on the presence of ordered water molecules to be made. Ion binding did not induce any noticeable conformational changes, because the structures of both the complexed and the uncomplexed protein are virtually identical (**Fig. 3b,c**). Mn^{2+} is coordinated by the carbonyl oxygen of the peptide bond connecting residues 223 and 224 at the

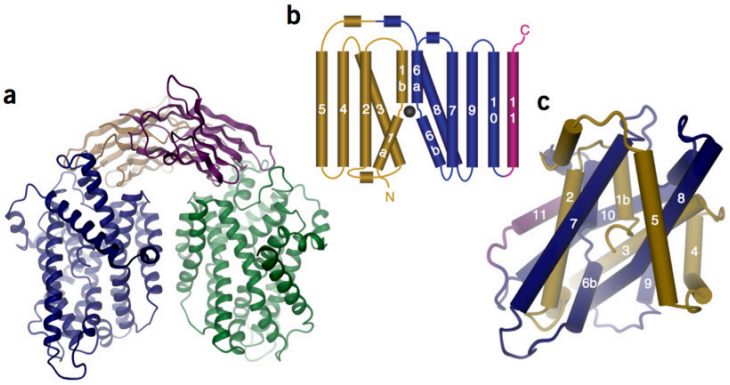

Figure 2 ScaDMT structure. (**a**) Ribbon representation of the dimeric ScaDMT^{tru}–nanobody complex crystallized in Ca^{2+} (ScaDMT^{tru}–Ca^{2+}). The view is perpendicular to the two-fold noncrystallographic symmetry axis. (**b,c**) Topology (**b**) and structure (**c**) of ScaDMT^{tru}. The two related halves of the protein are colored in brown and blue, and helix 11 is colored in magenta. Helices are represented as cylinders, and their numbers are labeled. In the topology, the bound ion is indicated by a gray sphere. **Figures 2–4** were prepared with DINO (http://www.dino3d.org/).

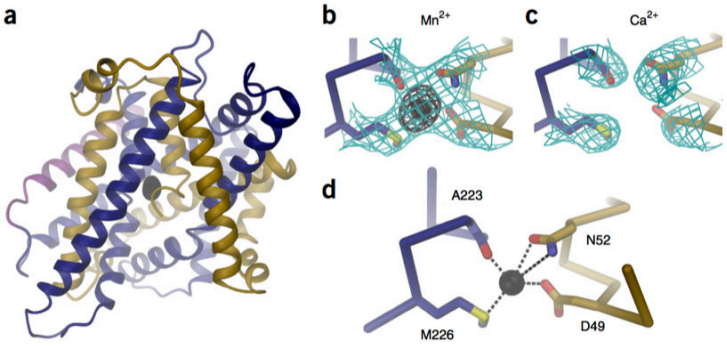

Figure 3 Ion coordination. (**a**) Ribbon representation of a single transporter in the ScaDMT^{tru}–nanobody structure in complex with Mn^{2+} (ScaDMT^{tru}–Mn^{2+}). The color coding of the protein is as in **Figure 2b**. The anomalous difference density of Mn^{2+} (calculated at 3.5 Å and contoured at 13σ) is shown as gray mesh. (**b**–**d**) Close-up view of the ion-binding site of ScaDMT. Sections of the protein are shown as Cα trace with selected main chain and side chain atoms as sticks. The refined Mn^{2+} ion is shown in gray. (**b**) ScaDMT^{tru}–Mn^{2+} with anomalous difference density of Mn^{2+} (contoured at 13σ) shown as gray mesh and the refined $2F_o - F_c$ density (contoured at 1σ) as cyan mesh. (**c**) ScaDMT^{tru}–Ca^{2+}. The refined $2F_o - F_c$ density (contoured at 1σ, cyan) does not show any density of bound ions. (**d**) Transition-metal ion coordination within the binding site. Interactions are indicated by dashed lines. Approximate ion-protein distances: Mn^{2+}-O (backbone, Ala 223), 2.2 Å; Mn^{2+}-S (Met 226), 2.7 Å; Mn^{2+}-O (Asp 49), 2.3 Å; Mn^{2+}-O and Mn^{2+}-N (Asn 52), 2.9 and 3.5 Å, respectively. The Mn^{2+} ion is shown as a gray sphere.

C-terminal end of α-helix 6a; the side chain of Met226 of the same helix; and side chains of Asp49 and Asn52 from the close-by α-helix 1 (**Fig. 3d**). The coordinating atoms, arranged in an approximately planar geometry, provide predominantly hard oxygen ligands along with a soft thioether sulfur ligand. Residues contributing to ion–side chain interactions are strongly conserved within the family, and they are identical in ScaDMT and human DMT1 (**Supplementary Fig. 1**). Our structural studies thus allowed us to identify a conserved binding mode for divalent transition-metal ions that is likely to be shared by all family members.

Because SLC11 transporters are selective for certain transition-metal ions, we were interested in whether the observed transport behavior would be reflected in the ion-coordination properties of the binding site. We hence collected data for ScaDMT^{tru} crystals soaked in solutions containing different mono- and divalent cations, detected by anomalous scattering properties (**Supplementary Table 1**). In that way, we identified Fe^{2+}, Co^{2+}, Ni^{2+}, Cd^{2+} and Pb^{2+} to occupy the same site as Mn^{2+} (**Fig. 4**). We confirmed transport of Mn^{2+}, Cd^{2+}, Co^{2+} and Ni^{2+} in our fluorescence-based transport assay (**Figs. 1b** and **4k**). Cu^{2+} binds to the same location, but its position is shifted (**Fig. 4e**). Zn^{2+}, which follows Cu^{2+} in the periodic table, no longer occupies the same site. Instead, it binds to the aqueous vestibule, where it interacts with the conserved His233, which has been implicated in pH regulation and proton transport (**Fig. 4h**)[11,30]. In transport assays, the presence of excess Zn^{2+} diminishes Mn^{2+} uptake; this suggests that the ion may be transported by ScaDMT or may alternatively act as an inhibitor (**Fig. 4l**). For alkaline earth metal ions, we observed either no binding, as for Ca^{2+}, or observed the ions bound at different locations (**Fig. 4i,j**). When added in ten-fold molar excess, none of these ions interfered with Mn^{2+} uptake, thus demonstrating that they are neither high-affinity substrates nor inhibitors of ScaDMT (**Fig. 4l**). The monovalent cation Cs^{+} was bound to sites located at the periphery of the protein, which are unlikely to be relevant for transport (**Supplementary Fig. 3e**). Our data hence indicate that the binding

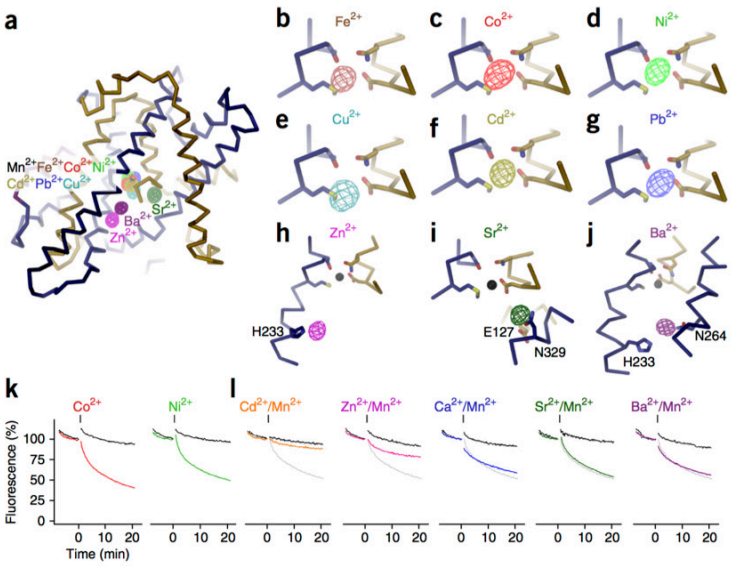

Figure 4 Transition-metal ion selectivity. (**a**) Location of bound ions in different complexes. (**b**–**j**) Close-up views of ion-binding sites with anomalous difference densities (ρ_{ano}) superimposed. (**b**) Fe^{2+} complex (ρ_{ano} calculated at 5 Å and contoured at 6.7σ). (**c**) Co^{2+} complex (5 Å, 7σ). (**d**) Ni^{2+} complex (5 Å, 6.5σ). (**e**) Cu^{2+} complex (6.5 Å, 6σ). (**f**) Cd^{2+} complex (4.5 Å, 10σ). (**g**) Pb^{2+} complex (5 Å, 18σ). (**h**) Zn^{2+} complex (5.5 Å, 7σ). (**i**) Sr^{2+} complex (5 Å, 7.5σ). (**j**) Ba^{2+} complex (5 Å, 9σ). In panels **h**–**j**, the position of Mn^{2+} is indicated by a gray sphere. (**k**) ScaDMT-mediated transport of Co^{2+} and Ni^{2+} into proteoliposomes. Graphs show time-dependent quenching of the fluorophore calcein, that is trapped inside the vesicle, upon addition of 300 μM of the respective ions to the external medium. Traces from liposomes devoid of protein are shown in black. (**l**) ScaDMT-mediated transport of Mn^{2+} into proteoliposomes in the presence of other divalent cations. Graphs show time-dependent quenching of the fluorophore calcein upon addition of 100 μM of Mn^{2+} and either 100 μM Cd^{2+} or 1 mM Zn^{2+}, Ca^{2+}, Sr^{2+} or Ba^{2+} to the external medium. Transport of 100 μM Mn^{2+} is shown in gray for comparison, and traces from liposomes devoid of protein are shown in black.

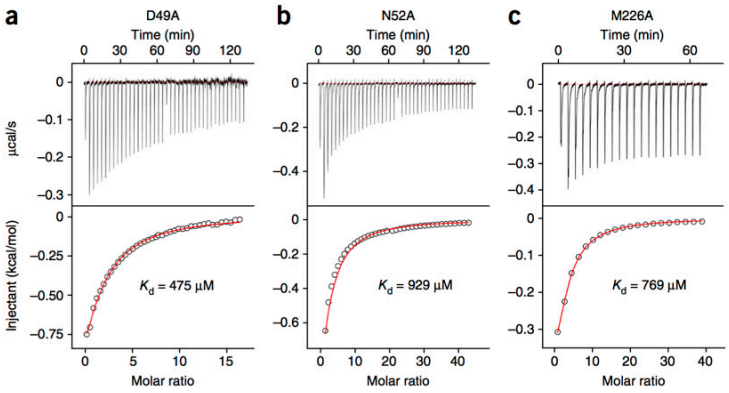

Figure 5 Cd^{2+} binding to ScaDMT binding-site mutants. (**a**–**c**) Cd^{2+} binding to the ScaDMT mutants D49A (**a**), N52A (**b**) and M226A (**c**), as determined by ITC. Top graphs, heat liberated upon injection of Cd^{2+} to the experimental chamber containing the respective protein. Bottom graphs, fit of the integrated and corrected heat to a binding isotherm (red line). The exponent *n* was constrained between 0.9 and 1.1.

of transition-metal ions to a conserved site in the center of the membrane is crucial for ion transport by SLC11 proteins.

Functional investigation of binding-site mutants

To probe the functional relevance of the observed interactions, we studied the effects of mutations of ion-coordinating residues on ScaDMT and human DMT1. Toward this end, we constructed the mutants D49A, N52A and M226A in ScaDMT, to remove residues involved in binding metal ions. After purification and reconstitution, all mutants showed reduced transport activity compared to that of wild-type ScaDMT; this demonstrates that the mutants retained the ability to facilitate transition-metal ion transport at high substrate gradients (**Supplementary Fig. 6**). However, using ITC, we found that the Cd^{2+} binding affinities of the three mutants were decreased by more than an order of magnitude (K_d of 475 ± 38 µM for D49A, 769 ± 27 µM for M226A and 929 ± 151 µM for N52A), as expected for the removal of a coordinating residue (**Fig. 5**). Because the mutation of a single site has a dramatic effect on the binding properties of ScaDMT, we next investigated whether equivalent mutations would show a similar effect on human DMT1. We thus studied DMT1-mediated transport of Cd^{2+} by two-electrode voltage-clamp electrophysiology. We expressed wild type and the mutants D86A, N89A and M265A in *Xenopus laevis* oocytes and recorded the dose-dependent steady-state transport currents with a protocol that was previously used to characterize ion transport by the protein[7]. Whereas the wild-type protein showed robust currents due to Cd^{2+}/H^+ cotransport that saturated with a K_m of 0.3 µM, the K_m of the mutant N89A was shifted by a factor of 19 toward higher concentrations (i.e., to a K_m of 5.6 µM; **Fig. 6a–c**). We observed no Cd^{2+} currents in the mutants D86A and M265A, even at a Cd^{2+} concentration of 1 mM and despite the strong expression of the protein (**Fig. 6d–g** and **Supplementary Data Set 1**). The results thus underline that the same set of residues coordinates divalent transition-metal ions in bacterial and human SLC11 family members.

DISCUSSION

The ScaDMT structure defines the common architecture of the SLC11 (NRAMP) family. These proteins share a conserved molecular scaffold that has previously been observed in different membrane transporters of unrelated sequence. The fold, which is characterized by a topological relationship of protein domains that are oppositely oriented within the membrane, allows for the recognition of substrates in the unwound parts of two symmetry-related helices in the center of the bilayer. In SLC11 transporters, this location contains residues that constitute a promiscuous transition metal ion–binding site. The ion is surrounded predominantly by harder ligands along with the soft sulfur of Met226. Because interacting residues are strongly conserved, it can be assumed that this binding mode is general for the family. The chemical composition of the ion-binding site reflects its preference for transition-metal ions. Mn^{2+} and Fe^{2+} have a tendency to bind to similar sites[31], but, although its thioether group can coordinate both metals, methionine is usually not an interacting residue. However, the

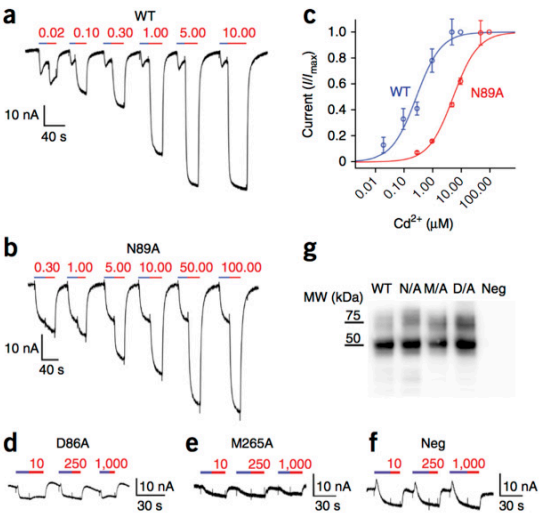

Figure 6 Functional properties of DMT1 binding-site mutants. (**a**,**b**) Concentration dependence of Cd^{2+} transport by human DMT1 expressed in *Xenopus laevis* oocytes. Currents were measured by two-electrode voltage-clamp electrophysiology. Representative current response of wild type (WT) (**a**) and the mutant N89A (**b**) after perfusion of oocytes with solutions containing the indicated amount of Cd^{2+} (in µM) at pH 5.5 (red bar) is shown. In each case, addition of Cd^{2+} was preceded by a pH step from 7.5 to 5.5 (blue bar). Voltage was clamped at −70 mV. (**c**) Dose-response curve of evoked currents in response to Cd^{2+}. Data are averages of either 4 (N52A) or 5 (wild type) independent experiments. Error bars, s.d. The solid lines show a fit to the Michaelis-Menten equation. (**d**–**f**) Representative current response of the binding-site mutants D86A (**d**) and M265A (**e**) and of noninjected oocytes (neg) (**f**) upon application of Cd^{2+}, as observed in 10 (D86A) and 7 (M265A and neg) independent measurements. Protocol is as in **a**. (**g**) Western blot of *Xenopus laevis* oocytes expressing human DMT1 (WT) and the DMT1 binding-site mutants N89A (N/A), M265A (M/A) and D86A (D/A). The positions of the molecular weight (MW) markers are indicated. Noninjected oocytes (neg) are shown as control. Uncropped western blot is shown in **Supplementary Data Set 1**. All oocytes were previously used for electrophysiology experiments.

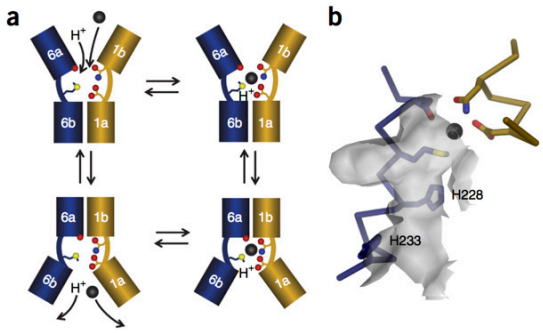

Figure 7 Transport mechanism. (**a**) Schematic drawing of the DMT transport cycle. Binding of a proton and a transition-metal ion to a site that is accessible from the outside is followed by a conformational change of the two halves of α-helices 1 and 6 around a hinge located at the ion-binding region. The rearrangement closes the extracellular pathway and opens an intracellular pathway to the ion-binding site. From this conformation, the two substrates are released into the cytoplasm, and the empty transporter returns to its outward-facing state. (**b**) Structure of the intracellular entry path to the ion-binding site. The bound Mn^{2+} (gray sphere) and the molecular surface around α-helix 6b are shown. Residues of the ion-binding site and two conserved histidines, which have been previously identified as potential H^+ acceptors during proton transport, are displayed as sticks.

fact that Fe^{2+}, Mn^{2+} and Cd^{2+} do frequently interact with the sulfur of cysteine[32,33] suggests that methionine may also be a suitable ligand for these ions. In contrast to transition-metal ions, methionine would be a poor ligand for Ca^{2+}. The binding site thus selects against alkaline earth metal ions, whereas it discriminates poorly between divalent transition-metal ions.

The importance of the observed interactions for binding and transport within the SLC11 family are underlined by mutagenesis, in which truncations of interacting side chains cause a marked decrease in the Cd^{2+} binding affinity of ScaDMT and in which equivalent mutations have a severe impact on Cd^{2+} transport in human DMT1. Because all mutations remove a side chain involved in metal-ion coordination, a similar phenotype can be expected for other transported ions. This would be unlike results from a study on a bacterial SLC30 transporter, in which a single conservative point mutation affected transport of Cd^{2+} but not Zn^{2+} (ref. 34). The binding-site aspartate and asparagine are part of a conserved DPGN motif located in the unwound part of α-helix 1 that was previously identified as a signature for the family[35] and whose mutations cause severe impairment of transport in different family members[36,37]. A similar phenotype was also previously observed for mutations of related residues in α-helix 6 (refs. 36,38).

In ScaDMT, the broad selectivity for transition-metal ions is emphasized by the strong correlation between binding and transport of Mn^{2+}, Fe^{2+}, Co^{2+} and Ni^{2+}, which are neighbors in the periodic table of elements. The next-higher element Cu^{2+} still binds to the same location, although with a slightly shifted position, whereas Zn^{2+} no longer occupies the same site. Our transport assay indicates that Zn^{2+} may act as either an inhibitor or a substrate of ScaDMT. In the latter case, Zn^{2+} would be the only instance that we found of transport being detected for an ion bound to a different region in the protein. Our data also illustrate the discrimination against the alkaline earth metal ions Ca^{2+}, Sr^{2+} and Ba^{2+}, which are not transported by ScaDMT and do not occupy the consensus site. The ion preference of ScaDMT correlates with the properties of DMT1 and other family members, in which Mn^{2+}, Fe^{2+}, Co^{2+} and Cd^{2+} have been shown to be efficiently transported, whereas Ni^{2+}, Cu^{2+} and Zn^{2+} are weaker substrates[5]. As in ScaDMT, alkaline earth metal ions are not transported by DMT1 (ref. 10); this illustrates how Fe^{2+} is selectively absorbed from the duodenum despite the presence of Ca^{2+}, which is several orders of magnitude more abundant[12]. The binding of Cd^{2+} and Pb^{2+} suggests a possible uptake mechanism for these toxic heavy metals[14].

The structure also reveals the location of residues whose mutation in DMT1 causes diseases in humans and rodents (**Supplementary Fig. 7**). The mutation of a conserved glycine residue at the extracellular side of α-helix 4 to arginine leads to severe anemia in mice and rats and has also been shown to be associated with an increased Ca^{2+} permeability of the protein[39]. Four mutations identified in human patients with anemia[40] are scattered in different parts of the protein. Remarkably all mutations affect residues in transmembrane helices remote from the ion-binding region, with all but one of them being conserved in ScaDMT. Because some residues contribute to packing interactions, compromised folding and function of these mutants appear plausible[41].

In the crystal, ScaDMT adopts an inward-facing conformation. Although a single structure provides only a snapshot of the transport cycle, the close structural relationship to the amino acid transporter LeuT and to other proteins sharing a similar protein fold, for which different conformations have been characterized[29,42], allows for the description of a potential outward-facing conformation (**Fig. 7a**). In such a state, the independent movement of both halves of α-helices 1 and 6 around a hinge located in the substrate-binding region would close the intracellular access path and open an extracellular access path to the site, without disrupting the geometry of interacting residues. In this conformation, the same residues probably contribute to the binding of ions from the extracellular environment. However, owing to local structural changes, the affinity in the outward-facing state, which is relevant for scavenging the ion in a physiological context, may be increased, as suggested by the low K_m of transport measured for DMT1.

In DMT1, metal-ion transport is coupled to the movement of protons in the same direction, but the coupling may not be as strict as in other secondary active transporters because uncoupled flows of either of the two substrates have been observed[11]. Although how protons are transported in DMT1 is still unclear, it is noteworthy that two histidines close to the substrate-binding site, which were previously identified to contribute to the pH dependence of transport in pro- and eukaryotic family members[11,30,36], are also conserved in ScaDMT (**Fig. 7b** and **Supplementary Fig. 1**). The presence of these residues suggests that the prokaryotic transporter may share a similar coupling mechanism.

Our study has revealed the structural basis of selectivity in a protein family that has an important role in the transmembrane transport of transition-metal ions in all kingdoms of life. It has thus prepared the ground for detailed investigations of transport mechanisms, which are still poorly understood.

METHODS

Methods and any associated references are available in the online version of the paper.

Accession codes. Coordinates and structure factors for the $ScaDMT^{tru}$–nanobody complex and the $ScaDMT^{tru}$–nanobody Mn^{2+} complex have been deposited in the Protein Data Bank under accession codes 4WGV and 4WGW, respectively.

Note: Any Supplementary Information and Source Data files are available in the online version of the paper.

ACKNOWLEDGMENTS

This research was supported by the Swiss National Science Foundation through the National Centre of Competence in Research TransCure. We thank the staff of the X06SA beamline for support during data collection, B. Blattman and C. Stutz-Ducommun of the Protein Crystallization Center at the University of Zurich for support with crystallization, B. Dreier for help with MALS experiments, the Center for Microscopy and Image Analysis at the University of Zurich for help with freeze-fracture EM, M. Hediger (University of Bern) for providing the cDNA of human DMT1 and E. Beke (Vrije Universiteit Brussel) for help with nanobody selection. All members of the Dutzler laboratory are acknowledged for help in all stages of the project. E.R.G. acknowledges a long-term postdoctoral fellowship from the Human Frontier Science Program (LT-00899/2008). I.A.E. is affiliated with the Biomolecular Structure and Mechanism PhD program of the University of Zurich (UZH) and the Swiss Federal Institute of Technology (ETH) Zurich. Data collection was performed at the X06SA beamline at the Swiss Light Source of the Paul Scherrer Institute.

AUTHOR CONTRIBUTIONS

I.A.E. carried out all experiments except for the initial nanobody selection. E.R.G. supported the high-throughput expression screening and transport assays and initiated nanobody selection by phage display. E.P. performed immunization, cloned and expressed nanobodies and performed the initial selections. J.S. supervised nanobody production. R.D. assisted I.A.E. in structure determination. I.A.E. and R.D. jointly planned the experiments, analyzed the data and wrote the manuscript.

COMPETING FINANCIAL INTERESTS

The authors declare no competing financial interests.

1. Nevo, Y. & Nelson, N. The NRAMP family of metal-ion transporters. *Biochim. Biophys. Acta* **1763**, 609–620 (2006).
2. Montalbetti, N., Simonin, A., Kovacs, G. & Hediger, M.A. Mammalian iron transporters: families SLC11 and SLC40. *Mol. Aspects Med.* **34**, 270–287 (2013).
3. Cellier, M.F., Bergevin, I., Boyer, E. & Richer, E. Polyphyletic origins of bacterial Nramp transporters. *Trends Genet.* **17**, 365–370 (2001).
4. Vidal, S.M., Malo, D., Vogan, K., Skamene, E. & Gros, P. Natural resistance to infection with intracellular parasites: isolation of a candidate for Bcg. *Cell* **73**, 469–485 (1993).
5. Illing, A.C., Shawki, A., Cunningham, C.L. & Mackenzie, B. Substrate profile and metal-ion selectivity of human divalent metal-ion transporter-1. *J. Biol. Chem.* **287**, 30485–30496 (2012).
6. Vidal, S.M., Pinner, E., Lepage, P., Gauthier, S. & Gros, P. Natural resistance to intracellular infections: Nramp1 encodes a membrane phosphoglycoprotein absent in macrophages from susceptible (Nramp1 D169) mouse strains. *J. Immunol.* **157**, 3559–3568 (1996).
7. Gunshin, H. *et al.* Cloning and characterization of a mammalian proton-coupled metal-ion transporter. *Nature* **388**, 482–488 (1997).
8. Beaumont, C. *et al.* Two new human DMT1 gene mutations in a patient with microcytic anemia, low ferritinemia, and liver iron overload. *Blood* **107**, 4168–4170 (2006).
9. Johnson, E.E. & Wessling-Resnick, M. Iron metabolism and the innate immune response to infection. *Microbes Infect.* **14**, 207–216 (2012).
10. Shawki, A., Knight, P.B., Maliken, B.D., Niespodzany, E.J. & Mackenzie, B.H. H^+-coupled divalent metal-ion transporter-1: functional properties, physiological roles and therapeutics. *Curr. Top. Membr.* **70**, 169–214 (2012).
11. Mackenzie, B., Ujwal, M.L., Chang, M.H., Romero, M.F. & Hediger, M.A. Divalent metal-ion transporter DMT1 mediates both H^+ -coupled Fe^{2+} transport and uncoupled fluxes. *Pflugers Arch.* **451**, 544–558 (2006).
12. Shawki, A. & Mackenzie, B. Interaction of calcium with the human divalent metal-ion transporter-1. *Biochem. Biophys. Res. Commun.* **393**, 471–475 (2010).
13. Au, C., Benedetto, A. & Aschner, M. Manganese transport in eukaryotes: the role of DMT1. *Neurotoxicology* **29**, 569–576 (2008).
14. Bressler, J.P., Olivi, L., Cheong, J.H., Kim, Y. & Bannona, D. Divalent metal transporter 1 in lead and cadmium transport. *Ann. NY Acad. Sci.* **1012**, 142–152 (2004).
15. Guerinot, M.L. Microbial iron transport. *Annu. Rev. Microbiol.* **48**, 743–772 (1994).
16. Makui, H. *et al.* Identification of the *Escherichia coli* K-12 Nramp orthologue (MntH) as a selective divalent metal ion transporter. *Mol. Microbiol.* **35**, 1065–1078 (2000).
17. Czachorowski, M., Lam-Yuk-Tseung, S., Cellier, M. & Gros, P. Transmembrane topology of the mammalian Slc11a2 iron transporter. *Biochemistry* **48**, 8422–8434 (2009).
18. Yamashita, A., Singh, S.K., Kawate, T., Jin, Y. & Gouaux, E. Crystal structure of a bacterial homologue of Na^+/Cl^--dependent neurotransmitter transporters. *Nature* **437**, 215–223 (2005).
19. Cellier, M.F. Nramp: from sequence to structure and mechanism of divalent metal import. *Curr. Top. Membr.* **69**, 249–293 (2012).
20. Cellier, M.F. Nutritional immunity: homology modeling of Nramp metal import. *Adv. Exp. Med. Biol.* **946**, 335–351 (2012).
21. Geertsma, E.R. & Dutzler, R. A versatile and efficient high-throughput cloning tool for structural biology. *Biochemistry* **50**, 3272–3278 (2011).
22. Pardon, E. *et al.* A general protocol for the generation of Nanobodies for structural biology. *Nat. Protoc.* **9**, 674–693 (2014).
23. Schulze, S., Koster, S., Geldmacher, U., Terwisscha van Scheltinga, A.C. & Kuhlbrandt, W. Structural basis of Na^+-independent and cooperative substrate/product antiport in CaiT. *Nature* **467**, 233–236 (2010).
24. Ressl, S., Terwisscha van Scheltinga, A.C., Vonrhein, C., Ott, V. & Ziegler, C. Molecular basis of transport and regulation in the Na^+/betaine symporter BetP. *Nature* **458**, 47–52 (2009).
25. Weyand, S. *et al.* Structure and molecular mechanism of a nucleobase-cation-symport-1 family transporter. *Science* **322**, 709–713 (2008).
26. Faham, S. *et al.* The crystal structure of a sodium galactose transporter reveals mechanistic insights into Na^+/sugar symport. *Science* **321**, 810–814 (2008).
27. Gao, X. *et al.* Structure and mechanism of an amino acid antiporter. *Science* **324**, 1565–1568 (2009).
28. Fang, Y. *et al.* Structure of a prokaryotic virtual proton pump at 3.2 Å resolution. *Nature* **460**, 1040–1043 (2009).
29. Krishnamurthy, H. & Gouaux, E. X-ray structures of LeuT in substrate-free outward-open and apo inward-open states. *Nature* **481**, 469–474 (2012).
30. Lam-Yuk-Tseung, S., Govoni, G., Forbes, J. & Gros, P. Iron transport by Nramp2/DMT1: pH regulation of transport by 2 histidines in transmembrane domain 6. *Blood* **101**, 3699–3707 (2003).
31. Edward, R.A., Whittaker, M.M., Whittaker, J.W., Jameson, G.B. & Baker, E.N. Distinct metal environment in Fe-substituted manganese superoxide dismutatse provides a structural basis of metal specificity. *J. Am. Chem. Soc.* **120**, 9684–9685 (1998).
32. Qi, W. & Cowan, J.A. Structural, mechanistic and coordination chemistry of relevance to the biosynthesis of iron-sulfur and related iron cofactors. *Coord. Chem. Rev.* **255**, 688–699 (2011).
33. Freisinger, E. & Vasak, M. Cadmium in metallothioneins. *Met. Ions. Life Sci.* **11**, 339–371 (2013).
34. Hoch, E. *et al.* Histidine pairing at the metal transport site of mammalian ZnT transporters controls $Zn2^+$ over $Cd2^+$ selectivity. *Proc. Natl. Acad. Sci. USA* **109**, 7202–7207 (2012).
35. Cellier, M. *et al.* Nramp defines a family of membrane proteins. *Proc. Natl. Acad. Sci. USA* **92**, 10089–10093 (1995).
36. Courville, P. *et al.* Solute carrier 11 cation symport requires distinct residues in transmembrane helices 1 and 6. *J. Biol. Chem.* **283**, 9651–9658 (2008).
37. Haemig, H.A. & Brooker, R.J. Importance of conserved acidic residues in mntH, the Nramp homolog of *Escherichia coli*. *J. Membr. Biol.* **201**, 97–107 (2004).
38. Haemig, H.A., Moen, P.J. & Brooker, R.J. Evidence that highly conserved residues of transmembrane segment 6 of *Escherichia coli* MntH are important for transport activity. *Biochemistry* **49**, 4662–4671 (2010).
39. Xu, H., Jin, J., DeFelice, L.J., Andrews, N.C. & Clapham, D.E. A spontaneous, recurrent mutation in divalent metal transporter-1 exposes a calcium entry pathway. *PLoS Biol.* **2**, E50 (2004).
40. Iolascon, A. & De Falco, L. Mutations in the gene encoding DMT1: clinical presentation and treatment. *Semin. Hematol.* **46**, 358–370 (2009).
41. Courville, P., Chaloupka, R. & Cellier, M.F. Recent progress in structure-function analyses of Nramp proton-dependent metal-ion transporters. *Biochem. Cell Biol.* **84**, 960–978 (2006).
42. Forrest, L.R. *et al.* Mechanism for alternating access in neurotransmitter transporters. *Proc. Natl. Acad. Sci. USA* **105**, 10338–10343 (2008).

ONLINE METHODS

Cloning and expression screening of prokaryotic DMT homologs. For expression screening, the genes of 105 prokaryotic SLC11 transporters were amplified from their respective genomic DNA and cloned into the arabinose-inducible expression vectors pBXNH3, pBXC3H and pBXC3GH with fragment-exchange (FX) cloning[21]. Primers were designed in an automated fashion with a Python script available online (http://www.fxcloning.org/). *Escherichia coli* MC1061 (ref. 43) was used as a cloning and expression strain. Expression and extraction properties were initially investigated in small-scale cultures. For that purpose, cells containing the respective constructs were grown in 24-well plates in terrific broth (TB) and induced with three different arabinose concentrations. Proteins with a periplasmic C terminus were detected by western blot with an anti-polyhistidine antibody (Roche 11965985001, at 1:1,000 dilution). Validation of the antibody can be found on the manufacturer's website. Proteins with a cytoplasmic C terminus were expressed as GFP fusion constructs and detected by the fluorescence of GFP as measured in whole cells and by in-gel fluorescence in SDS-PAGE. Stability and monodispersity of GFP constructs was monitored by fluorescence size-exclusion chromatography (FSEC) before purification[44]. For constructs with a periplasmic C terminus, these properties were assessed by SEC after scale-up and purification. As a result of these experiments, ScaDMT (from *S. capitis* DSM 20326) was identified as a promising candidate for structural studies. For large-scale expression and purification, ScaDMT and all modified constructs were fused to a C-terminal His_{10} tag separated from the protein by a human rhinovirus (HRV) 3C protease–cleavage site. Truncations and mutants of ScaDMT were prepared by PCR and the FX cloning method. For crystallization purposes, shortened constructs of ScaDMT were prepared by systematic truncation of both termini by increments of four residues and investigated by purification. In that way, $ScaDMT^{tru}$, lacking 41 amino acids at the N terminus was identified as the shortest well-behaved construct.

Protein expression and purification. The genes encoding ScaDMT and $ScaDMT^{tru}$ were cloned into the pBXC3H vector, where they were fused to a C-terminal His_{10} tag separated by a HRV 3C protease–cleavage site. Cells were grown by fermentation of 9- to 18-l cultures in TB medium to an OD_{600} of 2.5. Protein expression was induced by addition of 0.005% (w/v) arabinose at 25 °C. The temperature was decreased to 18 °C for overnight expression. All of the following steps were carried out at 4 °C. Cells were harvested by centrifugation and lysed in buffer A (50 mM potassium phosphate, pH 7.5, and 150 mM NaCl) with a custom-made cell disruptor. The lysate was cleared by low-spin centrifugation. Membranes were harvested by ultracentrifugation. For membrane-protein extraction, vesicles were suspended in buffer A containing 10% (w/v) glycerol and 1–2% (w/v) DM (Anatrace). After centrifugation, the protein was purified by immobilized metal affinity chromatography (IMAC). For cleavage of the His_{10} tag, the sample was incubated with HRV 3C protease (at a molar ratio of 5:1) for 2 h during dialysis into buffer B (20 mM HEPES, pH 7.5, 150 mM NaCl, 5% (w/v) glycerol, and 0.25% (w/v) DM). Histidine-tagged HRV 3C protease was subsequently removed by binding to Ni-NTA resin. The cleaved protein was concentrated and subjected to size-exclusion chromatography (SEC) on a Superdex S200 column (GE Healthcare) equilibrated in 10 mM HEPES, pH 7.5, 150 mM NaCl, and 0.25% (w/v) DM. The peak fractions were pooled and immediately used for experiments. Protein complexes were prepared by incubation of the SEC-purified and concentrated transporter with the SEC-purified and concentrated nanobody (supplemented with 0.25% (w/v) DM) at a molar ratio of 1:1.3 for 5 min. The complex was subjected to SEC (GE Healthcare). Protein–nanobody complexes were subsequently concentrated and used for crystallization. For preparation of crystals used for structure determination, DM was exchanged to *n*-nonyl-β-D-maltopyranoside (NM, 0.84% (w/v)) in SEC.

Generation of nanobodies. ScaDMT-specific nanobodies were generated essentially as previously described[22]. In brief, one llama (*Lama glama*) was immunized six times with 50 μg of detergent-solubilized ScaDMT (in 0.25% DM). 4 d after the final antigen boost, peripheral blood lymphocytes were extracted, and their RNA was purified and converted into cDNA via reverse-transcription PCR . The nanobody repertoire was cloned into the phage-display vector pMESy4 containing a C-terminal His_6 tag followed by the CaptureSelect C tag (Glu-Pro-Glu-Ala). 12 nanobody families that bound to ScaDMT or $ScaDMT^{tru}$ were identified in two rounds of biopanning. Targets were coated directly on a solid phase or immobilized via neutravidin capturing. Antigen-bound phages were recovered from antigen-coated wells without affecting phage infectivity by proteolysis with trypsin. After two rounds of selection, ELISAs were performed on periplasmic extracts of 48 individual colonies of each selection condition to screen for ScaDMT-specific nanobodies. Nb6616, which was crystallized in complex with $ScaDMT^{tru}$ for structure determination, was selected by solid phase–coated $ScaDMT^{tru}$ and neutravidin-captured biotinylated full-length ScaDMT.

Nanobody expression and purification. The 16 nanobodies identified in the initial selection were recloned into an arabinose-inducible expression vector containing an N-terminal pelB leader sequence, a His_{10} tag, a maltose-binding protein (MBP) tag and a HRV 3C protease site. *E. coli* MC1061 cells were grown in a fermenter in TB medium at 37 °C until an OD_{600} of ~3–4 was reached. Expression was induced by addition of 0.02% (w/v) arabinose, and cells were incubated for 6 h at 37 °C. Cells were harvested by centrifugation and lysed with a custom-made cell disruptor. All of the following steps were carried out at 4 °C. The lysate was cleared by centrifugation at 210,000*g*. IMAC was performed as described for the transporter, except that no detergent was used during purification. Peak fractions were mixed with HRV 3C protease at an 8:1 molar ratio and dialyzed against dialysis buffer overnight. Protease and MBP were removed by binding to Ni-NTA. The cleaved nanobody was concentrated by centrifugation (Millipore, MWCO 3 kDa) and subjected to SEC. Peak fractions were pooled and used for experiments.

Expression of selenomethionine-labeled protein. For preparation of selenomethionine-labeled protein, an overnight culture of $ScaDMT^{tru}$ grown in TB medium was diluted 1:100 into 30 l M9 medium supplemented with trace elements, Kao and Michayluk Vitamin solution (Sigma), 0.75% glycerol and 100 mg/l ampicillin. Cells were grown in shaking culture at a starting temperature of 37 °C. The temperature was gradually decreased over 5 h to 24 °C until an OD_{600} of 0.6 was reached. Amino acids L-lysine, L-threonine, and L-phenylalanine (each at a concentration of 125 mg/l) and L-leucine, L-isoleucine and L-valine (each at a concentration of 62.5 mg/l) were added to the culture to inhibit the methionine synthesis pathway[45]. Depletion of free L-methionine was performed for 1 h, and this was followed by addition of 50 mg/l L-selenomethionine. 1 h later, expression was induced by addition of 0.004% (w/v) arabinose. For overnight expression, the temperature was further decreased to 18 °C. Cells were harvested by centrifugation and lysed by sonication. Extraction was started from cleared lysate by addition of 1.5% DM (Anatrace). Purification and crystallization of the $ScaDMT^{tru}$–NB complex was carried out as described in Online Methods.

Crystallization. ScaDMT (5–10 mg/ml) was crystallized in sitting drops at 4 °C. The best crystals diffracting to 6.5 Å were obtained for protein purified in DM in reservoir solution containing 90 mM MES, pH 6.0, 90 mM NaCl, 200 mM $CaCl_2$ and 26–30% PEG 400 (v/v). Crystals of the $ScaDMT^{tru}$–nanobody complex (in NM) used for structure determination grew at 4 °C from a reservoir solution containing 50 mM HEPES, pH 7.4, 200 mM $CaCl_2$, and 22–26% PEG 400 (v/v). For cryoprotection, the PEG concentration was increased stepwise to 36%, and crystals were flash frozen in liquid propane. For generation of ion complexes, crystals were soaked for 1 min in freshly prepared solutions in which Ca^{2+} was replaced stepwise by the respective cation.

Structure determination. All data sets were collected on frozen crystals on the X06SA beamline at the Swiss Light Source of the Paul Scherrer Institut on a PILATUS 6M detector (Dectris; **Table 1** and **Supplementary Table 1**). The data were indexed, integrated and scaled with XDS[46] and further processed with CCP4 programs[47]. The structure of the $ScaDMT^{tru}$–nanobody complex was determined by the SAD method with data collected from crystals containing a selenomethionine-derivatized transporter. The selenium sites were identified with SHELX C and D[48,49]. Selenium sites were refined in SHARP[50], and phases were improved by solvent flattening and extended to 3.1 Å by two-fold NCS symmetry averaging with the program DM[51]. The model was built in O[52] and COOT[53] and initially refined, maintaining strict two-fold NCS constraints in CNS[54]. In later stages, the strict constraints were loosened, and restrained individual *B* factors and TLS parameters were refined in PHENIX[55]. *R* and R_{free} were monitored throughout. R_{free} was calculated by selecting 5% of the reflection data that were omitted in refinement. The final model has R/R_{free} values of 25.0% and 28.5%, good geometry and no residues in disallowed regions of the Ramachandran plot (**Table 1**). Data of ion complexes were collected at appropriate wavelengths to maximize the anomalous scattering of the bound ions (**Table 1** and **Supplementary Table 1**). The structure of the

ScaDMT^{tru}– nanobody Mn^{2+} complex at 3.4 Å was refined in PHENIX as described for the ScaDMT^{tru}–NB complex. For all other ion complexes, the refined structure of the ScaDMT^{tru}–NB Mn^{2+} complex served as start model, and coordinates were subsequently improved by rigid-body refinement in PHENIX. The structure of ScaDMT at 6.5 Å was determined by molecular replacement with Phaser[56] and improved by rigid-body refinement in PHENIX (**Table 1**).

Preparation of proteoliposomes. Proteoliposomes containing ScaDMT were prepared as described in ref. 57. In brief, *E. coli* polar lipid extract (Avanti Polar Lipids) was mixed with L-α phosphatidylcholine (from egg yolk, Sigma) both dissolved in chloroform at a w/w ratio of 3:1. Lipids were dried in a rotary evaporator and subsequently resuspended and sonicated in buffer containing 20 mM HEPES, pH 7.5, and 100 mM KCl. Large unilamellar vesicles were formed by alternating freeze-thaw cycles followed by extrusion through a 400-nm polycarbonate filter (Avestin, LiposoFast-Basic). Liposomes were diluted to 4 mg/ml and destabilized by addition of Triton X-100. The protein sample was incubated with destabilized liposomes at a protein-to-lipid ratio of 1:40 (w/w). Detergent was removed by addition of Bio-Beads SM-2 (Bio-Rad). Proteoliposomes were harvested by centrifugation for 30 min at 236,000*g*, resuspended in buffer and stored in liquid nitrogen.

Freeze-fracture electron microscopy. Freeze-fracture EM was used to monitor the incorporation of the protein into liposomes. For that purpose, proteoliposomes were initially subjected to two freeze-thaw cycles and applied on a copper grid. The grid was subsequently sandwiched between two aluminum specimen carriers and frozen in liquid nitrogen with a high-pressure freezing system (Leica EM HPM100). Glycerol (final concentration 10% (w/v)) was added to the sample if necessary. Freeze fracturing and shadowing were performed on a Leica EM BAF060 at −150 °C under high vacuum. The samples were coated with a 2.5-nm carbon/platinum layer at an angle of 45° immediately after fracturing and were subsequently coated with 20 nm carbon at an angle of 90°. Replicas were imaged with a Philips CM100 transmission electron microscope equipped with a Gatan Orius CCD camera.

Fluorescence-based transport assay. For transport assays, proteoliposomes were mixed with buffer C containing 25 mM HEPES, pH 7.5, 200 mM KCl and either 250 µM calcein or fura-2 (Invitrogen), sonicated, subjected to three freeze-thaw cycles and finally extruded through a 400-nm polycarbonate filter (Avestin, LiposoFast-Basic). Subsequently proteoliposomes were harvested by centrifugation and washed by resuspension in ten volumes of assay buffer without fluorophore. In total, three wash steps were performed. Control liposomes without protein were prepared with the same procedure. The assay was started by dilution of the sample to 2 mg lipid/ml in 100 µl buffer C in a black 96-well plate. Uptake of Me^{2+} into liposomes was monitored by the change of the fluorescence signal in a fluorimeter (Tecan Infinite M1000, calcein, λ_{ex} = 492 nm/λ_{em} = 518 nm; fura-2, λ_{ex} = 335 nm/λ_{em} = 505 nm). After stabilization of the fluorescence signal, ions were added, and fluorescence was recorded every 15 s. After 20 min, Me^{2+} ions were equilibrated by addition of the ionophore calcimycin, which acts as a Me^{2+}/H^+ exchanger. Experiments with Fe^{2+}, Cu^{2+} and Pb^{2+} were incompatible with the described procedure.

Isothermal titration calorimetry. Proteins were purified in DM as described above and dialyzed overnight against buffer D (25 mM HEPES, pH 7.5, 150 mM NaCl and 0.25% (w/v) DM). ITC experiments were performed with a MicroCal ITC200 system (GE Healthcare) at 6 °C. The sample cell was filled with protein solution at a concentration between 110 and 180 µM. The solution used for titration was prepared by addition of Cd^{2+} to buffer D at a concentration of 4–25 mM. Cd^{2+} was added to the protein by sequential injections of 2-µl aliquots followed by 200 s of equilibration after each injection. For the determination of the background, the same experiment was carried out, except that the protein solution was replaced by buffer D. For analysis, the heat released by each injection was integrated, and the background was subtracted with NITPIC[58]. The data were fit to the Wiseman isotherm with the Origin ITC analysis package. The exponent *n* was constrained between 0.9 and 1.1. ITC experiments were performed at least twice for each protein, with similar results.

Multiangle light scattering. MALS experiments were carried out at 20 °C on an HPLC system (Agilent 1100) connected to an Eclipse 3 system equipped with a miniDAWN TREOS MALS detector and an Optilab T-rEX refractometer (Wyatt Technology). 50 µg of purified protein (at 1 mg/ml) was injected onto a Superdex S200 column (GE Healthcare) equilibrated in 10 mM HEPES, pH 7.5, 150 mM NaCl, and 0.25% (w/v) DM. Molecular weights and s.d. were determined with the Astra package (Astra 6.0, Wyatt Technology).

Two-electrode voltage-clamp experiments. The genes encoding human DMT1 (isoform 3, splice variant 1A–IRE) and the mutants D86A, N89A and M265A (numbering of residues according to the reference sequence isoform 1) were cloned into a pTLN vector[59]. The plasmid was linearized with MluI and was used to prepare capped complementary mRNA with the mMessage mMachine kit (Ambion). mRNA was purified with the RNeasy kit (Qiagen) and injected into defolliculated *Xenopus laevis* oocytes (50 ng/oocyte). Oocytes were incubated at 16 °C for 2–4 d before two-electrode voltage-clamp experiments were performed. Currents were recorded at −70 mV on an OC-725B oocyte clamp (Warner Instrument Corp). Data were sampled at 2 kHz and filtered at 50 Hz. During experiments, oocytes were perfused with high-pH solution containing 100 mM NaCl, 1 mM KCl, 0.6 mM $CaCl_2$, 1 mM $MgCl_2$, and 10 mM HEPES, pH 7.4. Measurements of Cd^{2+}-induced transport currents were preceded by a change into low-pH solution (in which HEPES was replaced by 10 mM MES, pH 5.5) and then a change into low-pH solution containing the desired concentration of $CdCl_2$ (0.02–1,000 µM). Expression of DMT1 was confirmed by western blot with a mouse anti-human SLC11A2 antibody (Sigma WH0004891M1, at 1:5,000 dilution) and a goat anti-mouse antibody coupled to horseradish peroxidase (Dianova 115-035-146, at 1:10,000 dilution) for detection. Validation of antibodies used in the assay can be found on the respective manufacturers' websites.

***Xenopus laevis* oocyte membrane preparation for western blot analysis.** After two-electrode voltage-clamp recording, oocytes were homogenized in Barth's solution containing protease inhibitors (Complete EDTA-free, Roche). Cell debris was removed by centrifugation at 500*g*. Membranes were subsequently harvested by centrifugation at 10,000*g* at 4 °C and resuspended in buffer containing 10 mM HEPES, pH 7.5 and 100 mM NaCl. For extraction, 2% (w/v) *n*-dodecyl-β-D-maltopyranoside (Anatrace) was added, and the samples were incubated on ice for 1 h. Insoluble material was pelleted by centrifugation at 500*g*, and the supernatant was used for western blot analysis.

43. Casadaban, M.J. & Cohen, S.N. Analysis of gene control signals by DNA fusion and cloning in *Escherichia coli*. *J. Mol. Biol.* **138**, 179–207 (1980).
44. Kawate, T. & Gouaux, E. Fluorescence-detection size-exclusion chromatography for precrystallization screening of integral membrane proteins. *Structure* **14**, 673–681 2006).
45. Van Duyne, G.D., Standaert, R.F., Karplus, P.A., Schreiber, S.L. & Clardy, J. Atomic structures of the human immunophilin FKBP-12 complexes with FK506 and rapamycin. *J. Mol. Biol.* **229**, 105–124 (1993).
46. Kabsch, W. Automatic processing of rotation diffraction data from crystals of initially unknown symmetry and cell constants. *J. Appl. Crystallogr.* **26**, 795–800 (1993).
47. Collaborative Computational Project, Number 4. The CCP4 Suite: programs for X-ray crystallography. *Acta Crystallogr. D Biol. Crystallogr.* **50**, 760–763 (1994).
48. Schneider, T.R. & Sheldrick, G.M. Substructure solution with SHELXD. *Acta Crystallogr. D Biol. Crystallogr.* **58**, 1772–1779 (2002).
49. Pape, T. & Schneider, T.R. HKL2MAP: a graphical user interface for phasing with SHELX programs. *J. Appl. Crystallogr.* **37**, 843–844 (2004).
50. De La Fortelle, E. & Bricogne, G. Maximum-likelihood heavy-atom parameter refinement for multiple isomorphous replacement and multiwavelength anomalous diffraction methods. *Methods Enzymol.* **276**, 472–494 (1997).
51. Cowtan, K. dm: an automated procedure for phase improvement by density modification. *Joint CCP4 and ESF-EACBM Newslett. Protein Crystallogr.* **31**, 34–38 (1994).
52. Jones, T.A., Zou, J.Y., Cowan, S.W. & Kjeldgaard, M. Improved methods for building protein models in electron density maps and the location of errors in these models. *Acta Crystallogr. A* **47**, 110–119 (1991).
53. Emsley, P. & Cowtan, K. Coot: model-building tools for molecular graphics. *Acta Crystallogr. D Biol. Crystallogr.* **60**, 2126–2132 (2004).
54. Brünger, A.T. *et al.* Crystallography & NMR system: a new software suite for macromolecular structure determination. *Acta Crystallogr. D Biol. Crystallogr.* **54**, 905–921 (1998).
55. Adams, P.D. *et al.* PHENIX: building new software for automated crystallographic structure determination. *Acta Crystallogr. D Biol. Crystallogr.* **58**, 1948–1954 (2002).
56. McCoy, A.J. *et al.* Phaser crystallographic software. *J. Appl. Crystallogr.* **40**, 658–674 (2007).
57. Geertsma, E.R., Nik Mahmood, N.A., Schuurman-Wolters, G.K. & Poolman, B. Membrane reconstitution of ABC transporters and assays of translocator function. *Nat. Protoc.* **3**, 256–266 (2008).
58. Keller, S. *et al.* High-precision isothermal titration calorimetry with automated peak-shape analysis. *Anal. Chem.* **84**, 5066–5073 (2012).
59. Lorenz, C., Pusch, M. & Jentsch, T.J. Heteromultimeric CLC chloride channels with novel properties. *Proc. Natl. Acad. Sci. USA* **93**, 13362–13366 (1996).

doi:10.1038/nsmb.2904

2.7.1. Supplementary information

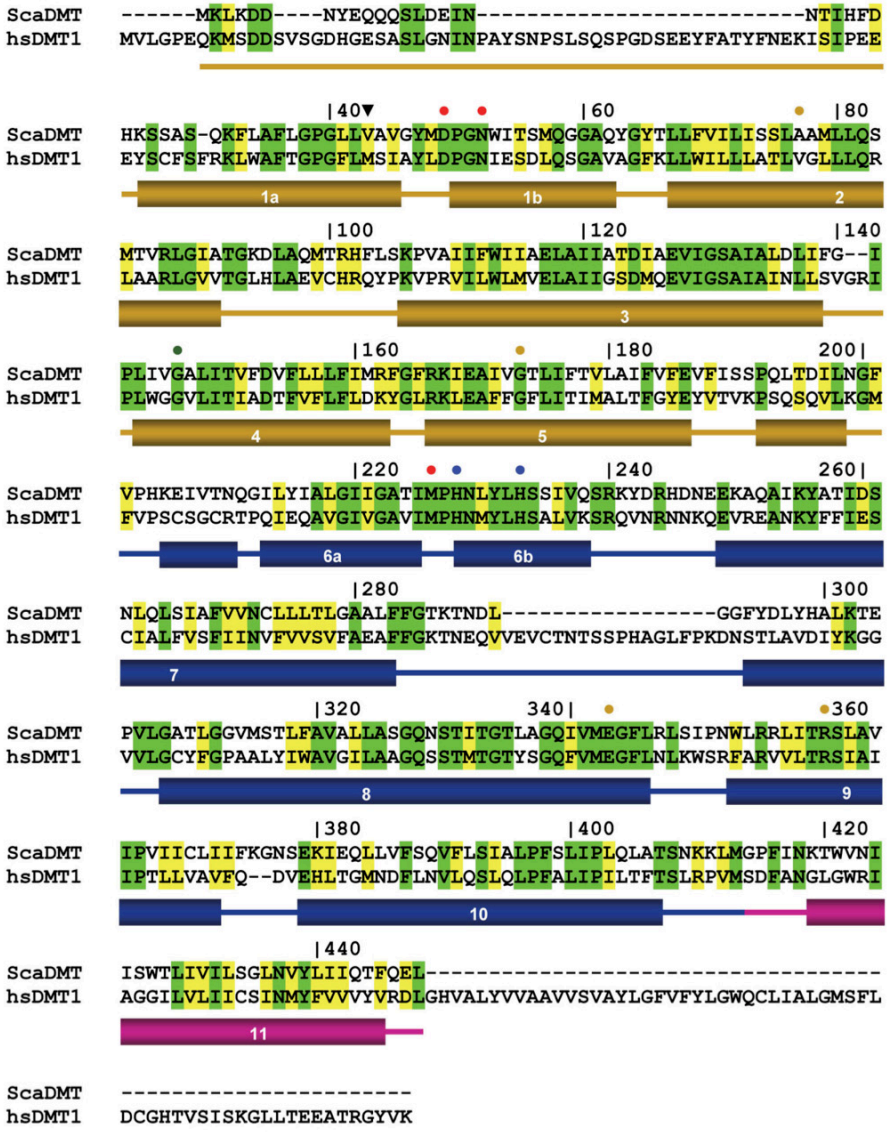

Supplementary Figure 1

Sequence alignment.

Sequences of ScaDMT and human DMT1 (isoform 3) were aligned with ClustalW. Identical residues are highlighted in green and homologous residues in yellow. Numbering corresponds to ScaDMT. Secondary structure elements are shown below. Labels indicate: (black triangle) Start of the truncated construct ScaDMT^{tru}, (red circle) residues of the transition metal binding site, (blue circle) residues involved in pH dependence and H^+ transport of DMT1, (green circle) DMT1 disease mutation in the Belgrade rat and the mk/mk mouse and (brown circle) DMT1 disease mutations in human.

Nature Structural and Molecular Biology: doi:10.1038/nsmb.2904

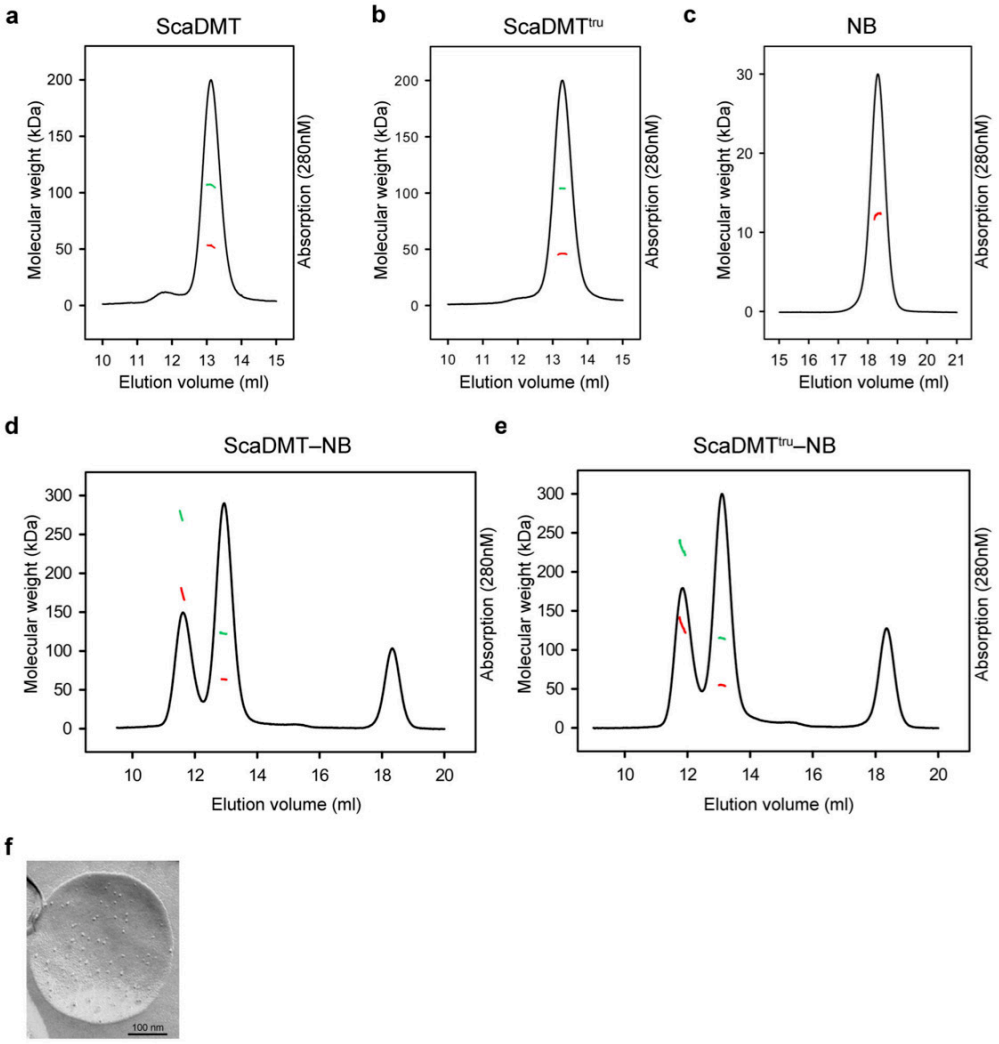

Supplementary Figure 2

Multiangle light-scattering and freeze-fracture EM.

Gel filtration and light scattering results for different protein constructs in the detergent DM. Continuous black traces correspond to the UV_{280} elution profiles. The respective molecular weight of the protein-detergent complex obtained from light scattering is shown at its corresponding position on the chromatogram in green, the molecular weight of the protein component alone in red. Panels show (**a**) ScaDMT, (**b**) ScaDMT^{tru}, (**c**) nanobody, (**d**) ScaDMT–nanobody complex, (**e**) ScaDMT^{tru}–nanobody complex. The first peak in panels (**c**) and (**d**) corresponds to a homo-dimer of the respective transporter-nanobody complex. (**f**) Freeze-fracture electron micrograph of proteoliposomes containing ScaDMT. The transporter was reconstituted at a protein to lipid ratio of 1:40 (w/w).

Nature Structural and Molecular Biology: doi:10.1038/nsmb.2904

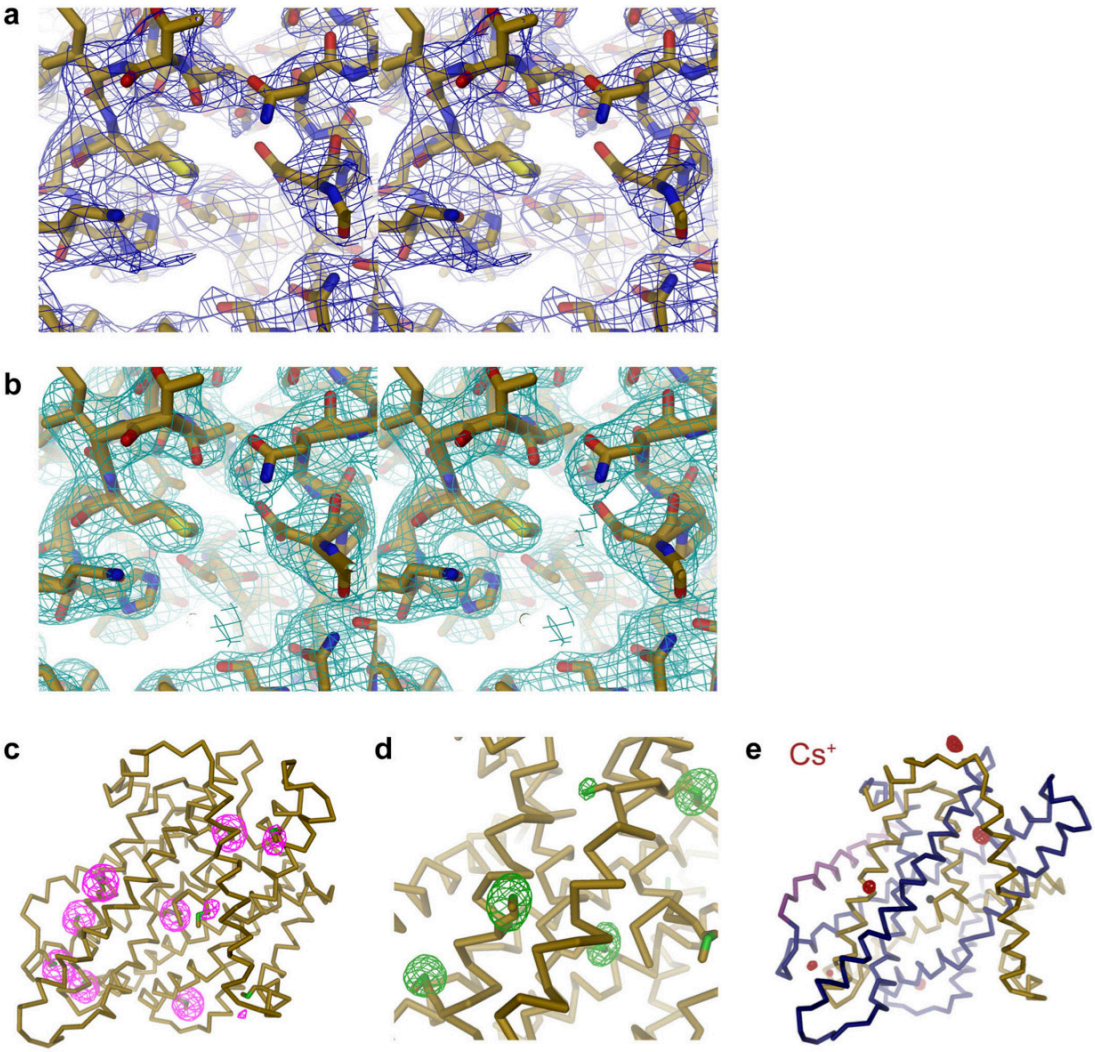

Supplementary Figure 3

Electron density.

(**a**) Stereo view of the ion-binding region. Experimental electron density calculated at 3.5 Å with Se-Met SAD phases that were improved by solvent flattening and cyclic 2-fold NCS symmetry averaging (blue mesh, contoured at 1 σ) is superimposed on the refined model of the ScaDMT^{tru}–NB complex. (**b**) The same region of the protein is shown with $2F_o$-F_c electron density superimposed (cyan mesh, contoured at 1 σ). The density at 3.1 Å was calculated with phases from the refined model. (**c**) Anomalous difference electron density of Se atoms (calculated at 3.5 Å and contoured at 5 σ) superimposed on the ScaDMT structure. Protein is shown as Cα-trace, methionine side-chains as sticks. (**d**) Anomalous difference density of data collected at a wavelength of 1.95 Å. Electron density calculated at 4.5 Å and contoured at 4 σ is superimposed on the model. The density shows peaks for sulfur atoms of methionine and cysteine residues but not for bound Ca^{2+}. (**e**) Anomalous difference density of Cs^+ (calculated at 4.5 Å and contoured at 5 σ, red) is shown superimposed on the ScaDMT structure. ScaDMT is represented as Cα-trace, the position of Mn^{2+} as black sphere.

Nature Structural and Molecular Biology: doi:10.1038/nsmb.2904

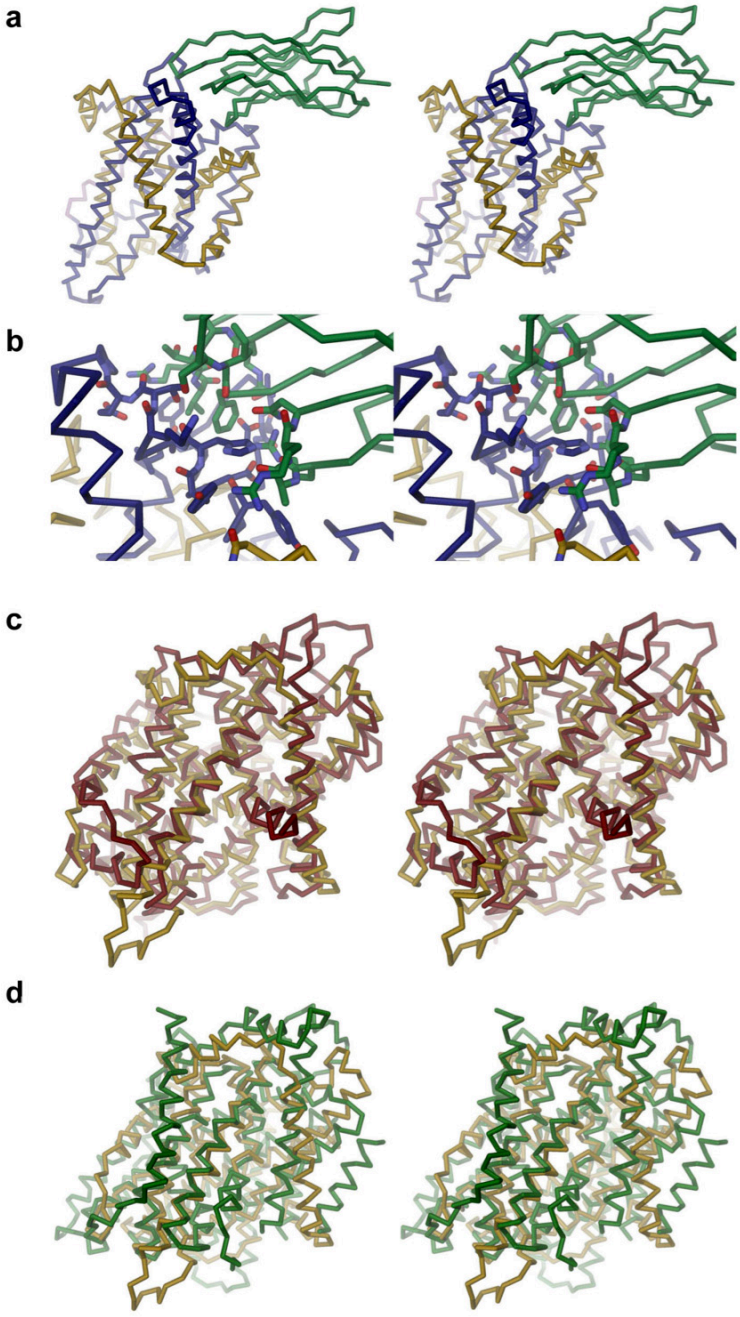

Supplementary Figure 4

Nature Structural and Molecular Biology: doi:10.1038/nsmb.2904

Nanobody complex and comparison with related proteins.

Stereo views of ScaDMT–nanobody interactions. (**a**) Structure of the ScaDMT–nanobody complex. Proteins are displayed as Cα-trace. The coloring of the protein is as in Fig. 2, the nanobody is colored in green. (**b**) Close-up of the interaction interface. Interacting residues are shown as sticks. (**c**) Stereo view of the superposition of ScaDMT on the inward-facing conformation of LeuT. The superposition was based on the Cα positions of equivalent residues in transmembrane helices (RMSD 3.2 Å). ScaDMT is colored in orange, LeuT in red. (**d**) Stereo view of the superposition of ScaDMT on the inward-facing conformation of vSGLT. The superposition was based on the Cα positions of equivalent residues in transmembrane helices (r.m.s.d. 3.9 Å). ScaDMT is colored in orange, vSGLT in green.

Nature Structural and Molecular Biology: doi:10.1038/nsmb.2904

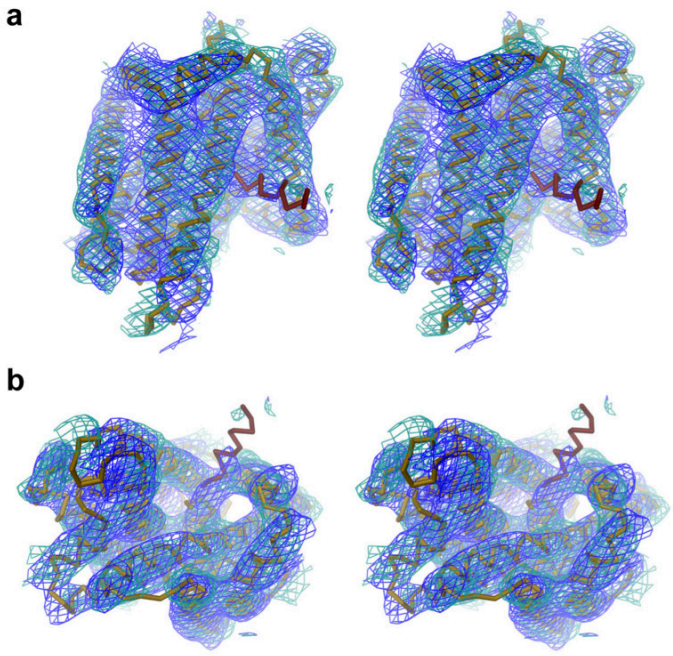

Supplementary Figure 5

Structure of full-length ScaDMT.

Stereo view of the full-length ScaDMT structure at 6.5 Å resolution. The structure shows one of the two transporters present in the asymmetric unit. The electron density calculated from phases obtained by molecular replacement with the program Phaser is colored in blue, electron density after rigid-body refinement in PHENIX is shown in cyan. Both electron densities are contoured at 1 σ. ScaDMT is colored in orange, α-helix 1a of LeuT from the superimposed model is shown in red. (**a**) View from within the membrane, (**b**) view from the cytoplasm.

Nature Structural and Molecular Biology: doi:10.1038/nsmb.2904

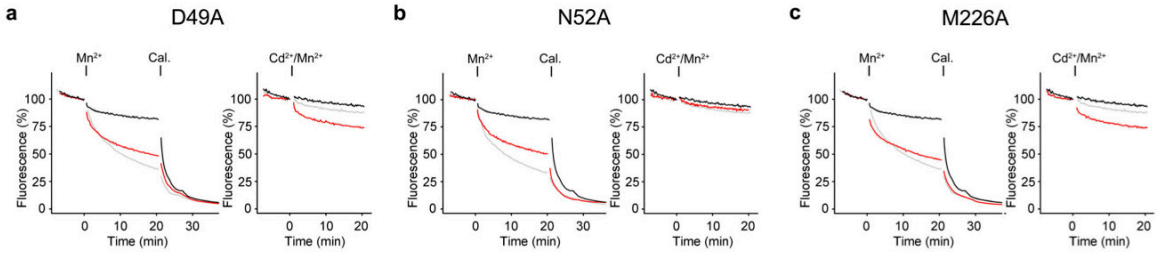

Supplementary Figure 6

Transport properties of ScaDMT binding-site mutants.

Transport of Mn^{2+} into proteoliposomes containing the ScaDMT binding site mutants D49A (**a**), N52A (**b**) and M226A (**c**). Left: Time-dependent quenching of the fluorophore calcein, that is trapped inside the vesicle, upon addition of 300 μM Mn^{2+} to the external medium. Addition of Mn^{2+} and the ionophore calcimycin (Cal.), which acts as Mn^{2+}/H^{+} exchanger, are indicated. A control trace from liposomes devoid of protein upon addition of 300 μM Mn^{2+} is shown in black, transport into proteoliposomes containing WT is shown in grey. Compared to WT, the proteoliposomes containing the mutants D49A, N52A and M226A show decreased activity. Right: ScaDMT-mediated transport of Mn^{2+} in the presence of Cd^{2+}. Time-dependent quenching of the fluorophore calcein, was monitored upon addition of 100 μM of Mn^{2+} and 100 μM Cd^{2+} to the external medium. Transport by WT under the same conditions is shown in grey for comparison, traces from liposomes devoid of protein are shown in black. In all cases the presence of Cd^{2+} decreases the transport of Mn^{2+} into liposomes.

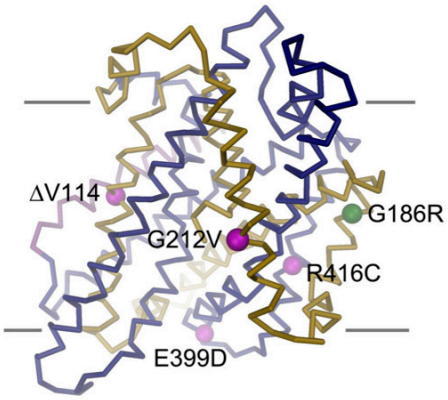

Supplementary Figure 7

Location of disease mutations.

The position of disease causing mutations in DMT1 in rodents (green) and human (magenta) are mapped on equivalent positions on the ScaDMT structure. The numbering corresponds to human DMT1. The protein is shown as Cα-trace, the mutated residues are indicated as spheres, the approximate membrane boundaries are indicated in grey.

Nature Structural and Molecular Biology: doi:10.1038/nsmb.2904

Supplementary Table 1 Data collection and refinement statistics of ion complexes

	Fe^{2+}	Cd^{2+}	Co^{2+}	Ni^{2+}	Cu^{2+}	Pb^{2+}	Zn^{2+}	Sr^{2+}	Ba^{2+}	Ca^{2+}	Cs^{+}
Data collection											
Wavelength (Å)	1.742	1.8	1.608	1.487	1.380	0.951	1.283	0.770	1.9	1.9	1.895
Space group	$P3_121$	$P3_121$	$P3_121$	$P3_121$	$P3_121$	$P3_121$	$P3_121$	$P3_121$	$P3_121$	$P3_121$	$P3_121$
Cell dim.											
a, *b*, *c* (Å)	114., 114., 261.	114., 114., 261.	114., 114., 263.	114., 114., 263.	114., 114., 267.	114., 114., 264.	114., 114., 261.	114., 114., 259.	114., 114., 261.	115., 115., 258.	114., 114., 259.
α, β, γ (°)	90.0, 90.0, 120.0	90.0, 90.0, 120.0	90.0, 90.0, 120.0	90.0, 90.0, 120.0	90.0, 90.0, 120.0	90.0, 90.0, 120.0	90.0, 90.0, 120.0	90.0, 90.0, 120.0	90.0, 90.0, 120.0	90.0, 90.0, 120.0	90.0, 90.0, 120.0
Resolution (Å)	50-4.0 (4.2-4.0)	50-3.8 (4.0-3.8)	50-3.8 (4.0-3.8)	50-4.3 (4.6-4.3)	50-5.0 (5.3-5.0)	50-3.8 (4.0-3.8)	50-3.9 (4.1-3.9)	50-3.7 (4.0-3.7)	50-4.1 (4.3-4.1)	50-3.7 (3.9-3.7)	50-3.5 (3.7-3.5)
R_{merge}	10.4 (146)	12.0 (136)	7.1 (88)	9.3 (91)	6.1 (137)	8.4 (124)	8.2 (141)	9.8 (110)	11.8 (123)	12.0 (140)	8.3 (98)
$I / \sigma I$	14.1 (2.7)	14.9 (2.8)	12.1 (1.9)	11.8 (2.6)	15.8 (1.8)	18.0 (2.5)	15.6 (2.2)	17.8 (2.6)	12.0 (2.5)	16.4 (2.8)	15.5 (2.3)
Completeness (%)	99.9 (100)	99.9 (100)	99.9 (100)	99.9 (99.9)	98.8 (93.2)	99.9 (100)	99.8 (99.1)	99.9 (100)	99.9 (100)	100 (100)	98.9 (93.3)
Redundancy	9.1 (10.2)	8.4 (8.0)	4.6 (4.6)	7.7 (7.5)	7.9 (7.5)	9.8 (9.9)	8.2 (7.8)	10.6 (10.4)	9.9 (10.0)	10.3 (10.3)	6.8 (6.4)
Refinement											
Resolution (Å)	20-4.0	20-3.8	20-3.8	20-4.3	20-5.0	20-3.8	20-3.9	20-3.7	20-4.1	20-3.7	20-3.5
R_{work} / R_{free}	26.4 / 30.4	27.0 / 29.4	25.7 / 29.2	27.2 / 30.3	30.3 / 31.3	26.9 / 29.8	27.2 / 30.2	26.2 / 29.2	25.9 / 29.3	25.4 / 28.0	26.3 / 28.7

*Values in parentheses are for highest-resolution shell.

Nature Structural and Molecular Biology: doi:10.1038/nsmb.2904

2.7.2. Supplementary data set 1

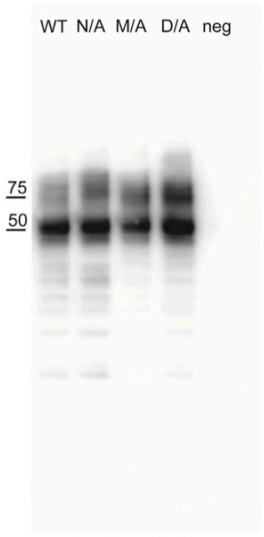

Supplementary Data Set 1

Western blot of human DMT1 mutants.

Western blot of *Xenopus laevis* oocytes expressing human DMT1 (WT) and the DMT1 binding site mutants N89A (N/A), M265A (M/A) and D86A (D/A). The positions of the molecular weight markers (kDa) are indicated. Non-injected oocytes (neg) are shown as control. All oocytes were previously used for electrophysiology experiments. The figure shows the uncropped version of the blot displayed in Fig. 6g.

Nature Structural and Molecular Biology: doi:10.1038/nsmb.2904

3. DISCUSSION

Discussion

With the structure determination of the prokaryotic transporter ScaDMT, the results of this thesis have allowed first detailed insight into the architecture of the SLC11 family and they have provided the structural basis of transition metal ion selectivity. ScaDMT adopts an inward-facing conformation that exposes a metal binding site to the cytoplasm. Three conserved residues that are located in the center of the transporter coordinate the divalent transition-metal ions Mn^{2+}, Fe^{2+} and Cd^{2+}. Fluorescence based assays have allowed me to measure transport of several transition-metal ions and they showed that the presence of the alkaline earth-metal ions Ca^{2+}, Sr^{2+} and Ba^{2+} does not affect the transport of manganese, thus indicating that they are neither substrates nor inhibitors of ScaDMT. Cadmium affinities of ScaDMT and mutants of ion-coordinating residues by ITC underline the important role of this binding site for ion coordination. The conservation of ion-protein interactions was confirmed by electrophysiology. Towards this end I have applied two-electrode voltage-clamp measurements to investigate the effect of binding site mutants in human DMT1. One mutant evokes cadmium induced currents only at higher concentrations compared to wild type hDMT1 and no cadmium-induced currents were observed for two other mutants despite their strong expression in *X. laevis* oocytes, thus suggesting that the same residues coordinate transition metal ions in SLC11 transporters from bacteria to human.

ScaDMT shares its fold with LeuT

The crystal structure of ScaDMT reveals that SLC11 transporter share a common architecture with otherwise unrelated transport proteins, which was first identified in the amino acid transporter LeuT from the bacterium *Aquifex aeolicus* (Yamashita et al., 2005). Our work thus confirms a previous bioinformatics analysis that has predicted a structural relationship to transporters sharing a LeuT-fold (Cellier, 2012a, 2012b). In these proteins two sub-domains of five transmembrane segments are organized as inverted structural repeats (Yamashita et al., 2005). In LeuT the transmembrane segments TM1-5 are related via a pseudo-symmetry axis, parallel to the membrane to the segments TM6-10. The first transmembrane helix of each repeat is unwound in its center with residues (in this unwound region) contributing to substrate binding (for a schematic drawing see Chapter 2.7, Figure 2b). Over the last years several secondary active transporters of unrelated sequence have been found to share the same fold (Forrest et al., 2011; Perez et al., 2012; Shi, 2013). All of them contain a core of two five-helix repeats, often followed by 1-2 additional helices.

The sodium/galactose symporter SGLT from the bacterium *Vibrio parahaemolyticus* (Faham et al., 2008) and the sodium/glycine-betaine symporter BetP (Ressl et al., 2009) from *Corynebacterium glutamicum* are examples where the core is preceded by either one or two N-terminal helices respectively. Besides their similar architecture these proteins have no apparent sequence homology and transport unrelated substrates such as amino acids, sugars, or ions (Forrest and Rudnick, 2009; Theobald and Miller, 2010). Several of them use the symport of sodium as the electrochemical driving force to transport a solute against its concentration gradient. Three bacterial transporters have been identified as antiporters: AdiC form *Salmonella typhimurium* and *E. coli* (Fang et al., 2009; Gao et al., 2010; Tsai and Miller, 2013) exchanges arginine with agmatine, and CaiT (*Proteus mirabilis* PmCaiT and *E. coli* EcCaiT) L-carnitine with γ-butyrobetaine (Schulze et al., 2010; Tang et al., 2010) and GadC from *E. coli* exchanges glutamate with GABA(Ma et al., 2012). The prokaryotic transporter ApcT from *Methanocaldococcus jannaschii* is a proton-coupled symporter for amino acids (Shaffer et al., 2009). Based on the alternate access model introduced ~50 years ago in the absence of structural information, transport of a solute requires at least three conformations. In two conformations the binding site of the transporter is exposed to either one or the other side of the membrane. Both states are connected by a transient conformation in which the binding site is closed to both sides (Jardetzky, 1966; Mitchell, 1957). Several structures of the amino acid transporter LeuT in different conformations have confirmed the alternating access model (Krishnamurthy and Gouaux, 2012; Singh et al., 2007, 2008; Yamashita et al., 2005). In Figure 53 the structures of LeuT in three distinct conformations are shown. In an outward-facing conformation (A, D) the residues coordinating the substrate are accessible from the outside. Upon substrate binding, conformational changes are induced that cause the closure of the extracellular binding cavity while the intracellular site remains closed. In this state the binding site is occluded to both sides of the membrane, completely surrounding the substrate. (B, E) The transient occlusion is followed by conformational rearrangements that cause the intracellular site to open up, hence allowing the release of the substrate to the cytoplasm (C, F). Structures of different conformations of other secondary active transporters sharing the LeuT fold, are in agreement with the alternate substrate access observed in LeuT, and have allowed the identification of additional conformations transiently present during the transport cycle (Faham et al., 2008; Fang et al., 2009; Gao et al., 2009; Ma et al., 2012; Malinauskaite et al., 2014; Penmatsa et al., 2013; Ressl et al., 2009; Schulze et al., 2010; Shaffer et al., 2009; Shimamura et al., 2010; Weyand et al., 2008). In agreement with the model, the substrate binding sites are generally located in the center of the transporter, where the energy for a hydrophilic substrate traversing the membrane would be at its maximum.

In the case of ScaDMT, soaks of several transition-metal ions have allowed us to identify a single binding site composed of conserved residues located in the center of the membrane, which coordinate Mn^{2+}, Fe^{2+}, Co^{2+}, Ni^{2+}, Cu^{2+}, Cd^{2+} and Pb^{2+}. This binding site is inaccessible from the extracellular side, since residues of α-helices TM1b TM6a, TM2 and TM10 seal the cavity.

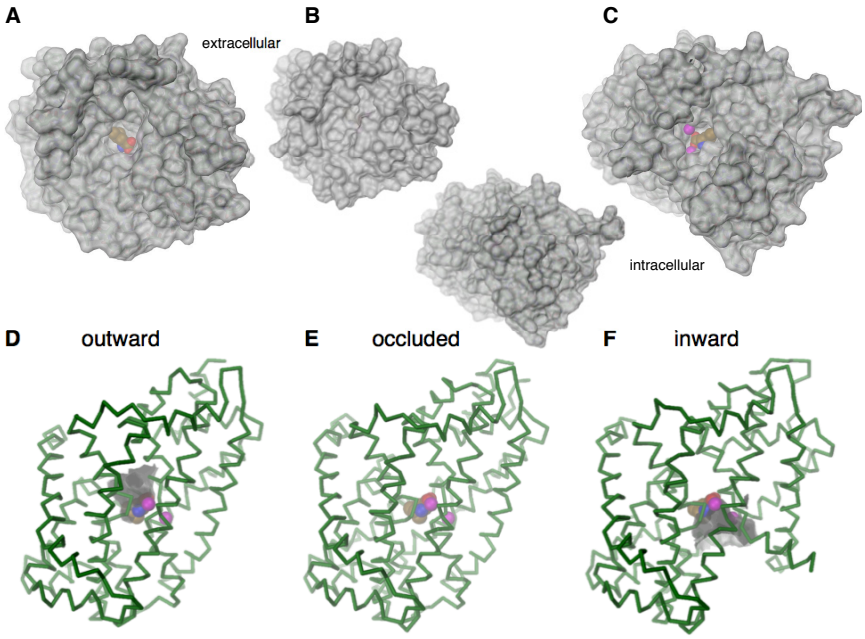

Figure 53 Structures of LeuT transporter in different conformations.
(A) View from the extracellular side of an outward-facing conformation with bound substrate. (B) Extracellular and cytoplasmic view of a substrate-bound occluded conformation. (C) Bottom-view of the inward-facing conformation of LeuT. Figures A-C are shown as surface representation. (D-F) C-α representation of the corresponding conformations shown in A-C. The view is from within the membrane. The surface of the substrate-binding pocket is shown in grey.

On the intracellular side, the binding site is partially shielded by residues of TM1a and the hinge between TM1a and TM1b, several residues of TM6b and two residues of TM8. Although the ScaDMT structure most likely shows an inward-facing conformation that is stable also in the absence of bound ions, the absence of part of helix 1 (in the construct used for structure determination) leaves some uncertainty on its exact correspondence to conformations of the transport cycle. Although the truncation was shown to have an unchanged binding affinity for ions, it cannot be excluded that in a full- length protein the N terminus could adopt a slightly different conformation. The fact that ions could be soaked into the crystals, without observed changes in the structure, is an indication that the binding site was easily accessible.

Based on the analysis of known structures, there were two models proposed of how substrate transport is conducted in transporters sharing a LeuT fold. These hypotheses are known as the "rocking-bundle" mechanism (Forrest and Rudnick, 2009; Rudnick, 2013) and the "hinge-bending" model (Penmatsa and Gouaux, 2014; Yamashita et al., 2005). The rocking-bundle mechanism suggests that a so-called bundle comprised of TM 1-2 and TM6-7 moves as a single rigid entity, relative to the scaffold domain comprised of TM3-5 and TM8-10 (Figure 54A). The "hinge-bending" model suggests that the two halves of TM1 and 6 as well as TM2 and 7 move independently (the authors call TM1-2 and TM-7 core-domain), with respect to the scaffold domain that is comprised of the same helices as suggested in the rocking-bundle model (Figure 54B). Remarkably, the rocking-bundle model does not explain the large outward movement of helix 1a, observed in the inward-facing conformation in LeuT (Forrest and Rudnick, 2009; Forrest et al., 2011).

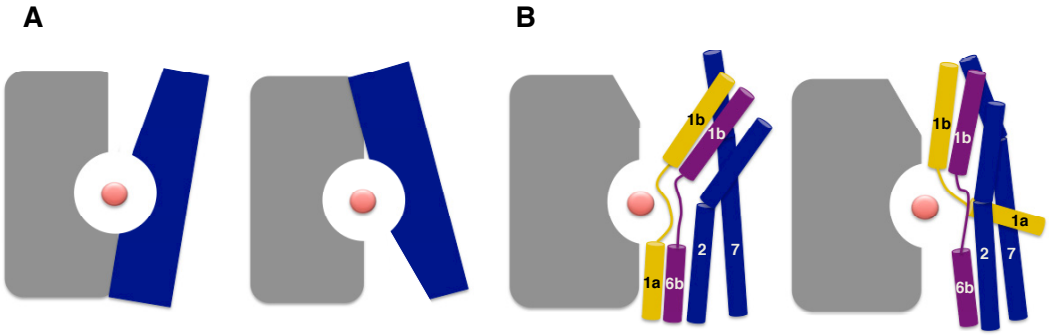

Figure 54 Rocking-bundle and Hinge-bending model.

(A) Rocking bundle mechanism. The bundle (blue) moves with respect to the scaffold domain (grey) around the binding site. (B) Hinge-bending model. Helices 1, 2, 6 and 7 move individually, with respect to the scaffolding domain (grey). The substrate is depicted as red sphere.

When comparing the inward-facing conformations of LeuT (pdb code 3TT3), Mhp1 (pdb code 2X79) and BetP (pdb code 4C7R) a striking difference has been noted in the location of the first part of α-helix 1: Whereas TM1a moves by ~45° in LeuT, the movement is intermediate in vSGLT (Faham et al., 2008), and lowest (~18°) in Mhp1 and BetP (Penmatsa and Gouaux, 2014). As all three structures were solved by crystallization of detergent-solubilized protein, it cannot be excluded that this local conformation is induced by the detergent, and would not occur if the protein would be embedded in a lipid bilayer (Forrest and Rudnick, 2009; Loland, 2014). The residual density we have observed in the low-resolution structure of full-length ScaDMT does not conclusively allow distinguishing if TM1a of ScaDMT is similar to the inward-facing conformation found in LeuT, or whether it closer resembles the inward-facing conformations of vSGLT, Mhp1 and BetP. Recent EPR and DEER studies of LeuT that tried to address this

question would be compatible with the hinge-bending mechanism (Kazmier et al., 2014). Given the structural similarity of ScaDMT to LeuT, a similar structural transition into an outward-facing conformation appears plausible (see chapter 2.7, Figure 7). However, a detailed understanding of the molecular and thermodynamic determinants driving the conformational changes of the transport cycle in ScaDMT requires further structural and functional analysis.

Proton-coupling in SLC11 transporters

Transition-metal ion transport in eukaryotic SLC11 transporter is coupled to the cotransport of protons, which provide the electrochemical driving force for concentrative substrate uptake. This process was initially investigated in the rat DMT1, where uptake of Fe^{2+} was increased with decreasing pH, and where the import of protons was directly measured with pH sensitive microelectrodes (Gunshin et al., 1997). Compared to other secondary active transporters, this coupling appears less strict, as uncoupled fluxes of either substrate were observed in conditions lacking the other ion (Mackenzie et al., 2006). pH dependent transport of metal ions was also observed for the SLC11 transporter of *E. coli,* based on radioactive uptake into cells (Makui et al., 2000). Unlike the determinants of metal ion selectivity, my study did not reveal the mechanisms underlying proton coupling. Due to limitation of the current transport assay, the question whether metal ion transport in ScaDMT would show a similar coupling, is still unresolved. The high sequence similarity to its mammalian counterparts and the strict conservation of residues in the proximity of the binding site makes a similar transport mechanism plausible.

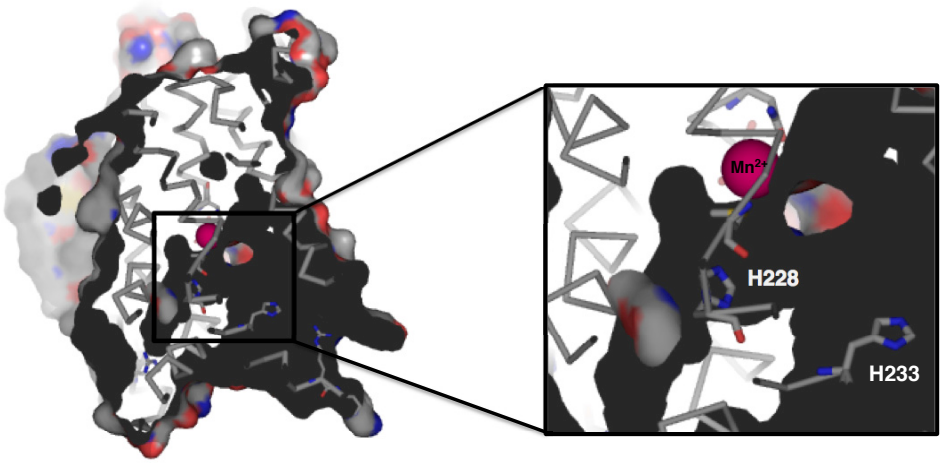

Figure 55 Conserved histidine residues in the vicinity of the metal binding site.

Surface representation of ScaDMT viewed from within the membrane (left). Zoom into the binding site with His228 and His232 shown as sticks (right).

In that respect it is remarkable to find that two histidines located in TM6, whose mutations were previously identified to affect proton coupling in human DMT, are conserved in ScaDMT. These residues are located in the aqueous pathway leading to the metal binding site, with one residue found in the immediate proximity of the site (Figure 55). Unexpectedly the effect of mutations is stronger for the histidine that is found at a larger distance from the site towards the cytoplasm. It is thus currently not clear whether these residues would be the only proton acceptors within the protein or whether there may be a extended proton pathway throughout the protein that was proposed for other proton coupled transport proteins (Lim and Miller, 2009; Lim et al., 2012). A recent study of a proton coupled transporter sharing the LeuT-fold, showed a potential proton-accepting residue at the equivalent position of the sodium binding site in LeuT, which suggests a way, how the ion-coupling could have been changed with minimal changes of the protein. Interestingly however, there is no suitable equivalent residue found in the ScaDMT structure, thus suggesting that the proton coupling in that protein may proceed by a different mechanism.

Outlook

Although the work of this thesis has provided a breakthrough in the structural understanding of the SLC11 family, it should be considered as one out of many steps to be taken towards a complete comprehension of the mechanisms of transition-metal ion transport by these secondary active transporters. Future investigations will have to employ different approaches to characterize SLC11 transporters in more depth. One challenge will be to obtain different conformations of the same or related homologs. Snap-shots of the binding site captured in different states of the transport cycle would allow to get insight into the residues involved in the formation of the, not yet identified, "thin gate" that might, similar as in sodium-coupled transporters sharing the LeuT-fold, protect the substrate from dissociation in an outward-facing conformation (Forrest et al., 2011; Loland, 2014; Perez and Ziegler, 2013). Towards this goal, specific mutations at strategic points within the protein might help to destabilize the inward-facing conformation that seems to be preferred by ScaDMT when solubilized in detergent. Additionally selection of nanobodies or other crystallization chaperones with ScaDMT (wt or mutants) embedded in a more native environment (e.g. in liposomes or nano-disks) might facilitate the selection of binders targeting different conformations (Inagaki et al., 2013; Pavlidou et al., 2013). Compounds that stabilize such conformations and thus inhibit transport might be useful for crystallization and functional analysis of ScaDMT (Cadieux et al., 2012; Zhang et al., 2012b).

Particular effort has to be put on improving the fluorescence-based assay described in this thesis. Although this assay was very useful for the initial functional characterization of ScaDMT, it has still several weaknesses that need to be resolved, in order to use the full potential of a reconstituted system. Due to the proton-leakage of the proteoliposomes observed during measurements, this assay cannot be used to investigate a potential proton coupling of metal ion transport in prokaryotic SLC11 homologs, which is an important question that has to be addressed. Future experiments to improve the transport assay, will have to explore other lipid sources, since a recent comparison of proteoliposomes in a study conducted, by Ming-Feng Tsai and Chris Miller revealed striking differences in proton-leakiness depending on the lipid composition (Tsai and Miller, 2013). The question whether zinc is a substrate or an inhibitor of ScaDMT should be elucidated by the use of zinc sensitive fluorescent dyes that are compatible with a liposomal assay. Alternatively, radioactive zinc could be used in uptake assays. Besides the direct investigation of coupled proton transport using pH-sensitive fluorescent dyes, an improved assay would also allow the determination of kinetic parameters such as K_m values and V_{max} for transport. Such quantitative assessment of transport would be very valuable, because it would allow us to characterize the substrate specificity of wild type ScaDMT and mutant constructs for different transition-metal ions.

The establishment of the expression of a mammalian homolog for purification and reconstitution would be a remarkable achievement that would allow the characterization of the isolated transporters under controlled conditions. This would multiply the possibilities to address questions concerning the detailed mechanism of ion transport and coupling in mammalian transporters, such as the proposed uncoupled transport of either protons or metals. Besides its use for functional experiments such an overexpression system would also provide protein for crystallization experiments that aim for the structure determination of a mammalian SLC11 transporter.

4. METHODS

Isolation of genomic DNA. Genomic DNA was prepared according to Sambrook and Russell 2001 (J. Sambrook, 2001) by phenol:chloroform extraction, with minor modifications: Additionally to Proteinase K and SDS which are components of the standard lysis-buffer, lysozyme was added to a final concentration of 5 mg/ml. In case incubation at the recommended 37 °C was not sufficient to lyse the cells, temperature was increased up to 80 °C and incubation time was prolonged for a maximum of 5 hours. The DNA was concentrated by sodium- acetate-isopropanol precipitation and resuspended in TE buffer.

PCR. Genes were amplified either with Phusion polymerase (Thermo Scientific Finnzymes or NEB) or Herculase II (Stratagene) or a PCR Mastermix containing Taq DNA polymerase (Thermo Scientific ABgene). Reactions were set up with 100-1000 ng genomic DNA, 0.5-1 μM of forward and reverse primer (Microsynth AG) and DMSO was added up to 3 % (v/v). The temperature settings for denaturation and elongation were chosen as suggested by the user manufacturer. The annealing temperature of 59 °C was decreased by 0.5 °C per cycle to reduce annealing at unspecific sequences in the first 15 cycles. The annealing temperature was set constant to 51 °C for additional 15 cycles. The PCR products were separated on a 1% agarose gel. DNA bands of the expected size were cut out and purified with High Pure PCR Product Purification Kit (Roche).

Restriction digest and ligation. PCR products were cloned into the pINITIAL vector according to Geertsma and Dutzler, 2011 . In brief, 50 ng vector was mixed with purified PCR product at a molar ratio of 1:5 and digested with SapI for 1 h at 37 °C. The reaction was incubated for 20 min at 65 °C to heat-inactivate the restriction enzyme. For ligation ATP and T4 ligase were added to the reaction and incubated for 1h at RT. Prior to transformation into chemo-competent *E.coli* MC1061 (Casadaban and Cohen, 1980) the ligase was heat inactivated by a 20 min incubation step at 65 °C.

Small-scale protein expression. *E.coli* MC1061 was used for all subsequent expression cultures. All cultures were supplemented with the appropriate antibiotics. Pre-cultures were grown o/n at 37 °C, 300rpm, in 96-deep-well plates (conical bottom) in TB medium supplemented with 0.75% (w/v) glycerol. Main cultures were grown in 4 ml (24-deep-well plates, conical bottom) TB supplemented with 0.75% (w/v) glycerol from a 1/100 inoculum. After 1.5 hours growth at 37 °C, 300 rpm the temperature was reduced to 25 °C and cells were allowed to grow for an additional hour. The cultures were induced with the desired amount of arabinose (initial screening concentrations: $4*10^{-2}$%, $4*10^{-3}$%, $4*10^{-4}$% (w/v) arabinose, as $4*10^{-2}$% (w/v) arabinose

was not resulting in more well behaved protein of the homologs tested in the first round and $4*10^{-4}$% (w/v) arabinose led to extremely low expression of the target protein only $4*10^{-3}$% (w/v) arabinose concentration was tested in the screening of subsequent homolog-rounds). Expression was carried out at 24 °C overnight, 300 rpm shaking. Cells were harvested by centrifugation at 2000 g, 4 °C, 15 min and immediately used for subsequent experiments.

Small-scale cell lysis and membrane protein extraction. The harvested cells were resuspended in 300 µl ice-cold PBS. Whole cell fluorescence was measured if the GFP-fusion construct was expressed: For this 150 µl of the cell suspension were transferred to a 96-black-well flat bottom plates (Greiner) and fluorescence was recorded in a Tecan Infinite M1000 plate reader (excitation at 485 nm, emission at 535 nm, gain = 60). The OD_{600} of the cells was measured in 96-well transparent, flat bottom plates (Nunc) and used to correct the fluorescence signal for the cell densities (Fluorescence signal divided by OD_{600}). For further analysis cells equalling ~3 mg total protein were resuspended in 400 µl pre-cooled lysis buffer (50 mM KP_i pH 7.5, 1 mM $MgSO_4$, 10% (w/v) glycerol, 1x Roche Complete Protease Inhibitor Cocktail, 25 µg/ml DNase), 300 mg glass beads (Sigma, 0.1 mm diameter) were added and cells were lysed using a bead-beating device (FastPrep-24, MP Biomedicals, two cycles, time 20 s, speed 6 m/s, 5 min incubation on ice after each cycle). To extract the membrane proteins 200 µl of the supernatant were mixed with DDM to a final concentration of 1 % (w/v) and incubated on ice for 1h (mixing every 20 min). The extract was cleared by ultracentrifugation (Beckman Optima MAX XP, TLA 100, 10 min at 220 000 g, 4 °C). Samples were taken after lysis and after ultracentrifugation and separated by SDS-PAGE (corresponding to 75 µg total protein/lane). Directly after SDS-PAGE, in-gel fluorescence was detected for GFP-fusion proteins with a Fujifilm LAS-3000 imaging system (Fujifilm Super CCD camera, 460 nm EPI blue light, Y515AttoPhos Filter, Iris F2.8). The protocol is modified from Geertsma et al., 2008.

Western blot analysis. Shortly after SDS-PAGE (gel was incubated 2 min in water) proteins were transferred onto a PVDF membrane (PVDF membranes were pre-soaked in methanol) by semi-dry electrophoretic transfer (BioRad Transblot SD, 50 min, 15 V). The filter paper was pre-soaked for 10 minutes in pre-chilled transfer buffer (25 mM Tris, 192 mM glycine, pH 8.3, 20% methanol). PVDF membranes were blocked for 1h at RT with 5% (w/v) milk powder in PBS and then incubated with an anti-polyhistidine antibody (Roche 11965985001, 1:1000 (v/v)) in PBS supplemented with 1% milk powder. The blots were developed with Immobilon Western

chemiluminescent HRP substrate (Millipore) and imaged with a Fujifilm LAS-3000 imaging system (Fujifilm Super CCD camera).

Large-scale expression of prokaryotic DMT homologs in fermenter culture. Cells were inoculated 1/100 in 9-18 l TB medium supplemented with 100 mg/l Ampicillin. Cells were allowed to grow for 1.5 hours at 37 °C with air supply (constant air flow air_{in} = 1.2 bar, air_{out} = 0.9 bar, stirring speed = 250-350 rpm). Over the following 4 hours the temperature was reduced in steps of 4 °C until 25 °C were reached. Cells were allowed to grow at 25 °C for 60 min until an OD_{600} of 2.5-3.0 was reached. Cells were induced with $4*10^{-3}$ % arabinose (w/v). Two hours after induction the temperature was reduced in two steps to 18 °C. 14-15 hours after induction cells were harvested by centrifugation at 5500 rpm for 15 min at 4 °C (rotor Sorvall F8S6x1000). The cell pellets were resuspended in pre-cooled 50 mM KP_i pH 7.5, 150 mM NaCl (buffer A) supplemented with 1mg/ml lysozyme, 40 µg/ml DNase and 5 mM magnesium sulfate. Cells were either lysed with a custom-made cell disruptor (French press technology) or a Constant Systems cell disruptor, with 3-4 passages at 15-35 kPsi. The lysate was cleared by centrifugation at 10,000 g for 30 min. Membranes were harvested by ultra-centrifugation at 43,000 rpm for 1 hour at 4 °C (rotor Beckman 45Ti or 70Ti). Membranes were diluted to 2 ml/1 g vesicle in pre-cooled buffer A supplemented with 10 % (w/v) glycerol in a Potter homogenizer, flash frozen in 10 ml aliquots (5g vesicles) in liquid nitrogen and stored at -80 °C.

Purification of prokaryotic DMT homologs. For membrane protein extraction membrane vesicles were quickly thawed (in a water bath at RT) and suspended in pre-cooled buffer A containing 10 % (w/v) glycerol and either 1-1.2 % (w/v) n-dodecyl-β-D-maltopyranosid (Anatrace) or 1-2 % (w/v) n-decyl-β-D-maltopyranosid (Anatrace). All subsequent steps were carried out at 4 °C. The suspension incubated for 1 h, mild stirring. Unsolubilized material was removed by ultra-centrifugation at 43,000 rpm for 30 min (rotor Beckman 45Ti or 70Ti). For each 1 g of vesicles 0.4 ml metal affinity resin (Qiagen) was incubated with the supernatant for 1 h, mild stirring. Unspecific binding of protein to the Ni-NTA resin was reduced by addition of 15 mM imidazole. Gravity flow columns were used to remove the flow through and subsequently wash the resin with 20-25 column volumes buffer B, supplemented with 10 % (w/v) glycerol and 50 mM imidazole (buffer B: 20 mM HEPES, pH 7.5, 150 mM NaCl, 0.05 % DDM or 0.25 % DM respectively). The protein was eluted with buffer B supplemented with 6% glycerol and 300 mM imidazole. For cleavage of the His_{10}-tag (or GFP-His_{10}-tag), the sample was digested for 2 h with 3C protease (~22 kDa) at a molar ratio of 5:1 while dialyzing into buffer C (20 mM HEPES, pH 7.5, 150 mM NaCl, 0.025 % DDM or 0.11 % DM respectively, 10 % glycerol) to lower the

imidazole concentration to 15 mM (Spectrapor Dialysismembranes MWCO 8 kDa). The His tag and the 3C protease were removed by incubation of the solution with (fresh) Ni-NTA resin for 15 min (1ml resin per 8 mg total amount of protein) and collection of the flow through, which contains the cleaved protein. The cleaved protein was concentrated to 10-20 mg/ ml with an Amicon Ultra Centrifugation device (Millipore, MWCO = 50 kDa) and filtered through a 0.22μm centrifugal filter device. The filtered protein was subjected to size exclusion chromatography on a Superdex S200 column (GE Healthcare) equilibrated in 10 mM HEPES, pH 7.5, 150 mM NaCl, supplemented with the appropriate amount of detergent (either 0.05% DDM, 0.25% DM or 0.84% NM, Anatrace). For crystallization experiments, peak fractions were pooled and concentrated to 5-12 mg/ml with an Amicon Ultra Centrifugation device (Millipore, MWCO=50 kDa).

Crystallization of ScaDMT. Purified ScaDMT concentrated to 7.5 mg/ml was used for crystallization. Crystallization trials were performed at the Protein Crystallization Facility at the University of Zurich. Crystallization trials were set up using sitting drop vapour diffusion, by mixing of the protein 1:1 (v/v) with mother liquor. ScaDMT crystals grew under conditions containing 25-35 % PEG 400 as precipitant, buffer at pH 4.5 to pH 7.5 and either $CaCl_2$ or $MgCl_2$.

Biotinylation of ScaDMT and ScaDMT^{tru} AVI tagged proteins. AVI-tagged transporters were purified following the standard purification protocol as described above. After the SEC run the peak fractions were pooled and concentrated to 8 mg/ml with an Amicon Ultra Centrifugation device (Millipore, MWCO=50 kDa). The biotinylation reaction was set-up with 2 mg of protein in SEC buffer supplemented with 5 mM ATP pH 7.0, 10 mM $MgSO_4$, 5 mM biotin (stock in bicine buffer, pH 9.0), 100 μg/ml BirA. The reaction was incubated o/n at 4 °C. Subsequently the solution was incubated with Ni-NTA resin to remove His-tagged BirA. The flow-through containing the biotinylated protein was subjected to another SEC run on a S200 column.

Shaker flask expression and purification of nanobodies. The nanobodies were cloned into an arabinose inducible expression vector containing an N-terminal pelB leader sequence, a His_{10} tag and the maltose-binding protein (MBP) located in front of the nanobody. For expression, 3 flasks with 600 ml TB medium supplemented with 100 μg/ml ampicillin were inoculated with an o/n culture of MC1061 cells containing the appropriate plasmid. Cells were grown at 37 °C to an OD_{600} of 0.6-0.8 and induced with $2*10^{-2}$ % arabinose. For o/n expression the temperature was

reduced to 25 °C. Cells were harvested by centrifugation at 5500 rpm (rotor Sorvall F8S6x1000) and resuspended in buffer R: 50 mM KP_i pH 7.5, 150 mM NaCl, 10 % glycerol supplemented with 1 mg/ml lysozyme, 40 µg/ml DNase and 5 mM magnesium sulfate. All following steps were carried out at 4 °C. Cells were lysed with a custom-made cell disruptor or with an Emulsiflex C3 high-pressure homogenizer (Avestin) with 3-4 passages at 15-35 kPsi. The lysate was cleared by ultracentrifugation at 43,000 rpm for 30 min (rotor Beckman 45Ti or 70Ti). The cleared lysate was complemented with 15 mM imidazole pH 7.5 and incubated for 1 h with 3 ml Ni-NTA metal affinity resin (Qiagen). IMAC was performed as described for the transporter. The eluted nanobody was incubated with 3C protease (molar ratio 8:1) during o/n dialysis against 20 mM Hepes pH 7.5, 150 mM NaCl. The his-tagged protease and the cleaved MBP-His_{10}-tag was removed by binding to fresh Ni-NTA (4 ml) resin. The nanobody was concentrated to 20 mg/ml with an Amicon Ultra Centrifugation device (Millipore, MWCO=3 kDa). The filtered (0.22µm centrifugal filter device) nanobody was subjected to SEC, and peak fractions were pooled and used for binding tests with ScaDMT.

Qualitative size exclusion chromatography to test complex-formation of nanobodies with ScaDMT. ScaDMT and the nanobodies were purified separately as described above. 15 µg ScaDMT were mixed with 5 µg nanobody and injected on a Superdex PC 3.2/300 (GE Healthcare) column equilibrated in 20 mM Hepes pH 7.5, 150 mM NaCl, 0.25% DM. The runs were performed on an Agilent 1100 HPLC system (Agilent technologies) and absorbance at 280 nm was recorded.

Large-scale expression of nanobodies and co-crystallization were performed as described (Ehrnstorfer et al., 2014); with following addition: During initial screening the SEC run of the ScaDMT or $ScaDMT^{tru}$ -nanobody complex was performed on a S200 column equilibrated in 10 mM Hepes, 150 mM NaCl, 0.25 % DM.

Expression of seleno-methionine labeled $ScaDMT^{tru}$. An o/n culture of $ScaDMT^{tru}$ grown in TB medium was diluted 1:100 into 50 flasks containing 0.6 l of M9 medium supplemented with trace elements, Kao and Michayluk-Vitamin solution (Sigma), 0.75 % glycerol and 100 mg/l ampicillin. Cells were grown at 37 °C, mild stirring and subsequently the temperature was decreased over 5 h to 24 °C until an OD_{600} of 0.6 was reached. The amino acid cocktail, containing L-Lys, L-Thr, L-Phe (each at a concentration of 125 mg/l), L-Leu, L-Ile and L-Val (each at a concentration of 62.5 mg/l) were added to the culture to inhibit the methionine synthesis pathway (Van Duyne et al., 1993). Cells were allowed to deplete from free L-Met for 1

h followed by addition of 50 mg/l L-seleno-methionine. One hour later, expression was induced by addition of $4*10^{-3}$ (w/v) arabinose. For o/n expression, the temperature was decreased to 18°C. Cells were harvested by centrifugation at 5500 rpm for 15 min at 4 °C (rotor Sorvall F8S6x1000) and lysed by sonication. No membrane vesicles were prepared. Extraction was started from the cleared lysate (supernatant after centrifugation at 10,000 g for 30 min) by addition of 1.5 % DM (Anatrace). Purification and crystallization of the ScaDMT^{tru}-nanobody complex were carried out as described in Ehrnstorfer et al., 2014.

CURRICULUM VITAE

EHRNSTORFER Ines Anna

Date of birth: 28.11.1984
Nationality: Austrian

Address: Sperletweg 36, 8052 Zurich
E-Mail: i.ehrnstorfer@bioc.uzh.ch

Education

Jan 2009 – Jan 2015	**PhD Thesis in the Group of Prof. Raimund Dutzler** Department of Biochemistry, University of Zurich, Switzerland Member of the Biomolecular Structure and Mechanism PhD program of the UZH and ETHZ
2008	**Master Thesis in the Group of Prof. Hans Brandstetter** Title: Prohibitin 1 and 2 from S.cerevidiae – Cloning, Expression and Refolding University of Salzburg, Salzburg, Austria
2007 - 2008	**Master of Science in Molecular Biosciences** University of Salzburg and University of Linz, Salzburg and Linz, Austria
2003 - 2007	**Bachelor of Science in Molecular Biology** University of Salzburg and University of Linz, Salzburg and Linz, Austria
June 2003	**Allgemeine Hochschulreife** Wirtschaftskundliches Realgymnasium, Salzburg, Austria

Advanced Training

since 2012	**Certificate of Advanced Studies** **"Pharmaceuticals - From Research to Market"** Postgraduate studies in pharmaceutical sciences, ETH Zurich, Switzerland

International Conferences

2014	**Gordon Research Conference: Membrane Transport Proteins** Talk and poster presentation, 13.7.- 18.7.2014, West Dover VT, United States
2014	**Gordon Research Conference: Ligand Recognition & Molecular Gating** Poster presentation, 23.3.- 28.3.2014, Ventura CA, United States

Publication

2014	**Crystal structure of a SLC11 (NRAMP) transporter reveals the basis for transition-metal ion transport** Ehrnstorfer I A, Geertsma E R, Pardon E, Steyaert J, Dutzler R Nat Struct Mol Biol, 2014 Nov; 21 (11), 990-6

BIBLIOGRAPHY

Abraham, N.G., and Kappas, A. (2008). Pharmacological and clinical aspects of heme oxygenase. Pharmacol. Rev. *60*, 79–127.

Adams, P.D., Grosse-Kunstleve, R.W., Hung, L.W., Ioerger, T.R., McCoy, A.J., Moriarty, N.W., Read, R.J., Sacchettini, J.C., Sauter, N.K., and Terwilliger, T.C. (2002). PHENIX: building new software for automated crystallographic structure determination. Acta Crystallogr. D. Biol. Crystallogr. *58*, 1948–1954.

Agranoff, D., Monahan, I.M., Mangan, J.A., Butcher, P.D., and Krishna, S. (1999). Mycobacterium tuberculosis expresses a novel pH-dependent divalent cation transporter belonging to the Nramp family. J. Exp. Med. *190*, 717–724.

Altschul, S.F., Gish, W., Miller, W., Myers, E.W., and Lipman, D.J. (1990). Basic local alignment search tool. J. Mol. Biol. *215*, 403–410.

Amunts, A., and Nelson, N. (2009). Plant photosystem I design in the light of evolution. Structure *17*, 637–650.

Andersen, J.K. (2004). Iron dysregulation and Parkinson's disease. J. Alzheimers. Dis. *6*, S47–S52.

Anderson, G.J., Frazer, D.M., and McLaren, G.D. (2009). Iron absorption and metabolism. Curr. Opin. Gastroenterol. *25*, 129–135.

Andrews, N.C. (2008). Forging a field: the golden age of iron biology. Blood *112*, 219–230.

Arnold, F. (2013). Overexpression and Crystallization Trials of Prokaryotic SLC11 Divalent Metal Ion Transporters for Structural Studies. University of Zurich.

Aziz, N., and Munro, H.N. (1987). Iron regulates ferritin mRNA translation through a segment of its 5' untranslated region. Proc. Natl. Acad. Sci. U. S. A. *84*, 8478–8482.

Babitt, J.L., Huang, F.W., Wrighting, D.M., Xia, Y., Sidis, Y., Samad, T.A., Campagna, J.A., Chung, R.T., Schneyer, A.L., Woolf, C.J., et al. (2006). Bone morphogenetic protein signaling by hemojuvelin regulates hepcidin expression. Nat. Genet. *38*, 531–539.

De Back, D.Z., Kostova, E.B., van Kraaij, M., van den Berg, T.K., and van Bruggen, R. (2014). Of macrophages and red blood cells; a complex love story. Front. Physiol. *5*, 9.

Bahassi, E.M., O'Dea, M.H., Allali, N., Messens, J., Gellert, M., and Couturier, M. (1999). Interactions of CcdB with DNA Gyrase: INACTIVATION OF GyrA, POISONING OF THE GYRASE-DNA COMPLEX, AND THE ANTIDOTE ACTION OF CcdA. J. Biol. Chem. *274*, 10936–10944.

Bardou-Jacquet, E., Island, M.-L., Jouanolle, A.-M., Détivaud, L., Fatih, N., Ropert, M., Brissot, E., Mosser, A., Maisonneuve, H., Brissot, P., et al. (2011). A novel N491S mutation in the human SLC11A2 gene impairs protein trafficking and in association with the G212V mutation leads to microcytic anemia and liver iron overload. Blood Cells. Mol. Dis. *47*, 243–248.

Beaumont, C., Delaunay, J., Hetet, G., Grandchamp, B., de Montalembert, M., and Tchernia, G. (2006). Two new human DMT1 gene mutations in a patient with microcytic anemia, low ferritinemia, and liver iron overload. Blood *107*, 4168–4170.

Belouchi, A., Cellier, M., Kwan, T., Saini, H.S., Leroux, G., and Gros, P. (1995). The macrophage-specific membrane protein Nramp controlling natural resistance to infections in mice has homologues expressed in the root system of plants. Plant Mol. Biol. *29*, 1181–1196.

Berg, D., Gerlach, M., Youdim, M.B., Double, K.L., Zecca, L., Riederer, P., and Becker, G. (2001). Brain iron pathways and their relevance to Parkinson's disease. J. Neurochem. *79*, 225–236.

Bernard, P., and Couturier, M. (1992). Cell killing by the F plasmid CcdB protein involves poisoning of DNA-topoisomerase II complexes. J. Mol. Biol. *226*, 735–745.

Bernsel, A., Viklund, H., Falk, J., Lindahl, E., von Heijne, G., and Elofsson, A. (2008). Prediction of membrane-protein topology from first principles. Proc. Natl. Acad. Sci. U. S. A. *105*, 7177–7181.

Bernsel, A., Viklund, H., Hennerdal, A., and Elofsson, A. (2009). TOPCONS: consensus prediction of membrane protein topology. Nucleic Acids Res. *37*, W465–W468.

Block, H., Maertens, B., Spriestersbach, A., Brinker, N., Kubicek, J., Fabis, R., Labahn, J., and Schäfer, F. (2009). Immobilized-metal affinity chromatography (IMAC): a review. Methods Enzymol. *463*, 439–473.

Cadieux, J.A., Zhang, Z., Mattice, M., Brownlie-Cutts, A., Fu, J., Ratkay, L.G., Kwan, R., Thompson, J., Sanghara, J., Zhong, J., et al. (2012). Synthesis and biological evaluation of substituted pyrazoles as blockers of divalent metal transporter 1 (DMT1). Bioorg. Med. Chem. Lett. *22*, 90–95.

Cailliatte, R., Lapeyre, B., Briat, J.-F., Mari, S., and Curie, C. (2009). The NRAMP6 metal transporter contributes to cadmium toxicity. Biochem. J. *422*, 217–228.

Cailliatte, R., Schikora, A., Briat, J.-F., Mari, S., and Curie, C. (2010). High-affinity manganese uptake by the metal transporter NRAMP1 is essential for Arabidopsis growth in low manganese conditions. Plant Cell *22*, 904–917.

Camaschella, C., and Poggiali, E. (2011). Inherited disorders of iron metabolism. Curr. Opin. Pediatr. *23*, 14–20.

Canonne-Hergaux, F., Fleming, M.D., Levy, J.E., Gauthier, S., Ralph, T., Picard, V., Andrews, N.C., and Gros, P. (2000). The Nramp2/DMT1 iron transporter is induced in the duodenum of microcytic anemia mk mice but is not properly targeted to the intestinal brush border. Blood *96*, 3964–3970.

Canonne-Hergaux, F., Levy, J.E., Fleming, M.D., Montross, L.K., Andrews, N.C., and Gros, P. (2001). Expression of the DMT1 (NRAMP2/DCT1) iron transporter in mice with genetic iron overload disorders. Blood *97*, 1138–1140.

Casadaban, M.J., and Cohen, S.N. (1980). Analysis of gene control signals by DNA fusion and cloning in Escherichia coli. J. Mol. Biol. *138*, 179–207.

Casey, J.L., Koeller, D.M., Ramin, V.C., Klausner, R.D., and Harford, J.B. (1989). Iron regulation of transferrin receptor mRNA levels requires iron-responsive elements and a rapid turnover determinant in the 3' untranslated region of the mRNA. EMBO J. *8*, 3693–3699.

Caughman, S.W., Hentze, M.W., Rouault, T.A., Harford, J.B., and Klausner, R.D. (1988). The iron-responsive element is the single element responsible for iron-dependent translational regulation of ferritin biosynthesis. Evidence for function as the binding site for a translational repressor. J. Biol. Chem. *263*, 19048–19052.

Cellier, M.F.M. (2012a). Nutritional immunity: homology modeling of Nramp metal import. Adv. Exp. Med. Biol. *946*, 335–351.

Cellier, M.F.M. (2012b). Nramp: from sequence to structure and mechanism of divalent metal import. Curr. Top. Membr. *69*, 249–293.

Cellier, M., Govoni, G., Vidal, S., Kwan, T., Groulx, N., Liu, J., Sanchez, F., Skamene, E., Schurr, E., and Gros, P. (1994). Human natural resistance-associated macrophage protein: cDNA cloning, chromosomal mapping, genomic organization, and tissue-specific expression. J. Exp. Med. *180*, 1741–1752.

Cellier, M., Privé, G., Belouchi, A., Kwan, T., Rodrigues, V., Chia, W., and Gros, P. (1995). Nramp defines a family of membrane proteins. Proc. Natl. Acad. Sci. U. S. A. *92*, 10089–10093.

De Champdoré, M., Staiano, M., Rossi, M., and D'Auria, S. (2007). Proteins from extremophiles as stable tools for advanced biotechnological applications of high social interest. J. R. Soc. Interface *4*, 183–191.

Chen, J., and Enns, C.A. (2012). Hereditary hemochromatosis and transferrin receptor 2. Biochim. Biophys. Acta *1820*, 256–263.

Chu, B.C., Garcia-Herrero, A., Johanson, T.H., Krewulak, K.D., Lau, C.K., Peacock, R.S., Slavinskaya, Z., and Vogel, H.J. (2010). Siderophore uptake in bacteria and the battle for iron with the host; a bird's eye view. Biometals *23*, 601–611.

Cooper, C. a, Shayeghi, M., Techau, M.E., Capdevila, D.M., MacKenzie, S., Durrant, C., and Bury, N.R. (2007). Analysis of the rainbow trout solute carrier 11 family reveals iron import < or = pH 7.4 and a functional isoform lacking transmembrane domains 11 and 12. FEBS Lett. *581*, 2599–2604.

Courville, P., Chaloupka, R., Veyrier, F., and Cellier, M.F.M. (2004). Determination of transmembrane topology of the Escherichia coli natural resistance-associated macrophage protein (Nramp) ortholog. J. Biol. Chem. *279*, 3318–3326.

Courville, P., Urbankova, E., Rensing, C., Chaloupka, R., Quick, M., and Cellier, M.F.M. (2008). Solute carrier 11 cation symport requires distinct residues in transmembrane helices 1 and 6. J. Biol. Chem. *283*, 9651–9658.

Cowtan, K. (1994). DM: an automated procedure for phase improvement by density modification. Newslett. Protein Crystallogr. *31*, 34–38.

Craven, C.M., Alexander, J., Eldridge, M., Kushner, J.P., Bernstein, S., and Kaplan, J. (1987). Tissue distribution and clearance kinetics of non-transferrin-bound iron in the hypotransferrinemic mouse: a rodent model for hemochromatosis. Proc. Natl. Acad. Sci. *84*, 3457–3461.

Curie, C., Alonso, J.M., Le Jean, M., Ecker, J.R., and Briat, J.F. (2000). Involvement of NRAMP1 from Arabidopsis thaliana in iron transport. Biochem. J. *347 Pt 3*, 749–755.

Czachorowski, M., Lam-Yuk-Tseung, S., Cellier, M., and Gros, P. (2009). Transmembrane topology of the mammalian Slc11a2 iron transporter. Biochemistry *48*, 8422–8434.

Darszon, A. (1979). Incorporation of membrane proteins into large single bilayer vesicles. Application to rhodopsin. J. Cell Biol. *81*, 446–452.

Dautry-Varsat, A., Ciechanover, A., and Lodish, H.F. (1983). pH and the recycling of transferrin during receptor-mediated endocytosis. Proc. Natl. Acad. Sci. *80*, 2258–2262.

Delaby, C., Vialaret, J., Bros, P., Gabelle, A., Lefebvre, T., Puy, H., Hirtz, C., and Lehmann, S. (2014). Clinical measurement of Hepcidin-25 in human serum: Is quantitative mass spectrometry up to the job? EuPA Open Proteomics *3*, 60–67.

Doherty, A.J., Ashford, S.R., Brannigan, J.A., and Wigley, D.B. (1995). A superior host strain for the over-expression of cloned genes using the T7 promoter based vectors. Nucleic Acids Res. *23*, 2074–2075.

De Domenico, I., McVey Ward, D., and Kaplan, J. (2008). Regulation of iron acquisition and storage: consequences for iron-linked disorders. Nat. Rev. Mol. Cell Biol. *9*, 72–81.

Donovan, A., Lima, C.A., Pinkus, J.L., Pinkus, G.S., Zon, L.I., Robine, S., and Andrews, N.C. (2005). The iron exporter ferroportin/Slc40a1 is essential for iron homeostasis. Cell Metab. *1*, 191–200.

Dosik, J.K., Barton, C.H., Holiday, D.L., Krall, M.M., Blackwell, J.M., and Mock, B.A. (1994). An Nramp-related sequence maps to mouse chromosome 17. Mamm. Genome *5*, 458–460.

Doublié, S. (2007). Production of selenomethionyl proteins in prokaryotic and eukaryotic expression systems. Methods Mol. Biol. *363*, 91–108.

Drew, D., Sjöstrand, D., Nilsson, J., Urbig, T., Chin, C., de Gier, J.-W., and von Heijne, G. (2002). Rapid topology mapping of Escherichia coli inner-membrane proteins by prediction and PhoA/GFP fusion analysis. Proc. Natl. Acad. Sci. U. S. A. *99*, 2690–2695.

Drew, D., Slotboom, D.-J., Friso, G., Reda, T., Genevaux, P., Rapp, M., Meindl-Beinker, N.M., Lambert, W., Lerch, M., Daley, D.O., et al. (2005). A scalable, GFP-based pipeline for membrane protein overexpression screening and purification. Protein Sci. *14*, 2011–2017.

Drew, D., Lerch, M., Kunji, E., Slotboom, D.-J., and de Gier, J.-W. (2006). Optimization of membrane protein overexpression and purification using GFP fusions. Nat. Methods *3*, 303–313.

Drew, D., Newstead, S., Sonoda, Y., Kim, H., von Heijne, G., and Iwata, S. (2008). GFP-based optimization scheme for the overexpression and purification of eukaryotic membrane proteins in Saccharomyces cerevisiae. Nat. Protoc. *3*, 784–798.

Van Duyne, G.D., Standaert, R.F., Karplus, P.A., Schreiber, S.L., and Clardy, J. (1993). Atomic structures of the human immunophilin FKBP-12 complexes with FK506 and rapamycin. J. Mol. Biol. *229*, 105–124.

Ehrnstorfer, I.A., Geertsma, E.R., Pardon, E., Steyaert, J., and Dutzler, R. (2014). Crystal structure of a SLC11 (NRAMP) transporter reveals the basis for transition-metal ion transport. Nat. Struct. Mol. Biol. 990–996.

Eisen, H.N., and Siskind, G.W. (1964). Variations in Affinities of Antibodies during the Immune Response *. Biochemistry *3*, 996–1008.

Emsley, P., and Cowtan, K. (2004). Coot: Model-building tools for molecular graphics. Acta Crystallogr. Sect. D Biol. Crystallogr. *60*, 2126–2132.

Esposito, D., and Chatterjee, D.K. (2006). Enhancement of soluble protein expression through the use of fusion tags. Curr. Opin. Biotechnol. *17*, 353–358.

Evdokimov, A. Making Se-Met proteins in non-auxotrophic E.coli http://www.xtals.org, 09/2014.

Fagerberg, L., Jonasson, K., von Heijne, G., Uhlén, M., and Berglund, L. (2010). Prediction of the human membrane proteome. Proteomics *10*, 1141–1149.

Faham, S., Watanabe, A., Besserer, G.M., Cascio, D., Specht, A., Hirayama, B.A., Wright, E.M., and Abramson, J. (2008). The crystal structure of a sodium galactose transporter reveals mechanistic insights into Na+/sugar symport. Science *321*, 810–814.

Fallingborg, J. (1999). Intraluminal pH of the human gastrointestinal tract. Dan. Med. Bull. *46*, 183–196.

Fang, Y., Jayaram, H., Shane, T., Kolmakova-Partensky, L., Wu, F., Williams, C., Xiong, Y., and Miller, C. (2009). Structure of a prokaryotic virtual proton pump at 3.2 A resolution. Nature *460*, 1040–1043.

Feder, J.N., Gnirke, A., Thomas, W., Tsuchihashi, Z., Ruddy, D.A., Basava, A., Dormishian, F., Domingo, R., Ellis, M.C., Fullan, A., et al. (1996). A novel MHC class I-like gene is mutated in patients with hereditary haemochromatosis. Nat. Genet. *13*, 399–408.

Fernandes, A., Preza, G.C., Phung, Y., De Domenico, I., Kaplan, J., Ganz, T., and Nemeth, E. (2009). The molecular basis of hepcidin-resistant hereditary hemochromatosis. Blood *114*, 437–443.

Finberg, K.E., Heeney, M.M., Campagna, D.R., Aydinok, Y., Pearson, H.A., Hartman, K.R., Mayo, M.M., Samuel, S.M., Strouse, J.J., Markianos, K., et al. (2008). Mutations in TMPRSS6 cause iron-refractory iron deficiency anemia (IRIDA). Nat. Genet. *40*, 569–571.

Forbes, J.R., and Gros, P. (2001). Divalent-metal transport by NRAMP proteins at the interface of host–pathogen interactions. Trends Microbiol. *9*, 397–403.

Forbes, J.R., and Gros, P. (2003). Iron, manganese, and cobalt transport by Nramp1 (Slc11a1) and Nramp2 (Slc11a2) expressed at the plasma membrane. Blood *102*, 1884–1892.

Forrest, L.R., and Rudnick, G. (2009). The rocking bundle: a mechanism for ion-coupled solute flux by symmetrical transporters. Physiology (Bethesda). *24*, 377–386.

Forrest, L.R., Krämer, R., and Ziegler, C. (2011). The structural basis of secondary active transport mechanisms. Biochim. Biophys. Acta *1807*, 167–188.

Ganz, T., and Nemeth, E. (2012). Hepcidin and iron homeostasis. Biochim. Biophys. Acta *1823*, 1434–1443.

Gao, X., Lu, F., Zhou, L., Dang, S., Sun, L., Li, X., Wang, J., and Shi, Y. (2009). Structure and mechanism of an amino acid antiporter. Science *324*, 1565–1568.

Gao, X., Zhou, L., Jiao, X., Lu, F., Yan, C., Zeng, X., Wang, J., and Shi, Y. (2010). Mechanism of substrate recognition and transport by an amino acid antiporter. Nature *463*, 828–832.

Geertsma, E.R., and Dutzler, R. (2011). A versatile and efficient high-throughput cloning tool for structural biology. Biochemistry *50*, 3272–3278.

Geertsma, E.R., Groeneveld, M., Slotboom, D.-J., and Poolman, B. (2008a). Quality control of overexpressed membrane proteins. Proc. Natl. Acad. Sci. U. S. A. *105*, 5722–5727.

Geertsma, E.R., Nik Mahmood, N.A.B., Schuurman-Wolters, G.K., and Poolman, B. (2008b). Membrane reconstitution of ABC transporters and assays of translocator function. Nat. Protoc. *3*, 256–266.

De Genst, E., Silence, K., Decanniere, K., Conrath, K., Loris, R., Kinne, J., Muyldermans, S., and Wyns, L. (2006). Molecular basis for the preferential cleft recognition by dromedary heavy-chain antibodies. Proc. Natl. Acad. Sci. U. S. A. *103*, 4586–4591.

Gera, N., Hussain, M., and Rao, B.M. (2013). Protein selection using yeast surface display. Methods *60*, 15–26.

Giannetti, A.M., and Björkman, P.J. (2004). HFE and transferrin directly compete for transferrin receptor in solution and at the cell surface. J. Biol. Chem. *279*, 25866–25875.

Gomes, M.S., Boelaert, J.R., and Appelberg, R. (2001). Role of iron in experimental Mycobacterium avium infection. J. Clin. Virol. *20*, 117–122.

Goujon, M., McWilliam, H., Li, W., Valentin, F., Squizzato, S., Paern, J., and Lopez, R. (2010). A new bioinformatics analysis tools framework at EMBL-EBI. Nucleic Acids Res. *38*, W695–W699.

Gourdon, P., Andersen, J.L., Hein, K.L., Bublitz, M., Pedersen, B.P., Liu, X.-Y., Yatime, L., Nyblom, M., Nielsen, T.T., Olesen, C., et al. (2011). HiLiDe—Systematic Approach to Membrane Protein Crystallization in Lipid and Detergent. Cryst. Growth Des. *11*, 2098–2106.

Govoni, G., Gauthier, S., Billia, F., Iscove, N.N., and Gros, P. (1997). Cell-specific and inducible Nramp1 gene expression in mouse macrophages in vitro and in vivo. J. Leukoc. Biol. *62*, 277–286.

Grenha, R., Slamti, L., Nicaise, M., Refes, Y., Lereclus, D., and Nessler, S. (2013). Structural basis for the activation mechanism of the PlcR virulence regulator by the quorum-sensing signal peptide PapR. Proc. Natl. Acad. Sci. U. S. A. *110*, 1047–1052.

Gruenheid, S., Cellier, M., Vidal, S., and Gros, P. (1995). Identification and characterization of a second mouse Nramp gene. Genomics *25*, 514–525.

Gruenheid, S., Canonne-Hergaux, F., Gauthier, S., Hackam, D.J., Grinstein, S., and Gros, P. (1999). The Iron Transport Protein NRAMP2 Is an Integral Membrane Glycoprotein That Colocalizes with Transferrin in Recycling Endosomes. J. Exp. Med. *189*, 831–841.

Guerinot, M.L. (1994). Microbial iron transport. Annu. Rev. Microbiol. *48*, 743–772.

Gunshin, H., Mackenzie, B., Berger, U. V, Gunshin, Y., Romero, M.F., Boron, W.F., Nussberger, S., Gollan, J.L., and Hediger, M. a (1997). Cloning and characterization of a mammalian proton-coupled metal-ion transporter. Nature *388*, 482–488.

Gunshin, H., Starr, C.N., Direnzo, C., Fleming, M.D., Jin, J., Greer, E.L., Sellers, V.M., Galica, S.M., and Andrews, N.C. (2005). Cybrd1 (duodenal cytochrome b) is not necessary for dietary iron absorption in mice. Blood *106*, 2879–2883.

Hall, J.L., and Williams, L.E. (2003). Transition metal transporters in plants. J. Exp. Bot. *54*, 2601–2613.

Hamers-Casterman, C., Atarhouch, T., Muyldermans, S., Robinson, G., Hamers, C., Songa, E.B., Bendahman, N., and Hamers, R. (1993). Naturally occurring antibodies devoid of light chains. Nature *363*, 446–448.

Harrison, P.M., and Arosio, P. (1996). The ferritins: molecular properties, iron storage function and cellular regulation. Biochim. Biophys. Acta *1275*, 161–203.

Von Heijne, G. (2006). Membrane-protein topology. Nat. Rev. Mol. Cell Biol. *7*, 909–918.

Hendrickson, W.A., Horton, J.R., and LeMaster, D.M. (1990). Selenomethionyl proteins produced for analysis by multiwavelength anomalous diffraction (MAD): a vehicle for direct determination of three-dimensional structure. EMBO J. *9*, 1665–1672.

Hentze, M.W., Caughman, S.W., Rouault, T.A., Barriocanal, J.G., Dancis, A., Harford, J.B., and Klausner, R.D. (1987). Identification of the iron-responsive element for the translational regulation of human ferritin mRNA. Science *238*, 1570–1573.

Hentze, M.W., Muckenthaler, M.U., Galy, B., and Camaschella, C. (2010). Two to tango: regulation of Mammalian iron metabolism. Cell *142*, 24–38.

Hershko, C., and Skikne, B. (2009). Pathogenesis and management of iron deficiency anemia: emerging role of celiac disease, helicobacter pylori, and autoimmune gastritis. Semin. Hematol. *46*, 339–350.

Hicke, L., and Dunn, R. (2003). Regulation of membrane protein transport by ubiquitin and ubiquitin-binding proteins. Annu. Rev. Cell Dev. Biol. *19*, 141–172.

Hirsch, E.C. (2009). Iron transport in Parkinson's disease. Parkinsonism Relat. Disord. *15 Suppl 3*, S209–S211.

Inagaki, S., Ghirlando, R., and Grisshammer, R. (2013). Biophysical characterization of membrane proteins in nanodiscs. Methods *59*, 287–300.

Iolascon, A., and De Falco, L. (2009). Mutations in the gene encoding DMT1: clinical presentation and treatment. Semin. Hematol. *46*, 358–370.

Iolascon, A., d'Apolito, M., Servedio, V., Cimmino, F., Piga, A., and Camaschella, C. (2006). Microcytic anemia and hepatic iron overload in a child with compound heterozygous mutations in DMT1 (SCL11A2). Blood *107*, 349–354.

J. Sambrook, D.W.R. (2001). Molecular cloning, a laboratory manual (Cold Spring Harbor Laboratory).

Jabado, N. (2000). Natural resistance to intracellular infections: natural resistance-associated macrophage protein 1 (NRAMP1) functions as a pH-dependent manganese transporter at the phagosomal membrane. J. Exp. Med. *192*, 1237–1248.

Jabado, N., Canonne-Hergaux, F., Gruenheid, S., Picard, V., and Gros, P. (2002). Iron transporter Nramp2/DMT-1 is associated with the membrane of phagosomes in macrophages and Sertoli cells. Blood *100*, 2617–2622.

Janeway, J. (2001). The generation of diversity in immunoglobulins.

Jardetzky, O. (1966). Simple Allosteric Model for Membrane Pumps. Nature *211*, 969–970.

Jefferies, W.A., Brandon, M.R., Hunt, S. V, Williams, A.F., Gatter, K.C., and Mason, D.Y. (1984). Transferrin receptor on endothelium of brain capillaries. Nature *312*, 162–163.

Kabsch, W. (1993). Automatic processing of rotation diffraction data from crystals of initially unknown symmetry and cell constants. J. Appl. Crystallogr. *26*, 795–800.

Kantardjieff, K.A., and Rupp, B. (2003). Matthews coefficient probabilities: Improved estimates for unit cell contents of proteins, DNA, and protein-nucleic acid complex crystals. Protein Sci. *12*, 1865–1871.

Kawate, T., and Gouaux, E. (2006). Fluorescence-detection size-exclusion chromatography for precrystallization screening of integral membrane proteins. Structure *14*, 673–681.

Kazmier, K., Sharma, S., Quick, M., Islam, S.M., Roux, B., Weinstein, H., Javitch, J.A., and McHaourab, H.S. (2014). Conformational dynamics of ligand-dependent alternating access in LeuT. Nat. Struct. Mol. Biol. *21*, 472–479.

Kehres, D.G., and Maguire, M.E. (2003). Emerging themes in manganese transport, biochemistry and pathogenesis in bacteria. FEMS Microbiol. Rev. *27*, 263–290.

Kehres, D.G., Zaharik, M.L., Finlay, B.B., and Maguire, M.E. (2000). The NRAMP proteins of Salmonella typhimurium and Escherichia coli are selective manganese transporters involved in the response to reactive oxygen. Mol. Microbiol. *36*, 1085–1100.

De Kerpel, M., Van Molle, I., Brys, L., Wyns, L., De Greve, H., and Bouckaert, J. (2006). N-terminal truncation enables crystallization of the receptor-binding domain of the FedF bacterial adhesin. Acta Crystallogr. Sect. F. Struct. Biol. Cryst. Commun. *62*, 1278–1282.

Kishi, F. (1994). Isolation and characterization of human Nramp cDNA. Biochem. Biophys. Res. Commun. *204*, 1074–1080.

Koide, S. (2009). Engineering of recombinant crystallization chaperones. Curr. Opin. Struct. Biol. *19*, 449–457.

Kong, S.K., and Lee, C.Y. (1995). The use of fura 2 for measurement of free calcium concentration. Biochem. Educ. *23*, 97–98.

Krishnamurthy, H., and Gouaux, E. (2012). X-ray structures of LeuT in substrate-free outward-open and apo inward-open states. Nature *481*, 469–474.

Kuhn, D.E., Baker, B.D., Lafuse, W.P., and Zwilling, B.S. (1999). Differential iron transport into phagosomes isolated from the RAW264.7 macrophage cell lines transfected with Nramp1Gly169 or Nramp1Asp169. J. Leukoc. Biol. *66*, 113–119.

Kuhn, D.E., Lafuse, W.P., and Zwilling, B.S. (2001). Iron transport into mycobacterium avium-containing phagosomes from an Nramp1(Gly169)-transfected RAW264.7 macrophage cell line. J. Leukoc. Biol. *69*, 43–49.

Kunji, E.R.S., Harding, M., Butler, P.J.G., and Akamine, P. (2008). Determination of the molecular mass and dimensions of membrane proteins by size exclusion chromatography. Methods *46*, 62–72.

De La Fortelle, E., and Bricogne, G. (1997). Macromolecular Crystallography Part A (Elsevier).

Laederach, J. (2011). Identification and Overexpression of Prokaryotic SLC11 Divalent Metal Ion Transporters for Structural Studies. University of Zurich.

Landau, E.M., and Rosenbusch, J.P. (1996). Lipidic cubic phases: A novel concept for the crystallization of membrane proteins. Proc. Natl. Acad. Sci. *93*, 14532–14535.

Lanquar, V., Ramos, M.S., Lelièvre, F., Barbier-Brygoo, H., Krieger-Liszkay, A., Krämer, U., and Thomine, S. (2010). Export of vacuolar manganese by AtNRAMP3 and AtNRAMP4 is required for optimal photosynthesis and growth under manganese deficiency. Plant Physiol. *152*, 1986–1999.

Larkin, M.A., Blackshields, G., Brown, N.P., Chenna, R., McGettigan, P.A., McWilliam, H., Valentin, F., Wallace, I.M., Wilm, A., Lopez, R., et al. (2007). Clustal W and Clustal X version 2.0. Bioinformatics *23*, 2947–2948.

Lee, D.W., and Andersen, J.K. (2010). Iron elevations in the aging Parkinsonian brain: a consequence of impaired iron homeostasis? J. Neurochem. *112*, 332–339.

Lewin, M.R., Wills, M.R., and Baron, D.N. (1969). Ultramicrofluorimetric determination of calcium in plasma. J. Clin. Pathol. *22*, 222–225.

Li, J.-Y., Liu, J., Dong, D., Jia, X., McCouch, S.R., and Kochian, L. V (2014). Natural variation underlies alterations in Nramp aluminum transporter (NRAT1) expression and function that play a key role in rice aluminum tolerance. Proc. Natl. Acad. Sci. U. S. A. *111*, 6503–6508.

Lieberman, R.L., Culver, J.A., Entzminger, K.C., Pai, J.C., and Maynard, J.A. (2011). Crystallization chaperone strategies for membrane proteins. Methods *55*, 293–302.

Lim, H.-H., and Miller, C. (2009). Intracellular proton-transfer mutants in a CLC Cl-/H+ exchanger. J. Gen. Physiol. *133*, 131–138.

Lim, H.-H., Shane, T., and Miller, C. (2012). Intracellular proton access in a Cl(-)/H(+) antiporter. PLoS Biol. *10*, e1001441.

Lipovsek, D., and Plückthun, A. (2004). In-vitro protein evolution by ribosome display and mRNA display. J. Immunol. Methods *290*, 51–67.

Liu, H., Huang, R.Y.-C., Chen, J., Gross, M.L., and Pakrasi, H.B. (2011). Psb27, a transiently associated protein, binds to the chlorophyll binding protein CP43 in photosystem II assembly intermediates. Proc. Natl. Acad. Sci. U. S. A. *108*, 18536–18541.

Liu, Q., Davidoff, O., Niss, K., and Haase, V.H. (2012). Hypoxia-inducible factor regulates hepcidin via erythropoietin-induced erythropoiesis. J. Clin. Invest. *122*, 4635–4644.

Loland, C.J. (2014). The use of LeuT as a model in elucidating binding sites for substrates and inhibitors in neurotransmitter transporters. Biochim. Biophys. Acta.

Löw, C., Yau, Y.H., Pardon, E., Jegerschöld, C., Wåhlin, L., Quistgaard, E.M., Moberg, P., Geifman-Shochat, S., Steyaert, J., and Nordlund, P. (2013). Nanobody mediated crystallization of an archeal mechanosensitive channel. PLoS One *8*, e77984.

Ludwiczek, S., Theurl, I., Muckenthaler, M.U., Jakab, M., Mair, S.M., Theurl, M., Kiss, J., Paulmichl, M., Hentze, M.W., Ritter, M., et al. (2007). Ca2+ channel blockers reverse iron overload by a new mechanism via divalent metal transporter-1. Nat. Med. *13*, 448–454.

Ma, D., Lu, P., Yan, C., Fan, C., Yin, P., Wang, J., and Shi, Y. (2012). Structure and mechanism of a glutamate-GABA antiporter. Nature *483*, 632–636.

MacCallum, R.M. (2004). Striped sheets and protein contact prediction. Bioinformatics *20 Suppl 1*, i224–i231.

Mackenzie, B., Ujwal, M.L., Chang, M.-H., Romero, M.F., and Hediger, M. a (2006). Divalent metal-ion transporter DMT1 mediates both H+ -coupled Fe2+ transport and uncoupled fluxes. Pflugers Arch. *451*, 544–558.

Mackenzie, B., Takanaga, H., Hubert, N., Rolfs, A., and Hediger, M.A. (2007). Functional properties of multiple isoforms of human divalent metal-ion transporter 1 (DMT1). Biochem. J. *403*, 59–69.

Mackenzie, B., Shawki, A., Ghio, A.J., Stonehuerner, J.D., Zhao, L., Ghadersohi, S., Garrick, L.M., and Garrick, M.D. (2010). Calcium-channel blockers do not affect iron transport mediated by divalent metal-ion transporter-1. Blood *115*, 4148–4149.

Maisetta, G., Vitali, A., Scorciapino, M.A., Rinaldi, A.C., Petruzzelli, R., Brancatisano, F.L., Esin, S., Stringaro, A., Colone, M., Luzi, C., et al. (2013). pH-dependent disruption of Escherichia coli ATCC 25922 and model membranes by the human antimicrobial peptides hepcidin 20 and 25. FEBS J. *280*, 2842–2854.

Makui, H., Roig, E., Cole, S.T., Helmann, J.D., Gros, P., Cellier, M.F.M., and Hv, L. (2000). Identification of the Escherichia coli K-12 Nramp orthologue (MntH) as a selective divalent metal ion transporter. Mol. Microbiol. *35*, 1065–1078.

Malinauskaite, L., Quick, M., Reinhard, L., Lyons, J. a, Yano, H., Javitch, J. a, and Nissen, P. (2014). A mechanism for intracellular release of Na(+) by neurotransmitter/sodium symporters. Nat. Struct. Mol. Biol. 1–9.

Malo, D., Vogan, K., Vidal, S., Hu, J., Cellier, M., Schurr, E., Fuks, A., Bumstead, N., Morgan, K., and Gros, P. (1994). Haplotype mapping and sequence analysis of the mouse Nramp gene predict susceptibility to infection with intracellular parasites. Genomics *23*, 51–61.

Maser, P. (2001). Phylogenetic Relationships within Cation Transporter Families of Arabidopsis. PLANT Physiol. *126*, 1646–1667.

Matthews, B.W. (1968). Solvent content of protein crystals. J. Mol. Biol. *33*, 491–497.

McKie, A.T. (2008). The role of Dcytb in iron metabolism: an update.

McKie, A.T., Barrow, D., Latunde-Dada, G.O., Rolfs, A., Sager, G., Mudaly, E., Mudaly, M., Richardson, C., Barlow, D., Bomford, A., et al. (2001). An iron-regulated ferric reductase associated with the absorption of dietary iron. Science *291*, 1755–1759.

McWilliam, H., Li, W., Uludag, M., Squizzato, S., Park, Y.M., Buso, N., Cowley, A.P., and Lopez, R. (2013). Analysis Tool Web Services from the EMBL-EBI. Nucleic Acids Res. *41*, W597–W600.

Mills, R.F., Krijger, G.C., Baccarini, P.J., Hall, J.L., and Williams, L.E. (2003). Functional expression of AtHMA4, a P1B-type ATPase of the Zn/Co/Cd/Pb subclass. Plant J. *35*, 164–176.

Mims, M.P., Guan, Y., Pospisilova, D., Priwitzerova, M., Indrak, K., Ponka, P., Divoky, V., and Prchal, J.T. (2005). Identification of a human mutation of DMT1 in a patient with microcytic anemia and iron overload. Blood *105*, 1337–1342.

Mitchell, P. (1957). A General Theory of Membrane Transport From Studies of Bacteria. Nature *180*, 134–136.

Mock, D.M., Matthews, N.I., Zhu, S., Strauss, R.G., Schmidt, R.L., Nalbant, D., Cress, G.A., and Widness, J.A. (2011). Red blood cell (RBC) survival determined in humans using RBCs labeled at multiple biotin densities. Transfusion *51*, 1047–1057.

Mori, S., and Barth, H.G. (1999). Size Exclusion Chromatography (Berlin, Heidelberg: Springer Berlin Heidelberg).

Munro, H.N., and Linder, M.C. (1978). Ferritin: structure, biosynthesis, and role in iron metabolism. Physiol. Rev. *58*, 317–396.

Nairz, M., Schroll, A., Sonnweber, T., and Weiss, G. (2010). The struggle for iron - a metal at the host-pathogen interface. Cell. Microbiol. *12*, 1691–1702.

Nairz, M., Haschka, D., Demetz, E., and Weiss, G. (2014). Iron at the interface of immunity and infection. Front. Pharmacol. *5*, 152.

Nemeth, E., Tuttle, M.S., Powelson, J., Vaughn, M.B., Donovan, A., Ward, D.M., Ganz, T., and Kaplan, J. (2004). Hepcidin regulates cellular iron efflux by binding to ferroportin and inducing its internalization. Science *306*, 2090–2093.

Ng, D.P., Poulsen, B.E., and Deber, C.M. (2012). Membrane protein misassembly in disease. Biochim. Biophys. Acta *1818*, 1115–1122.

Ohgami, R.S., Campagna, D.R., McDonald, A., and Fleming, M.D. (2006). The Steap proteins are metalloreductases. Blood *108*, 1388–1394.

Oomen, R.J.F.J., Wu, J., Lelièvre, F., Blanchet, S., Richaud, P., Barbier-Brygoo, H., Aarts, M.G.M., and Thomine, S. (2009). Functional characterization of NRAMP3 and NRAMP4 from the metal hyperaccumulator Thlaspi caerulescens. New Phytol. *181*, 637–650.

P Truffa-Bachi, and, and Cohen, G.N. (1968). Some Aspects of Amino Acid Biosynthesis in Microorganisms.

Pagani, I., Liolios, K., Jansson, J., Chen, I.-M.A., Smirnova, T., Nosrat, B., Markowitz, V.M., and Kyrpides, N.C. (2012). The Genomes OnLine Database (GOLD) v.4: status of genomic and metagenomic projects and their associated metadata. Nucleic Acids Res. *40*, D571–D579.

Pardon, E., Laeremans, T., Triest, S., Rasmussen, S.G.F., Wohlkönig, A., Ruf, A., Muyldermans, S., Hol, W.G.J., Kobilka, B.K., and Steyaert, J. (2014). A general protocol for the generation of Nanobodies for structural biology. Nat. Protoc. *9*, 674–693.

Park, E., and Rapoport, T.A. (2012). Mechanisms of Sec61/SecY-mediated protein translocation across membranes. Annu. Rev. Biophys. *41*, 21–40.

Park, C.H., Valore, E. V, Waring, A.J., and Ganz, T. (2001). Hepcidin, a urinary antimicrobial peptide synthesized in the liver. J. Biol. Chem. *276*, 7806–7810.

Pavlidou, M., Hänel, K., Möckel, L., and Willbold, D. (2013). Nanodiscs allow phage display selection for ligands to non-linear epitopes on membrane proteins. PLoS One *8*, e72272.

Penmatsa, A., and Gouaux, E. (2014). How LeuT shapes our understanding of the mechanisms of sodium-coupled neurotransmitter transporters. J. Physiol. *592*, 863–869.

Penmatsa, A., Wang, K.H., and Gouaux, E. (2013). X-ray structure of dopamine transporter elucidates antidepressant mechanism. Nature *503*, 85–90.

Perez, C., and Ziegler, C. (2013). Mechanistic aspects of sodium-binding sites in LeuT-like fold symporters. Biol. Chem. *394*, 641–648.

Perez, C., Koshy, C., Yildiz, O., and Ziegler, C. (2012). Alternating-access mechanism in conformationally asymmetric trimers of the betaine transporter BetP. Nature *490*, 126–130.

Pietrangelo, A. (2007). Hemochromatosis: an endocrine liver disease. Hepatology *46*, 1291–1301.

Pigeon, C., Ilyin, G., Courselaud, B., Leroyer, P., Turlin, B., Brissot, P., and Loréal, O. (2001). A new mouse liver-specific gene, encoding a protein homologous to human antimicrobial peptide hepcidin, is overexpressed during iron overload. J. Biol. Chem. *276*, 7811–7819.

Plant, J., and Glynn, A.A. (1974). Natural resistance to Salmonella infection, delayed hypersensitivity and Ir genes in different strains of mice. Nature *248*, 345–347.

Plant, J., and Glynn, A.A. (1976). Genetics of Resistance to Infection with Salmonella typhimurium in Mice. J. Infect. Dis. *133*, 72–78.

Plant, J., and Glynn, A.A. (1979). Locating salmonella resistance gene on mouse chromosome 1. Clin. Exp. Immunol. *37*, 1–6.

Ponka, P., and Lok, C.N. (1999). The transferrin receptor: role in health and disease. Int. J. Biochem. Cell Biol. *31*, 1111–1137.

Porath, J., and Flodin, P. (1959). Gel filtration: a method for desalting and group separation. Nature *183*, 1657–1659.

Porath, J., Carlsson, J., Olsson, I., and Belfrage, G. (1975). Metal chelate affinity chromatography, a new approach to protein fractionation. Nature *258*, 598–599.

Rajagopal, A., Rao, A.U., Amigo, J., Tian, M., Upadhyay, S.K., Hall, C., Uhm, S., Mathew, M.K., Fleming, M.D., Paw, B.H., et al. (2008). Haem homeostasis is regulated by the conserved and concerted functions of HRG-1 proteins. Nature *453*, 1127–1131.

Ramalingam, T.S., West, A.P., Lebrón, J.A., Nangiana, J.S., Hogan, T.H., Enns, C.A., and Bjorkman, P.J. (2000). Binding to the transferrin receptor is required for endocytosis of HFE and regulation of iron homeostasis. Nat. Cell Biol. *2*, 953–957.

Rasmussen, S.G.F., Choi, H.-J., Fung, J.J., Pardon, E., Casarosa, P., Chae, P.S., Devree, B.T., Rosenbaum, D.M., Thian, F.S., Kobilka, T.S., et al. (2011). Structure of a nanobody-stabilized active state of the β(2) adrenoceptor. Nature *469*, 175–180.

Ressl, S., Terwisscha van Scheltinga, A.C., Vonrhein, C., Ott, V., and Ziegler, C. (2009). Molecular basis of transport and regulation in the Na(+)/betaine symporter BetP. Nature *458*, 47–52.

Roetto, A., Daraio, F., Alberti, F., Porporato, P., Calì, A., De Gobbi, M., and Camaschella, C. (2002). Hemochromatosis due to mutations in transferrin receptor 2. Blood Cells. Mol. Dis. *29*, 465–470.

Rosenbaum, D.M., Cherezov, V., Hanson, M. a, Rasmussen, S.G.F., Thian, F.S., Kobilka, T.S., Choi, H.-J., Yao, X.-J., Weis, W.I., Stevens, R.C., et al. (2007). GPCR engineering yields high-resolution structural insights into beta2-adrenergic receptor function. Science *318*, 1266–1273.

Rouault, T.A., Hentze, M.W., Caughman, S.W., Harford, J.B., and Klausner, R.D. (1988). Binding of a cytosolic protein to the iron-responsive element of human ferritin messenger RNA. Science *241*, 1207–1210.

Rudnick, G. (2013). How do transporters couple solute movements? Mol. Membr. Biol. *30*, 355–359.

Rupp, B. (2010). Biomolecular Crystallography - Principles, Practice, and Application to Structural Biology (Garland Science).

Saerens, D., and Muyldermans, S. (2012). Introduction to heavy chain antibodies and derived Nanobodies. Methods Mol. Biol. *911*, 15–26.

Salazar, J., Mena, N., Hunot, S., Prigent, A., Alvarez-Fischer, D., Arredondo, M., Duyckaerts, C., Sazdovitch, V., Zhao, L., Garrick, L.M., et al. (2008). Divalent metal transporter 1 (DMT1) contributes to neurodegeneration in animal models of Parkinson's disease. Proc. Natl. Acad. Sci. U. S. A. *105*, 18578–18583.

Sanders, C.R., and Nagy, J.K. (2000). Misfolding of membrane proteins in health and disease: the lady or the tiger? Curr. Opin. Struct. Biol. *10*, 438–442.

Sasaki, A., Yamaji, N., Yokosho, K., and Ma, J.F. (2012). Nramp5 is a major transporter responsible for manganese and cadmium uptake in rice. Plant Cell *24*, 2155–2167.

Schacter, B.A. (1988). Heme catabolism by heme oxygenase: physiology, regulation, and mechanism of action. Semin. Hematol. *25*, 349–369.

Schatz, G. (2003). Mighty manganese. FEBS Lett. *551*, 1–2.

Schneider, T.R., and Sheldrick, G.M. (2002). Substructure solution with SHELXD. Acta Crystallogr. D. Biol. Crystallogr. *58*, 1772–1779.

Schroeder, H.W. (2006). Similarity and divergence in the development and expression of the mouse and human antibody repertoires. Dev. Comp. Immunol. *30*, 119–135.

Schulze, S., Köster, S., Geldmacher, U., Terwisscha van Scheltinga, A.C., and Kühlbrandt, W. (2010). Structural basis of Na(+)-independent and cooperative substrate/product antiport in CaiT. Nature *467*, 233–236.

Sendamarai, A.K., Ohgami, R.S., Fleming, M.D., and Lawrence, C.M. (2008). Structure of the membrane proximal oxidoreductase domain of human Steap3, the dominant ferrireductase of the erythroid transferrin cycle. Proc. Natl. Acad. Sci. U. S. A. *105*, 7410–7415.

Shaffer, P.L., Goehring, A., Shankaranarayanan, A., and Gouaux, E. (2009). Structure and mechanism of a Na+-independent amino acid transporter. Science *325*, 1010–1014.

Shawki, A., Knight, P.B., Maliken, B.D., Niespodzany, E.J., and Mackenzie, B. (2012). H(+)-coupled divalent metal-ion transporter-1: functional properties, physiological roles and therapeutics. Curr. Top. Membr. *70*, 169–214.

Shi, Y. (2013). Common folds and transport mechanisms of secondary active transporters. Annu. Rev. Biophys. *42*, 51–72.

Shimamura, T., Weyand, S., Beckstein, O., Rutherford, N.G., Hadden, J.M., Sharples, D., Sansom, M.S.P., Iwata, S., Henderson, P.J.F., and Cameron, A.D. (2010). Molecular basis of alternating access membrane transport by the sodium-hydantoin transporter Mhp1. Science *328*, 470–473.

Singh, S.K., Yamashita, A., and Gouaux, E. (2007). Antidepressant binding site in a bacterial homologue of neurotransmitter transporters. Nature *448*, 952–956.

Singh, S.K., Piscitelli, C.L., Yamashita, A., and Gouaux, E. (2008). A competitive inhibitor traps LeuT in an open-to-out conformation. Science *322*, 1655–1661.

Sipe, D.M., and Murphy, R.F. (1991). Binding to cellular receptors results in increased iron release from transferrin at mildly acidic pH. J. Biol. Chem. *266*, 8002–8007.

Skaar, E.P. (2010). The battle for iron between bacterial pathogens and their vertebrate hosts. PLoS Pathog. *6*, e1000949.

Smith, M.A., Harris, P.L., Sayre, L.M., and Perry, G. (1997). Iron accumulation in Alzheimer disease is a source of redox-generated free radicals. Proc. Natl. Acad. Sci. U. S. A. *94*, 9866–9868.

Soda, R., and Tavassoli, M. (1984). Liver endothelium and not hepatocytes or Kupffer cells have transferrin receptors. Blood *63*, 270–276.

Soe-Lin, S., Sheftel, A.D., Wasyluk, B., and Ponka, P. (2008). Nramp1 equips macrophages for efficient iron recycling. Exp. Hematol. *36*, 929–937.

Soe-Lin, S., Apte, S.S., Andriopoulos, B., Andrews, M.C., Schranzhofer, M., Kahawita, T., Garcia-Santos, D., and Ponka, P. (2009). Nramp1 promotes efficient macrophage recycling of iron following erythrophagocytosis in vivo. Proc. Natl. Acad. Sci. U. S. A. *106*, 5960–5965.

Soe-Lin, S., Apte, S.S., Mikhael, M.R., Kayembe, L.K., Nie, G., and Ponka, P. (2010). Both Nramp1 and DMT1 are necessary for efficient macrophage iron recycling. Exp. Hematol. *38*, 609–617.

States, D.J., and Gish, W. (1994). Combined use of sequence similarity and codon bias for coding region identification. J. Comput. Biol. *1*, 39–50.

Steinbicker, A.U., and Muckenthaler, M.U. (2013). Out of balance--systemic iron homeostasis in iron-related disorders. Nutrients *5*, 3034–3061.

Takahashi, R., Ishimaru, Y., Senoura, T., Shimo, H., Ishikawa, S., Arao, T., Nakanishi, H., and Nishizawa, N.K. (2011). The OsNRAMP1 iron transporter is involved in Cd accumulation in rice. J. Exp. Bot. *62*, 4843–4850.

Tandy, S., Williams, M., Leggett, A., Lopez-Jimenez, M., Dedes, M., Ramesh, B., Srai, S.K., and Sharp, P. (2000). Nramp2 Expression Is Associated with pH-dependent Iron Uptake across the Apical Membrane of Human Intestinal Caco-2 Cells. J. Biol. Chem. *275*, 1023–1029.

Tang, L., Bai, L., Wang, W., and Jiang, T. (2010). Crystal structure of the carnitine transporter and insights into the antiport mechanism. Nat. Struct. Mol. Biol. *17*, 492–496.

Tereshko, V., Uysal, S., Koide, A., Margalef, K., Koide, S., and Kossiakoff, A.A. (2008). Toward chaperone-assisted crystallography: protein engineering enhancement of crystal packing and X-ray phasing capabilities of a camelid single-domain antibody (VHH) scaffold. Protein Sci. *17*, 1175–1187.

Theobald, D.L., and Miller, C. (2010). Membrane transport proteins: surprises in structural sameness. Nat. Struct. Mol. Biol. *17*, 2–3.

Thomine, S., Wang, R., Ward, J.M., Crawford, N.M., and Schroeder, J.I. (2000). Cadmium and iron transport by members of a plant metal transporter family in Arabidopsis with homology to Nramp genes. Proc. Natl. Acad. Sci. U. S. A. *97*, 4991–4996.

Tsai, M.-F., and Miller, C. (2013). Substrate selectivity in arginine-dependent acid resistance in enteric bacteria. Proc. Natl. Acad. Sci. U. S. A. *110*, 5893–5897.

Ujwal, R., and Bowie, J.U. (2011). Crystallizing membrane proteins using lipidic bicelles. Methods *55*, 337–341.

Vidal, S., Belouchi, A.M., Cellier, M., Beatty, B., and Gros, P. (1995a). Cloning and characterization of a second human NRAMP gene on chromosome 12q13. Mamm. Genome *6*, 224–230.

Vidal, S., Tremblay, M.L., Govoni, G., Gauthier, S., Sebastiani, G., Malo, D., Skamene, E., Olivier, M., Jothy, S., and Gros, P. (1995b). The Ity/Lsh/Bcg locus: natural resistance to infection with intracellular parasites is abrogated by disruption of the Nramp1 gene. J. Exp. Med. *182*, 655–666.

Vidal, S.M., Malo, D., Vogan, K., Skamene, E., and Gros, P. (1993). Natural resistance to infection with intracellular parasites: isolation of a candidate for Bcg. Cell *73*, 469–485.

Viklund, H., Bernsel, A., Skwark, M., and Elofsson, A. (2008). SPOCTOPUS: a combined predictor of signal peptides and membrane protein topology. Bioinformatics *24*, 2928–2929.

Vulpe, C.D., Kuo, Y.M., Murphy, T.L., Cowley, L., Askwith, C., Libina, N., Gitschier, J., and Anderson, G.J. (1999). Hephaestin, a ceruloplasmin homologue implicated in intestinal iron transport, is defective in the sla mouse. Nat. Genet. *21*, 195–199.

Wagner, S., Baars, L., Ytterberg, a J., Klussmeier, A., Wagner, C.S., Nord, O., Nygren, P.-A., van Wijk, K.J., and de Gier, J.-W. (2007). Consequences of membrane protein overexpression in Escherichia coli. Mol. Cell. Proteomics *6*, 1527–1550.

Waldo, G.S., Standish, B.M., Berendzen, J., and Terwilliger, T.C. (1999). Rapid protein-folding assay using green fluorescent protein. Nat. Biotechnol. *17*, 691–695.

Weyand, S., Shimamura, T., Yajima, S., Suzuki, S., Mirza, O., Krusong, K., Carpenter, E.P., Rutherford, N.G., Hadden, J.M., O'Reilly, J., et al. (2008). Structure and molecular mechanism of a nucleobase-cation-symport-1 family transporter. Science *322*, 709–713.

White, S.H., and von Heijne, G. (2004). The machinery of membrane protein assembly. Curr. Opin. Struct. Biol. *14*, 397–404.

White, C., Yuan, X., Schmidt, P.J., Bresciani, E., Samuel, T.K., Campagna, D., Hall, C., Bishop, K., Calicchio, M.L., Lapierre, A., et al. (2013). HRG1 is essential for heme transport from the phagolysosome of macrophages during erythrophagocytosis. Cell Metab. *17*, 261–270.

White, J.K., Stewart, A., Popoff, J.-F., Wilson, S., and Blackwell, J.M. (2004). Incomplete glycosylation and defective intracellular targeting of mutant solute carrier family 11 member 1 (Slc11a1). Biochem. J. *382*, 811–819.

Williams, L.E., Pittman, J.K., and Hall, J.. (2000). Emerging mechanisms for heavy metal transport in plants. Biochim. Biophys. Acta - Biomembr. *1465*, 104–126.

Winter, G., Griffiths, A.D., Hawkins, R.E., and Hoogenboom, H.R. (1994). Making antibodies by phage display technology. Annu. Rev. Immunol. *12*, 433–455.

World Health Organization (2008). Worldwide prevalence of anaemia 1993-2005 WHO Global Database on Anaemia.

Xie, H., and Hong, Æ.X.G.Æ. (2009). Making the Most of Fusion Tags Technology in Structural Characterization of Membrane Proteins. Mol. Biotechnol. 135–145.

Xue, R., Wang, S., Qi, H., Song, Y., Xiao, S., Wang, C., and Li, F. (2009). Structure and topology of Slc11a1(164-191) with G169D mutation in membrane-mimetic environments. J. Struct. Biol. *165*, 27–36.

Yamashita, A., Singh, S.K., Kawate, T., Jin, Y., and Gouaux, E. (2005). Crystal structure of a bacterial homologue of Na+/Cl--dependent neurotransmitter transporters. Nature *437*, 215–223.

Yeh, K.-Y., Yeh, M., Mims, L., and Glass, J. (2009). Iron feeding induces ferroportin 1 and hephaestin migration and interaction in rat duodenal epithelium. Am. J. Physiol. Gastrointest. Liver Physiol. *296*, G55–G65.

Yeh, K.Y., Yeh, M., Watkins, J.A., Rodriguez-Paris, J., and Glass, J. (2000). Dietary iron induces rapid changes in rat intestinal divalent metal transporter expression. Am. J. Physiol. Gastrointest. Liver Physiol. *279*, G1070–G1079.

Yruela, I. (2013). Transition metals in plant photosynthesis. Metallomics *5*, 1090–1109.

Zaharik, M.L., Cullen, V.L., Fung, A.M., Libby, S.J., Choy, S.L.K., Coburn, B., Kehres, D.G., Maguire, M.E., Fang, F.C., and Finlay, B.B. (2004). The Salmonella enterica Serovar Typhimurium Divalent Cation Transport Systems MntH and SitABCD Are Essential for Virulence in an Nramp1 G169 Murine Typhoid Model. Society *72*, 5522–5525.

Zakin, M. (1992). Regulation of transferrin gene expression. FASEB J *6*, 3253–3258.

Zhang, F., Tao, Y., Zhang, Z., Guo, X., An, P., Shen, Y., Wu, Q., Yu, Y., and Wang, F. (2012a). Metalloreductase Steap3 coordinates the regulation of iron homeostasis and inflammatory responses. Haematologica *97*, 1826–1835.

Zhang, Z., Kodumuru, V., Sviridov, S., Liu, S., Chafeev, M., Chowdhury, S., Chakka, N., Sun, J., Gauthier, S.J., Mattice, M., et al. (2012b). Discovery of benzylisothioureas as potent divalent metal transporter 1 (DMT1) inhibitors. Bioorg. Med. Chem. Lett. *22*, 5108–5113.

Zheng, W., Xin, N., Chi, Z.-H., Zhao, B.-L., Zhang, J., Li, J.-Y., and Wang, Z.-Y. (2009). Divalent metal transporter 1 is involved in amyloid precursor protein processing and Abeta generation. FASEB J. *23*, 4207–4217.

(2011). OCTOPUS: Prediction of membrane protein topology http://octopus.cbr.su.se/. Bioinformatics 2011–2011.